



<https://theses.gla.ac.uk/>

Theses Digitisation:

<https://www.gla.ac.uk/myglasgow/research/enlighten/theses/digitisation/>

This is a digitised version of the original print thesis.

Copyright and moral rights for this work are retained by the author

A copy can be downloaded for personal non-commercial research or study, without prior permission or charge

This work cannot be reproduced or quoted extensively from without first obtaining permission in writing from the author

The content must not be changed in any way or sold commercially in any format or medium without the formal permission of the author

When referring to this work, full bibliographic details including the author, title, awarding institution and date of the thesis must be given

Enlighten: Theses

<https://theses.gla.ac.uk/>
research-enlighten@glasgow.ac.uk

**UNIVERSITY OF GLASGOW
DEPARTMENT OF AEROSPACE ENGINEERING**



**UNIVERSITY
of
GLASGOW**

Dynamics, Stability and Control of Displaced Non-Keplerian Orbits

A thesis submitted to the Department of Aerospace Engineering of
the University of Glasgow by

John Paterson Bookless

in fulfilment of the requirements for degree of
Doctor of Philosophy

Supervisors:

Prof Colin McInnes
&
Dr Gianmarco Radice

ProQuest Number: 10390553

All rights reserved

INFORMATION TO ALL USERS

The quality of this reproduction is dependent upon the quality of the copy submitted.

In the unlikely event that the author did not send a complete manuscript and there are missing pages, these will be noted. Also, if material had to be removed, a note will indicate the deletion.



ProQuest 10390553

Published by ProQuest LLC (2017). Copyright of the Dissertation is held by the Author.

All rights reserved.

This work is protected against unauthorized copying under Title 17, United States Code
Microform Edition © ProQuest LLC.

ProQuest LLC.
789 East Eisenhower Parkway
P.O. Box 1346
Ann Arbor, MI 48106 – 1346

GLASGOW
UNIVERSITY
LIBRARY:

Abstract

Non-Keplerian trajectories around the Lagrange points of the three-body problem have been thoroughly investigated enabling many novel space science missions. Identification of heteroclinic manifolds linking halo orbits around the L_1 and L_2 Lagrange points has led to the discovery of the so-called interplanetary superhighway. This thesis considers possible periodic and quasi-periodic non-Keplerian orbits around artificial libration points generated using solar sail propulsion.

Dynamical models are developed to represent the motion of a solar sail in a two- and three-body context. Artificial libration points are identified using the solar sail to provide a constant axial force. The stability of these libration points is investigated using a linear approximation of the equations of motion and a non-linear analysis. Established techniques are applied to identify halo orbits and Lissajous trajectories around these libration points. Manifolds are identified to provide transfer trajectories to these orbits from near the Earth. Solar sail control techniques are developed to prevent escape from the nominal orbit after insertion.

Acknowledgements

I would like to thank my supervisors, Prof Colin McInnes and Dr Gianmarco Radice for their advice and encouragement throughout my PhD research. I would also like to thank the staff and research students in the Aerospace Engineering department at the University of Glasgow and in the Mechanical Engineering department at the University of Strathclyde for their support and friendship.

I would like to thank Lockheed Martin and University of Glasgow for their financial support which has allowed me to complete this research. I would also like to thank the Royal Academy of Engineering, the Cross Trust and the ESA Outreach scheme for giving me the opportunity to attend conferences and present my research.

Finally, I would like to thank my Mum and Dad for their patience, encouragement and support throughout my university studies. I would also like to thank Karen, Jamie and Pauline for helping me keep things in perspective and remain sane.

Nomenclature

a	-	solar sail acceleration due to solar radiation pressure
A	-	linear coefficient matrix
B	-	linear control matrix
c	-	speed of light
C	-	Jacobi constant
e	-	orbit eccentricity
e_p, e_θ, e_z	-	cylindrical polar coordinates unit vectors
E	-	total orbit energy
F	-	force due to solar radiation pressure
G	-	gain matrix
h_z	-	z-component of angular momentum
H	-	Hamiltonian
i, j, k	-	Cartesian unit vectors
I	-	identity matrix
J	-	Bessel function of the first kind
L	-	characteristic length
m	-	mass of solar sail
M	-	mass of primary bodies
n	-	solar sail surface normal vector
N	-	control weighting matrix
P_x, P_y, P_z	-	Cartesian coordinate momenta terms
P_ρ, P_θ, P_z	-	cylindrical polar coordinate momenta terms
Q	-	state weighting matrix
r	-	separation distance between solar sail and central body
R	-	separation distance between primary bodies
R_s	-	separation distance between Sun and solar sail
t	-	time
T	-	kinetic energy
u	-	control matrix
U	-	pseudo-potential energy
v	-	solar sail velocity magnitude
V	-	gravitational potential energy

x,y,z	-	Cartesian coordinates with x -axis orientated along the Sun-line
\mathbf{x}	-	state matrix
\mathbf{y}	-	output matrix
X,Y,Z	-	Cartesian coordinates in inertial reference frame
α	-	solar sail pitch angle relative to Sun-line
β	-	lightness number
Δv	-	change in velocity
ε	-	Poincaré-Lindstedt expansion parameter
ϕ	-	sail yaw angle
Φ	-	Hamilton-Jacobi separation constant
κ	-	non-dimensionalised solar sail acceleration
μ	-	gravitational parameter
μ_s	-	solar gravitational parameter
Θ	-	angular position of planet orbiting the Sun
ω	-	angular velocity of circular displaced orbit
Ω	-	angular velocity of planet orbiting the Sun
ρ, θ, z	-	cylindrical polar coordinates with z -axis orientated along Sun-line
σ	-	mass loading parameter
τ	-	characteristic time
ξ, η	-	parabolic coordinates/ confocal elliptical coordinates

Contents

Abstract	i
Acknowledgements.....	ii
Nomenclature	iii
Contents	v
List of figures	ix
List of tables	xiv
Chapter 1 Introduction.....	1
1.1 Contribution of thesis	1
1.2 Keplerian motion.....	3
1.3 The three-body problem	5
1.4 Non-Keplerian orbits.....	7
1.4.1 Orbits around the Lagrange points	7
1.4.2 Invariant manifolds.....	9
1.4.3 Lagrange point missions	12
1.4.3.1 ISEE-3 spacecraft	12
1.4.3.2 MAP spacecraft	13
1.4.3.3 Genesis mission	13
1.5 Solar Sailing.....	15
1.5.1 Solar sail concept.....	15
1.5.2 Solar sails – current technology	17
1.5.3 Solar sail acceleration	20
1.5.4 Artificial libration points.....	24
1.5.5 Sun displaced non-Keplerian orbits.....	27
1.6 Objectives of thesis	33
1.7 Outline of thesis	34
Chapter 2 Two-body Non-Keplerian Orbits	38
2.1 Two-body problem.....	38
2.2 Stability analysis	43
2.2.1 Linear stability condition	43
2.2.2 Nonlinear stability condition.....	47
2.2.3 Jacobi-type energy surfaces	51
2.3 Closed form solution of two-body problem.....	53

2.3.1	Closed form solution using parabolic coordinates	53
2.3.2	Paraboloid bounding surfaces	57
2.3.3	Periodic Looping Trajectory	60
2.3.4	Orbit insertion via invariant manifolds	66
2.4	Linear control techniques	69
2.4.1	Feedback control theory	69
2.4.2	Controllability and observability	71
2.4.3	Root locus plot	72
2.4.4	Optimal control – linear quadratic regulator	74
2.4.5	Solar sail area variation control	75
2.4.5.1	Design of state equations	75
2.4.5.2	Root-locus method	76
2.4.5.3	Optimal Control Method	79
2.4.6	Solar sail pitch angle control	81
2.4.6.1	Design of state equations	81
2.4.6.2	Root locus method	82
2.4.6.3	Optimal control method	85
2.5	Conclusions	88
Chapter 3	Three Body Non-Keplerian Orbits – Hill’s approximation	89
3.1	Hill’s approximation of the three-body problem	89
3.2	Libration points	93
3.2.1	On-axis libration points	93
3.2.2	Jacobi integral	95
3.3	Circular displaced non-Keplerian orbit	101
3.3.1	Planet dependant acceleration perturbation	101
3.3.2	Stability of circular displaced non-Keplerian orbit	102
3.3.3	Periodic looping trajectories	105
3.3.4	Optimal control of circular displaced orbits	111
3.3.4.1	Hill’s sail area controller	111
3.3.4.2	Sail pitch and yaw controller	114
3.4	Non-Keplerian orbit dynamics far from the central-body	118
3.4.1	Linear solution to Hill’s approximation	118
3.4.2	Lissajous orbits using Hill’s equations	122
3.4.3	Optimal controller for Lissajous orbits	125
3.4.3.1	Solar sail area control	125
3.4.3.2	Solar sail pitch and yaw control	127

3.4.4	Lissajous orbit control near L_1 and L_2	128
3.4.4.1	Solar sail control near L_2	128
3.4.4.2	Solar sail control near L_1	132
3.5	Conclusions.....	138
Chapter 4	Three body non-Keplerian orbits – Restricted Problem.....	139
4.1	Restricted three-body problem.....	139
4.1.1	Circular restricted three-body problem.....	139
4.1.2	Elliptical restricted three-body problem.....	143
4.2	Ballistic and artificial Lagrange points.....	149
4.2.1	Classical Lagrange points.....	149
4.2.2	Artificial libration points.....	150
4.2.3	Libration points in the elliptical restricted problem.....	151
4.3	Jacobi integral.....	153
4.3.1	Jacobi integral of the circular restricted problem.....	153
4.3.2	Zero-velocity surfaces of the Lagrange points.....	154
4.3.3	Zero-velocity surfaces of artificial libration points.....	155
4.4	Periodic halo orbits.....	157
4.4.1	Richardson's method.....	157
4.4.2	Approximate periodic solution.....	162
4.4.2.1	Linear solution.....	163
4.4.2.2	Second order solution.....	166
4.4.2.3	Third order solution.....	168
4.4.3	Halo orbits around artificial libration points.....	171
4.4.3.1	Differential correction methods.....	171
4.4.3.2	Halo orbits sunward of L_2	177
4.4.3.3	Halo orbits sunward of L_1	178
4.4.4	Control of periodic halo orbits using solar sail control laws.....	180
4.4.4.1	Three-axis controller design.....	180
4.4.4.2	Control of periodic halo orbit sunward of L_2	183
4.4.4.3	Control of periodic halo orbit sunward of L_1	187
4.5	Conclusions.....	193
Chapter 5	Two-Centre Problem.....	194
5.1	Gravitational two-centre problem.....	194
5.1.1	Gravitational two-centre equations of motion.....	194
5.1.2	On-axis libration points.....	196
5.1.3	Halo orbits around Libration points.....	198

5.2	Photo-gravitational two-centre problem.....	202
5.2.1	Investigation of interstellar libration points.....	202
5.2.2	Photo-gravitational two-centre equations of motion.....	203
5.2.3	Light extinction.....	205
5.2.4	Halo orbits around libration points.....	206
5.3	Closed-form solution of the two-centre problem.....	209
5.3.1	Derivation using confocal elliptical coordinates.....	209
5.3.2	Stable halo orbits bound by elliptical surfaces.....	213
5.3.3	Elliptical bounding surfaces for unstable initial conditions.....	216
5.3.4	Stellar transfer trajectories.....	219
5.4	Effect of additional body on two-centre dynamics.....	221
5.4.1	Local stellar neighbourhood.....	221
5.4.2	Derivation of gravity perturbed two-centre equations.....	223
5.4.3	Gravity perturbed two-centre libration points.....	225
5.5	Two-centre problem with relative stellar motion.....	229
5.5.1	Relative stellar motion.....	229
5.5.2	Derivation of two-centre equations including relative stellar motion.....	230
5.5.3	Motion of on-axis libration point.....	231
5.5.4	Halo orbits including the effects of stellar motion.....	233
5.6	Conclusions.....	239
Chapter 6	Mission Analysis.....	240
6.1	Geomagnetic tail mission.....	240
6.1.1	Mission outline.....	240
6.1.2	Hohmann transfer manoeuvre.....	241
6.1.3	Trajectory analysis.....	243
6.1.4	Conclusions.....	248
6.2	Geostorm mission.....	249
6.2.1	Mission outline.....	249
6.2.2	Trajectory analysis.....	250
6.2.3	Conclusions.....	255
Chapter 7	Conclusions and Further Work.....	256
Chapter 8	References.....	263
Chapter 9	Appendix 1.....	272

List of figures

Figure 1-1 Schematic representing elliptical orbit with the Sun located at the focus S	4
Figure 1-2 Schematic of Lagrange points in synodic reference frame.....	6
Figure 1-3 (a) Halo orbit around L_2 generated using Richardson's 3 rd order solution (b) Lissajous orbit around L_2 generated using 1st order solution	7
Figure 1-4 Invariant manifold surface produced for the Sun-Jupiter system [Koon et al, 1999].....	10
Figure 1-5 ISEE-C Insertion to halo orbit at L_1 [Farquhar, 2001].....	12
Figure 1-6 MAP spacecraft trajectory for insertion to L_2 Lissajous orbit	13
Figure 1-7 The Genesis trajectory centred on the Earth [Serban et al, 2002].....	14
Figure 1-8 Incident and reflected photons on a flat sail.....	21
Figure 1-9 Schematic representing photons incident on a non-perfectly reflecting sail	23
Figure 1-10 Schematic representing circular restricted three-body problem [McInnes, 1998a].....	24
Figure 1-11 Possible libration points in the Earth-Sun system for ideal flat solar sail	26
Figure 1-12 Possible libration points in the Earth-Sun system for partially reflecting flat solar sail ($\rho_s=0.9$)	27
Figure 1-13 Sun-centred displaced orbits [McInnes, 1992a]	28
Figure 1-14 Sail loading parameter contours for Mercury synchronous orbits.....	31
Figure 1-15 Sail loading parameter contours for Venus synchronous orbits	31
Figure 1-16 Sail loading parameter contours for Earth synchronous orbits	32
Figure 1-17 Sail loading parameter contours for Mars synchronous orbits	32
Figure 2-1 Schematic of two-body displaced non-Keplerian orbit.....	39
Figure 2-2 $\kappa(\rho,z)$ acceleration contours for range of orbit displacement and radius	42
Figure 2-3 $\dot{\theta}(\rho,z)$ angular velocity contours for range of orbit displacements and radii	42
Figure 2-4 Stable non-Keplerian orbit with perturbation applied.....	46
Figure 2-5 Unstable non-Keplerian orbit with perturbation applied.....	46
Figure 2-6 Potential energy function for stable initial orbit conditions	49
Figure 2-7 Potential energy function for unstable initial orbit conditions	50
Figure 2-8 Stability of orbits investigated using an iterative method.....	50
Figure 2-9 Zero velocity surface of a stable non-Keplerian orbit.....	52
Figure 2-10 Zero velocity surface of an unstable non-Keplerian orbit	53
Figure 2-11 Stable displaced non-Keplerian orbit bound between parabolae	58
Figure 2-12 Enlarged view of bound orbit provided in Fig 2-11.....	58
Figure 2-13 Stable displaced non-Keplerian orbit bound between parabolae	59
Figure 2-14 Stable displaced non-Keplerian orbit bound between parabolae	59
Figure 2-15 Stable displaced non-Keplerian orbit with initial velocity applied	60
Figure 2-16 Stable orbit with small acceleration perturbation applied ($\Lambda=0.01$).....	61
Figure 2-17 Radial and z-displacement variation due to small acceleration perturbation	61
Figure 2-18 3D Cartesian plot of stable orbit with small acceleration perturbation	62
Figure 2-19 Unstable orbit with small acceleration perturbation	63
Figure 2-20 Unstable orbit with small acceleration perturbation	63
Figure 2-21 Periodic looping trajectory generated by perturbing the nominal acceleration	64

Figure 2-22 Radial and z-displacement variation due to small acceleration perturbation.....	64
Figure 2-23 3D Cartesian representation of looping orbit bound within paraboloid surfaces.....	65
Figure 2-24 Closest approach distance to central body for range of initial orbit conditions ($\Delta=0.01$)	66
Figure 2-25 Periodic looping orbit inserted at $r_{min} = 3.6382 L$ from the central body.....	68
Figure 2-26 Closed-loop system with unity feedback	69
Figure 2-27 System $H(s)$ with negative feedback control using gain G	72
Figure 2-28 Root-locus plot for area variation control	78
Figure 2-29 Orbit insertion with linear area control	78
Figure 2-30 Solar sail acceleration variation and area variation	79
Figure 2-31 Orbit insertion with optimal linear area control	80
Figure 2-32 Solar sail acceleration variation and area variation	80
Figure 2-33 Root-locus plot for pitch angle variation control.....	83
Figure 2-34 Orbit insertion with linear pitch angle control.....	84
Figure 2-35 Pitch angle variation required to control orbit.....	84
Figure 2-36 Acceleration directed along e_p and e_z axes normalized with respect to κ_0	85
Figure 2-37 Orbit insertion with optimal linear pitch angle control.....	86
Figure 2-38 Pitch angle variation achieved using an optimal controller.....	86
Figure 2-39 Acceleration directed along e_p and e_z axes normalized with respect to κ_0	87
Figure 3-1 Schematic of Hill's problem with displaced solar sail orbit.....	89
Figure 3-2 Artificial libration points generated using solar sail acceleration.....	94
Figure 3-3 Constant energy surfaces corresponding to libration points sunward of L_2	97
Figure 3-4 Constant energy surfaces corresponding to libration points sunward of L_1	97
Figure 3-5 Series of zero-velocity surfaces for the ballistic case ($\kappa=0$).....	98
Figure 3-6 Trajectory bound within zero-velocity surface.....	99
Figure 3-7 Transfer from exterior region to interior region via gap in zero-velocity surface	99
Figure 3-8 Series of zero-velocity surfaces of increasing energy for $\kappa=2.5$	100
Figure 3-9 Series of zero-velocity surfaces of increasing energy for $\kappa=0.0592$	101
Figure 3-10 Stable circular displaced orbit computed using Hill's equations.....	103
Figure 3-11 Unstable circular displaced orbit computed using Hill's equations.....	103
Figure 3-12 Stability of circular displaced Hills orbits.....	104
Figure 3-13 Stable orbit with perturbed acceleration computed using Hill's equations	106
Figure 3-14 Unstable orbit with perturbed acceleration computed using Hill's equations	106
Figure 3-15 Periodic looping trajectory computed using Hill's equations.....	107
Figure 3-16 Trajectories generated using mirror image theorem	110
Figure 3-17 Circular planet displaced orbit achieved using sail area control.....	113
Figure 3-18 Solar sail acceleration and area variation required to control orbit.....	113
Figure 3-19 Converting cylindrical polar pitch and roll angles into corresponding Cartesian pitch and yaw angles.....	115
Figure 3-20 Circular Earth displaced orbit achieved using sail pitch and yaw angle control.....	116
Figure 3-21 Pitch and yaw angle variation required to control orbit.....	116
Figure 3-22 Yaw against pitch angle representing motion of the solar sail normal.....	117
Figure 3-23 Quasi-periodic Lissajous trajectory	122
Figure 3-24 Lissajous trajectory generated by integrating linearised Hills equations about L_2	123

Figure 3-25 Lissajous trajectories around L_2 for A_y amplitude equal to orbit number	124
Figure 3-26 Lissajous trajectory around L_2 computed using corrected initial conditions	125
Figure 3-27 Hill's surface bounding insertion conditions to Lissajous orbit near L_2	129
Figure 3-28 Insertion to Lissajous orbit around $x_0=230 R_E$ controlled using sail area variation.....	129
Figure 3-29 Enlarged view of Lissajous orbit around $x_0=230 R_E$	130
Figure 3-30 Acceleration and area variation required to control Lissajous orbit	130
Figure 3-31 Insertion to Lissajous orbit around $x_0=230R_E$ controlled using pitch and yaw angle variation ..	131
Figure 3-32 Enlarged view of Lissajous orbit around $x_0=230R_E$	131
Figure 3-33 Pitch and Yaw angle variation required to control Lissajous orbit.....	132
Figure 3-34 Hill's surface bounding insertion conditions to Lissajous orbit near L_1	133
Figure 3-35 Insertion to Lissajous orbit around $x_0=-240 R_E$ controlled using sail area variation.....	134
Figure 3-36 Enlarged view of Lissajous orbit around $x_0=-240R_E$	134
Figure 3-37 Acceleration and area variation required to control Lissajous orbit	135
Figure 3-38 Insertion to Lissajous orbit around $x_0=-240 R_E$ controlled using pitch and yaw angle variation	136
Figure 3-39 Enlarged view of Lissajous orbit around $x_0=-240 R_E$	136
Figure 3-40 Pitch and yaw angle variation required to control Lissajous orbit.....	137
Figure 4-1 Schematic of circular restricted three-body problem	139
Figure 4-2 Schematic of elliptical orbit where eccentricity $e=0.6$	144
Figure 4-3 Schematic of Lagrange points in the circular restricted problem	150
Figure 4-4 Artificial libration points generated using solar sail acceleration.....	151
Figure 4-5 Variation of artificial libration point position for eccentric orbit	153
Figure 4-6 Zero-velocity surfaces in vicinity of Earth for $C=C_{L1}$ and $C=C_{L2}$	155
Figure 4-7 Zero-velocity surfaces for series of artificial libration points sunward of L_1 and L_2	156
Figure 4-8 Schematic of three-body system with motion of M_3 derived relative to L_1	157
Figure 4-9 Class I and Class II halo orbits around L_2 of Sun-Earth system ($A_x=280,000\text{km}$).....	171
Figure 4-10 Iterative method improving initial conditions towards a periodic halo orbit around L_2	175
Figure 4-11 Iterative method improving initial conditions towards a periodic halo orbit around L_1	176
Figure 4-12 Family of periodic halo orbits around artificial libration sunward of L_2 ($150R_E$ from Earth)	177
Figure 4-13 Minimum y -axis and x -axis amplitude for periodic halo orbit sunward of L_2 ($A_z=0$)	178
Figure 4-14 Family of periodic halo orbits around artificial libration sunward of L_1 ($-300R_E$ from Earth)...	179
Figure 4-15 Minimum y -axis and x -axis amplitude for periodic halo orbit sunward of L_1 ($A_z=0$)	179
Figure 4-16 Controlled periodic halo orbit around artificial libration point in the circular restricted problem	183
Figure 4-17 Solar sail acceleration and corresponding area variation required to control halo orbit.....	184
Figure 4-18 Solar sail pitch and yaw angle variation required to control halo orbit.....	184
Figure 4-19 Controlled periodic halo orbit around artificial libration point in the elliptical restricted problem	185
Figure 4-20 Solar sail acceleration and corresponding area variation required to control halo orbit.....	186
Figure 4-21 Solar sail pitch and yaw angle variation required to control halo orbit.....	186
Figure 4-22 Controlled periodic halo orbit around artificial libration point in the circular restricted problem	187
Figure 4-23 Solar sail acceleration and corresponding area variation required to control halo orbit.....	188
Figure 4-24 Solar sail pitch and yaw angle variation required to control halo orbit.....	188

Figure 4-25 Controlled periodic halo orbit around artificial libration point in the elliptical restricted problem	190
Figure 4-26 Acceleration components for orbit control at orbit sunward of L_1	190
Figure 4-27 Controlled periodic halo orbit around artificial libration point in the elliptical restricted problem	191
Figure 4-28 Solar sail acceleration and corresponding area variation required to control halo orbit.....	192
Figure 4-29 Solar sail pitch and yaw angle variation required to control halo orbit.....	192
Figure 5-1 Schematic of two-centre problem with fixed masses M_1 and M_2	194
Figure 5-2 Eigenvalues of linearised equations over range of equilibria between $0 < z_0 < 1$	198
Figure 5-3 Potential energy function $U(\rho, z)$ for rotating frame around z -axis.....	199
Figure 5-4 Potential energy function $U(\rho, z)$ for rotating frame around z -axis.....	199
Figure 5-5 Contours represent halo orbit initial conditions for varying h_z	200
Figure 5-6 Two-centre halo orbits for system with mass ratio $\lambda=2$	201
Figure 5-7 Schematic of Sun-Centauri system.....	204
Figure 5-8 Possible halo orbit ρ - z values for different particle loading values.....	207
Figure 5-9 Possible halo orbits for particles with loading 3 gm^{-2} (1,2,3) and 0.7 gm^{-2} (4).....	208
Figure 5-10 'Homoclinic-like' trajectory of unstable halo orbit.....	209
Figure 5-11 Perturbed stable orbit bounded by elliptical surfaces.....	214
Figure 5-12 Closer view of bounded perturbed stable orbit.....	214
Figure 5-13 Stable Orbit near Centauri bound by elliptical surfaces.....	215
Figure 5-14 Closer view of stable orbit near Centauri.....	215
Figure 5-15 Stable orbit for particle with loading 0.7 gm^{-2}	216
Figure 5-16 Elliptical surfaces bounding homoclinic trajectory between unstable limit cycle and the Centauri system	217
Figure 5-17 Homoclinic trajectory between unstable limit cycle and the Centauri system	217
Figure 5-18 Elliptical surfaces bounding homoclinic trajectory between unstable limit cycle and the Sun	218
Figure 5-19 Homoclinic trajectory between unstable limit cycle and the Sun.....	218
Figure 5-20 Elliptical surfaces bounding transfer trajectory between the Sun and Centauri.....	220
Figure 5-21 Transfer trajectory between the Sun and Centauri.....	220
Figure 5-22 Local stellar neighbourhood within 3pc.....	221
Figure 5-23 Schematic of three fixed stars Sun-Centauri-Sirius.....	224
Figure 5-24 Potential energy contours of Sun-Centauri-Sirius system ignoring solar radiation pressure.....	226
Figure 5-25 Potential energy contours for particle loading $\sigma=7 \text{ gm}^{-2}$	227
Figure 5-26 Potential energy contours for particle loading $\sigma=3 \text{ gm}^{-2}$	228
Figure 5-27 Potential energy contours for particle loading $\sigma=5 \text{ gm}^{-2}$	228
Figure 5-28 Potential energy contours of the Sun-Centauri system when time $t=0$	232
Figure 5-29 Potential energy contours of the Sun-Centauri system when time $t=1 \times 10^5$ years.....	232
Figure 5-30 Motion of the Centauri system relative to the Sun	233
Figure 5-31 Unstable halo orbit excluding stellar motion.....	234
Figure 5-32 Unstable halo orbit including stellar motion	234
Figure 5-33 Stable halo orbits excluding stellar motion	235
Figure 5-34 Stable halo orbit including stellar motion	235

Figure 5-35 Stable halo orbit including stellar motion	236
Figure 5-36 Bound orbit for case where relative star velocity is of order 1 ms^{-1}	237
Figure 5-37 View of x-y plane for case where relative star velocity is of order 1 ms^{-1}	237
Figure 5-38 Transfer of particle between stars for relative stellar velocity of order 10 ms^{-1}	238
Figure 6-1 Insertion to non-Keplerian orbit with two kick stages	244
Figure 6-2 Sail area variation controlling a non-Keplerian orbit within the Geomagnetic tail	245
Figure 6-3 Required sail area and acceleration variation to prevent escape from a non-Keplerian orbit	245
Figure 6-4 Sail pitch and yaw angle variation controlling a non-Keplerian orbit within the Geomagnetic tail	246
Figure 6-5 Required sail pitch and yaw angle variation to prevent escape from a non-Keplerian orbit	246
Figure 6-6 Pitch and yaw variation required to control orbit	247
Figure 6-7 Required solar sail surface area for increasing total mass	247
Figure 6-8 Required solar sail loading parameter for increasing total mass	248
Figure 6-9 Uncontrolled insertion to a Lissajous orbit from near the Earth with Jacobi Constant $C=-0.01226$	252
Figure 6-10 Insertion from LEO to stable manifold using Hohmann ellipse	252
Figure 6-11 Insertion to Lissajous trajectory at L_1 followed by slow solar sail deployment	253
Figure 6-12 Lissajous trajectory around libration point sunward of L_1	254
Figure 6-13 Solar sail area variation for Geostorm mission	255

List of tables

Table 2-1 Parabolic coordinate values for perturbed initial conditions	57
Table 2-2 Parabolic coordinates representing surfaces bounding a periodic looping trajectory.....	62
Table 2-3 Initial conditions calculated using intersecting paraboloid surfaces	67
Table 2-4 Numerator/Denominator polynomials in terms of s	77
Table 2-5 Numerator/Denominator Polynomials in terms of s	82
Table 3-1 Parameters for selection of planets.....	92
Table 3-2 Location of L_1 and L_2 for various planets in the solar system	94
Table 3-3 Jacobi constants at the Lagrange point (1) and a series of artificial libration points (2-8).....	96
Table 3-4 Lissajous trajectory initial conditions for contours 1-5.....	123
Table 4-1 Location of Lagrange points in ballistic case ($\kappa=0$).....	150
Table 4-2 Position of Lagrange points relative to planet at periapsis and apoapsis.....	152
Table 4-3 Parameters for zero-velocity surfaces evaluated at artificial libration	156
Table 4-4 Initial conditions yielded from the third order approximation and the corrected conditions of L_2 orbit.....	175
Table 4-5 Initial conditions yielded from the third order approximation and the corrected conditions of L_1 orbit.....	176
Table 5-1 Numerically calculated initial conditions for two-centre halo orbits ($\lambda=2$).....	201
Table 5-2 Spectral properties of nearby stars from the NStars database.....	203
Table 5-3 Sail loading a corresponding lightness numbers for Sun-Centauri system.....	207
Table 5-4 Halo orbit initial conditions including orbit period.....	207
Table 5-5 Elliptical coordinates representing surfaces bounding stable orbit	216
Table 5-6 Elliptic coordinates representing surfaces bounding unstable orbit	218
Table 5-7 Elliptic coordinates representing surfaces bounding transfer trajectory.....	219
Table 5-8 Position and spectral data of all stars within 3pc of the Sun	222
Table 5-9 Spectral classification of stars.....	222
Table 5-10 Proper and radial motion of stars relative to the Sun	229
Table 6-1 Insertion conditions for Geomagnetic tail mission	244
Table 6-2 Insertion conditions to uncontrolled Lissajous orbit around L_1	251

1.1 Contribution of thesis

The main objective of this thesis is to investigate possible near-term applications of solar sail technology. Several missions have been achieved using conventional propulsion methods to deliver a payload to an orbit around the L_1 and L_2 Lagrange points. As the solar sail is not reliant on stored reaction mass, continuous thrust can be applied to generate artificial libration points displaced from the ballistic Lagrange points. Previously applied methods to define periodic and quasi-periodic orbits around L_1 and L_2 will be applied in the solar sail dynamical problem to generate orbits around these artificial libration points.

The main contributions of this thesis include:

- Development of dynamical models in a two-body and three-body context to represent the motion of a solar sail in the vicinity of a planet. The acceleration due to solar radiation pressure was included assuming an ideal solar sail surface.
- A two-body stability condition was derived for circular displaced orbits using a linear approximation of the equations of motion and a non-linear analysis. Energy methods were used to verify this condition. It was demonstrated that the two-body stability condition is valid in the three-body problem when the circular displaced orbit is near to the central body.
- Identification of a new family of highly perturbed homoclinic orbits which enable orbit insertion to a circular displaced orbit from near the central body. A closed-form solution to the two-body problem including a uniform axial force was obtained using parabolic coordinates. It was demonstrated that the homoclinic orbits are bound to the surface of a paraboloid which can be used to determine the closest approach distance to the central body explicitly.
- Development of two-body solar sail optimal control techniques to provide station-keeping at a circular displaced orbit. The two techniques investigated were solar sail area variation and sail attitude variation, facilitating control of the sail

acceleration magnitude. These control methods were demonstrated for control of circular displaced orbits in the context of Hill's approximation of the three-body problem.

- Lissajous orbits were generated around artificial libration points using Hill's equations. Manifolds were identified to enable insertion to Lissajous orbits from a point near the Earth. Station-keeping was demonstrated using a similar optimal control technique to that developed for the two-body problem.
- Investigation of halo orbits around artificial libration points in the circular restricted three body problem. Using previously established methods from the ballistic case, such as Richardson's third order approximation it was demonstrated that similar results are achieved around artificial libration points. A three-axis optimal control method combining the sail area and sail attitude control methods applied previously was developed.
- The two-centre problem was applied to approximate the dynamics of particles between two stars. An explicit solution was derived using confocal elliptical coordinates. Homoclinic manifolds were shown to exist which wind on and off an unstable halo orbit. It was demonstrated that these manifolds are bound to an ellipsoid surface.
- Investigation of possible near-term missions which could be enabled using solar sail propulsion. These include a mission to position a science payload in the geomagnetic tail to investigate the processes of magnetic reconnection and another mission to deliver a payload to analyse the solar wind upstream of the L_1 Lagrange point.

1.2 Keplerian motion

Johannes Kepler (1571-1630) formulated his famous three laws of planetary motion during the early decades of the seventeenth century. These three laws are stated as follows

1. The locus plot representing the orbit of a planet around the Sun forms an ellipse with the Sun located at a focus
2. The area swept out by the radial vector representing the position of the planet relative to the Sun is constant for equal times
3. The relationship between the semi-major axis, a , and the orbit period, T , of two planets is defined as

$$\frac{a_1^3}{T_1^2} = \frac{a_2^3}{T_2^2} = c \quad (1.1)$$

where c is a constant [Baker and Makemson, 1960].

These laws were developed while Kepler was investigating the orbit of Mars using observational data obtained by his mentor, Tycho Brahe (1546-1601). The significance of the first two laws is outlined in Fig 1-1. The area swept out by the radial vector forming the arc, **NSO** is equal to the area swept out forming the arc, **PSQ** evaluated over an equal time period. These areas are denoted as A_1 and A_2 respectively. The semi-major and semi-minor axis are denoted as a and b respectively. The centre of the ellipse is represented by **C** and is located at distance ae from the focus **S**, where e represents the orbit eccentricity.

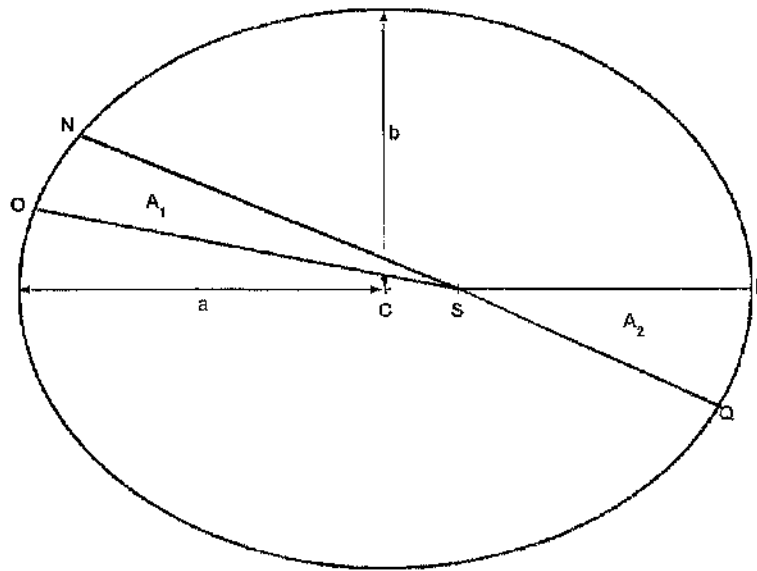


Figure 1-1 Schematic representing elliptical orbit with the Sun located at the focus S

The radial distance, r from the focus S at polar angle θ , measured from the line SP, is expressed using the orbit equation

$$r = \frac{a(1-e^2)}{1+e \cos \theta} \quad (1.2)$$

where $\theta=0$ is referred to as the perihelion of the ellipse and is located at P while the apoapsis is located at $\theta=\pi$.

A scientific explanation for the elliptical motion was provided by Newton (1642-1727) when he devised the universal law of gravity. He postulated that the force due to gravitational attraction between two masses is proportional to the inverse square of the separation distance. Newton demonstrated that the universal law of gravitation provided greater accuracy when predicting planetary position than the approximate calculations of Kepler.

The dynamical two-body problem exhibits Keplerian motion. The two-body model obtains good approximate trajectories for transfers between planets using a patched conic approach. The three-body problem exhibits non-Keplerian motion near the Lagrange points where the gravitational attractions between the two primary masses cancel.

1.3 The three-body problem

Euler (1707-1783) is credited with developing the three-body problem while attempting to produce an accurate model for lunar motion, which could explain the deviation of the observed lunar motion from an ellipse. Perturbations to the elliptical motion of moons were known from observations of the moons of Jupiter.

The three-body equations model the dynamics of a third body in the vicinity of two co-orbiting primary bodies. Euler developed a rotating coordinate system (synodic), which contains the motion of the two primaries [Szebehely, 1967]. Although the three-body problem cannot be solved explicitly, applying some approximations to simplify the dynamics enables solutions to be determined via numerical or perturbation methods.

Approximations include assuming the mass of the third body is infinitely smaller than the mass of the two primary bodies, which leads to the restricted three-body problem. The separation distance between the two primary bodies can also be assumed constant which yields the circular restricted three-body problem. Jacobi (1804-1851) successfully identified an integral in the restricted three-body problem, known as the Jacobi Integral. This integral relates the energy of the infinitesimal body to its velocity in the synodic frame of reference and can be used to determine surfaces which bound a trajectory without the need to solve the non-linear three-body equations [Szebehely, 1967; Marchal, 1990].

Hill (1838-1914) developed a useful representation for lunar motion using an expansion theorem [Hagihara, 1975a]. Hill's problem considers the planar case of three-bodies M_1 , M_2 and M_3 where the mass M_1 is much greater than M_2 or M_3 . If the distance between M_2 and M_3 is large, then the dynamics can be approximated by separate two-body problems M_1 - M_2 and M_1 - M_3 ignoring the gravitational interaction between M_2 and M_3 . If the distance between M_2 and M_3 becomes relatively small, such as the case of the Sun-Earth-Moon three body problem, then the interaction between M_2 and M_3 must also be included [Hénon and Petit, 1986].

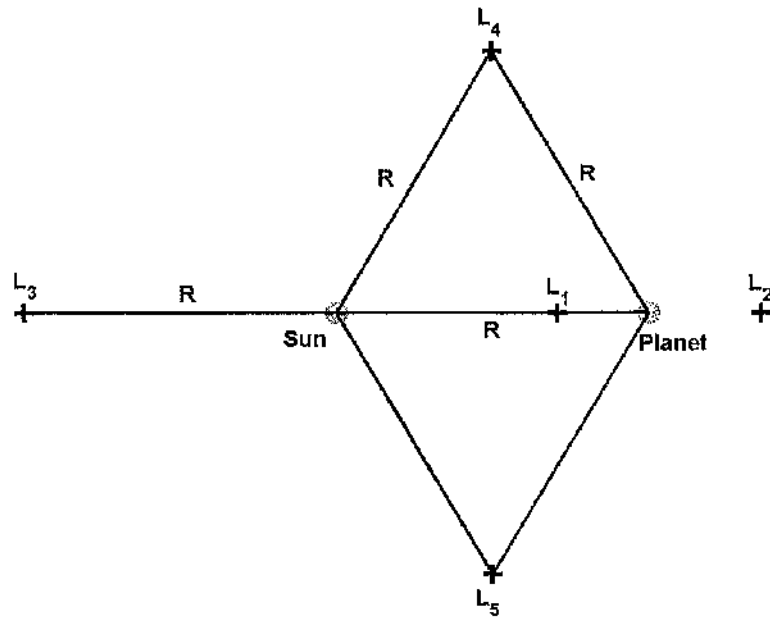


Figure 1-2 Schematic of Lagrange points in synodic reference frame

Solutions exist in the circular restricted three-body problem, which represent equilibrium points in the synodic frame. Euler identified three collinear libration points (L_1 , L_2 , L_3) while two triangular libration points (L_4 , L_5) were identified by Lagrange (1736-1813). The positions of these libration points, referred to as the Lagrange points, are shown in Fig 1-2.

It will be demonstrated, using eigenvalue methods, that the collinear libration points (L_1 , L_2 , L_3) are unstable. This means that a spacecraft initially in the vicinity of these points will escape. The triangular libration points are stable provided the system mass parameter $\mu \leq 0.03852$. The mass parameter is defined in the non-dimensionalised three-body problem as $\mu = M_2 / (M_1 + M_2)$ where M_1 and M_2 represent the primary masses [Szebehely, 1967]. Families of orbits have been identified around these libration points which can be generated using 1st order and 3rd order approximations of the non-linear three-body equations.

1.4 Non-Keplerian orbits

1.4.1 Orbits around the Lagrange points

Darwin (1845-1912) identified a set of periodic orbits around the libration points during the late nineteenth century while investigating the simple planar case of the circular restricted three-body problem. Using numerical methods he was also able to perform a stability analysis of these periodic orbits. During the early twentieth century, Strömgren [1870-1947] and colleagues at the Copenhagen observatory performed similar studies of periodic orbits in the planar three-body case, attempting to classify these orbits depending on stability and their associated libration point [Hagihara, 1975b].

Since these early studies of libration point orbits, the development of the digital computer has enabled more detailed studies. Three types of natural orbit that exist around the collinear Lagrange points include Lyapunov orbits, quasi-periodic Lissajous orbits and periodic halo orbits. Lyapunov orbits exist in the orbit plane of the primary bodies. Halo and Lissajous orbits both contain out-of-plane components so exist in three-dimensions. Examples of these trajectories generated around the L_2 point are provided in Fig 1-3, where the axes scale has units R_E (Earth Radii). As neither of the primary bodies intersects the plane of the orbit, these orbits do not agree with Kepler's laws of motion. It is clear that libration point orbits can be described as non-Keplerian orbits.

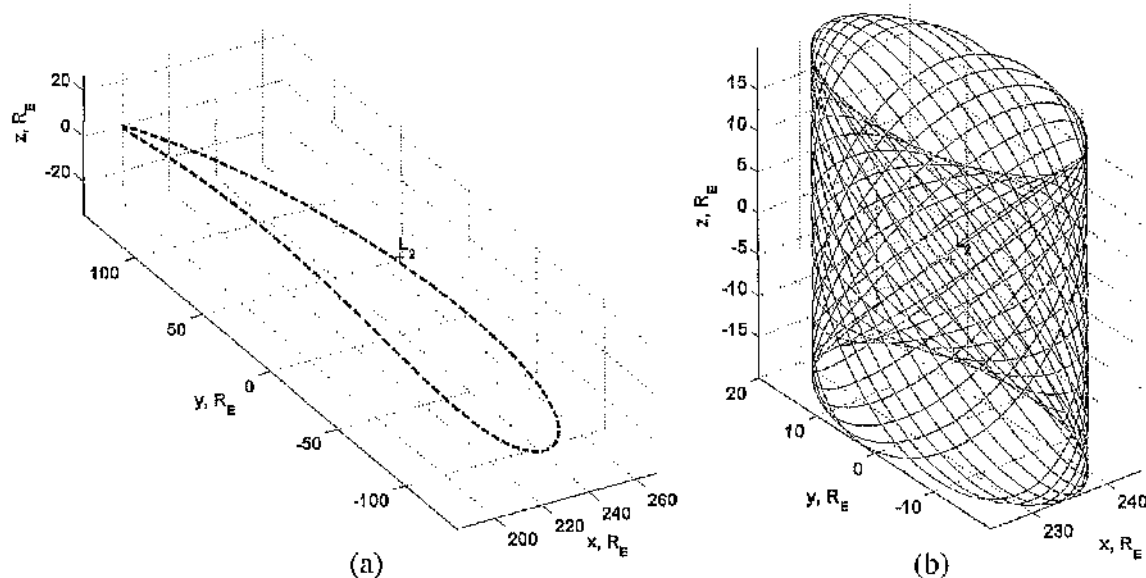


Figure 1-3 (a) Halo orbit around L_2 generated using Richardson's 3rd order solution
(b) Lissajous orbit around L_2 generated using 1st order solution

During the 1960s, libration point orbits became of increasing interest with the possibility of positioning a communication satellite at the Earth-Moon L_2 Lagrange point to enable continuous contact between the Earth and a lunar lander on the rear of the moon. Colombo demonstrated that the stationkeeping requirement to maintain a libration point orbit was dependant on the accuracy of the nominal orbit [Colombo, 1961]. If the approximated nominal orbit agrees closely to the actual non-linear trajectory then the station-keeping requirement is minimised. An inaccurate nominal orbit requires a greatly increased Δv as the controller performs manoeuvres forcing the spacecraft to follow the desired trajectory.

In 1966, Farquhar designed a Lissajous orbit which would be visible from the Earth requiring a small Δv of 10ms^{-1} per year for station-keeping [Dunham and Farquhar, 2002]. Quasi-periodic Lissajous orbits can be generated by linearising the three-body equations of motion. In the x - y plane, the linearised equations have four eigenvalues – two real and two imaginary. By selecting initial conditions which suppress the real eigenvalues, an oscillatory solution is obtained. The out-of-plane motion produces two imaginary eigenvalues. As the ratio of out-of-plane to in-plane oscillation frequency is non-rational, the resulting trajectory is periodic in the x - y plane but there is a precession in the y - z plane. These trajectories are therefore described as quasi-periodic.

The amount of fuel required to provide stationkeeping depends on the accuracy of the nominal orbit when all significant perturbations are included. Farquhar and Kamel [1973] used perturbation methods to derive accurate quasi-periodic orbits in the Earth-Moon system, minimising the stationkeeping requirements. The Linstedt-Poincaré method was applied to develop a third order solution of the non-linear equations including perturbations due to solar gravity and the eccentricity of the Earth-Moon orbit.

By including higher order terms in the approximation of the non-linear equations it is possible to select orbit amplitudes and frequencies which produce a periodic orbit. The resulting ratio of the out-of-plane and in-plane frequency is rational. Farquhar coined the term 'halo' orbits for these trajectories and he used the method of successive approximations to define halo orbits in the Earth-Moon system, including the perturbations caused by orbit eccentricity and the gravitational influence of the Sun [Farquhar, 1970a].

Breakwell and Brown [1979] investigated halo orbits around the L_1 and L_2 Lagrange points in the Earth-Moon system. A differential correction method was applied to improve the

initial conditions which generate the nominal halo orbit. The stability of these orbits was investigated by examining the eigenvalues of the monodromy matrix, constructed by evaluating the fundamental solution matrix at one orbit period. This study identified a family of stable periodic halo orbits halfway between the Lagrange points and the moon. Howell [1984] extended this stability study to consider other three-body mass ratios. Identifying stable periodic orbits would significantly reduce the station-keeping requirements.

Richardson [1980a; 1980b] developed an approximation of the nonlinear Sun-Earth three-body equations by expressing the gravitational potentials in terms of Legendre polynomials. He applied the Lindstedt-Poincaré perturbation method to obtain a third order solution, removing unbound secular terms. A constraint was found relating the out-of-plane amplitude to the in-plane amplitude in order to achieve equal in-plane and out-of-plane frequencies.

1.4.2 Invariant manifolds

Manifolds represent a subspace of dimension m embedded in a space of dimension n , where $m \leq n$. Therefore, a manifold represents a surface in real space such as the surface of a sphere, which has dimension $m=2$ in space \mathcal{R}^3 . The term 'invariant manifold' refers to a manifold to which the motion of a particle is bound for all time [Jordan and Smith, 1999].

Three classes of manifold that will be investigated are stable, unstable and centre manifolds. Halo orbits represent centre manifolds in the three-body dynamics problem. Trajectories which wind-off and wind-onto the centre manifold, asymptotically, represent stable and unstable manifolds of dimension $m=1$. An invariant manifold surface of dimension $m=2$ can be generated by numerically identifying a series of stable and unstable manifolds around the halo orbit. This surface of stable invariant manifolds represents possible transfer trajectories for insertion to a halo orbit from near to the central body. An individual transfer trajectory can be described as a sub-manifold of a 2 dimensional invariant manifold surface [Folta, 2004].

A heteroclinic connection exists between the stable and unstable manifolds winding on and off halo orbits around the L_1 and L_2 Lagrange points. Figure 1-4 shows the intersection between stable and unstable manifolds in the Sun-Jupiter system winding off halo orbits

around L_1 and L_2 , produced by Koon, Lo, Marsden and Ross [Koon et al, 1999]. Transit orbits refer to those inside the tube and non-transit orbits to those outside the tube. The manifold tubes act as a separatrix which defines the boundary between transit orbits and non-transit orbits [Gómez et al, 2004]. The tubes are generated by numerically identifying unstable manifolds which wind off the L_2 halo orbit and pass near to the central body. Stable manifolds, with matching energy to the unstable manifolds, which wind onto a halo orbit around L_1 are identified starting near to the central body. These surfaces represent possible transfer trajectories from halo orbits at L_2 to halo orbits at L_1 . Similarly, a heteroclinic manifold surface connecting halo orbits around L_1 to halo orbits around L_2 can be generated by numerically identifying an intersection between the stable and unstable manifolds.

Transit orbits, which pass through the manifold surface, offer the possibility of low energy transfers between the exterior and interior region of a planetary Hill surface. During 1991, the Japanese Hiten spacecraft used a transit orbit to achieve ballistic capture at the moon with a lower Δv requirement than offered by a direct Hohmann transfer [Belbruno and Miller, 1993]. Belbruno demonstrates that starting from a 200km altitude Earth orbit, transfer to a 100km altitude lunar orbit with ballistic capture is achievable requiring 25% less Δv than performing a Hohmann transfer manoeuvre at the expense of an increase in transfer time [Belbruno and Carrico, 2000].

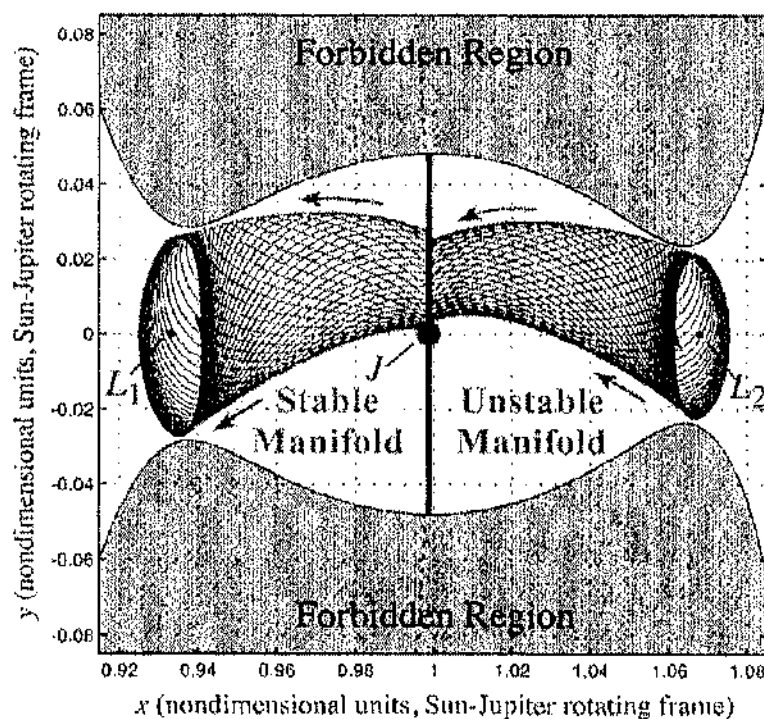


Figure 1-4 Invariant manifold surface produced for the Sun-Jupiter system [Koon et al, 1999]

The lunar ballistic transfer trajectories are identified by first generating stable manifolds in the Sun-Earth three body system. Manifold surfaces which lead to lunar capture are investigated in the Earth-Moon three-body system and the point where both sets of manifolds interact is determined. By connecting the manifold surface and selecting a trajectory that meets the mission Δv and duration requirements, a possible ballistic transfer from low Earth orbit to a low lunar orbit can be determined. Treating the problem as two coupled three-body models offers a good preliminary analysis of the system dynamics but further analysis is then required by performing numerical integration of the 4-body problem to minimise the required trajectory corrections during an actual mission [Koon et al, 2001a].

Koon, Marsden, Lo and Ross extended the work on ballistic capture and escape via the weak stability boundary in the Jupiter system and identified a possible trajectory for low Δv exploration of the Jovian moons Europa, Ganymede and Callisto. By independently identifying ballistic capture and escape trajectories in the Jupiter-Europa, Jupiter-Ganymede and Jupiter-Callisto three body systems, trajectories which lead to temporary capture at these moons are identified. After escape from the moon, the spacecraft follows a planet-centred orbit with complex gravitational perturbations due to the presence of other moons. Using a combination of gravity assists and small impulsive manoeuvres the capture and escape trajectories at each moon can be patched forming a complete grand tour of the Jovian system. The tour could be achieved with a Δv of 22ms^{-1} at the expense of a long mission duration [Ross et al, 2003].

Intersections between the manifold surfaces passing through the Lagrange points of planetary systems gives rise to the so called Interplanetary Superhighway. This complex network of dynamical pathways facilitates transfer of comets, asteroids and zodiacal dust throughout the solar system [Lo and Ross, 2001]. These pathways led comet Shoemaker-Levy 9 to a collision with Jupiter during July, 1994. Also, the comets Oterma and Gehrels 3 frequently transfer between the exterior and interior regions of Jupiter via the heteroclinic connection of L_1 and L_2 . These comets exhibit a mean motion resonance of 3:2 when interior and 2:3 when exterior to Jupiter's orbit [Koon et al, 2001b].

1.4.3 Lagrange point missions

1.4.3.1 ISEE-3 spacecraft

Periodic halo orbits are beneficial at the Sun-Earth L_1 Lagrange point to ensure the spacecraft remains outside the solar telemetry exclusion zone. Communication with the spacecraft is restricted within this region due to solar radio interference. To avoid this exclusion zone, the first Lagrange point orbiting spacecraft ISEE-3 (International Sun Earth Explorer-3) was inserted onto a halo orbit around L_1 during 1978, illustrated in Fig 1-5. The exclusion zone has an angular radius of 3.5° , which corresponds to a radius of 90,000 km radius at L_1 [Farquhar et al, 1977].

The ISEE-3 orbit dimensions were selected such that the z-axis amplitude was 120,000 km with corresponding y-axis amplitude of 666,000 km to avoid the exclusion zone. Stationkeeping costs required a Δv of less than 10 ms^{-1} per year during the four year period the ISEE-3 spent at the L_1 halo orbit [Farquhar, 2001].

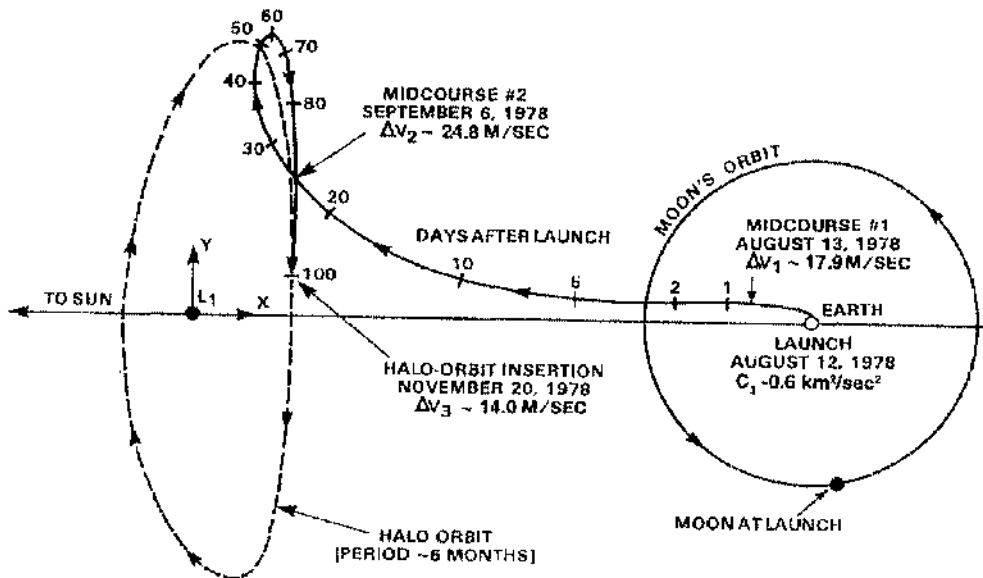


Figure 1-5 [ISEE-C Insertion to halo orbit at L_1] [Farquhar, 2001]

1.4.3.2 MAP spacecraft

MAP (Microwave Anisotropy Probe), the first L_2 orbiter mission, was launched during 2001. The mission aim is to map the cosmic background radiation. The Lissajous trajectory at L_2 offers an uninterrupted view of space as the Earth, moon and Sun are always behind the spacecraft [Bennet et al, 2003]. Insertion to the orbit used lunar gravity assists to lower the Δv requirement. The time elapsed between launch and arrival at the nominal orbit was approximately 3 months and the planned mission duration was 2 years. Figure 1-6 shows a schematic of the trajectory used to deliver MAP to the desired Lissajous orbit. The spacecraft still remains in the Lissajous trajectory 4 years after launch.

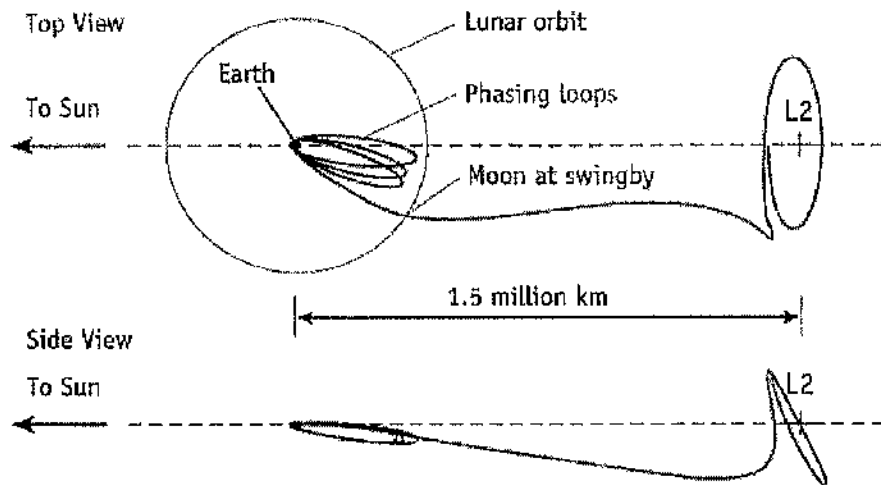


Figure 1-6 MAP spacecraft trajectory for insertion to L_2 Lissajous orbit
Image from <http://map.gsfc.nasa.gov/index.html>

1.4.3.3 Genesis mission

Also during 2001, the Genesis spacecraft was inserted into a halo orbit around L_1 . A 'heteroclinic-like' trajectory was identified which would deliver the spacecraft to a halo orbit around L_1 and facilitate return to the Earth via an unstable manifold with low Δv requirements, as shown in Fig 1-7 [Marsden and Ross, 2005]. Genesis is the first mission to be fully designed using dynamical systems theory and could not have been developed using a patched conic approach [Serban et al, 2002].

From its vantage point at L_1 , the spacecraft collected samples of solar wind plasma particles on a series of metallic and silicon wafers. The mission objectives were to return the collected solar wind particles to Earth for extensive analysis providing information into the origins of the universe. As the spacecraft passed within the vicinity of the Earth during September, 2004, a sample return capsule was released. Meanwhile, the Genesis spacecraft returned to the L_1 region and escaped into the interior region of the Earth-Sun system.

Similar non-Keplerian orbits and transfer trajectories will be investigated around artificial libration points generated using a constant axial acceleration provided by a solar sail.

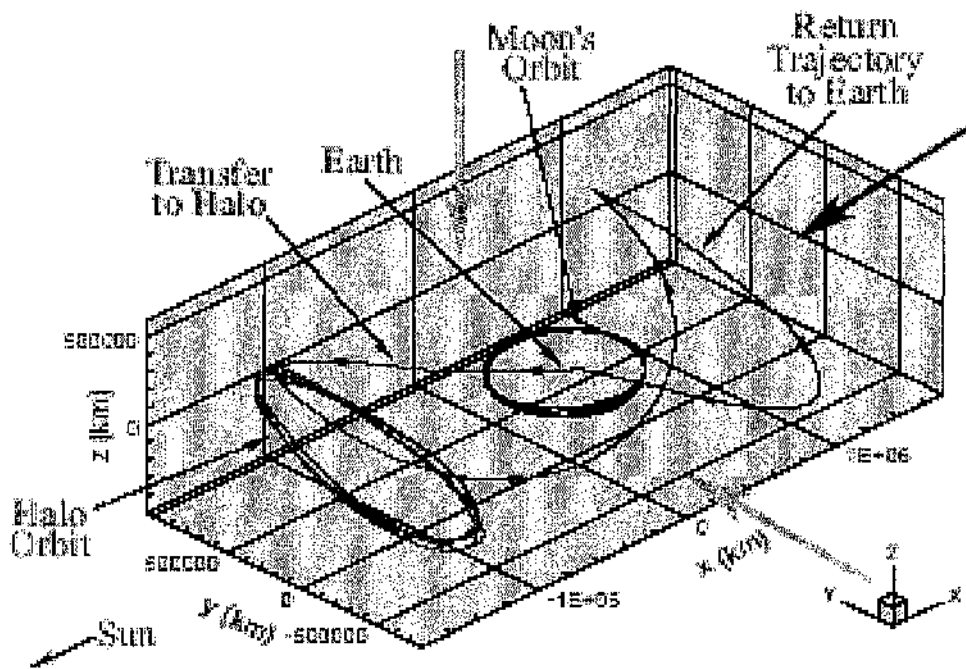


Figure 1-7 The Genesis trajectory centred on the Earth [Serban et al, 2002]

1.5 Solar Sailing

1.5.1 Solar sail concept

The concept of solar sailing is accredited to Konstantin Tsiolkovsky and Friedrich Tsander who suggested, during the 1920s, that the pressure of sunlight could be used to “propel large mirrors and attain cosmic velocities” [Tsander, 1924]. Since then, several authors have considered solar sails as a viable means of propulsion which could enable many exotic, high-energy space missions not achievable with conventional propulsion systems. Garwin [1957] published a paper demonstrating that a solar sail could be used to escape from an Earth orbit by strategically furling and unfurling the sail to increase the orbit angular momentum. Tsu [1959] demonstrated the application of solar sails for interplanetary travel using an approximate spiral trajectory.

Since then, there have been many studies investigating applications of solar sails. Columbo [1961] and Farquhar [1970b] demonstrated that small area solar sails could be applied to provide control of halo orbits around the Lagrange points. The potential offered by solar sails for planetary and small body sample returns has been investigated by many authors including Leipold [1999; 1996], Seboldt [2003], Dachwald [2003], Macdonald [2004] and Hughes [2004].

McInnes [1994; 1998a; 1999b], Forward [1991] and Morrow [2001] have demonstrated that solar sails can be used to generate artificial libration points in the circular restricted three-body problem. These artificial equilibria are of interest since the solar sail is being used to provide new vantage points for observation, rather than as an efficient means of transferring payloads between orbits.

Solar sails require a large gossamer structure with a reflective surface in order to intercept a flux of photons and so generating thrust. The sail consists of a suitable substrate, such as Mylar or Kapton, which is required to be of low areal density and resistant to both tears and ‘flex crack’. The substrate, with thickness of order 1-2 μm , is folded and stored during launch. Various designs of solar sail have been proposed including square sail, circular sail and the heliogyro [Wright 1992].

The substrate is coated with a thin layer of aluminium, of order 100 nm, to provide a reflective surface. Aluminium is selected due to its relatively low density of 2.70 gm^{-3} and reasonably high melting point of 933 K. The aluminium coating is also reflective over a wide range of the optical spectrum, including UV wavelengths. This is important to prevent degradation of the substrate due to UV exposure after sail deployment. Kapton is less susceptible to degradation caused by exposure to UV radiation than Mylar. The substrate can be coated with a thin layer of aluminium using vapour deposition. This technique involves vapourising aluminium in a vacuum chamber with the substrate positioned below. The aluminium atoms condense on the substrate surface forming a thin, reflective layer. To prevent the sail surface heating significantly, it is necessary to coat the rear of the sail with a high emissivity film to radiate heat. A rear coating such as chromium enables passive control of the sail surface temperature.

A reduction of the sail mass increases the achievable acceleration. Possible techniques to reduce the sail mass include removal of the substrate after the sail is deployed or perforation of the sail film. Scaglione considers two methods which could be used to separate the aluminium layer from the substrate - chemical etching or UV degradation of a buffer layer [Scaglione and Vulpett, 1999; Genta and Brusa, 1999].

Chemical etching makes use of atomic oxygen which is abundant (10^9 atoms/cm^3) at 200km - 600km altitude [Peters et al, 1986]. Exposed polymer surfaces are etched by the oxygen atoms due to the low activation energy required for reaction to occur. Using this method, the substrate could be removed after solar sail deployment in a low Earth orbit to obtain an ultra-thin metal sail of 100nm thickness. Alternatively, Scaglione considered the use of a thin buffer layer, which is susceptible to UV degradation, between the aluminium coating and the substrate. A suitable buffer candidate is DLC (Diamond Like Carbon) which is a meta-stable solid consisting of amorphous carbon. When exposed to UV radiation, the DLC layer degrades until separation of the substrate from the reflective sail film is achieved.

Another technique to improve the solar sail performance, proposed by Dyson and Forward is to reduce the solar sail mass by perforating the sail film. A significant reduction in reflectivity is not experienced provided the perforations have a diameter smaller than the wavelength of the incident photons [Forward, 1985].

1.5.2 Solar sails – current technology

A range of engineering issues have yet to be overcome before the potential of solar sails can be realised. A space demonstration of solar sail technology is required to enable future science missions. Deployment of large gossamer structures in space has been thoroughly investigated but there is a lack of successful demonstrations.

A solar sail mission feasibility study was conducted by collaboration between DLR (German Aerospace Centre) and JPL (Jet Propulsion Laboratory). The mission was known as ODISSEE (Orbital Demonstration of an Innovative, Solar Sail driven Expandable structure Experiment) and aimed to demonstrate and validate solar sail technology. The solar sail structure consisted of a 40m x 40m square sail supported by deployable booms attached to a central hub. The payload is connected to the sail via a 10m gimbaled boom. The study considered actuating steering by controlling the position of the gimbaled boom to off-set the sails centre-of-pressure with respect to the centre-of-mass, producing steering torques. The total mass of the sail and payload was estimated as 77.5 kg. The sail areal density of 48.4 gm^{-2} would enable an acceleration of 0.17 mms^{-2} . After deploying the sail and demonstrating attitude control, the mission goal would be to orientate the solar sail relative to the Sun such that it spirals outwards from the Earth reaching lunar distance within 550 days [Leipold, 1999].

Although the ODISSEE mission has not yet been realised, the feasibility study led to a ground test of a solar sail during 1999 by DLR and ESA (European Space Agency). The ground deployment was successful and tested sail fabrication techniques as well as demonstrating basic principles such as folding and storage of a solar sail. Light weight CFRP (Carbon Fiber Reinforced Plastic) booms of 14 m length were used to support the sail. A novel approach to simulate 0g conditions was employed using helium filled balloons to support the weight of the solar sail booms [Leipold, 2003].

The sail consisted of 4 triangular segments each of area 82.6 m^2 . To test and compare the properties of various sail substrates, two of the segments were manufactured using a $7.5 \text{ }\mu\text{m}$ Kapton substrate, one consisted of $4 \text{ }\mu\text{m}$ PEN (polyethylene naphthalate) and the other of $12 \text{ }\mu\text{m}$ thick Mylar. A thin Mylar film of $3 \text{ }\mu\text{m}$ thickness was also deployed by JPL with the required area specified by DLR.

The ground deployment investigated several substrate materials for the sail. Kapton is suitable as it is space qualified and UV resistant but is only available in sheets of thickness down to 7.5 μm . The PEN film can be produced with lower thickness than Kapton, reducing the sail mass, but might not be suitable at high temperatures [Seboldt, 2003]. Extrapolating the sail size to the 40m x 40m sail proposed for ODISSEE, a total sail loading of 35 gm^{-2} would be achievable for a 4 μm thick PEN sail film including the boom and deployment module masses. The redundant deployment module can be jettisoned after the sail is fully deployed reducing the sail loading to 19 gm^{-2} [Leipold, 2003].

On the 9th August 2004, the Japanese space agency JAXA successfully deployed two 10m diameter solar sails. These solar sails were released from an S-310 rocket at altitudes of 122 km and 169 km. The sails were fabricated using 7.5 μm Kapton and demonstrated two different deployment methods – Clover and Fan. After deployment, the orbit rapidly decayed and the solar sails ‘burnt-up’ in the atmosphere.

Recently, an attempt by a privately funded organization, The Planetary Society, to deploy the first solar in an orbit at 800 km altitude was performed. Cosmos 1 was launched on June 21st, 2005 after several delays. The sail configuration was an 8 bladed heliogyro with total sail area of 600 m^2 . The sail was manufactured using 5 μm thick PET (polyethylene terephthalate) with areal density of 11 gm^{-2} [Friedman, 2004].

The aim of the mission was to demonstrate sail deployment and attitude control. The mission objective was to use the sail to spiral outwards from the Earth. The solar sail was launched using a Volna rocket, a converted ICBM (Inter-Continental Ballistic Missile). This was launched from the submarine Borisoglebsk of the Russian Northern Fleet in the Barents Sea. Unfortunately, the rocket’s 1st stage failed 83 seconds into the flight at an altitude of 75 km. The rocket including payload continued on a parabolic trajectory eventually falling into the sea 6 minutes after launch [Friedman, 2005].

Proposed near-term missions which could be achieved using solar sail technology include the Solar Polar Orbiter, the Geostorm and the Geosail mission. These missions will be briefly outlined including the solar sail technology requirements. The Geosail mission uses a solar sail to precess an elliptical Earth orbit by 1° per day so that the solar sail stays continuously within the geomagnetic tail. This would enable scientific investigation of the plasma sheet and give better understanding of reconnection processes. Without the solar

sail, the spacecraft would remain within the magnetotail for only one month per year as the Earth orbits the Sun.

Macdonald and McInnes [2003] performed a study to identify the solar sail requirements and payload mass for the mission. The payload bus mass was estimated as 74.8 kg including science payload. The specified sail area is 1500 m² manufactured using a PET film of 3.5 μm thickness. The total sail assembly mass is 54.6 kg with total sail areal density of 86.3 gm⁻². The solar sail is required to achieve an acceleration of 0.1 mms⁻².

The Geosail mission is a good precursor to more advanced solar sail missions, although SEP (Solar Electric Propulsion) could also be used to achieve the mission, with the drawback that the mission duration is limited by the stored Xenon reaction mass. A more exotic mission which could only be achieved using the continuous acceleration provide by a solar sail is Geostorm, proposed by JPL in 1996. The aim of this mission is to use a solar sail to generate an artificial libration point sunwards of the L_1 Lagrange point. The suggested libration point position 0.02 AU sunwards of the Earth requires a sail acceleration of 0.31 mms⁻² [Yen, 2004].

The mission aims to provide an advance warning of increased solar wind charge density caused during Coronal mass ejections (CME) which leads to magnetic storms. The warning time available at L_1 is 30 minutes to 1 hour. The ACE (Advanced Composition Explorer) and SOHO (Solar Heliospheric Observatory) currently orbit this location. A solar sail can be used to control a halo orbit around an artificial libration sunwards of L_1 providing an increase in warning time by a factor of 2-3 [West and Dcrbes, 2000].

A solar sail can also be used to maneuver to high inclinations for the Solar Polar Orbiter mission. High inclination orbits require large Δv which makes solar sails a suitable candidate. This mission would enable continuous observation of the solar poles. After deployment, the solar sail can be used to spiral inwards to a distance of 0.48 AU from the Sun. The solar sail is then used to crank the orbit to an inclination of 82°, taking advantage of the increased solar radiation pressure nearer to the Sun. The required sail area is 23,000 m² using a sail manufactured from 2 μm thick CP-1 film. The total mission duration is calculated as 5 years and the solar sail characteristic acceleration is 0.42 mms⁻² [McInnes, 2004].

1.5.3 Solar sail acceleration

Solar sails obtain thrust by intercepting a flux of photons, as shown in Fig 1-8. Incident photons impart their momentum to the sail and the reflection results in an equal reaction force, with the resulting thrust directed normal to the sail surface. Maxwell predicted the phenomenon of radiation pressure from his electromagnetic equations in 1879. This was confirmed experimentally by Peter Lebedew during the early 1900s using a torsion balance experiment.

McInnes [1999a] outlines two complete derivations of acceleration due to solar radiation pressure exerted on a flat reflecting sail surface using both a quantum and electromagnetic description of the radiation properties. The intensity of solar radiation at distance R from the Sun is defined as

$$W = \frac{L_s}{4\pi R^2} \quad (1.3)$$

where L_s is the solar luminosity and W is the radiation intensity. This represents the power per unit area on the surface of a sphere with radius R . The energy transported across a cross sectional area A for time period Δt can be expressed as

$$\Delta E = WA\Delta t \quad (1.4)$$

The momentum, Δp , of a photon is related to its energy as

$$\Delta p = \frac{\Delta E}{c} \quad (1.5)$$

where c is the speed of light. The pressure, P , exerted by the photon on a surface of area A is then

$$P = \frac{1}{A} \left(\frac{\Delta p}{\Delta t} \right) \quad (1.6)$$

Substituting Eq (1.5) and Eq (1.4) into Eq (1.6) provides the relationship between solar radiation pressure and solar radiation intensity

$$P = \frac{W}{c} \quad (1.7)$$

McInnes [1999a] demonstrates that this relationship, derived using a quantum description of photons, agrees with the relationship obtained using the electromagnetic wave description.

Figure 1-8 shows the forces acting upon the sail surface in the ideal sail case, which assumes the sail surface is flat and perfectly reflecting. The force resulting from the photons incident on the sail surface and the reaction force caused by photon reflection is defined as

$$\mathbf{f}_i = PA(\mathbf{v}_i \cdot \mathbf{n})\mathbf{v}_i \quad (1.8.1)$$

$$\mathbf{f}_r = -PA(\mathbf{v}_i \cdot \mathbf{n})\mathbf{v}_r \quad (1.8.2)$$

where P is the radiation pressure and A is the sail surface area.

The vector identity $\mathbf{v}_i - \mathbf{v}_r = 2(\mathbf{v}_i \cdot \mathbf{n})\mathbf{n}$ can be used to express the force directed normal to the sail surface as

$$\mathbf{F} = 2PA(\mathbf{v}_i \cdot \mathbf{n})^2 \mathbf{n} \quad (1.9)$$

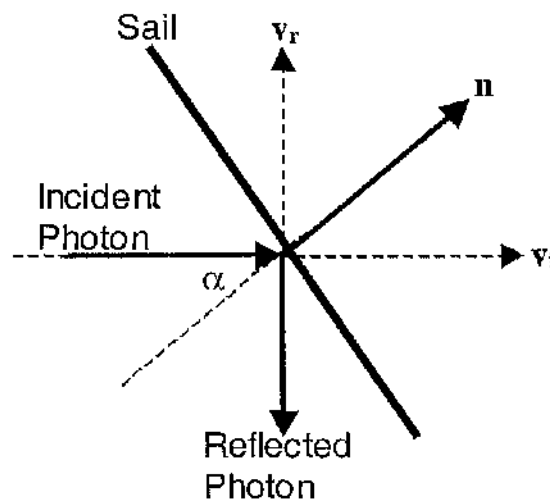


Figure 1-8 Incident and reflected photons on a flat sail

The dot product can also be evaluated as $\mathbf{v}_1 \cdot \mathbf{n} = \cos \alpha$ where α represents the sail pitch angle. The sail pitch is the angle between the sail surface normal and the Sun-line. The expression for radiation pressure provided in Eq (1.7) can be substituted into Eq (1.9). This leads to the expression for solar sail acceleration as

$$\mathbf{a} = \beta \frac{GM_s}{R_s^2} \cos^2 \alpha \mathbf{n} \quad (1.10)$$

where G is the gravitational constant, R_s is the separation distance between the solar sail and the Sun, M_s is the solar mass and β is a dimensionless parameter known as the sail lightness number. This parameter represents the ratio of solar radiation pressure induced acceleration to gravitational acceleration and is defined as

$$\beta = \frac{L_s}{2\pi c GM_s \sigma} \quad (1.11)$$

where L_s represents the solar luminosity, c is the speed of light and sail loading parameter $\sigma = m/A$ where m is the total sail mass.

Equation (1.10) represents the acceleration case for an ideal solar sail which assumes no non-specular reflections. The thrust is directed normal to the sail surface in the anti-Sun direction and there are no transverse components of thrust due to diffuse reflection. For comparison, an acceleration model can be derived which includes non-specular reflection for a partially reflecting flat sail.

Figure 1-9 shows a non-perfectly reflecting solar sail [Wie, 2002]. The actual thrust direction is denoted by \mathbf{m} , the sail normal direction denoted by \mathbf{n} and the sail transverse direction by \mathbf{t} . The reflection index, ρ_s , represents the fraction of photons which are specularly reflected resulting in a reaction force directed normal to the sail surface. The total force exerted on the sail is defined as

$$\mathbf{F} = F_n \mathbf{n} + F_t \mathbf{t} \quad (1.12)$$

where the force components are determined as

$$F_n = PA(1 + \rho_s) \cos^2 \alpha \quad (1.13.1)$$

$$F_t = PA(1 - \rho_s) \cos \alpha \sin \alpha \quad (1.13.2)$$

Substituting Eq (1.7) enables the acceleration, \mathbf{a} , to be expressed as

$$\mathbf{a} = \frac{\beta GM_s}{2 R^2} (1 + \eta) \cos^2 \alpha \mathbf{n} + \frac{\beta GM_s}{2 R^2} (1 - \eta) \cos \alpha \sin \alpha \mathbf{t} \quad (1.14)$$

where the thrust direction is denoted by \mathbf{m} [McInnes, 1999b]. The angle between the thrust vector and the sail normal vector is defined as

$$\tan \gamma = \frac{(1 - \rho_s)}{(1 + \rho_s)} \tan \alpha \quad (1.15)$$

The solar sail acceleration can be used to generate artificial libration points in the two and three-body problems. These problems including solar radiation pressure will be briefly investigated to compare the ideal and non-perfect sail acceleration models.

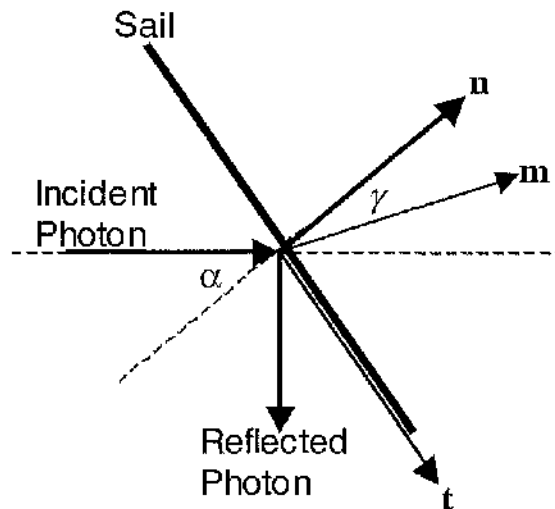


Figure 1-9 Schematic representing photons incident on a non-perfectly reflecting sail

1.5.4 Artificial libration points

The circular restricted three-body problem represents the dynamics of a negligible mass in the vicinity of two primary bodies. The two primaries orbit around a common barycentre in a circular motion, shown in Fig 1-10. The complete derivation for this model will be examined in greater detail throughout Chapter 3 and Chapter 4. In this section, it will be used to provide a comparison of the two sail acceleration models.

The circular restricted three-body problem is derived by McInnes [1998a] using a rotating reference frame with angular velocity ω as

$$\frac{d^2\mathbf{r}}{dt^2} + 2\boldsymbol{\omega} \times \frac{d\mathbf{r}}{dt} + \Delta U = \mathbf{a} \quad (1.16)$$

where \mathbf{a} represents the acceleration due to solar radiation pressure, \mathbf{r} is the position relative to the barycentre and the pseudo-potential U is expressed as

$$U = -\frac{1}{2}(x^2 + y^2) - \frac{(1-\mu)}{|\mathbf{r}_1|} - \frac{\mu}{|\mathbf{r}_2|} \quad (1.17)$$

where \mathbf{r}_1 and \mathbf{r}_2 represents the distance of the solar sail from the Sun and Earth respectively. The angular velocity is directed perpendicular to the orbit plane of the two primaries, such that $\boldsymbol{\omega} = \omega \mathbf{k}$.

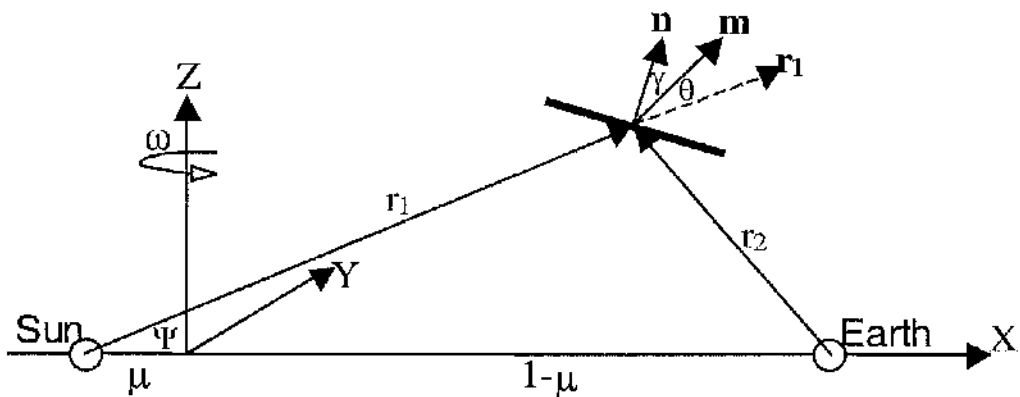


Figure 1-10 Schematic representing circular restricted three-body problem [McInnes, 1999b]

In the case of a non-perfect solar sail, the thrust direction deviates from the sail surface normal by the center-line angle, γ . Selecting a suitable sail lightness parameter and orientation, it is possible to generate artificial libration points [Forward, 1991]. A comparison is performed between the ideal and non-perfect reflectivity models for artificial libration points which lie in the x-z plane of the Sun-Earth three-body system.

It can be seen from Eq (1.16) that the direction of the solar sail acceleration $\mathbf{a} = \nabla U / |\nabla U|$ for an artificial equilibrium point. The acceleration components can be evaluated as

$$a_x = -x + \frac{(1-\mu)(x+\mu)}{|\mathbf{r}_1|^3} + \frac{\mu(x-1+\mu)}{|\mathbf{r}_2|^3} \quad (1.18.1)$$

$$a_z = \frac{(1-\mu)z}{|\mathbf{r}_1|^3} + \frac{\mu z}{|\mathbf{r}_2|^3} \quad (1.18.2)$$

The magnitude of the acceleration is then determined as $|\mathbf{a}| = \sqrt{a_x^2 + a_z^2}$ and the angle of the sail thrust relative to the x-axis is calculated using $\tan \Phi = a_z / a_x$. The angle of the Sun-line relative to the x-axis can be expressed as $\tan \Psi = z / \rho$ so that the angle between the Sun-line and the thrust direction can be expressed as $\theta = \Phi - \Psi$, which is referred to as the cone angle.

As the solar sail thrust is generated using solar radiation pressure, the thrust vector must always be directed in the anti-Sun direction. This imposes a limit on the sail pitch angle $-\pi/2 < \alpha < \pi/2$. Figure 1-11 shows the region in the vicinity of the Earth where off-axis artificial libration points can be generated using an ideal solar sail. The L_1 and L_2 Lagrange points are also shown. The natural Lagrange points and their stability will be discussed in greater detail during Chapter 4. In the case of an ideal sail, it is clear that artificial libration points can be generated earthwards of L_2 and sunwards of L_1 .

In the case of the non-perfect sail model, the thrust direction relative to the sail normal varies as pitch angle is increased. The cone angle is calculated from the acceleration components as discussed previously. The required pitch angle of the sail to achieve this thrust direction is determined as $\alpha = \theta + \gamma$. The centre-line angle, γ , can be expressed in terms of the cone-angle θ by substituting the relationship for pitch angle into Eq (1.15) [Molostov, 1992]. After some reduction, the relationship is obtained as follows

$$\tan \gamma = \frac{\rho_s}{(1 + \rho_s) \tan \theta} \left[1 - \left(1 - \frac{1 - \rho_s^2}{\rho_s^2} \tan^2 \theta \right)^{1/2} \right] \quad (1.19)$$

A limit is imposed on the cone angle, θ , to avoid imaginary centre-line angles where

$$\tan \theta \leq \left(\frac{\rho_s^2}{1 - \rho_s^2} \right)^{1/2} \quad (1.20)$$

For the ideal sail case $\rho_s=1$, which yields the expected pitch angle restriction $-\pi/2 < \alpha < \pi/2$ required to ensure the thrust is always directed in the anti-Sun direction. Figure 1-12 shows the region of possible solutions achievable using a non-perfect solar sail with $\rho_s=0.9$. Substituting this reflective index into Eq (1.20), it is clear that the limit imposed on the thrust direction for the non-perfect solar sail is $\theta=64.2^\circ$. This reduces the achievable levitation distance above the ecliptic. Reduction of the reflective index value subsequently reduces the maximum levitation distance sunward of L_2 .

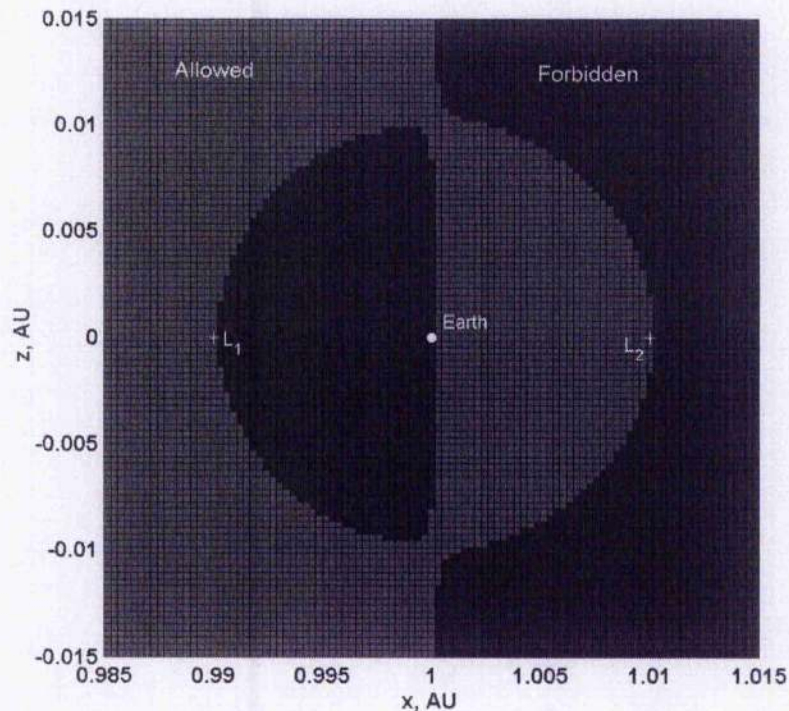


Figure 1-11 Possible libration points in the Earth-Sun system for ideal flat solar sail
(Solutions possible – Light region; No solutions – Dark region)

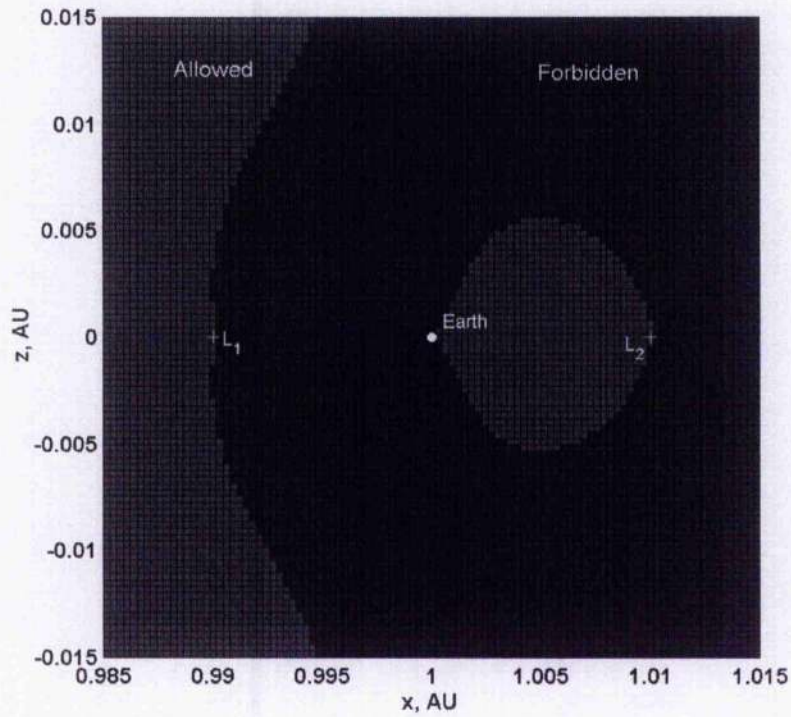


Figure 1-12 Possible libration points in the Earth-Sun system for partially reflecting flat solar sail ($\rho_s=0.9$)
(Solutions possible – Light region; No solutions – Dark region)

1.5.5 Sun displaced non-Keplerian orbits

The continuous acceleration produced by a solar sail can be used to displace a circular orbit above the ecliptic plane. A dynamical model can be developed using the two-body problem, as demonstrated by McInnes and Simmons [1992a]. A thorough analysis of non-Keplerian orbits developed in a two-body context is provided in Chapter 2.

The two-body problem models the gravitational interaction between the Sun and the solar sail including the acceleration due to solar radiation pressure. Figure 1-13 shows a schematic of such a Sun displaced non-Keplerian orbit.

The two-body problem can be expressed as

$$\ddot{\mathbf{r}} = -\frac{\mu_s \mathbf{r}}{|\mathbf{r}|^3} + \mathbf{a} \quad (1.21)$$

where μ_s is the solar gravitational parameter and \mathbf{a} is the acceleration due to solar radiation pressure. The radial position relative to the Sun is defined in the inertial frame as \mathbf{r} , where $|\mathbf{r}| = \sqrt{\rho^2 + z^2}$. For the orbit shown in Fig 1-13, the two-body problem can be expressed in a rotating reference frame with angular velocity ω .

Representing the relative position to the Sun in the rotating reference frame as $\bar{\mathbf{r}}$, the velocity in the inertial frame can be evaluated as $\dot{\mathbf{r}} = \dot{\bar{\mathbf{r}}} + \omega \times \bar{\mathbf{r}}$. The acceleration in the inertial frame can be converted to the rotating frame using

$$\ddot{\mathbf{r}} = \ddot{\bar{\mathbf{r}}} + \dot{\omega} \times \bar{\mathbf{r}} + 2\omega \times \dot{\bar{\mathbf{r}}} + \omega \times \omega \times \bar{\mathbf{r}} \quad (1.22)$$

Substituting into Eq (1.20) and assuming the angular velocity is constant, $\dot{\omega} = 0$, the two body equations can be expressed as

$$\ddot{\bar{\mathbf{r}}} + 2\omega \times \dot{\bar{\mathbf{r}}} + \nabla U(\bar{\mathbf{r}}) = \mathbf{a} \quad (1.23)$$

where the pseudo-potential is formed by combining the centripetal term with the gravitational acceleration as follows

$$U(\bar{\mathbf{r}}) = \frac{1}{2} |\omega \times \bar{\mathbf{r}}|^2 - \frac{\mu}{|\bar{\mathbf{r}}|} \quad (1.24.1)$$

$$\nabla U(\bar{\mathbf{r}}) = \omega \times \omega \times \bar{\mathbf{r}} + \frac{\mu}{|\bar{\mathbf{r}}|^3} \bar{\mathbf{r}} \quad (1.24.2)$$

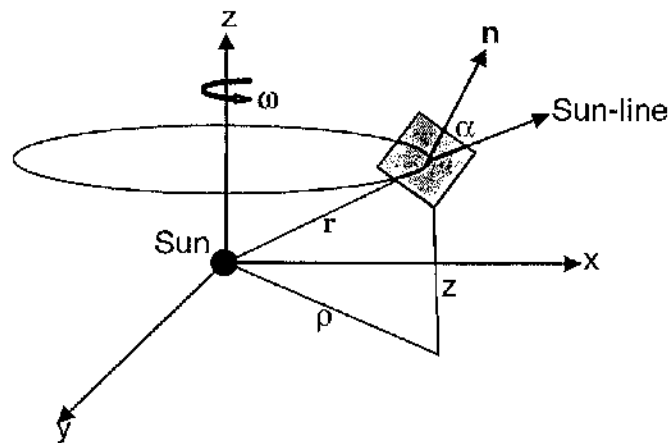


Figure 1-13 Sun-centred displaced orbits [McInnes, 1992a]

The ρ - and z - axis directions are represented by the unit vectors \mathbf{e}_ρ and \mathbf{e}_z respectively. The position of the solar sail relative to the Sun can be expressed as $\bar{\mathbf{r}} = \rho\mathbf{e}_\rho + z\mathbf{e}_z$ using cylindrical polar coordinates. The angular velocity is directed normal to the plane such that $\boldsymbol{\omega} = \omega\mathbf{e}_z$. The pseudo-potential from Eqn (1.23) can be expressed as

$$U(\rho, z) = -\frac{1}{2}(\rho\omega)^2 - \frac{\mu}{|\bar{\mathbf{r}}|} \quad (1.25.1)$$

$$\nabla U(\rho, z) = \left(-\rho\omega^2 + \frac{\mu\rho}{|\bar{\mathbf{r}}|^3}\right)\mathbf{e}_\rho + \left(\frac{\mu z}{|\bar{\mathbf{r}}|^3}\right)\mathbf{e}_z \quad (1.25.2)$$

To achieve a circular orbit displaced a constant distance from the Sun, the velocity and acceleration components $\ddot{\bar{\mathbf{r}}} = \dot{\bar{\mathbf{r}}} = 0$. The required sail acceleration $\mathbf{a} = \nabla U(\rho, z)$ and the sail normal direction is defined by $\mathbf{n} = \nabla U/|\nabla U|$. The pitch angle required to generate a circular orbit displaced above the ecliptic is expressed as

$$\tan(\alpha) = \frac{|\bar{\mathbf{r}} \times \nabla U(\rho, z)|}{\bar{\mathbf{r}} \cdot \nabla U(\rho, z)} \quad (1.26)$$

The angular velocity of a circular orbit, with radial distance $\bar{\mathbf{r}}$ from the central body can be expressed as $\omega_*^2 = \mu/|\bar{\mathbf{r}}|^3$. Substituting this term into Eq (1.25) obtains

$$\tan(\alpha) = \frac{\rho z \omega^2}{\omega_*^2(\rho^2 + z^2) - \rho^2 \omega^2} \quad (1.27)$$

McInnes [1992a] extracts a factor of $(\omega/\omega_*)^2$ from the denominator, which after some reduction leads to the following expression for pitch angle

$$\tan(\alpha) = \frac{(z/\rho)(\omega/\omega_*)^2}{1 + (z/\rho) - (\omega/\omega_*)^2} \quad (1.28)$$

Similarly, the sail lightness number required to generate a circular displaced orbit can be determined by re-arranging Eq (1.10) to obtain

$$\beta(\bar{\mathbf{r}}) = \frac{|\bar{\mathbf{r}}|^4 \nabla \mathbf{U} \cdot \mathbf{n}}{\mu (\bar{\mathbf{r}} \cdot \mathbf{n})^2} \quad (1.29)$$

After some reduction this yields the scalar form

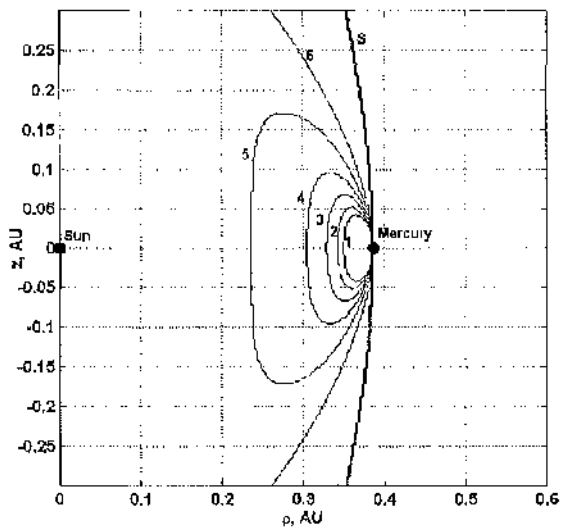
$$\beta(\rho, z) = \left[1 + \left(\frac{z}{\rho} \right)^2 \right]^{1/2} \frac{\left\{ (z/\rho)^2 + [1 - (\omega/\omega_s)^2]^2 \right\}^{3/2}}{\left\{ (z/\rho)^2 + [1 - (\omega/\omega_s)^2] \right\}^2} \quad (1.30)$$

These expressions will be used to determine the solar sail pitch angle and lightness number required to generate a displaced Sun-centred circular orbit. These values can then be used to determine the required sail acceleration and loading.

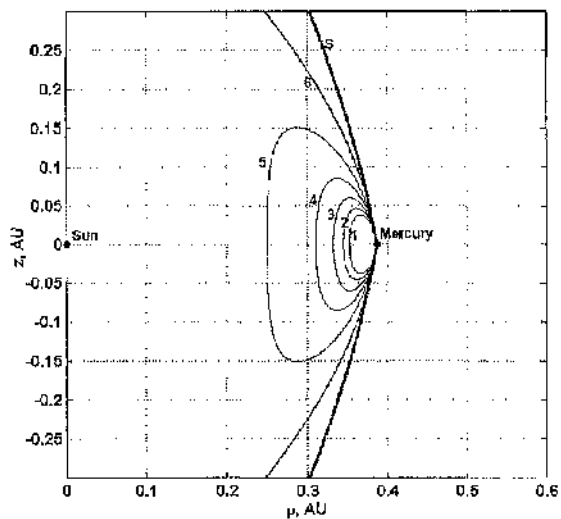
It is possible to generate an orbit displaced above the ecliptic plane which has the same orbit period as a Keplerian body. Assuming the planet has a circular orbit around the Sun, the angular momentum can be defined as $\omega = R_p^{-3/2}$, where R_p represents the length of the semi-major axis. Figure 1-14 to Figure 1-17 represent sail loading contours for a range of orbit radius and displacement distances for each of the inner planets – Mercury, Venus, Earth and Mars. The left hand figures, (a), assume the ideal solar sail case where the thrust vector is directed normal to the sail surface. The right hand figures, (b), represent a non-perfect solar sail with reflectivity $\rho_s=0.9$.

For the ideal sail case, the sail lightness number and pitch angle are calculated for each ρ and z value using Eq (1.28) and Eq (1.30). The sail loading parameter is then calculated by rearranging Eq (1.11) and substituting the lightness number value. The S surface represents the constraint for acceleration directed in the anti-Sun direction. The sail pitch angle is constrained by $-\pi/2 \leq \alpha \leq \pi/2$, where S defines the surface $\bar{\mathbf{r}} \cdot \mathbf{n} = 0$. Using Eq (1.29), it can be shown that the constraining surface $S = \mu/\bar{\mathbf{r}} - \rho^2 \omega^2$.

It is clear in the case of a non-perfect solar sail, the maximum levitation altitude achieved for any loading parameter is less than the ideal sail case. This reduction becomes more pronounced the greater the levitation above the ecliptic. Also, the S contour, which represents the constraint on the orbit parameters, is more acute in the case of a non-perfect solar sail indicating that achievable orbit radius is reduced as levitation height is increased.

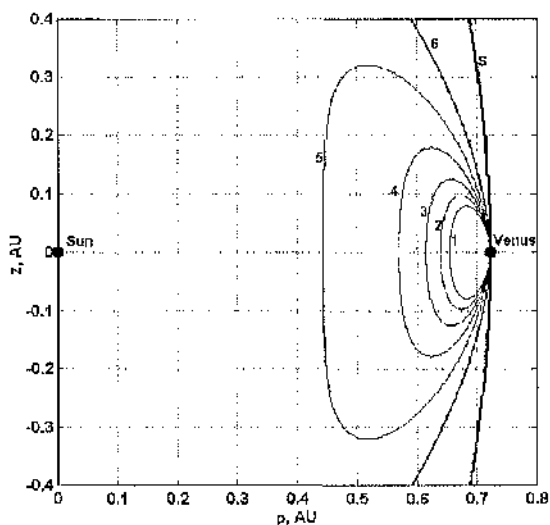


(a)

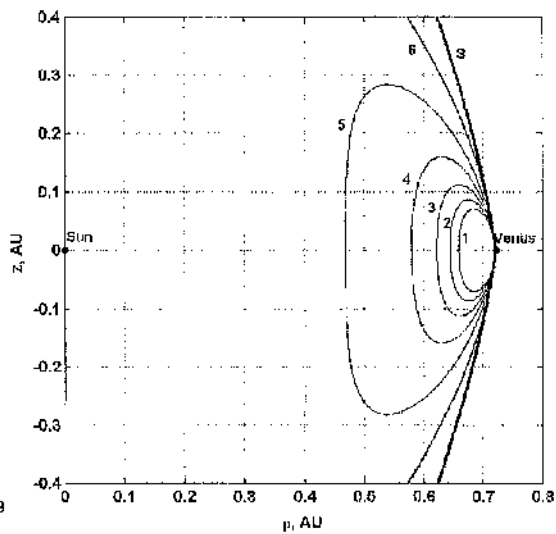


(b)

Figure 1-14 Sail loading parameter contours for Mercury synchronous orbits
 {1 - 6gm^{-2} , 2 - 5gm^{-2} , 3 - 4gm^{-2} , 4 - 3gm^{-2} , 5 - 2gm^{-2} , 6 - 1gm^{-2} }



(a)



(b)

Figure 1-15 Sail loading parameter contours for Venus synchronous orbits
 {1 - 6gm^{-2} , 2 - 5gm^{-2} , 3 - 4gm^{-2} , 4 - 3gm^{-2} , 5 - 2gm^{-2} , 6 - 1gm^{-2} }

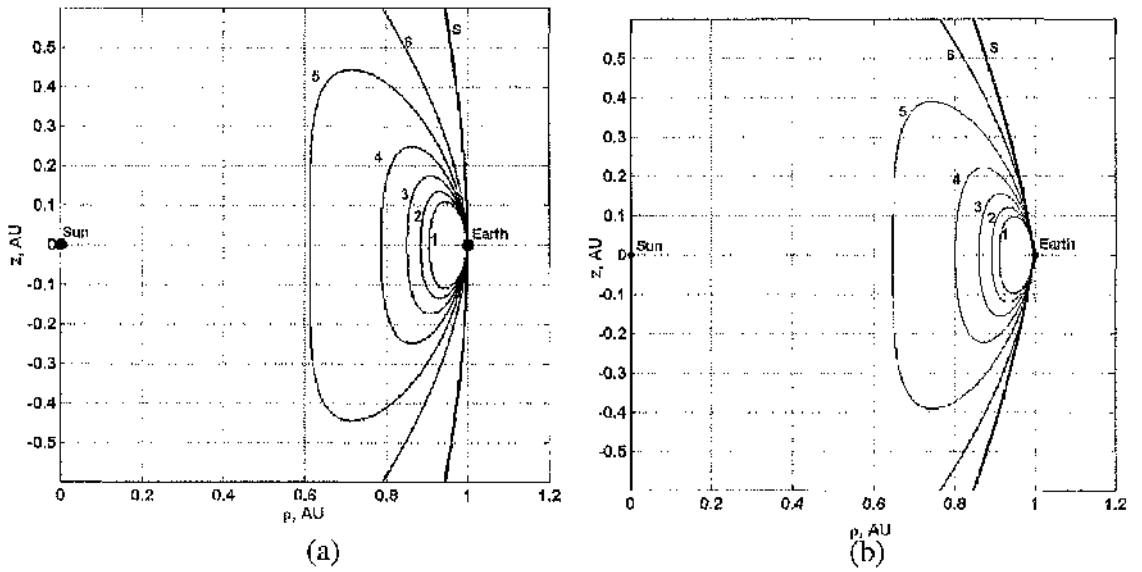


Figure 1-16 Sail loading parameter contours for Earth synchronous orbits
 $\{1 - 6\text{gm}^{-2}, 2 - 5\text{gm}^{-2}, 3 - 4\text{gm}^{-2}, 4 - 3\text{gm}^{-2}, 5 - 2\text{gm}^{-2}, 6 - 1\text{gm}^{-2}\}$

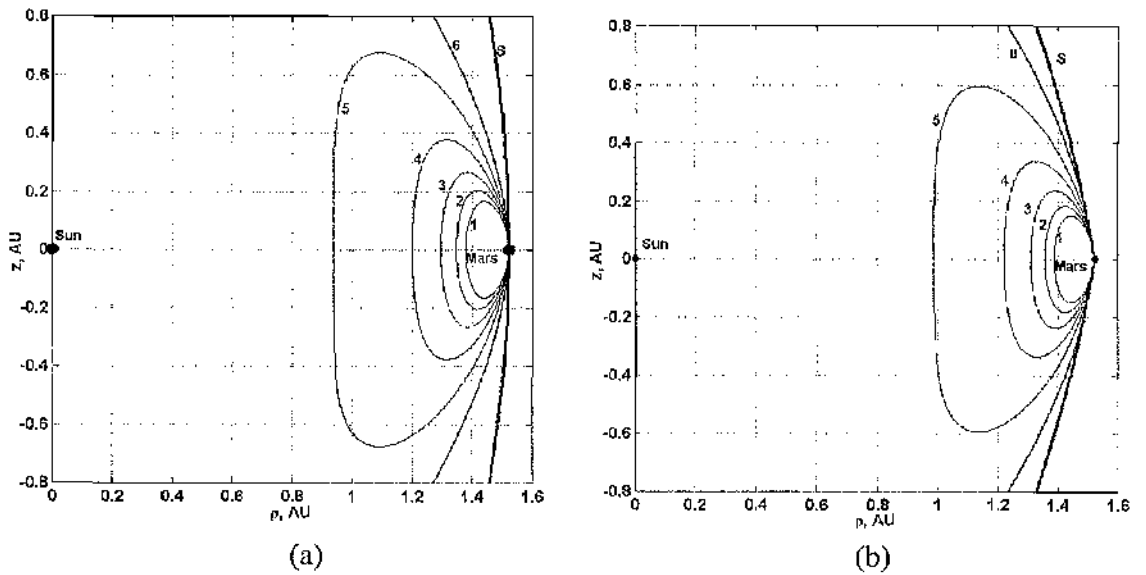


Figure 1-17 Sail loading parameter contours for Mars synchronous orbits
 $\{1 - 6\text{gm}^{-2}, 2 - 5\text{gm}^{-2}, 3 - 4\text{gm}^{-2}, 4 - 3\text{gm}^{-2}, 5 - 2\text{gm}^{-2}, 6 - 1\text{gm}^{-2}\}$

It has been demonstrated that a non-perfect flat solar sail results in deviation of the sail thrust vector from the sail surface normal due to transverse acceleration components. The deviation angle is significant when the sail is pitched at large angles relative to the Sun-line. For small pitch angles, the ideal and non-ideal cases closely agree. As this thesis will mainly consider on-axis artificial libration points, the ideal sail model will be assumed when calculating sail acceleration requirements.

1.6 Objectives of thesis

The objectives of this thesis are to:

- Develop appropriate dynamical models representing the motion of a solar sail in the vicinity of a planet. These models should include both the gravitational influence of the relevant bodies and the acceleration due to solar radiation pressure.
- Identify artificial libration points using these dynamical models including the acceleration due to solar radiation pressure. The stability of these libration points can be determined using eigenvalue analysis methods.
- Generate non-Keplerian orbits around artificial libration points. This will include both Lissajous and halo orbits demonstrated around the L_1 and L_2 Lagrange points of the three-body problem. The stability of these orbits will be evaluated using eigenvalue and energy analysis methods.
- Identify manifolds associated with the non-Keplerian orbits which can be utilised for orbit insertion from a point near to the central body.
- Investigate solar sail station-keeping techniques to prevent escape from the desired orbits after insertion. Two possible methods to control the solar sail acceleration include variation of the solar sail area and variation of the solar sail attitude.

1.7 Outline of thesis

The problem of highly non-Keplerian orbits will be investigated in Chapter 2 using a two-body context by modeling the dynamics of a solar sail in the vicinity of planet. The assumption is made that the solar sail is orientated such that the sail normal vector is parallel to the Sun-planet axis. It will be demonstrated that a constant axial force due to solar radiation pressure can produce a circular planet displaced orbit in the anti-Sun direction. The stability of these orbits will be analysed using both a linear approximation of the equations of motion and a non-linear analysis.

New families of highly perturbed periodic orbits are then generated by perturbing the constant acceleration. This new family of orbits provides a set of homoclinic manifolds which can be used for orbit insertion to a circular displaced orbit from a point near the Earth. It is demonstrated that these manifolds are constrained to a paraboloid surface which enables the closest approach distance to the Earth to be determined explicitly. Solar sail station-keeping techniques will be investigated, which include sail surface area variation or sail pitch angle variation, to prevent escape after insertion to an unstable displaced circular orbit.

In Chapter 3, the problem will be further developed in a three-body context using Hill's approximation to the three-body problem, including the acceleration due to solar radiation pressure. Hill's approximation includes the coriolis and centripetal terms due to the planet orbiting the Sun and also includes solar tide terms due to the gravitational influence of the Sun on the sail. Similar analysis is performed, identifying circular displaced orbits in the Sun-Earth-sail problem. As expected, it is found that when the displaced orbits are relatively close to the Earth, the two-body analysis provides a good approximation of the dynamics of the problem. When the solar sail is displaced far from the Earth, perturbations due to the solar tide terms result in orbit instability.

The previously developed two-body control methods will be applied to provide orbit control at circular displaced orbits generated using Hill's equations. The perturbed homoclinic manifolds will also be generated, again enabling insertion from a point near to the Earth.

Quasi-periodic Lissajous orbits around artificial libration points will then be explored in the context of Hill's approximation. These trajectories are generated by linearising Hill's equations about the libration point. By suppressing real eigenvalues, which lead to escape, an oscillatory solution can be derived. This yields initial conditions which converge to a Lissajous orbit. During numerical integration including the nonlinear terms, the solar sail eventually escapes the nominal Lissajous orbit. Solar sail control techniques will be applied to prevent escape from the nominal Lissajous orbit after insertion.

In Chapter 4, the problem will be further extended to include the barycentric motion of the Sun and Earth using the circular restricted three body problem. In the circular restricted problem the L_1 and L_2 Lagrange points are not symmetrically located either side of the Earth, unlike the case of Hill's approximation. For comparison, the elliptical restricted problem will also be derived using a power series to represent the variation of the separation between the primaries due to the eccentric motion of the planet. Artificial libration points will be identified in both dynamical models using the solar sail acceleration.

In the elliptical problem, there is an oscillation of the libration point position due to the varying separation distance between the primaries. This oscillation perturbs the behaviour of a spacecraft orbiting a libration point. The solar sail controller must be able to dampen these perturbations to provide complete orbit control.

Richardson's method is applied to develop a third order approximation of the equations of motion. A third order solution is derived using the Lindstedt-Poincaré perturbation method to remove secular terms which lead to unbounded solutions. The third order solution yields initial conditions which converge to a periodic halo orbit about the libration point. A differential correction method is applied to generate a periodic halo orbit by numerical integration of the non-linear circular restricted three-body equations.

The precision of the halo orbits generated is reasonable to assume they are periodic for one orbit period. However, inaccuracies during numerical integration due to neglected higher order terms lead to gradual escape from the nominal orbit. A three-axis solar sail control method is developed which provides full controllability at the nominal orbit. This controller combines the solar sail area variation and attitude variation methods which were applied to demonstrate control of the circular displaced orbits and Lissajous trajectories. A combination of these control techniques enables the solar sail thrust magnitude and

direction to be controlled to drive the sail towards the nominal orbit. The control technique is demonstrated at halo orbits in the circular restricted case sunwards of the L_2 and L_1 Lagrange points. Control of halo orbits in the elliptical restricted problem is also demonstrated.

The two-centre problem, a special case of the restricted three-body problem investigated by Euler, is considered in Chapter 5 as a possible method to examine libration points between stars. This problem assumes the two primaries are fixed in the inertial frame, thus the libration points exist where the gravitational acceleration due to the primary bodies cancel. This investigation considers the stability of these libration points and the possibility of interstellar dust becoming temporarily trapped between stars.

The two-centre approximation is valid provided the relative stellar motion is negligible during the period of particle trapping. To validate this approximation, several cases will be examined including the effects of stellar radiation pressure, the gravitational perturbation due to the presence of a third star and the perturbations due to relative stellar motion. Halo orbits around these libration points will be investigated in both the gravitational and photogravitational cases. The stability of these orbits is investigated to determine the likelihood of interstellar particles becoming trapped at these orbits.

Homoclinic manifolds are investigated which wind off and onto the unstable halo orbit. These manifolds could represent transfer trajectories for particles ejected by one star system and transferred to another. An explicit solution is derived by converting the problem to confocal elliptical coordinates. It is demonstrated that the homoclinic manifolds are bound to ellipsoid surfaces.

Finally, in Chapter 6 the solar sail dynamical models are used to investigate some feasible missions which could be enabled by solar sail technology. These missions include delivering a science payload to a circular displaced orbit $30 R_E$ (Earth Radii) from the Earth using a high performance solar sail. The objective of this mission would be to provide continuous observation of the magnetic and electrodynamics in the magnetotail and examine the processes of magnetic reconnection. The next mission considers a trajectory which could deliver a solar sail to a halo orbit sunward of L_1 . This mission outlines an initial delivery of an undeployed solar sail to a Lissajous orbit at L_1 . Upon arrival, the solar sail is then gradually deployed and slowly spirals sunwards to a new halo orbit. Positioning a science payload nearer to the Sun enables advance warning of coronal

mass ejections which lead to magnetic storms. Both missions will be designed starting from a low Earth orbit using a Hohmann transfer to deliver the craft to the selected transfer trajectory. The Δv and sail performance requirements will be discussed. It will be demonstrated that the sail requirements for these missions are achievable with near-term technology.

2.1 Two-body problem

The two-body problem mathematically models the gravitational forces between two masses. In Chapter 1 it was demonstrated that the two-body problem can be used to model the gravitational influence of the Sun acting on a solar sail. Using the constant acceleration provided by the sail, a planet synchronous orbit can be displaced above the ecliptic plane. Similar analysis can be performed using the two-body problem to model the dynamics of a solar sail in the vicinity of a planet or small body including the acceleration due to solar radiation pressure.

Using the constant thrust provided by a solar sail, a continuum of artificial libration points can be generated. Displaced non-Keplerian orbits can be generated around artificial libration points where the central body is not located on the orbit plane [McInnes, 1998b; 1994; Forward, 1991]. The stability of non-Keplerian orbits will be investigated in a two-body context and possible station-keeping techniques will be examined.

The ideal sail model, derived in Chapter 1, will be assumed with the acceleration due to solar radiation pressure, \mathbf{a} , defined as

$$\mathbf{a} = \frac{\beta\mu_s}{|\mathbf{R}_s|^2} \cos^2 \alpha \mathbf{n} \quad (2.1)$$

where β is the sail lightness number, μ_s is the solar gravitational parameter, \mathbf{R}_s is the radial distance between the solar sail and the Sun. The pitch angle α is defined as the angle between the Sun-line and the sail normal unit vector \mathbf{n} .

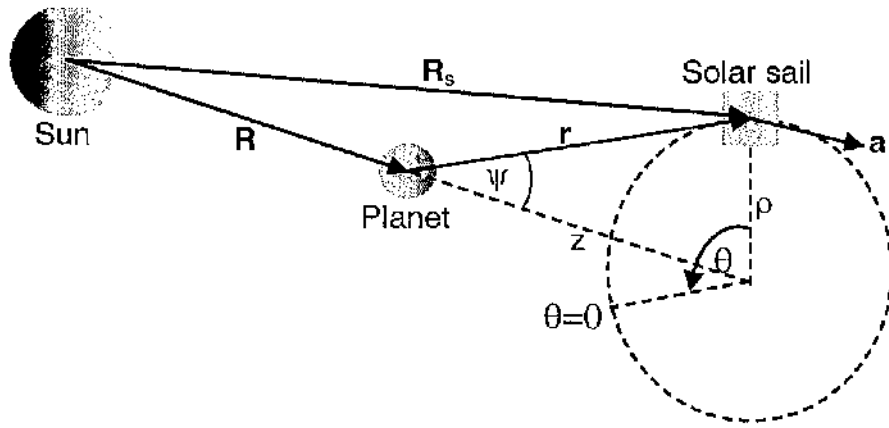


Figure 2-1 Schematic of two-body displaced non-Keplerian orbit

To generate a displaced non-Keplerian orbit, the solar sail is orientated so the force due to solar radiation pressure is directed in the anti-Sun direction with the sail pitch angle $\alpha=0$. A constant acceleration displaces the orbit in the anti-Sun direction leading to a highly non-Keplerian orbit.

A schematic of a displaced non-Keplerian orbit in a two-body context is provided in Fig 2-1. As the orbit radius is much smaller than the separation distance between the Sun and sail, the Sun-line is assumed to be parallel to the z -axis. The ρ -axis represents the radial distance from the z -axis with unit vector \mathbf{e}_ρ and the z -axis represents the displacement distance from the central body with unit vector \mathbf{e}_z . The distance between the solar sail and the central body is represented by the vector $\mathbf{r} = z\mathbf{e}_z + \rho\mathbf{e}_\rho$, with magnitude $|\mathbf{r}| = \sqrt{z^2 + \rho^2}$. The direction of angular motion orientated around the z -axis is represented by the unit vector \mathbf{e}_θ where the angular position $\theta = \theta\mathbf{e}_\theta$.

In the two-body problem, the solar tide gravitational terms and the centripetal effects of the Earth orbiting the Sun are ignored. Only the gravitational acceleration of the Earth acting on the solar sail is considered in this model. The total force, \mathbf{F} , acting on the sail is composed of the gravitational attraction of the central body and the acceleration due to solar radiation pressure directed along the Sun-line

$$\mathbf{F} = -\frac{GMm}{|\mathbf{r}|^3}\mathbf{r} + ma\mathbf{e}_z \quad (2.2)$$

where G represents the universal gravitational constant, M is the mass of the central body, m is the mass of the solar sail and a the constant acceleration due to solar radiation pressure directed along the z axis, $a = \beta\mu_s/|\mathbf{R}_s|^2$.

The two-body equations of motion for the problem can be derived using the Hamiltonian method. The kinetic energy, T , can be written in cylindrical polar coordinates and the potential energy can be derived using Eq (2.2) as $V = -\int \mathbf{F} \cdot d\mathbf{r}$ which obtains

$$T = \frac{1}{2}m(\dot{z}^2 + \dot{\rho}^2 + \rho^2\dot{\theta}^2) \quad (2.3.1)$$

$$V = -\frac{GMm}{|\mathbf{r}|} - maz \quad (2.3.2)$$

where the transverse velocity component of the solar sail is defined in cylindrical polar coordinates as $\rho\dot{\theta}$.

The two-body Hamiltonian, H , is analogous to the total orbit energy defined as $H = T + V$. The Hamiltonian can be represented by the cylindrical polar coordinate momenta terms $P_z = m\dot{z}$, $P_\rho = m\dot{\rho}$ and $P_\theta = m\rho^2\dot{\theta}$ such that

$$H = \frac{1}{2m}\left(P_z^2 + P_\rho^2 + \frac{P_\theta^2}{\rho^2}\right) - \frac{\mu m}{|\mathbf{r}|} - maz \quad (2.4)$$

where $\mu = GM$ is the gravitational parameter of the central body.

The equations of motion can now be obtained from the Hamiltonian using $\partial H/\partial P_q = \dot{q}$ and $\partial H/\partial q = -\dot{P}_q$, where $q=(\rho, \theta, z)$. This results in the following equations of motion

$$\dot{\rho} = \rho\dot{\theta}^2 - \frac{\mu\rho}{|\mathbf{r}|^3} \quad (2.5.1)$$

$$\dot{\theta} = -\frac{2\rho\dot{\theta}}{\rho} \quad (2.5.2)$$

$$\ddot{z} = -\frac{\mu z}{|\mathbf{r}|^3} + a \quad (2.5.3)$$

These equations can be non-dimensionalised selecting the radius of the central body, L , as the characteristic length. The resulting characteristic time is defined as $\tau = \sqrt{\mu/L^3}$ which has the same effect as setting the gravitational parameter $\mu=1$.

The angular momentum of the problem can be derived by re-arranging Eq (2.5.2) as

$$\rho\ddot{\theta} + 2\dot{\rho}\dot{\theta} = \frac{1}{\rho} \frac{d}{dt} (\rho^2\dot{\theta}) = 0 \quad (2.6)$$

which demonstrates that $\rho^2\dot{\theta}$ is constant. This constant is the component of angular momentum directed along the z-axis and is denoted by h_z . The non-dimensionalised equations can then be re-written in terms of the constant angular momentum as

$$\ddot{\rho} = \frac{h_z^2}{\rho^3} - \frac{\rho}{|\mathbf{r}|^3} \quad (2.7.1)$$

$$\ddot{\theta} = -\frac{2\dot{\rho}\dot{\theta}}{\rho} \quad (2.7.2)$$

$$\ddot{z} = -\frac{z}{|\mathbf{r}|^3} + \kappa \quad (2.7.3)$$

where κ represents the non-dimensionalised acceleration due to solar radiation pressure.

For a circular, planet displaced non-Keplerian orbit, the initial conditions require constant displacement distance $\dot{z} = 0$ and constant radial distance $\dot{\rho} = 0$. Re-arranging Eq (2.7.1) to obtain $h_z = \rho^2|\mathbf{r}|^{-3/2}$ and substituting $h_z = \rho^2\dot{\theta}$, the required angular velocity for a circular orbit can be derived as

$$\dot{\theta} = \sqrt{\frac{1}{|\mathbf{r}|^3}} \quad (2.8)$$

The required acceleration can be derived by re-arranging Eq (2.7.3) to obtain

$$\kappa = \frac{z}{|\mathbf{r}|^3} \quad (2.9)$$

A series of contours representing the required acceleration and angular velocity for a range of nominal orbit displacement and radius are provided in Fig 2-2 and Fig 2-3 respectively.

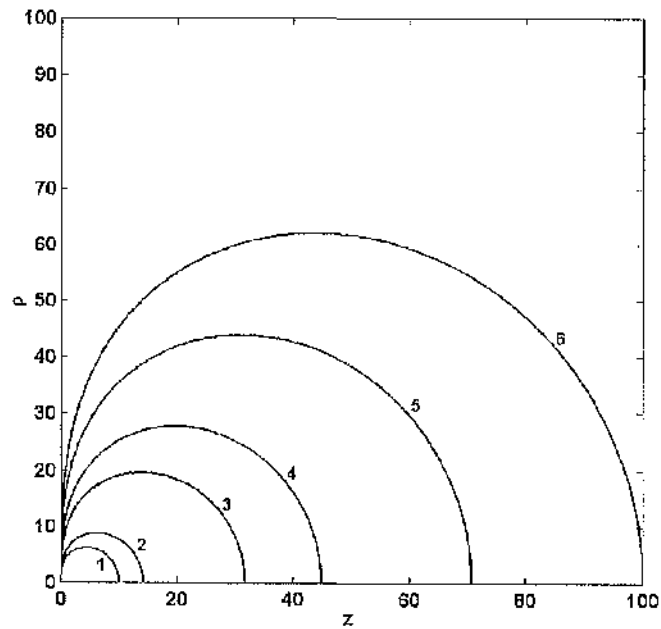


Figure 2-2 $\kappa(\rho, z)$ acceleration contours for range of orbit displacement and radius
 Contours: 1) $\kappa=0.01$, 2) $\kappa=0.005$, 3) $\kappa=0.001$, 4) $\kappa=0.0005$, 5) $\kappa=0.0002$, 6) $\kappa=0.0001$

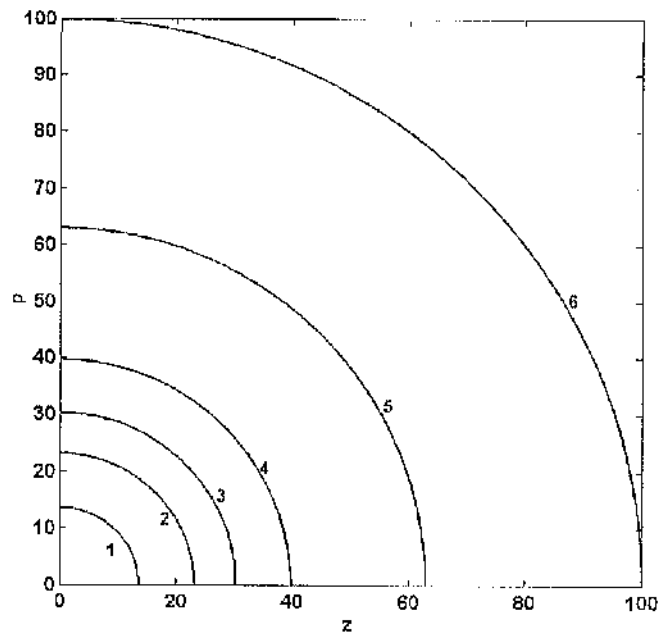


Figure 2-3 $\dot{\theta}(\rho, z)$ angular velocity contours for range of orbit displacements and radii
 Contours: 1) $\dot{\theta}=0.02$, 2) $\dot{\theta}=0.009$, 3) $\dot{\theta}=0.006$, 4) $\dot{\theta}=0.004$, 5) $\dot{\theta}=0.002$, 6) $\dot{\theta}=0.001$

2.2 Stability analysis

2.2.1 Linear stability condition

Consider a displaced non-Keplerian orbit with nominal displacement distance z_o and radius ρ_o . The stability of such orbits can be investigated by applying a small perturbation to the nominal orbit conditions and observing the resulting trajectory. If the solar sail remains within the vicinity of the nominal orbit after the conditions are perturbed the orbit can be described as stable; escape indicates the orbit is unstable.

The resulting trajectory variation due to small perturbations $\delta\rho$ and δz applied to the ρ - and z -axis respectively can be determined using Taylor's theorem [McInnes, 1998a]. The functions $f_\rho(\rho, z) = \ddot{\rho}$ and $f_z(\rho, z) = \ddot{z}$ are related to Eq (2.7.1) and Eq (2.7.3) as

$$f_\rho(\rho, z) = \frac{h_z}{\rho^3} - \frac{\rho}{|\mathbf{r}|^3} \quad (2.10.1)$$

$$f_z(\rho, z) = -\frac{z}{|\mathbf{r}|^3} + \kappa \quad (2.10.2)$$

The equations can be expanded to first order about $\rho = \rho_o + \delta\rho$ and $z = z_o + \delta z$ with the form

$$f_\rho(\rho_o + \delta\rho, z_o + \delta z) = f_\rho(\rho_o, z_o) + \left[\frac{\partial f_\rho}{\partial \rho} \right]_o \delta\rho + \left[\frac{\partial f_\rho}{\partial z} \right]_o \delta z \quad (2.11.1)$$

$$f_z(\rho_o + \delta\rho, z_o + \delta z) = f_z(\rho_o, z_o) + \left[\frac{\partial f_z}{\partial \rho} \right]_o \delta\rho + \left[\frac{\partial f_z}{\partial z} \right]_o \delta z \quad (2.11.2)$$

A variational equation can then be obtained by noting that $f(\rho_o, z_o) = 0$ which gives

$$\frac{d^2(\delta\rho)}{dt^2} = \left[\frac{\partial f_\rho}{\partial \rho} \right]_o \delta\rho + \left[\frac{\partial f_\rho}{\partial z} \right]_o \delta z \quad (2.12.1)$$

$$\frac{d^2(\delta z)}{dt^2} = \left[\frac{\partial f_z}{\partial \rho} \right]_o \delta\rho + \left[\frac{\partial f_z}{\partial z} \right]_o \delta z \quad (2.12.2)$$

Treating the non-dimensionalised acceleration, κ , and the orbit angular momentum, h_z , as constants the partial derivatives can be evaluated as

$$\left[\frac{\partial f_\rho}{\partial \rho} \right]_o = -\frac{3h_z^2}{\rho_o^4} - \frac{1}{r_o^3} + \frac{3\rho_o^2}{r_o^5} \quad (2.13.1)$$

$$\left[\frac{\partial f_\rho}{\partial z} \right]_o = \frac{3\rho_o z_o}{r_o^5} = \left[\frac{\partial f_z}{\partial \rho} \right]_o \quad (2.13.2)$$

$$\left[\frac{\partial f_z}{\partial z} \right]_o = -\frac{1}{r_o^3} + \frac{3z_o^2}{r_o^5} \quad (2.13.3)$$

The perturbations can be represented as a column vector $\delta\mathbf{Q} = [\delta\rho \ \delta z]^T$ enabling Eq (2.12.1) and Eq (2.12.2) to be written in matrix form as

$$\begin{bmatrix} 1 & 0 \\ 0 & 1 \end{bmatrix} \delta\ddot{\mathbf{Q}} - \begin{bmatrix} A_{11} & A_{12} \\ A_{21} & A_{22} \end{bmatrix} \delta\mathbf{Q} = \begin{bmatrix} 0 \\ 0 \end{bmatrix} \quad (2.14)$$

where the notation A_{11} , A_{12} , A_{21} , A_{22} represents the partial derivatives $\partial f_\rho/\partial\rho$, $\partial f_\rho/\partial z$, $\partial f_z/\partial\rho$ and $\partial f_z/\partial z$ respectively, evaluated on the nominal displaced circular orbit.

For a constant coefficient problem it can be assumed that $\delta\mathbf{Q} = \mathbf{Q}_o \exp(\lambda t)$, where λ is a constant. The two matrices on the left hand side of Eq (2.14) can be merged into one 2x2 nonsingular matrix by substituting $\delta\ddot{\mathbf{Q}} = \lambda^2 \delta\mathbf{Q}$ to obtain

$$\begin{bmatrix} \lambda^2 - A_{11} & -A_{12} \\ -A_{21} & \lambda^2 - A_{22} \end{bmatrix} = 0 \quad (2.15)$$

The characteristic equation of Eq (2.15) has the form

$$\lambda^4 - \lambda^2(A_{11} + A_{22}) + (A_{11}A_{22} - A_{12}^2) = 0 \quad (2.16)$$

where λ represents the eigenvalues of the matrix. For a stable orbit, the trajectory must exhibit oscillatory motion with no positive real eigenvalues. This is achieved when $\lambda^2 < 0$

resulting in eigenvalues which lie along the imaginary axis. Using this condition, and solving Eq (2.16) for λ^2 with a simple quadratic solution

$$\lambda^2 = \frac{(A_{11} + A_{22}) \pm \sqrt{(A_{11} + A_{22})^2 - 4(A_{11}A_{22} - A_{12}^2)}}{2} < 0 \quad (2.17)$$

Equation (2.17) can be simplified with some re-arranging to obtain the discriminant $A_{11}A_{22} - A_{12}^2 > 0$ for a stable orbit. Substituting the partial derivatives provided in Eq (2.13), the discriminant can be expressed as

$$\left(-\frac{3h_z^2}{\rho_o^4} - \frac{1}{r_o^3} + \frac{3\rho_o^4}{r_o^5} \right) \left(-\frac{1}{r_o^3} + \frac{3z_o^2}{r_o^5} \right) - \left(\frac{3\rho_o z_o}{r_o^5} \right)^2 > 0 \quad (2.18)$$

Simplifying the expression further by using $r_o^2 = z_o^2 + \rho_o^2$, the resulting inequality can be written as

$$\frac{3h_z^2}{\rho_o^4 r_o^3} - \frac{9h_z^2 z_o^2}{\rho_o^4 r_o^5} - \frac{2}{r_o^6} > 0 \quad (2.19)$$

Combining the expression for constant angular momentum $h_z = \rho^2 \dot{\theta}$ and the angular velocity of a displaced circular orbit $\dot{\theta}^2 = |\mathbf{r}|^{-3}$, the resulting expression $h_z^2 = \rho_o^4 / r_o^3$ can be used to simplify Eq (2.19) which obtains the constraint

$$\rho_o > 2\sqrt{2}z_o \quad (2.20)$$

This is the linear stability condition for a displaced non-Keplerian orbit derived from the linearised two-body equations of motion. Provided the nominal conditions agree with Eq (2.20), a small perturbation will not excite any divergent modes and the solar sail will remain in the vicinity of the nominal orbit.

Figure 2-4 shows a stable orbit displaced $z_o = 15$ L (radius of central body) along the Sun-line with a radius of $\rho_o = 50$ L. The nominal orbit conditions correspond to a stable orbit. Applying a small perturbation to the initial conditions it is found that the solar sail remains in the vicinity of the nominal orbit.

Figure 2-5 shows an unstable orbit produced by initial conditions $z_o = 20 L$ and $\rho_o = 50 L$. After applying a small perturbation, the solar sail is found to escape in the anti-Sun direction. Although this is a necessary condition for linear stability it is not sufficient for non-linear stability which must be derived using other methods.

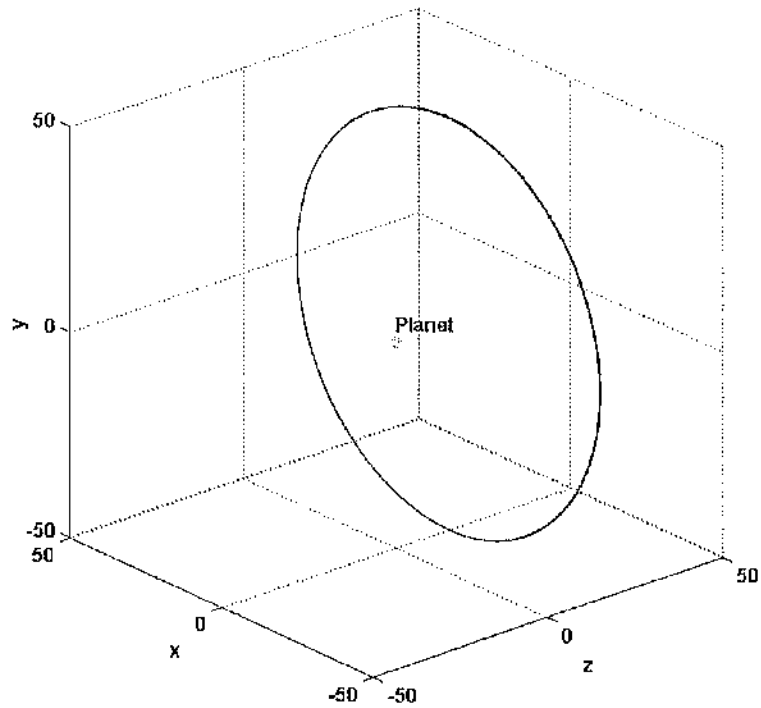


Figure 2-4 Stable non-Keplerian orbit with perturbation applied
 $\rho_o=50 L, z_o=15 L, \kappa=1.0545 \times 10^{-4}, \delta\rho=\delta z=0.01L$

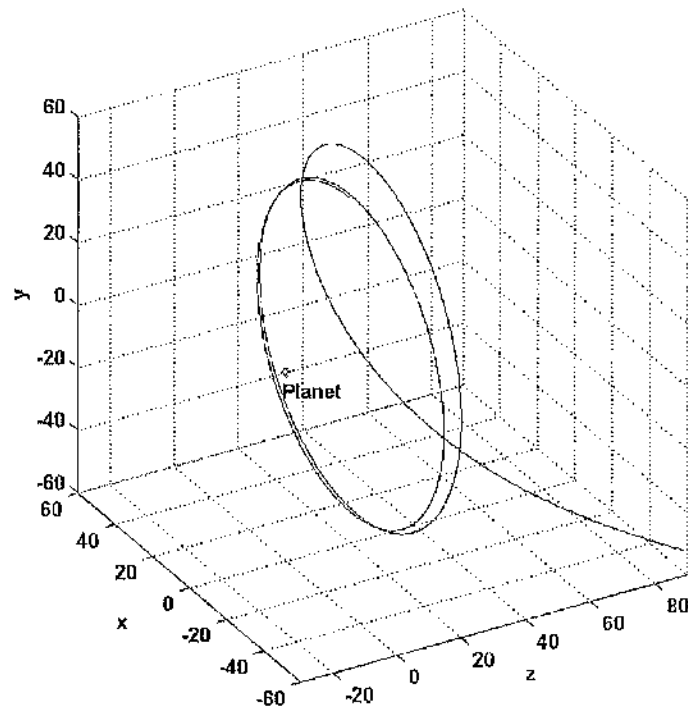


Figure 2-5 Unstable non-Keplerian orbit with perturbation applied
 $\rho_o=50 L, z_o=20 L, \kappa=1.2807 \times 10^{-4}, \delta\rho=\delta z=0.01L$

2.2.2 Nonlinear stability condition

A nonlinear method to determine orbit stability can be derived by considering the effective potential energy of the orbit. A pseudo-potential can be derived in the ρ - z plane which includes the terms due to constant angular momentum, h_z . The pseudo-potential analyses the potential energy in a reference frame rotating around the Sun-line.

The nominal conditions of a stable orbit will be located at a local minimum of the pseudo-potential energy. A small perturbation to these conditions will result in a restoring force that drives the sail back towards the nominal orbit. For solar sail escape to occur, the perturbation to the initial conditions must be large enough that the solar sail potential energy rises out of the of the local minima. Unstable orbit initial conditions will be located at a saddle point or local maxima of the pseudo-potential function.

The non-dimensionalised pseudo-potential function, $U(\rho, z)$, can be derived using the partial derivatives $\partial U/\partial\rho = -\ddot{\rho}$ and $\partial U/\partial z = -\ddot{z}$. These expressions can be solved for $U(\rho, z)$ by integrating Eq (2.7.1) and Eq (2.7.3) to obtain

$$U(\rho, z) = \frac{h_z^2}{2\rho^2} - \frac{1}{|\mathbf{r}|} - kz \quad (2.21)$$

A local minimum of this function is identified when $U_{\rho\rho} > 0$, $U_{zz} > 0$ and $U_{\rho\rho}U_{zz} - U_{\rho z}^2 > 0$ where U_{ij} denotes the derivative $\partial^2 U/\partial i\partial j$. The derivatives are evaluated as

$$U_{\rho\rho} = \frac{3h_z^2}{\rho^4} + \frac{1}{|\mathbf{r}|^3} - \frac{3\rho^2}{|\mathbf{r}|^5} \quad (2.22.1)$$

$$U_{zz} = \frac{1}{|\mathbf{r}|^5} - \frac{3z^2}{|\mathbf{r}|^5} \quad (2.22.2)$$

$$U_{\rho z} = -\frac{3\rho z}{|\mathbf{r}|^5} = U_{z\rho} \quad (2.22.3)$$

It can be demonstrated that $U_{\rho\rho} > 0$ for all real values of ρ and z by rearranging Eq (2.22.1) to show that this condition is met while $\rho^2 > -4z^2$. As ρ^2 and z^2 are always positive, this condition is always true. By deduction, if $U_{\rho\rho} > 0$ and $U_{\rho\rho}U_{zz} - U_{\rho z}^2 > 0$ then $U_{zz} > 0$.

The condition which must be met for a local minimum of the potential energy function, $U_{\rho\rho}U_{zz} - U_{\rho z}^2 > 0$ can be expressed as

$$\left(-\frac{3h_z^2}{\rho^4} - \frac{1}{|\mathbf{r}|^3} + \frac{3\rho^4}{|\mathbf{r}|^5}\right)\left(-\frac{1}{|\mathbf{r}|^3} + \frac{3z^2}{|\mathbf{r}|^5}\right) - \left(\frac{3\rho z}{|\mathbf{r}|^5}\right)^2 > 0 \quad (2.23)$$

It is clear that this expression is equivalent to Eq (2.18). As before, expanding the brackets and substituting $|\mathbf{r}|^2 = z^2 + \rho^2$ obtains

$$\frac{3h_z^2}{\rho^4|\mathbf{r}|^3} - \frac{9h_z^2 z^2}{\rho^4|\mathbf{r}|^5} - \frac{2}{|\mathbf{r}|^6} > 0 \quad (2.24)$$

Non-dimensionalised angular velocity is equivalent to $\dot{\theta}^2 = |\mathbf{r}|^{-3}$ and angular momentum $h_z = \rho^2 \dot{\theta}$. This can be substituted into Eq (2.24) to obtain

$$\frac{\dot{\theta}^2}{|\mathbf{r}|^3} - \frac{9\dot{\theta}^2 z^2}{|\mathbf{r}|^5} > 0 \quad (2.25)$$

Multiplying by $|\mathbf{r}|^5$ and dividing by $\dot{\theta}^2$, the expression can be re-arranged to demonstrate that the condition for stability is met provided $\rho > 2\sqrt{2}z$. Conversely, a local saddle point exists in the potential energy function if $\rho < 2\sqrt{2}z$ with $U_{zz} < 0$ which indicates unstable initial conditions. This proves that the non-linear condition for stability agrees with the condition derived using a linear approximation, provided in Eq (2.20).

The derived stability condition agrees with a study by Dankowicz [1996] which regularizes the two body problem using KS (Kustannheimo-Stiefel) variables [Stiefel and Scheifele, 1971] and investigated the stability of orbits displaced by a constant axial force. In order

to illustrate the stability condition, the nominal angular momentum and nominal sail acceleration are evaluated at initial orbit conditions ρ_0 and z_0 . The potential energy function is then evaluated to generate a contour surface. Figure 2-6 shows a contour plot of the potential energy function for an orbit with stable initial conditions. It is clear that a local minimum of the function exists at the nominal orbit conditions in this case. The potential energy function for a set of unstable initial conditions is shown in Figure 2-7. In this case, a saddle point is found to exist about the initial orbit conditions.

Figure 2-8 demonstrates that the resulting two-body stability using iterative methods agrees with the derived stability condition. The darker region represents unstable orbit conditions and the lighter region represents stable orbit conditions. The stability condition is represented by the line with gradient $2\sqrt{2}$ which dissects the stable and unstable orbit region. These results were obtained over a range of nominal orbit displacement and radius. A small perturbation of $\delta\rho=\delta z=0.01L$ was applied to the initial conditions and each orbit was numerically integrated over a timescale of $4T$, where the orbit period $T = 2\pi/\dot{\theta} = 2\pi|r|^{3/2}$. An orbit was considered to be stable if the calculated trajectory remained within $2z_0$ of the central body, where z_0 is the nominal displacement distance. Unstable orbits result in an escape in the anti-Sun direction after the integration time.

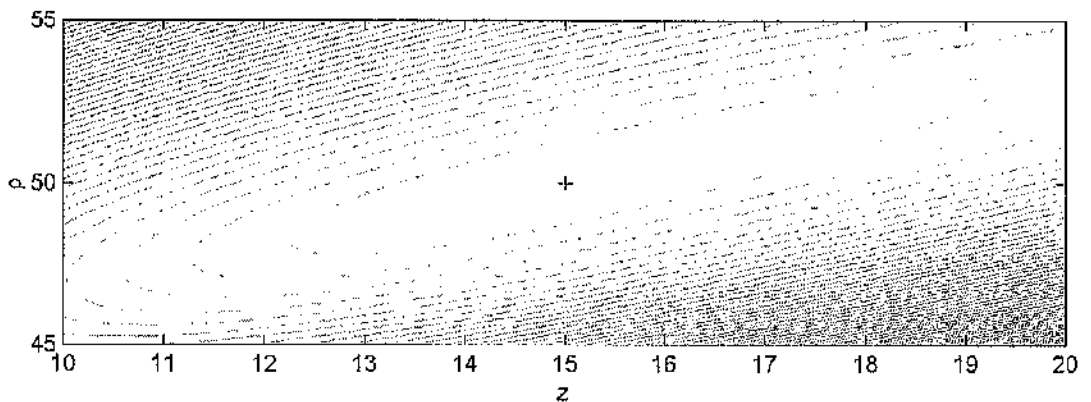


Figure 2-6 Potential energy function for stable initial orbit conditions

$$\rho_0=50 L, z_0=15 L, \kappa=1.0545 \times 10^{-4}$$

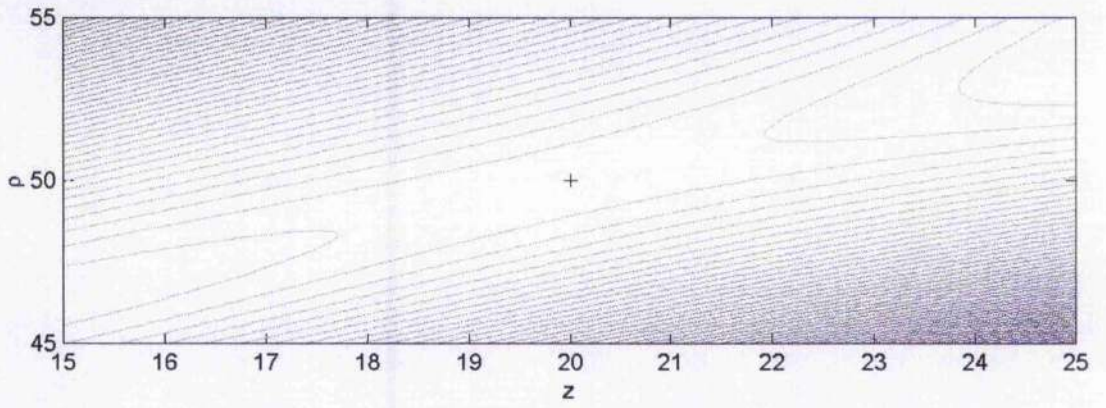


Figure 2-7 Potential energy function for unstable initial orbit conditions

$$\rho_0=50 \text{ L}, z_0=20 \text{ L}, \kappa=1.2807 \times 10^{-4}$$

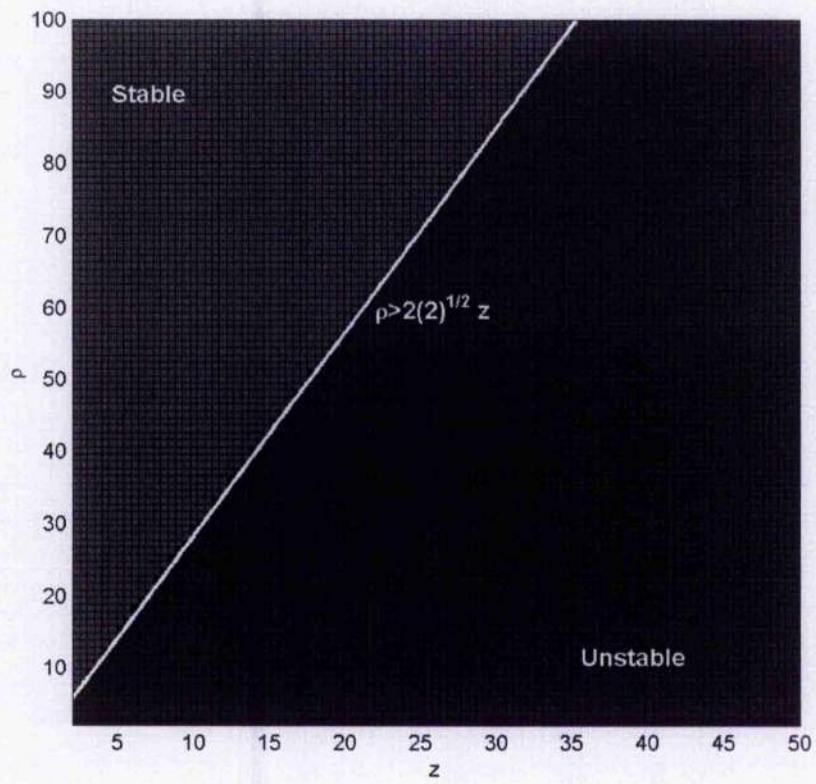


Figure 2-8 Stability of orbits investigated using an iterative method

2.2.3 Jacobi-type energy surfaces

A method to visualize regions of bound orbital motion in the ρ - z plane can be obtained by multiplying Eq (2.7.1) and Eq (2.7.3) by their respective velocity terms $\dot{\rho}$ and \dot{z} then summing the resulting expressions together as

$$\dot{\rho}\ddot{\rho} + \dot{z}\ddot{z} = -\left[\dot{\rho}\frac{\partial U}{\partial \rho} + \dot{z}\frac{\partial U}{\partial z}\right] \quad (2.26)$$

The partial derivatives of the pseudo-potential, in the right hand side of the expression, can be reduced to dU/dt as a consequence of the simple chain-rule of differentiation. An integral can now be formed by factorizing the time derivative to obtain

$$\frac{d}{dt}\left(\frac{\dot{\rho}^2}{2} + \frac{\dot{z}^2}{2} + U\right) = 0 \quad (2.27)$$

It can be seen that $(\dot{\rho}^2 + \dot{z}^2)/2 + U = E$ where the constant of integration, E , is equivalent to the total energy of the system. Substituting the pseudo-potential energy, Eq (2.21), gives the total energy in the form

$$E = \frac{1}{2}(\dot{\rho}^2 + \dot{z}^2) + \frac{h_z^2}{2\rho^2} - \frac{1}{|\mathbf{r}|} - \kappa z \quad (2.28)$$

As the total energy is conserved, the initial energy $E_0 = E$. Given the initial orbit conditions $(\rho_0, z_0, \dot{\rho}_0, \dot{z}_0)$, a value for E_0 can be calculated from Eq (2.28). For a nominal orbit with constant displacement distance and constant radius $\dot{z}_0 = \dot{\rho}_0 = 0$.

Regions of bound motion can be identified by considering the solar sail velocity, $|\mathbf{v}|^2 = \dot{\rho}^2 + \dot{z}^2$. Imaginary velocity, $|\mathbf{v}|^2 < 0$, corresponds to a region of forbidden motion. The condition for allowed motion is therefore $|\mathbf{v}|^2 \geq 0$. The surface representing the zero-velocity boundary can be calculated from Eq (2.28) as

$$E_0 - U(\rho, z) \geq 0 \quad (2.29)$$

Figure 2-9 represents the zero-velocity surface for a stable orbit. The lighter region indicates forbidden motion and the darker region represents allowed motion. The white line represents the resulting trajectory in the ρ - z plane. A small initial kinetic energy is applied to perturb the solar sail from the nominal orbit. It is clear that the solar sail motion is bound within a confined region of allowed motion which prevents the solar sail leaving the vicinity of the nominal orbit.

Figure 2-10 represents the zero-velocity surface for an unstable orbit. As before, a small initial kinetic energy is applied to perturb the solar sail from the nominal orbit. In this case, there is no region which confines the solar sail motion near to the vicinity of the nominal orbit. Instead, the solar sail is free to escape.

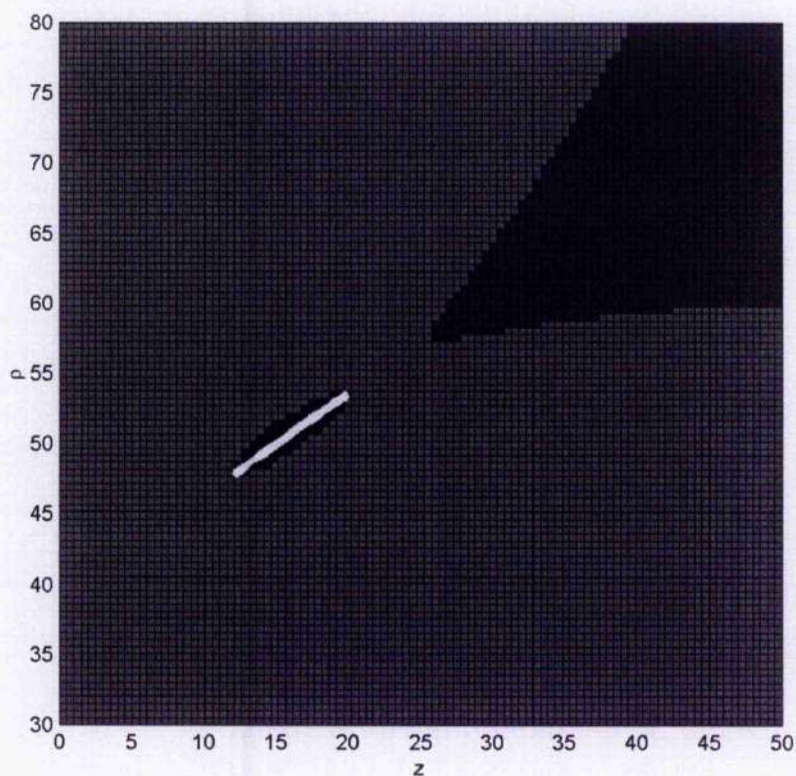


Figure 2-9 Zero velocity surface of a stable non-Keplerian orbit

$$\rho_0=50 \text{ L}, z_0=15 \text{ L}, \kappa=1.0545 \times 10^{-4}, \dot{\rho}_0 = \dot{z}_0 = 0.003$$

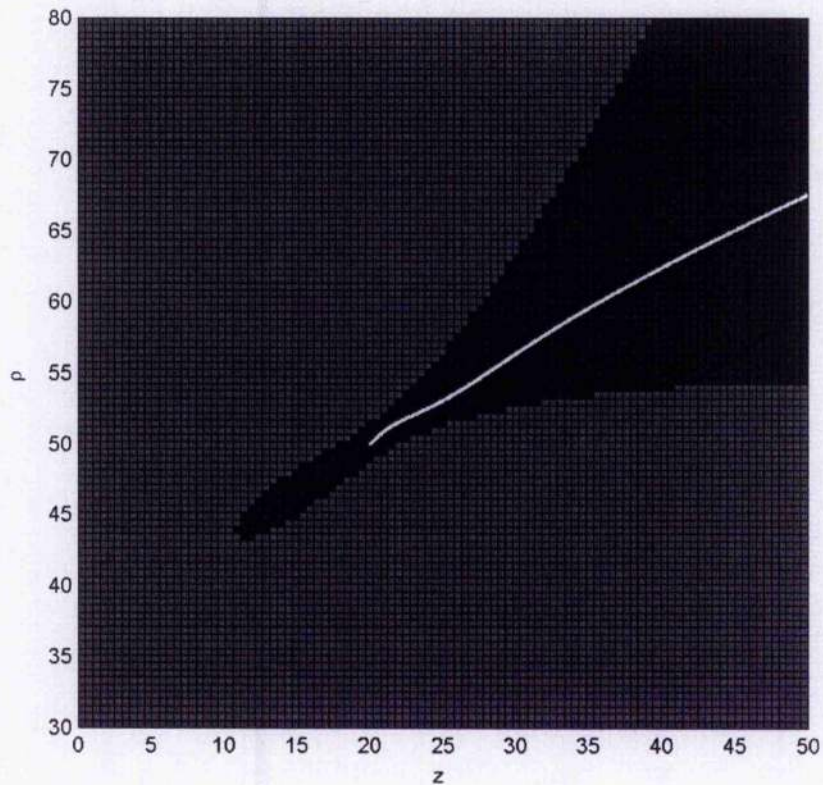


Figure 2-10 Zero velocity surface of an unstable non-Keplerian orbit

$$\rho_o=50 \text{ L}, z_o=20 \text{ L}, \kappa=1.2807 \times 10^{-4}, \dot{\rho}_o = \dot{z}_o = 0.003$$

2.3 Closed form solution of two-body problem

2.3.1 Closed form solution using parabolic coordinates

The gravitational two-body problem with a uniform force due to solar radiation pressure is analogous to electron motion in the presence of a Coulomb field (hydrogen atom) with an external homogeneous electric field, the so called Stark effect. It has been demonstrated by several authors [Born, 1927; Burns, 1968; Howard, 1995a; Bookless, 2005] that the Hamiltonian of such a problem is separable by transforming the problem using parabolic coordinates (ξ, η, θ) .

Parabolic coordinates represent constant paraboloid surfaces in Euclidean space which are generated by rotating a parabola about its axis of symmetry. For a paraboloid surface symmetric around the z -axis (Sun-line), the conversion between parabolic coordinates and polar coordinates (ρ, z) is define by $\rho = \xi\eta$ and $z = (\xi^2 - \eta^2)/2$ with time derivatives

$$\dot{\rho} = \dot{\xi}\eta + \dot{\eta}\xi \quad (2.30.1)$$

$$\dot{z} = \dot{\xi}\xi - \dot{\eta}\eta \quad (2.30.2)$$

The radial distance of the solar sail from the central body is given by $|\mathbf{r}| = (\xi^2 + \eta^2) / 2$. The two-body Hamiltonian, provided in Eq (2.4), can be non-dimensionalised and rewritten using parabolic coordinates. The polar coordinate momenta terms (P_ρ, P_z, P_θ) can be rewritten as

$$P_\rho^2 = m^2 \dot{\rho}^2 = m^2 \left((\dot{\xi}\eta)^2 + \dot{\xi}\eta\dot{\eta}\xi + (\dot{\eta}\xi)^2 \right) \quad (2.31.1)$$

$$P_z^2 = m^2 \dot{z}^2 = m^2 \left((\dot{\xi}\xi)^2 - \dot{\xi}\xi\dot{\eta}\eta + (\dot{\eta}\eta)^2 \right) \quad (2.31.2)$$

$$P_\theta^2 / \rho^2 = m^2 \rho^2 \dot{\theta}^2 = m^2 (\xi\eta)^2 \dot{\theta}^2 \quad (2.31.3)$$

Substituting these terms into Eq (2.4) yields

$$H(\xi, \eta, \theta) = \frac{m}{2} \left((\dot{\xi}\eta)^2 + \dot{\xi}\eta\dot{\eta}\xi + (\dot{\eta}\xi)^2 + (\dot{\xi}\xi)^2 - \dot{\xi}\xi\dot{\eta}\eta + (\dot{\eta}\eta)^2 + (\dot{\theta}\eta\xi)^2 \right) - \frac{2\mu m}{(\xi^2 + \eta^2)} - \frac{ma}{2} (\xi^2 - \eta^2) \quad (2.32)$$

As before, this equation can be non-dimensionalised with characteristic length L and characteristic time $\tau = \sqrt{\mu/L^3}$. The resulting gravitational parameter $\mu = 1$ and acceleration due to solar radiation pressure, a , is represented using the non-dimensionalised nomenclature $\kappa = a\mu/L^4$. The Hamiltonian can be expressed in terms of the parabolic momenta P_ξ , P_η and P_θ which are equivalent to

$$P_\xi = \frac{\partial H}{\partial \dot{\xi}} = \xi(\xi^2 + \eta^2) \quad (2.33.1)$$

$$P_\eta = \frac{\partial H}{\partial \dot{\eta}} = \eta(\xi^2 + \eta^2) \quad (2.33.2)$$

$$P_\theta = \frac{\partial H}{\partial \dot{\theta}} = (\xi\eta)^2 \dot{\theta} = \rho^2 \dot{\theta} \quad (2.33.3)$$

The following expression is obtained for the non-dimensionalised Hamiltonian

$$H(\xi, \eta) = \frac{1}{2(\xi^2 + \eta^2)} \left(P_\xi^2 + P_\eta^2 + P_\theta^2 \left(\frac{1}{\xi^2} + \frac{1}{\eta^2} \right) \right) - \frac{2}{\xi^2 + \eta^2} - \frac{\kappa}{2} (\xi^2 - \eta^2) \quad (2.34)$$

Equation (2.34) is variable separable using the Hamilton-Jacobi method [Landau, 1976; Goldstein, 1959]. A transforming function $S(t, \xi, \eta)$ is required with the form

$$S(t, \xi, \eta) = -Et + P_\theta \theta + S_\xi(\xi) + S_\eta(\eta) \quad (2.35)$$

where E represents the conserved total energy of the system, $S_\xi(\xi)$ and $S_\eta(\eta)$ are variable separated functions, t is the time and θ is the angular position. The transforming function is defined such that it satisfies the Hamilton-Jacobi equation $\partial S / \partial t + H(\xi, \eta) = 0$. Substituting Eq (2.34) and re-arranging yields

$$-2E\xi^2 - 2E\eta^2 + P_\xi^2 + P_\eta^2 + \frac{P_\theta^2}{\xi^2} + \frac{P_\theta^2}{\eta^2} - 4 - \kappa(\xi^4 - \eta^4) = 0 \quad (2.36)$$

Equation (2.36) can be re-arranged so that all terms containing ξ are on the left and all terms containing η are on the right hand side of the equation. The momenta terms $P_\xi = \partial S_\xi / \partial \xi$ and $P_\eta = \partial S_\eta / \partial \eta$ can also be substituted into Eq (2.36) as follows

$$-2E\xi^2 + \left(\frac{\partial S_\xi}{\partial \xi} \right)^2 + \frac{P_\theta^2}{\xi^2} - 4 - \kappa\xi^4 = 2E\eta^2 - \left(\frac{\partial S_\eta}{\partial \eta} \right)^2 - \frac{P_\theta^2}{\eta^2} - \kappa\eta^4 \quad (2.37)$$

The coordinates ξ and η are independent, but arbitrary values must always produce an agreement with the equality in Eq (2.37). A separation constant, Φ , can therefore be defined and the resulting variable separated expressions are

$$\left(\frac{\partial S_\xi}{\partial \xi} \right)^2 - 2\xi^2 E - \kappa\xi^4 + \frac{P_\theta^2}{\xi^2} - 4 = -\Phi \quad (2.38.1)$$

$$\left(\frac{\partial S_\eta}{\partial \eta} \right)^2 - 2\eta^2 E + \kappa\eta^4 + \frac{P_\theta^2}{\eta^2} = \Phi \quad (2.38.2)$$

As demonstrated by McInnes [1999a], these expressions can be solved for $\partial S_\xi / \partial \xi$ and $\partial S_\eta / \partial \eta$ to obtain two bi-cubic polynomial solutions of the two-body equations

$$\frac{\partial S_\xi}{\partial \xi} = \frac{\sqrt{\kappa}}{\xi} \left[\xi^6 + \frac{2E}{\kappa} \xi^4 + \frac{(4-\Phi)}{\kappa} \xi^2 - \frac{P_\theta^2}{\kappa} \right]^{1/2} \quad (2.39.1)$$

$$\frac{\partial S_\eta}{\partial \eta} = \frac{\sqrt{\kappa}}{\eta} \left[-\eta^6 + \frac{2E}{\kappa} \eta^4 + \frac{\Phi}{\kappa} \eta^2 - \frac{P_\theta^2}{\kappa} \right]^{1/2} \quad (2.39.2)$$

The constants E , P_θ and Φ can be evaluated at the initial orbit conditions. The constant angular momentum $P_\theta = \rho^2 \dot{\theta}$ and the constant energy can be calculated using Eq (2.28). The separation constant, Φ can be calculated using either Eq (2.38.1) or Eq (2.38.2) evaluated at the initial conditions. For initial conditions $(\rho_o, z_o, \dot{\rho}_o, \dot{z}_o)$, the corresponding parabolic coordinates can be evaluated by substituting $\eta_o = \rho_o / \xi_o$ into $z_o = (\xi_o^2 - \eta_o^2) / 2$ and re-arranging to obtain

$$\xi_o^4 - 2z_o \xi_o^2 - \rho_o^2 = 0 \quad (2.40)$$

This quadratic can be solved to obtain four solutions for ξ_o with corresponding values of η_o . To calculate the initial momenta terms, P_ξ and P_η , Eq (2.30.1) and Eq (2.30.2) can be treated as simultaneous equations and solved for $\dot{\xi}_o$ using

$$\dot{\xi}_o = \frac{\dot{\rho}_o \eta_o + \dot{z}_o \xi_o}{(\xi_o^2 + \eta_o^2)} \quad (2.41)$$

where the resulting value can be substituted back into Eq (2.30.1) or Eq (2.30.2) to find the corresponding value for $\dot{\eta}_o$. The momenta terms, P_ξ and P_η are then calculated using Eq (2.33.1) and Eq (2.33.2) respectively.

To identify paraboloid surfaces which bound the orbital motion, the parabolic coordinates are evaluated when the momenta terms, $P_\xi = \partial S_\xi / \partial \xi = 0$ and $P_\eta = \partial S_\eta / \partial \eta = 0$ using the previously calculated constants E , P_θ and Φ . Equation (2.39.1) and Eq (2.39.2) can be

solved for ξ and η to identify paraboloid surfaces which bound the solar sail motion for a given set of initial conditions.

2.3.2 Paraboloid bounding surfaces

Consider a displaced non-Keplerian orbit with stable initial conditions, as defined by the stability condition $\rho_o > 2\sqrt{2}z_o$. Table 2-1 provides a set of parabolic coordinates which bound the stable orbit after a small perturbation is applied. It was found that a stable orbit is bound between four paraboloid surfaces. This is demonstrated in Fig 2-11 where the perturbed orbit is clearly bound between the intersecting parabolae. An enlarged section of the orbit is provided in Fig 2-12.

The applied perturbation introduces a periodic oscillation to the solar sail orbit. From Fig 2-13, it is clear that the smaller the magnitude of the applied perturbation, the smaller the amplitude of the resulting oscillation. Figure 2-14 demonstrates another bound orbit for an orbit of smaller radius, displaced nearer to the central body.

Similarly, if an initial velocity is applied to $\dot{\rho}_o$ and \dot{z}_o , a periodic oscillation is also introduced to the solar sail orbit. Figure 2-15 demonstrates a bound orbit with initial conditions comparable to the stable orbit produced in Fig 2-4. This shows an agreement between the zero-velocity surfaces produced using the Jacobi-type integral and the paraboloid surfaces produced using the closed-form solution.

Initial Conditions			Bounding Surface Parabolic Coordinates			
z_o	ρ_o	$\delta\rho, \delta z$	ξ_1	ξ_2	η_1	η_2
15	50	0.1	8.2113	8.7645	6.1311	6.1013
15	50	0.01	8.1990	8.2310	6.1025	6.0995
15	50	0.001	8.1978	8.2009	6.0996	6.0993
10	30	0.1	6.8282	7.2582	5.1770	5.1405
10	30	0.01	6.8134	6.8430	5.1420	5.1384
10	30	0.001	6.8120	6.8148	5.1385	5.1382

Table 2-1 Parabolic coordinate values for perturbed initial conditions

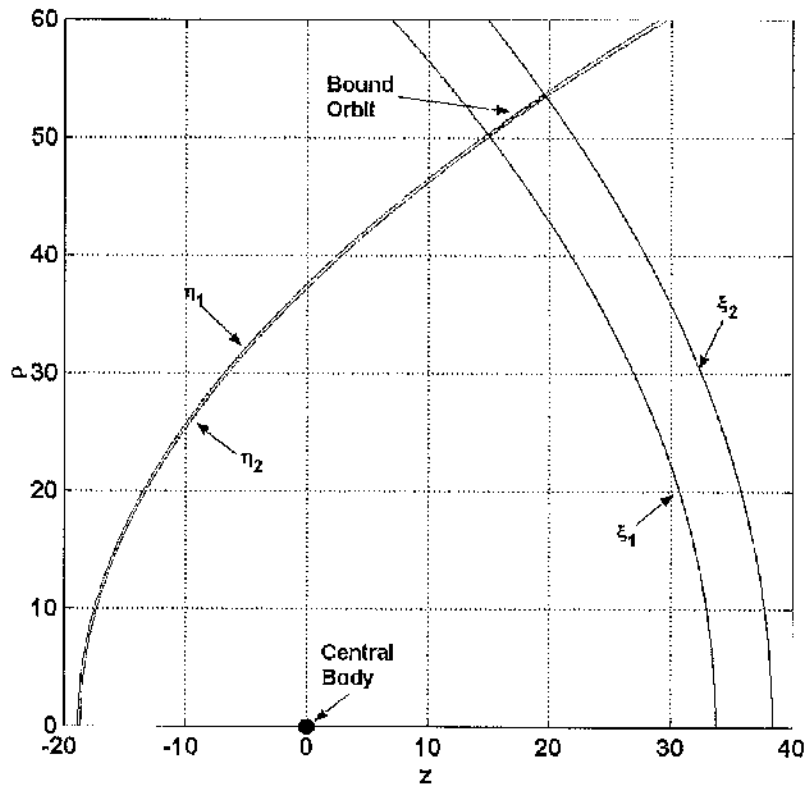


Figure 2-11 Stable displaced non-Keplerian orbit bound between parabolae
 $\rho_0=50 L, z_0=15 L, \kappa=1.0545 \times 10^{-4}, \delta\rho=\delta z=0.1L$

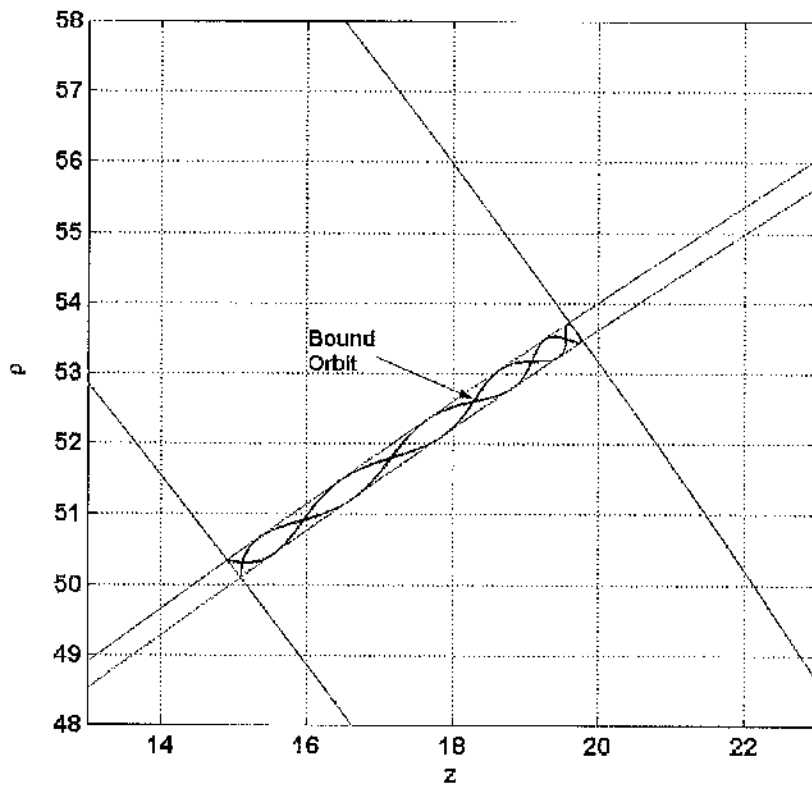


Figure 2-12 Enlarged view of bound orbit provided in Fig 2-11

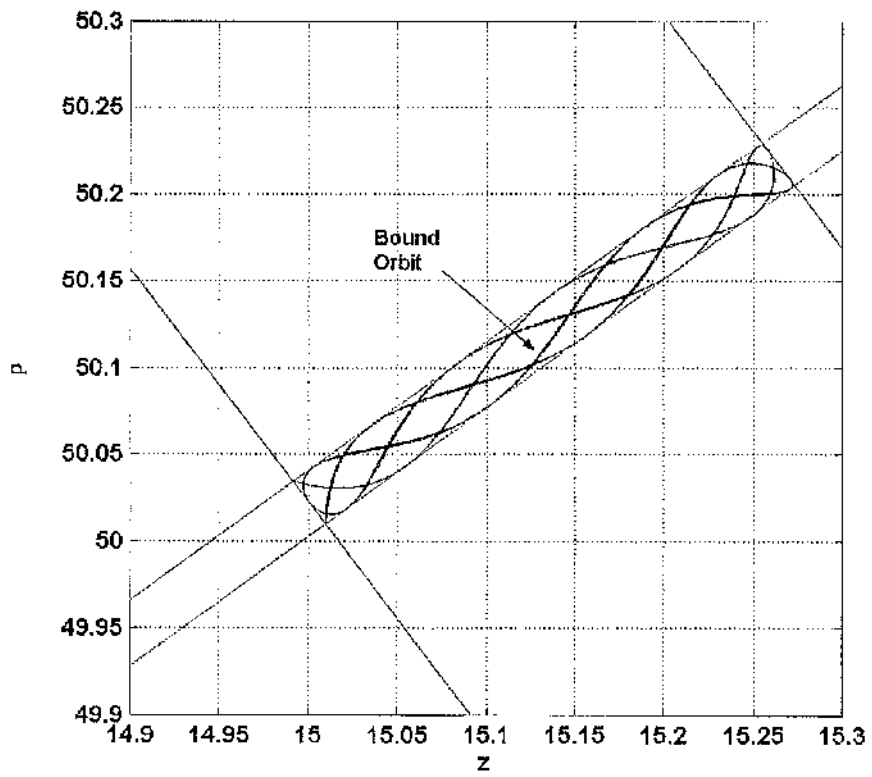


Figure 2-13 Stable displaced non-Keplerian orbit bound between parabolae
 $\rho_0=50 L, z_0=15 L, \kappa=1.0545 \times 10^{-4}, \delta\rho=\delta z=0.01L$

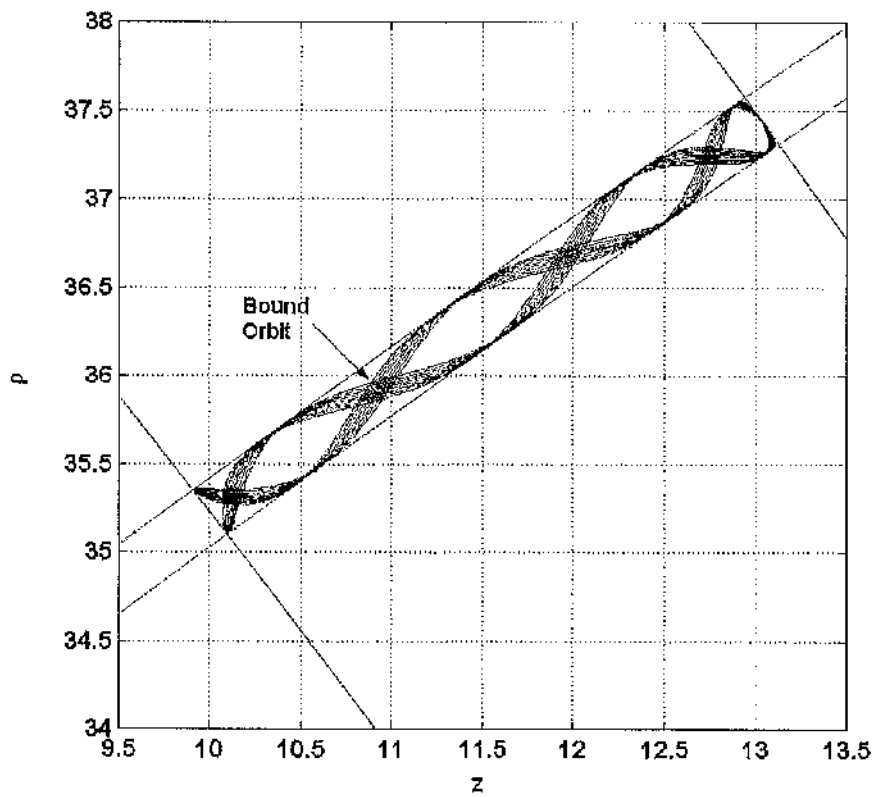


Figure 2-14 Stable displaced non-Keplerian orbit bound between parabolae
 $\rho_0=35 L, z_0=10 L, \kappa=2.0734 \times 10^{-4}, \delta\rho=\delta z=0.1L$

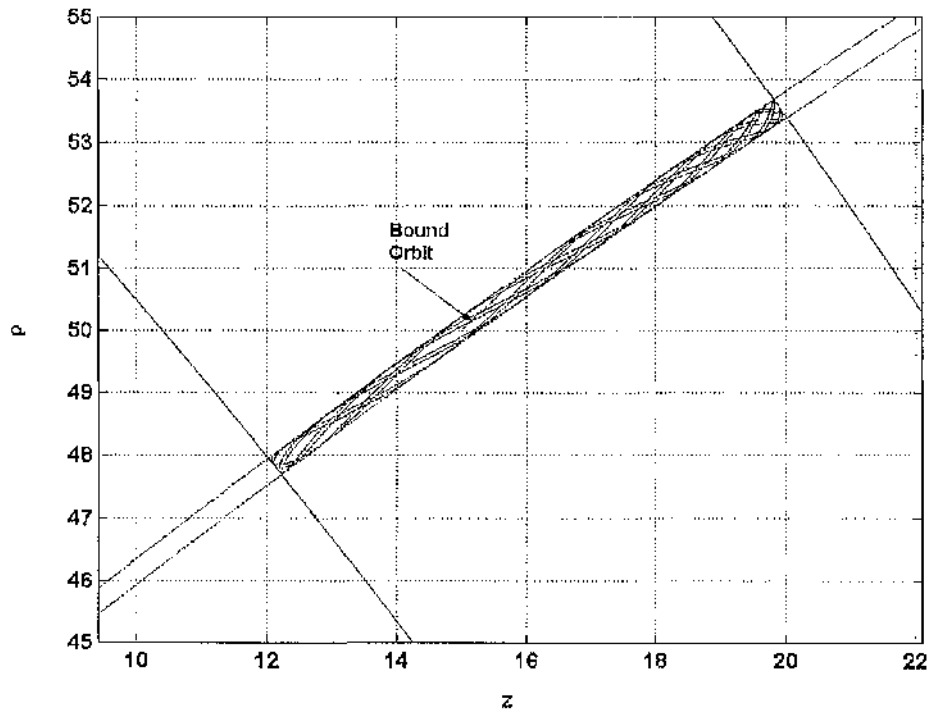


Figure 2-15 Stable displaced non-Keplerian orbit with initial velocity applied

$$\rho_o=50 L, z_o=15 L, \kappa=1.0545 \times 10^{-4}, \dot{\rho}_o=\dot{z}_o=0.003$$

2.3.3 Periodic Looping Trajectory

Applying a small perturbation to the nominal acceleration, κ_o , introduces a periodic oscillation to the solar sail trajectory. In the case of a stable orbit, applying a small perturbation such that the acceleration $\kappa = \kappa_o(1 - \Delta)$ results in the parabolic surface provided in Fig 2-16 where $\Delta=0.01$.

Figure 2-17 shows the resulting ρ and z displacement versus time due to the small reduction in the acceleration value. Over this time period, the range of radial distance $\rho = (49.097L \rightarrow 50.067L)$ and displacement distance $z = (13.750L \rightarrow 15L)$. Figure 2-18 represents this trajectory in a Cartesian plot and includes the bounding paraboloid surfaces.

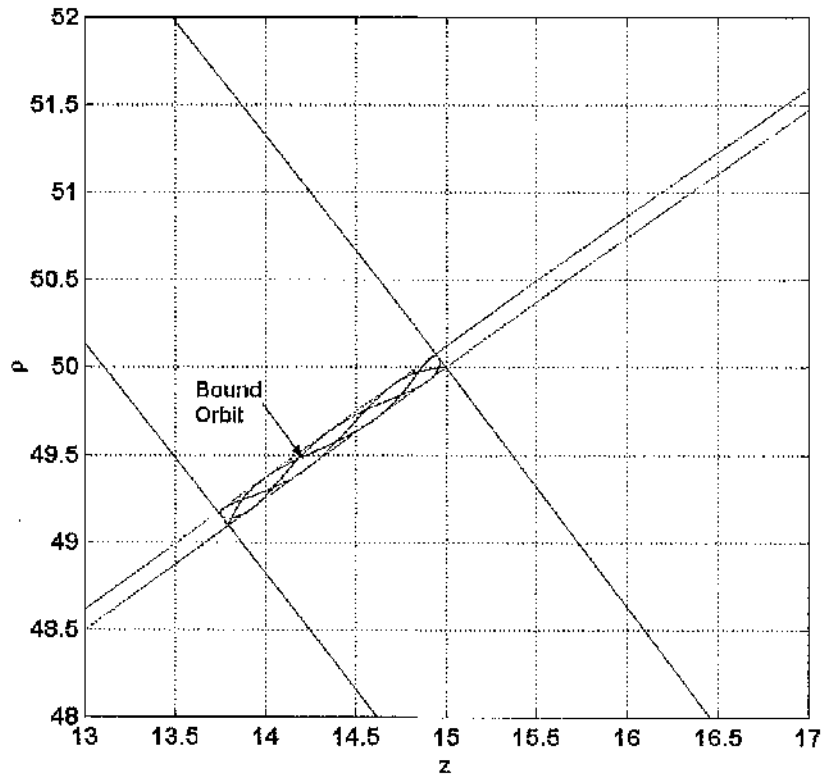


Figure 2-16 Stable orbit with small acceleration perturbation applied ($\Delta=0.01$)

$$\rho_0=50 \text{ L}, z_0=15 \text{ L}, \kappa= 1.0439 \times 10^{-4} \Delta=0.01$$

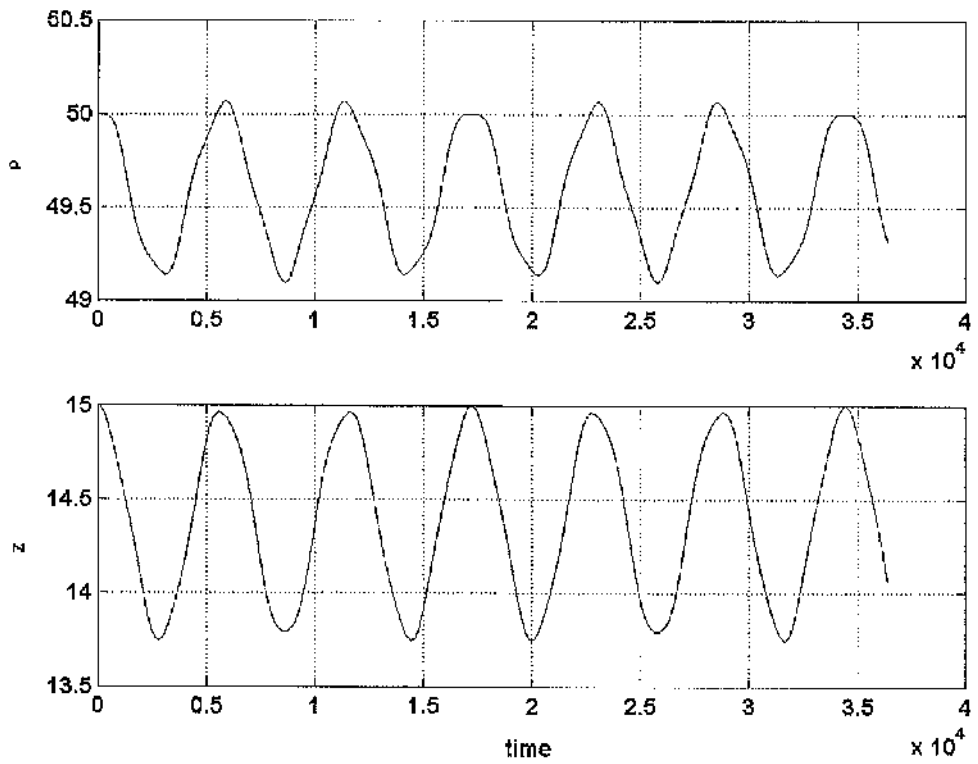


Figure 2-17 Radial and z-displacement variation due to small acceleration perturbation

$$\rho_0=50 \text{ L}, z_0=15 \text{ L}, \kappa= 1.0439 \times 10^{-4} \Delta=0.01$$

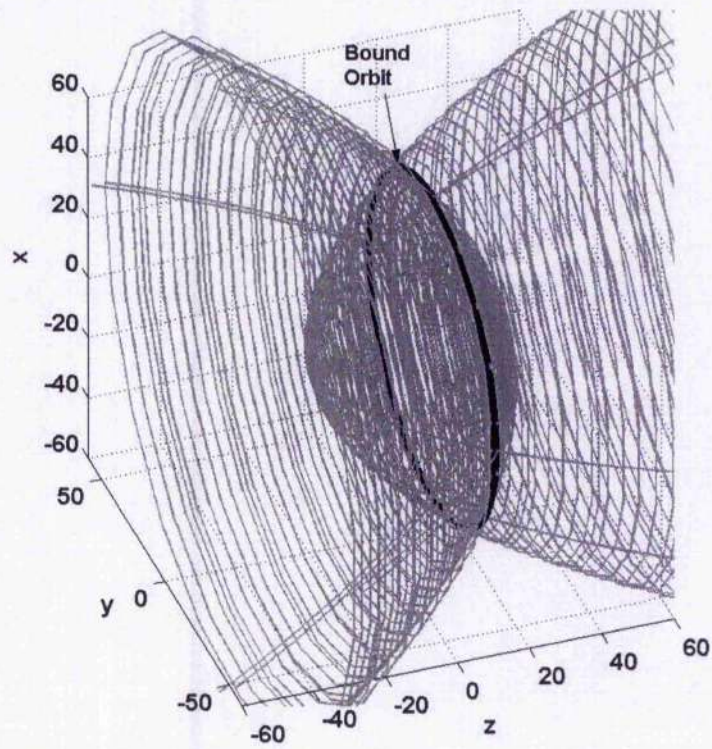


Figure 2-18 3D Cartesian plot of stable orbit with small acceleration perturbation
 $\rho_o=50 L, z_o=15 L, \kappa= 1.0439 \times 10^{-4} \Delta=0.01$

In the case of an unstable orbit, the application of a small reduction in acceleration, again $\Delta=0.01$, results in a highly perturbed trajectory. Two examples of the bounding parabolic curves are provided in Fig 2-19 and Fig 2-20. The parabolic coordinate values for both these surfaces are provided in Table 2-2.

Initial Conditions		Bounding Surface Parabolic Coordinates ($\Delta=0.01$)			
z_o	ρ_o	ξ_1	ξ_2	η_1	η_2
50	15	8.0496	8.1977	6.1087	6.0993
50	20	7.3997	8.5937	5.8285	5.8182
20	30	1.1050	8.1275	2.4667	2.4608

Table 2-2 Parabolic coordinates representing surfaces bounding a periodic looping trajectory

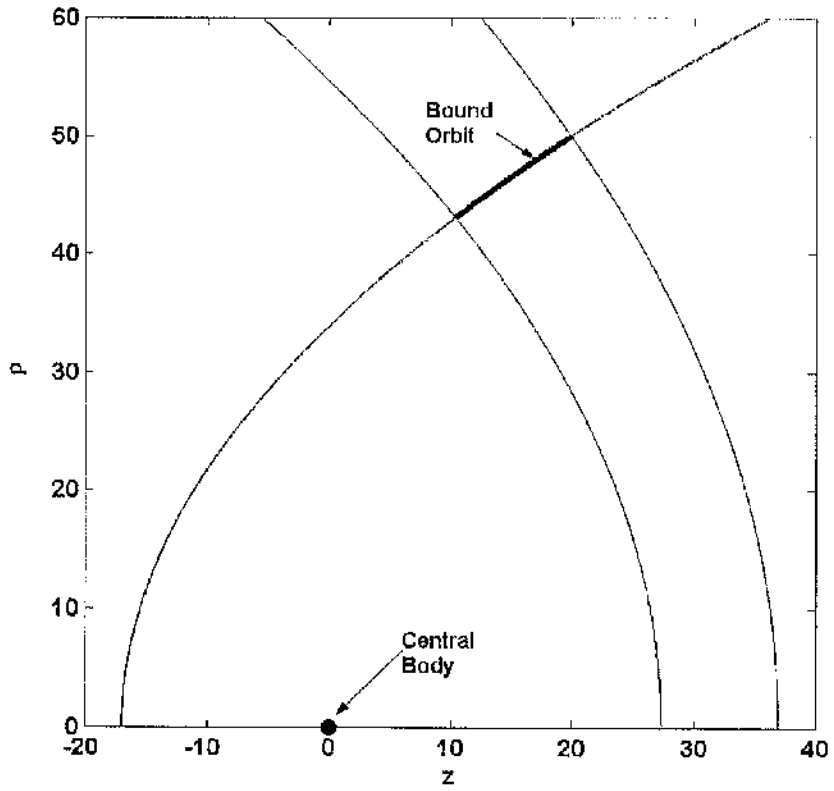


Figure 2-19 Unstable orbit with small acceleration perturbation

$$\rho_0=50 L, z_0=20 L, \kappa=1.2679 \times 10^{-4}, \Delta=0.01$$

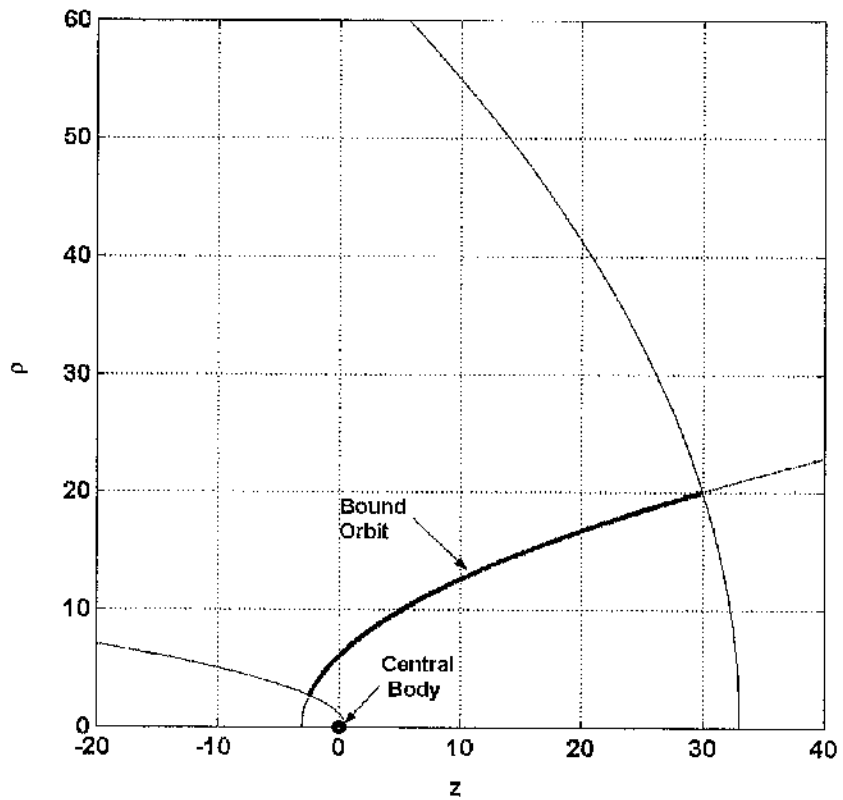


Figure 2-20 Unstable orbit with small acceleration perturbation

$$\rho_0=20 L, z_0=30 L, \kappa=6.3364 \times 10^{-4}, \Delta=0.01$$

It is evident that the further the initial conditions are from the $\rho > 2\sqrt{2}z$ stability boundary, the closer to the central body the solar sail trajectory passes. Figure 2-21 shows a Cartesian plot of the bound trajectory provided in Fig 2-20. In this case, the solar sail leaves the nominal orbit and performs a loop around the central body before returning to the nominal orbit. This trajectory is repeated periodically with a minimum approach distance to the central body of 3.64 L. Figure 2-22 shows the radial and z-displacement variation with time.

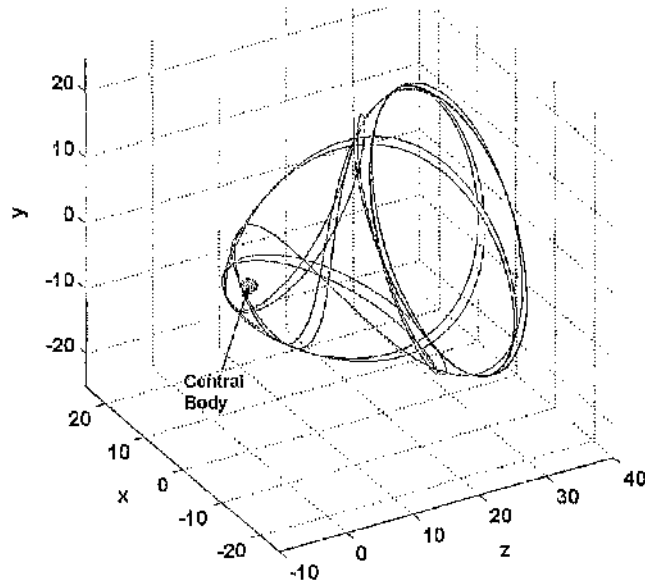


Figure 2-21 Periodic looping trajectory generated by perturbing the nominal acceleration
 $\rho_0=20$ L, $z_0=30$ L, $\kappa=6.3364 \times 10^{-4}$, $\Delta=0.01$

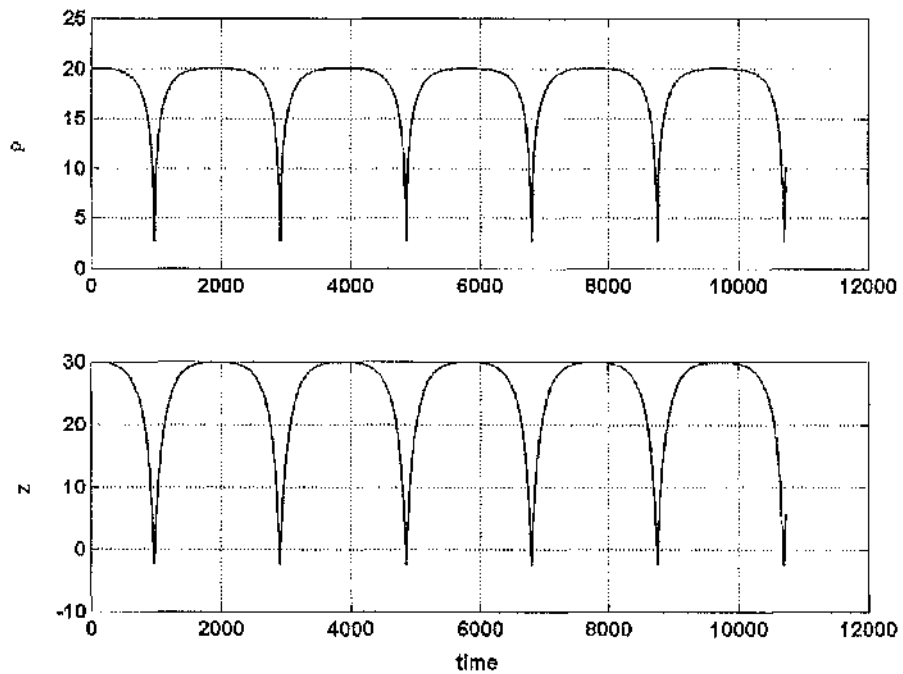


Figure 2-22 Radial and z-displacement variation due to small acceleration perturbation
 $\rho_0=20$ L, $z_0=30$ L, $\kappa=6.3364 \times 10^{-4}$, $\Delta=0.01$

This periodic looping trajectory is shown in Fig 2-23 fixed within a set of four paraboloid surfaces. The trajectory is bound to the surfaces represented by parabolic coordinates η_1 and η_2 . The furthest distance of the solar sail from the central body is constrained by surface ξ_2 and the closest approach distance to the central body is constrained by surface ξ_1 . Identifying where surface ξ_1 and η_2 intersect, the closest approach distance, r_{min} , can be calculated using

$$r_{min} = \frac{(\xi_1^2 + \eta_2^2)}{2} \quad (2.42)$$

Using the values provided in Table 2.2, the closest approach distance calculated using Eq (2.42) for the orbit in Fig 2-23 is 3.6382 L. This value agrees with r_{min} calculated for the same orbit conditions using numerical methods.

Figure 2-24 represents the closest approach distance calculated using Eq (2.42) for a range of initial orbit radius and z-displacement values. It is clear that the greater the instability of the initial orbit, the closer the solar sail approaches the central body. Identifying trajectories which pass near to the central body is important for manifold insertion to non-Keplerian orbits.

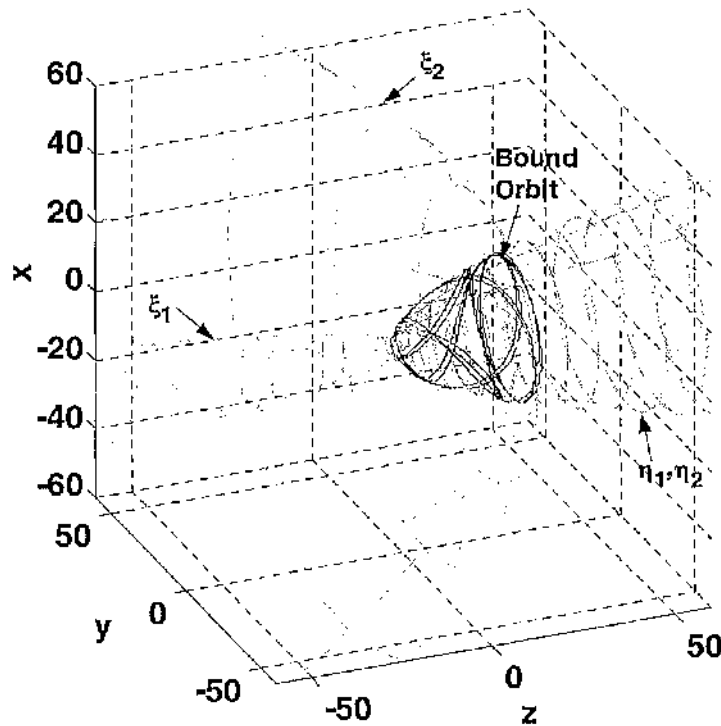


Figure 2-23 3D Cartesian representation of looping orbit bound within paraboloid surfaces

$$\rho_0=20 \text{ L}, z_0=30 \text{ L}, \kappa=6.3364 \times 10^{-4}, \Delta=0.01$$

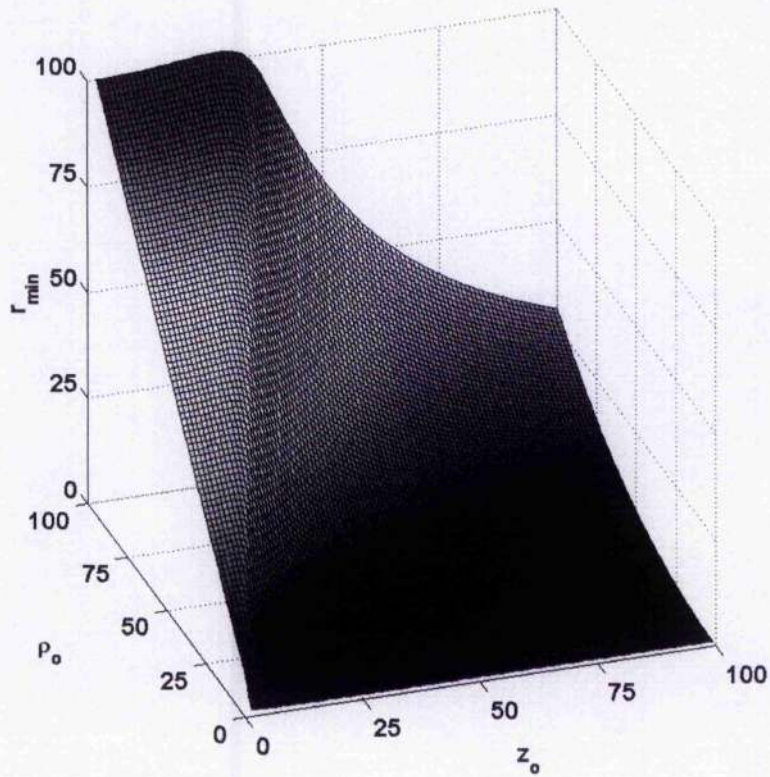


Figure 2-24 Closest approach distance to central body for range of initial orbit conditions ($\Delta=0.01$)

2.3.4 Orbit insertion via invariant manifolds

Periodic looping trajectories provide a set of invariant manifolds that wind onto and off of a limit cycle. Paths which approach the limit cycle as $t \rightarrow -\infty$ are described as unstable manifolds, commonly denoted as W^u . Paths which approach the limit cycle as $t \rightarrow \infty$ are described as stable manifolds, commonly denoted as W^s [Jordan and Smith, 1999].

Periodic looping trajectories can be described as homoclinic as the phase paths connect the nominal orbit back to itself after passing near to the central body. As the invariant manifolds are bound to the surface of a paraboloid, the manifold surface is of dimension 2 when represented in 3 dimensional Cartesian space.

A set of initial conditions can be calculated from the intersecting parabolic coordinates (ξ, η) . The total energy, E_o , can be determined using Eq (2.28), evaluated at the nominal orbit conditions $(\rho_o, z_o, \dot{\rho}_o, \dot{z}_o)$. Initial conditions, denoted by the subscript 'i', which wind onto a nominal orbit are calculated using $\rho_i = \xi\eta$ and $z_i = (\xi^2 - \eta^2)$. The z-component of angular momentum, $h_z = \rho^2 \dot{\theta}$, can also be evaluated using the nominal orbit conditions.

As the angular momentum is constant, the value of angular velocity required at the initial insertion point can be calculated using $\dot{\theta}_i = h_z / \rho_i$.

Table 2-3 provides a set of calculated initial conditions that wind onto a range of desired orbits. All these conditions were calculated with an acceleration perturbation $A=0.01$. The value of $\dot{\rho}_i$ is calculated by re-arranging Eq (2.28) and it is assumed that $\dot{z}_i = 0$, where $\dot{\rho}_i \equiv 0$ in comparison to the magnitude of the initial angular velocity $\dot{\theta}_i$. It should be noted that the initial conditions for $\rho_o=10$ L and $z_o=30$ L result in closest approach distance $r_{min}=0.8553$ L. These initial conditions are forbidden as $r_{min}<1$ L, which represents insertion conditions located below the surface of the central body, with radius L .

Figure 2-25 demonstrates orbit insertion from near the central body to a nominal orbit with conditions $\rho_o=20$ L and $z_o=30$ L. The initial conditions which deliver the solar sail onto this orbit are provided in Table 2-3. Upon arrival at the nominal orbit, linear control techniques must be applied to prevent the solar sail from returning towards the central body via the unstable manifold.

Nominal		Parabolic Coord		Initial Conditions			
ρ_o	z_o	ξ	η	ρ_i	$\dot{\rho}_i$	$\dot{\theta}_i$	z_i
50	30	5.1458	5.3207	27.3793	2.6×10^{-9}	0.00749	-0.9149
40	30	3.6424	4.4721	16.2894	3.7×10^{-9}	0.01706	-3.3664
30	30	2.2658	3.5251	7.9871	5.3×10^{-9}	0.05105	-3.6463
20	30	1.1050	2.4608	2.7191	1.1×10^{-8}	0.02499	-2.4173
10	30	0.2962	1.2739	0.3774	3.7×10^{-8}	3.9488	-0.7675

Table 2-3 Initial conditions calculated using intersecting paraboloid surfaces

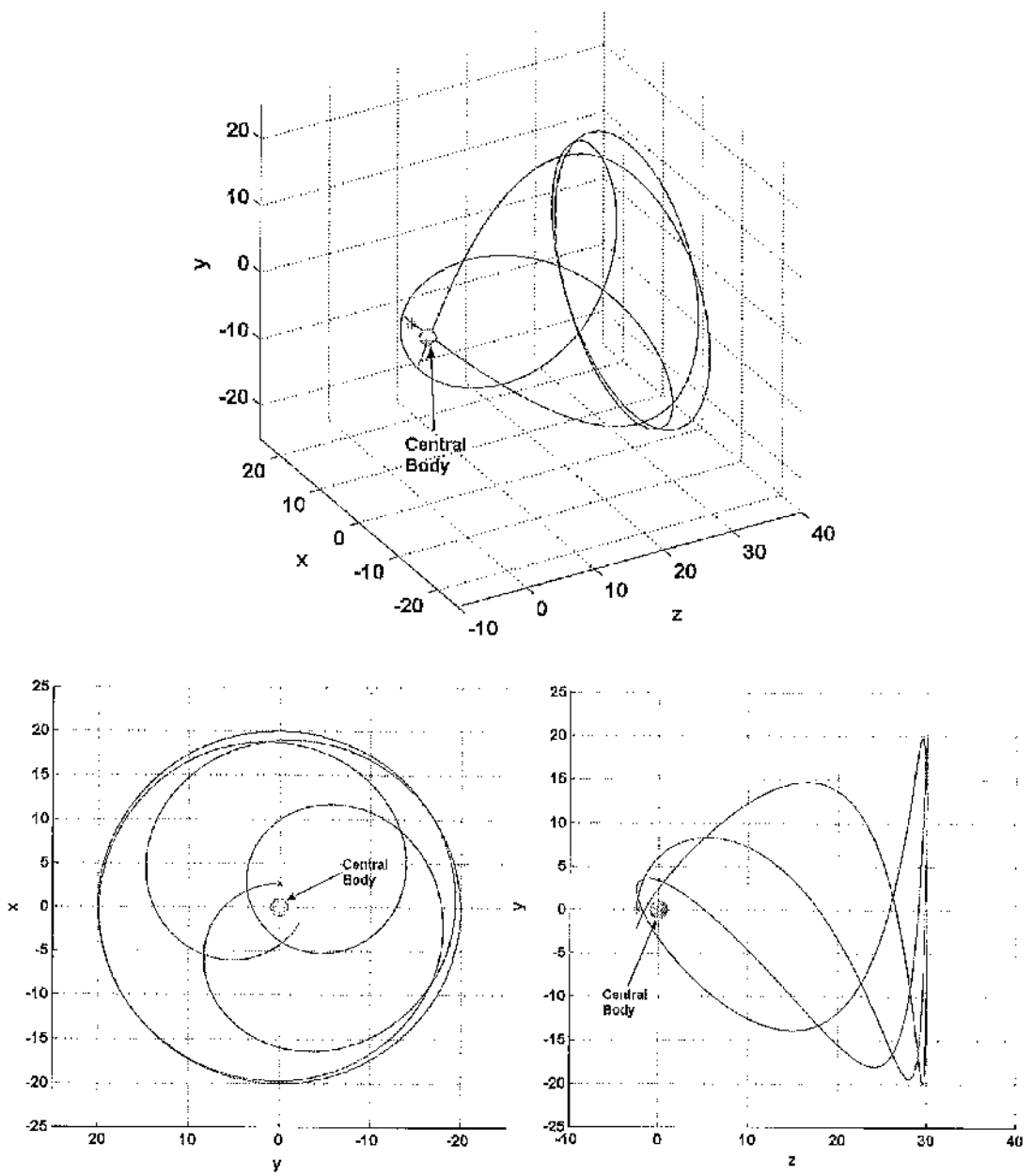


Figure 2-25 Periodic looping orbit inserted at $r_{min} = 3.6382 L$ from the central body

$$\rho_0 = 20 L, z_0 = 30 L, \kappa = 6.3364 \times 10^{-4}, \Lambda = 0.01$$

2.4 Linear control techniques

2.4.1 Feedback control theory

To prevent the solar sail escaping from the desired non-Keplerian orbit after insertion via the stable manifold, station-keeping techniques must be applied. Linear feedback control can be utilised by designing a closed-loop system to keep the solar sail within the vicinity of the desired trajectory. The basic principle is that a control signal $u(t)$ is used to drive a system towards some desirable output value. Proportional feedback is the most basic method for calculating the control signal $u(t) = G(\bar{x}(t) - x(t))$ where G is the gain coefficient, $\bar{x}(t)$ is the desired output and $x(t)$ is the actual output of the system. The expression in the brackets is equivalent to the system error $e(t)$.

Other control methods which can be used to improve system response are outlined by Barr [2002]. Derivative control uses the rate of change of the output signal to determine the size of the control signal $u(t) = G(x(t - T) - x(t))$ where T is the feedback delay time [Li-Xiang, 2001]. Integral control uses the system errors summed over a period of time such that $u(t) = G \sum_i (\bar{x}(t) - x(t))$. It is common to use a combination of proportional and derivative methods (PD) or of all three (PID) to improve the system response and avoid large amplitude oscillations or overshoots from the desired output.

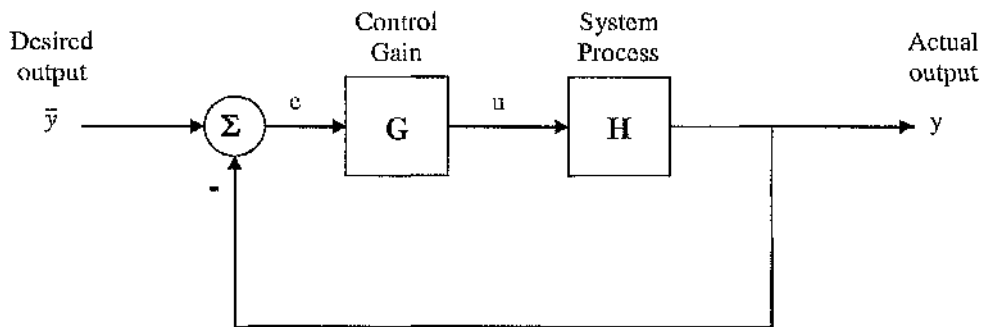


Figure 2-26 Closed-loop system with unity feedback

A schematic of a basic closed loop system with unity feedback is included in Fig 2-26 [Jacobs, 1993]. The system error is defined as $e = (\bar{y} - y)$ where \bar{y} represents the desired output and y represents the actual output. The forward loop transfer function is defined by GH which, in this case is equivalent to the loop transfer function with unity feedback. The proportional control technique is employed with control signal $u = Ge$, where G represents the gain of the control system. The actual output of the system $y = uH$, where H represents the system process transfer function which defines the frequency response of the state-space equation.

The control system transfer function, Y , which is defined as the ratio of system output to input can be represented by the transform

$$Y = \frac{GH}{1+GH} \quad (2.43)$$

where the system objective is to ensure the actual system output tracks the desired output value. From Eq (2.43), it is clear this occurs if $GH \gg 1$ resulting in a ratio approximately equal to unity. This is a very basic example and the transfer function becomes increasingly complex if noise and disturbance terms are modeled within the system.

The zeros of the system represented by Eq (2.43) occur when $GH=0$ and the poles occur when $1+GH=0$ (when the transfer function tends to infinity). In order to obtain a stable system, the roots of the transfer function must not contain positive real values. Transfer functions are frequency domain representations of the dynamical equations. The conversion between the time-domain and frequency domain is achieved via the Laplace transform

$$L[x(t)] = \int_0^{\infty} x(t)e^{-st} dt = X(s) \quad (2.44)$$

where the resulting function $X(s)$ is dependant on the complex operator s .

To design a proportional controller which demonstrates station-keeping at a desired non-Keplerian orbit, the linearised two-body equations of motion can be expressed in the form of state equations

$$\dot{\mathbf{x}}(t) = \mathbf{A}\mathbf{x}(t) + \mathbf{B}\mathbf{u}(t) \quad (2.45.1)$$

$$\mathbf{y}(t) = \mathbf{C}\mathbf{x}(t) + \mathbf{D}\mathbf{u}(t) \quad (2.45.2)$$

The matrix A is a square matrix of size $n \times n$ and is referred to as the linear coefficient matrix. Matrix B is the control matrix which has same number of rows as A but has an independent number of columns with dimensions $n \times m$. The input vector $\mathbf{x}(t)$, control vector $\mathbf{u}(t)$ and output vector $\mathbf{y}(t)$ are all column vectors of length n . The output matrix C must have the same number of columns as A with dimensions $l \times n$. The feed-forward matrix D has dimensions $l \times m$ so has the same number of rows as C and the same number of columns as B .

The transfer function for this state equation can be expressed in the form

$$H(s) = \mathbf{C}(s\mathbf{I} - \mathbf{A})^{-1}\mathbf{B} + \mathbf{D} \quad (2.46)$$

where I is an identity matrix and $H(s) = Y(s)/U(s)$. The term in the brackets $(s\mathbf{I} - \mathbf{A})^{-1}$, arises from the Laplace transform $L[dx/dt] = sX(s) - x_0$ used when converting Eq (2.45.1) into the frequency domain. This term is equivalent to the Laplace transform of $L[e^{At}]$ where $\mathbf{x}(t) = e^{At}$ is a solution to the state equation $\dot{\mathbf{x}}(t) = \mathbf{A}\mathbf{x}(t)$ [Friedland, 1986].

2.4.2 Controllability and observability

When designing a controller it is important to mathematically prove that the control matrix, B , is capable of providing stable control at the desired output value. A simple method exists to demonstrate controllability for the linear system represented by Eq (2.43). The controllability matrix, M_c , is defined as

$$M_c = \begin{bmatrix} B & AB & A^2B & A^3B \dots A^{n-1}B \end{bmatrix} \quad (2.47.1)$$

For a system to be fully controllable the controllability matrix must be full-rank, corresponding to a non-singular matrix. A completely controllable system can transfer any initial state $\mathbf{x}(t_0)$ to any final state $\mathbf{x}(t_f)$ via the control signal $\mathbf{u}(t)$ for all state space.

The observability of a system can be examined using the observability matrix, M_o , defined as

$$M_o = [C' \quad A'C' \quad (A')^2 C' \quad (A')^3 C' \dots (A')^{n-1} C'] \quad (2.47.2)$$

where C' and A' represent the transpose of matrix C and A respectively. A system can be described as fully observable if the observability matrix is full-rank. A fully observable system enables every initial state $\mathbf{x}(t_0)$ to be determined from the output $\mathbf{y}(t)$. Essentially this means $\mathbf{y}(t)$ is dependant on every state $\mathbf{x}(t)$ [D'azzo, 1995].

2.4.3 Root locus plot

To aid with the design of control systems, W.S. Evans devised the root-locus plot. As the values of s essentially corresponds to the eigenvalues of the linear coefficient matrix A , a stable orbit will have poles which lie in the left quadrants of the s -plane [Marshall, 1978]. The performance of a control system can be accessed by selecting gains which move the poles to the left-quadrants. The root locus is based on a negative feedback controller shown in Figure 2-27.

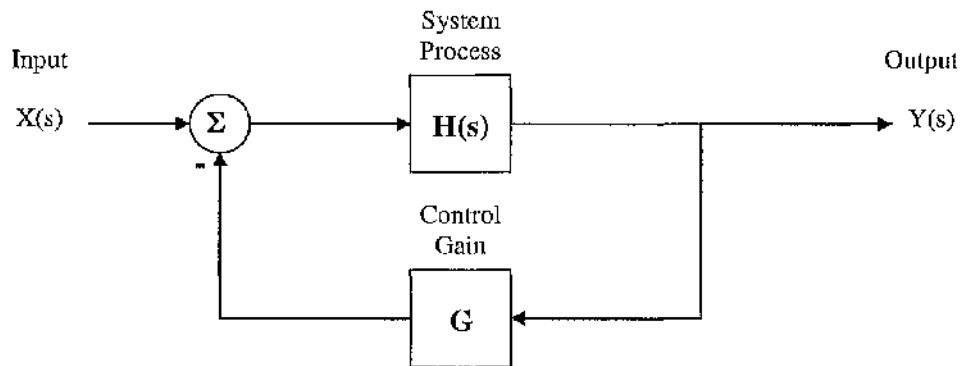


Figure 2-27 System $H(s)$ with negative feedback control using gain G

The resulting transfer function can be written as

$$F(s) = \frac{Y(s)}{X(s)} = \frac{H(s)}{1 + GH(s)} \quad (2.48)$$

where $H(s)$ is the system transfer function calculated from Eq (2.46) and G is the control gain. The zeros of the system are located when the transfer function $F(s) = 0$ and the poles are located when $F(s) = \infty$. These can be located by examining the denominator of $F(s)$ which is equivalent to $1 + GH(s)$.

The system transfer function has the form $H(s) = N(s)/D(s)$ where $N(s)$ represents the transfer function numerator and $D(s)$ the denominator. These can both be represented by polynomials where $N(s) = a_n s^n + a_{n-1} s^{n-1} + \dots a_1 s + a_0$ and $D(s) = b_m s^m + b_{m-1} s^{m-1} + \dots b_1 s + b_0$. The number of branches of the root loci is determined from the order of the polynomial $D(s)$, denoted by m [Dougherty, 1995].

When drawing the root loci branches, the characteristic equation $1 + GH(s) = 0$ can be rearranged into the more useful form $D(s) + GN(s) = 0$. This represents a polynomial in s with coefficients including the gain G . The open-loop pole can be evaluated when the gain $G = 0$. The open loop zeros can be located when $H(s) = 0$, which is equivalent to numerator $N(s) = 0$.

The pole trajectories start on an open-loop pole and terminate either at an open-loop zero or tend to infinity with the direction defined by an asymptote. The trajectories are plotted by varying the gain, G , between 0 and infinity. It can be demonstrated the angle of the asymptotes, $\angle a$, may be calculated using the angle condition

$$\angle a = (1 + 2l)\pi / (m - n) \quad (2.49.1)$$

where the integer series $l=0,1,\dots,(m-n-1)$. The symbol m represents the number of poles and n represents the number of zeros. The real axis intersection of the asymptotes can be calculated using

$$\sigma_a = \left[\sum_{\mu=1}^m \text{Re}(p_\mu) - \sum_{v=1}^n \text{Re}(z_v) \right] / (m - n) \quad (2.49.2)$$

where p_μ represents the position of the poles and z_v represents the position of the zeros. Using these rules, a root locus plot can be generated for a control system to aid design [D'azzo, 1966].

2.4.4 Optimal control – linear quadratic regulator

The root-locus diagram provides a useful method to select gains which produce a stable system. These gains may result in undesirable overshoots or may require control signals which are too large for the actuator to produce in the real system. Design limits may require a system that can maintain control to within a certain error of the desired output and be achieved with a limited control signal size. An optimal controller can be utilised to select gains which are optimised based on a performance criteria.

Consider the linear system represented by Eq (2.45). Optimal control theory provides a method for selecting a gain matrix which suppresses any unstable eigenvalues by minimizing the cost function V

$$V = \int_t^{\infty} [\mathbf{x}'(\tau)Q\mathbf{x}(\tau) + \mathbf{u}'(\tau)N\mathbf{u}(\tau)]d\tau \quad (2.50)$$

where t is the initial integration time, Q is the state-weighting matrix and N is the control-weighting matrix. The first term inside the square brackets represents the penalty on the deviation of state vector \mathbf{x} from the desired state and the 2nd term represents the cost of control which limits the control signal size.

The aim is to select a gain matrix G that minimises the performance function V . This can be achieved using the Ricatti Equation

$$-\dot{M} = MA + A'M - MBN^{-1}B'M + Q \quad (2.51)$$

where M is the performance matrix and is related to the performance function such that $V = \mathbf{x}'M\mathbf{x}$. Provided that M converges to a limit as $t \rightarrow \infty$, it can be assumed that $\dot{M} \rightarrow 0$. Equation (2.51) can be solved for M which enables the optimal gain matrix to be calculated using $G = N^{-1}B'M$ [Friedland, 1986].

2.4.5 Solar sail area variation control

2.4.5.1 Design of state equations

An area variation controller can be designed using the linearised two-body equations and constructing them in the state-space form of Eq (2.45). The input vector has the form $\mathbf{x}(t) = [\rho, z, \dot{\rho}, \dot{z}]^T$ and the linear coefficient matrix is defined as

$$A = \begin{bmatrix} 0 & 0 & 1 & 0 \\ 0 & 0 & 0 & 1 \\ \frac{\partial f_\rho}{\partial \rho} & \frac{\partial f_\rho}{\partial z} & 0 & 0 \\ \frac{\partial f_z}{\partial \rho} & \frac{\partial f_z}{\partial z} & 0 & 0 \end{bmatrix} \quad (2.52)$$

where the partial derivatives are provided in Eq (2.13). The control matrix is dependant on the variation of acceleration with respect to solar sail area. The acceleration components \mathbf{a}_z and \mathbf{a}_ρ directed along the \mathbf{e}_z and \mathbf{e}_ρ axes respectively are defined as

$$\mathbf{a}_z = \kappa \cos^3 \alpha \mathbf{e}_z \quad (2.53.1)$$

$$\mathbf{a}_\rho = \kappa \cos^2 \alpha \sin \alpha \mathbf{e}_\rho \quad (2.53.2)$$

The control matrix can be constructed as $B = [0 \quad 0 \quad \partial \mathbf{a}_z / \partial \kappa \quad \partial \mathbf{a}_\rho / \partial \kappa]^T$ using the partial derivatives of Eq (2.53) which are evaluated at the nominal pitch angle, $\alpha=0$, as

$$\frac{\partial a_\rho}{\partial \kappa} = \cos^2 \alpha \sin \alpha = 0 \quad (\alpha = 0) \quad (2.54.1)$$

$$\frac{\partial a_z}{\partial \kappa} = \cos^3 \alpha = 1 \quad (\alpha = 0) \quad (2.54.2)$$

This yields the control matrix $B = [0 \ 0 \ 0 \ 1]^T$ for the sail area variation controller. Using Eq (2.47.1), it can be demonstrated that this control matrix produces a full-rank controllability matrix (in this case rank 4). This proves that the control method is capable of providing station-keeping at the desired non-Keplerian orbit.

The observability matrix, $C = I_{4 \times 4}$ is simply a 4x4 identity matrix which produces a full-rank observability matrix using Eq (2.47.2). The feed-forward matrix is null as it is not required within this system such that $D = [0 \ 0 \ 0 \ 0]^T$. A suitable gain matrix is obtained using either root-locus methods or optimal control methods. Both these techniques will be demonstrated.

The control requirement to maintain station-keeping at the desired orbit can be modelled using a linear control law with the form

$$\delta k = G_1(\rho - \rho_o) + G_2(z - z_o) + G_3(\dot{\rho} - \dot{\rho}_o) + G_4(\dot{z} - \dot{z}_o) \quad (2.55)$$

where δk represents the acceleration variation directed along the sun-line, $\rho, z, \dot{\rho}, \dot{z}$ are the integrated orbit conditions and $\rho_o, z_o, \dot{\rho}_o, \dot{z}_o$ are the desired orbit conditions. For a circular orbit displaced a constant distance from the central body $\dot{\rho}_o = 0$ and $\dot{z}_o = 0$.

2.4.5.2 Root-locus method

Consider applying solar sail area variation control as a stationkeeping method. To make use of this technique would require the ability to slightly furl/unfurl the solar sail or employ reflective tip-vanes which can be used to vary the total reflecting area.

Gains are selected such that the pole positions lie in the left quadrant of the root-locus plot, suppressing the positive real eigenvalues which lead to system instability. For an orbit of radius 60 L displaced 20 L from the central body, the state equations result in the four transfer functions with a common denominator, provided in Table 2-4. The order of the denominator is 4, which results in 4 branches of the root locus plot for each transfer function. Transfer functions 1-4 respectively correspond to the state equations for $\rho, z, \dot{\rho}$ and \dot{z} .

The root-locus method will be used with the aim of selecting a gain matrix which gives a good response time and dampens any unwanted oscillations. The root-locus plots for each transfer function are provided in Fig 2-28. The gains must also produce a reasonable control signal size which can be generated using modest sail area variations.

Each subplot corresponds to the pole variation for gains associated with the position and velocity components highlighted in Eq (2.55) where 'Gain1' - ρ , 'Gain2' - z , 'Gain 3' - $\dot{\rho}$ and 'Gain 4' - \dot{z} . The respective gains are represented by the notation (G_1, G_2, G_3, G_4). Each transfer function produces four poles, where the '+' symbol represents the case when $G \rightarrow 0$, known as the open-loop pole and the 'o' symbol represents the case when $G \rightarrow \infty$, the open-loop zero.

Using the root locus diagram, suitable gains were selected as $G = [3.1 \times 10^{-5} \quad 7.6 \times 10^{-6} \quad 0.01 \quad 0.05]$. Figure 2-29 demonstrates a controlled orbit after insertion 1.71 L from the central body. Figure 2-30 demonstrates the solar sail area variation and the corresponding solar sail acceleration required to provide stationkeeping in the vicinity of the nominal orbit. The sail area variation is normalized with respect to the nominal sail area, A_o .

	s^4	s^3	s^2	s^1	s^0
N(s) 1	0	0	0	0	3.5576×10^{-6}
N(s) 2	0	0	1	0	1.4626×10^{-5}
N(s) 3	0	0	0	3.5576×10^{-6}	0
N(s) 4	0	1	0	1.4626×10^{-5}	0
D(s)	1	0	7.9057×10^{-6}	0	-1.1094×10^{-10}

Table 2-4 Numerator/Denominator polynomials in terms of s

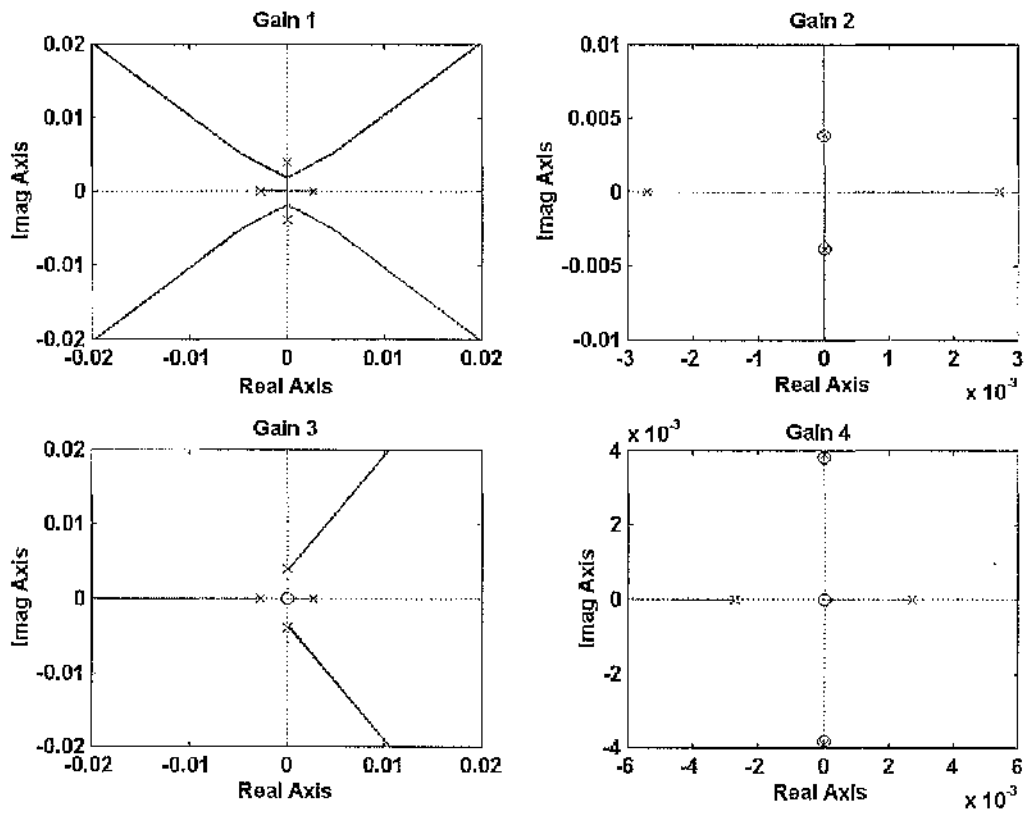


Figure 2-28 Root-locus plot for area variation control

$$\rho_0 = 20L, z_0 = 60L, \kappa = 2.3717 \times 10^{-4}$$

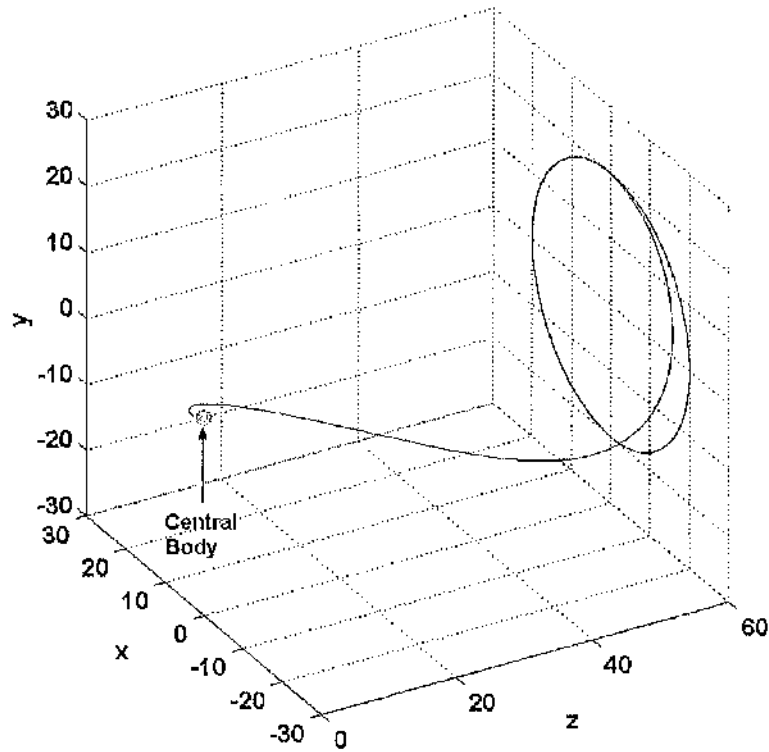


Figure 2-29 Orbit insertion with linear area control

$$\rho_0 = 60L, z_0 = 20L, \kappa = 2.3717 \times 10^{-4}$$

$$G_1 = 3.1 \times 10^{-5} \quad G_2 = 7.6 \times 10^{-6} \quad G_3 = 0.01 \quad G_4 = 0.05$$

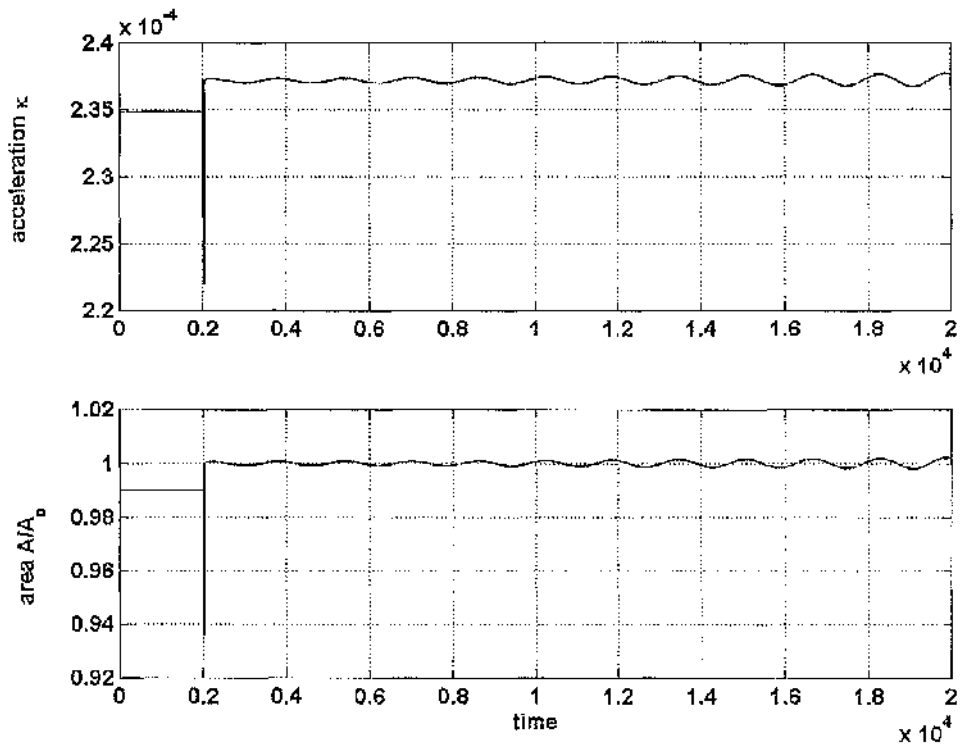


Figure 2-30 Solar sail acceleration variation and area variation

2.4.5.3 Optimal Control Method

Using the performance criterion provided in Eq (2.50), optimal gains can be selected which improve the controller response time and limits the size of the control signal. Suitable gains were obtained using a state cost function $Q = 5I_{4 \times 4}$ and a control cost function $N = 1 \times 10^{13}$. The control cost function imposes a limit on the control signal size. The smaller the value of N , the larger the optimal gain values which can result in large control signals. Similarly, the state cost imposes a limit on the allowable error between the desired and the actual orbit conditions. Small values for the matrix Q reduce the overshoot during control.

Figure 2-31 shows an orbit insertion 1.71 L from the central body where optimal control is employed upon arrival of the solar sail at the nominal orbit. Figure 2-32 shows the acceleration variation throughout this trajectory and the required sail area variation normalized with respect to the nominal sail area, A_0 .

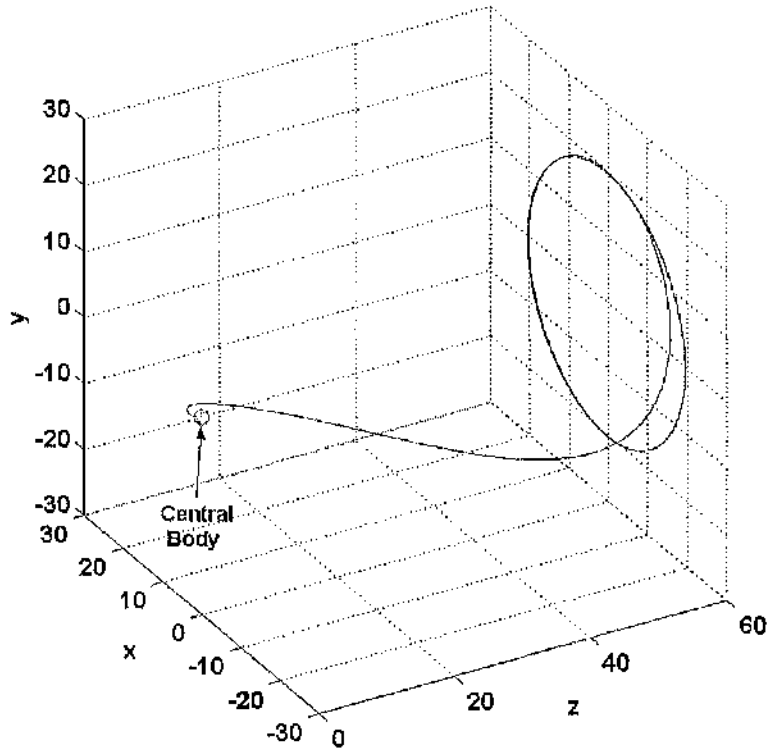


Figure 2-31 Orbit insertion with optimal linear area control

$$\rho_0 = 60 \text{ L}, z_0 = 20 \text{ L}, \kappa = 2.3717 \times 10^{-4}$$

$$G_1 = 1.727 \times 10^{-6} \quad G_2 = 1.479 \times 10^{-5} \quad G_3 = 8.188 \times 10^{-4} \quad G_4 = 5.438 \times 10^{-3}$$

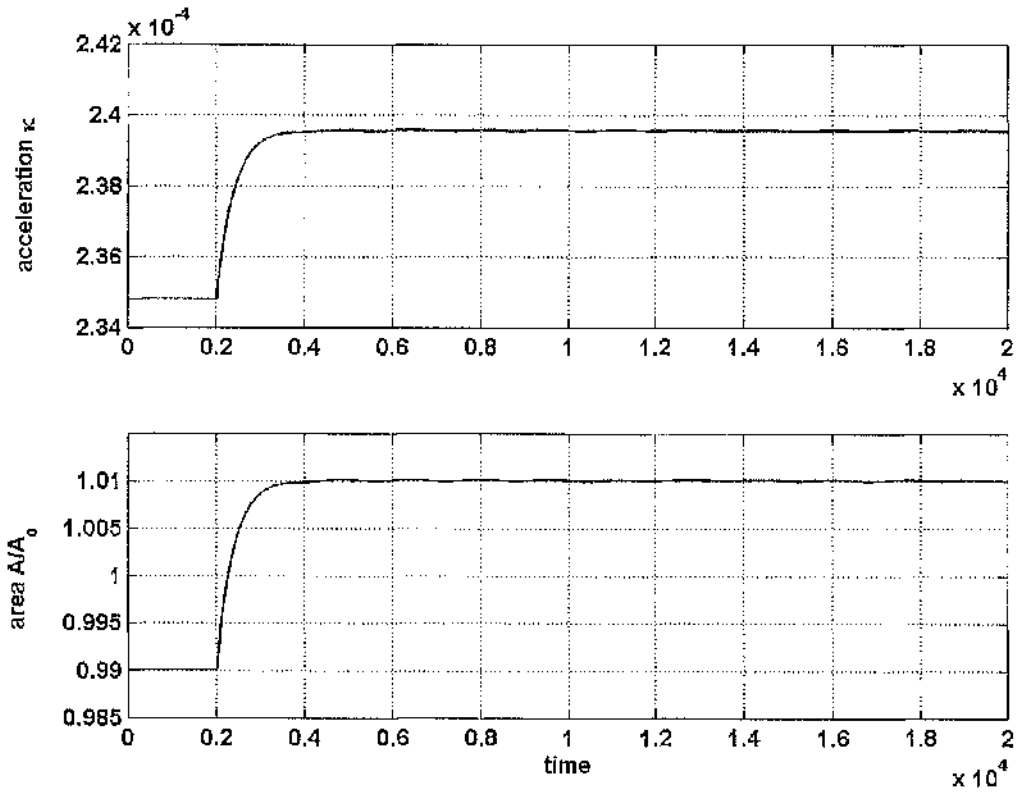


Figure 2-32 Solar sail acceleration variation and area variation

2.4.6 Solar sail pitch angle control

2.4.6.1 Design of state equations

In the case of a pitch-angle controller, the $\cos^2 \alpha$ acceleration dependency is used to provide linear control at the nominal orbit. The partial derivatives of Eq (2.53) with respect to pitch angle α are evaluated as

$$\frac{\partial a_z}{\partial \alpha} = -3\kappa \cos^2 \alpha \sin \alpha \quad (2.56.1)$$

$$\frac{\partial a_\rho}{\partial \alpha} = \kappa \cos^3 \alpha (1 + \tan^2 \alpha) \quad (2.56.2)$$

which reduce to $\partial a_z / \partial \alpha = 0$ and $\partial a_\rho / \partial \alpha = \kappa$ at the nominal pitch angle $\alpha = 0$. The control matrix $B = [0 \ 0 \ \kappa \ 0]^T$ again produces a full-rank controllability matrix. The linear coefficient matrix A , the output matrix C , and the feed-forward matrix D are equivalent to those defined in Section 2.4.5.1.

The control signal required to maintain station-keeping at the desired orbit can be modelled using the linear control law

$$\delta\alpha = G_1(\rho - \rho_o) + G_2(z - z_o) + G_3(\dot{\rho} - \dot{\rho}_o) + G_4(\dot{z} - \dot{z}_o) \quad (2.57)$$

where $\delta\alpha$ represents the solar sail pitch angle variation, $\rho, z, \dot{\rho}, \dot{z}$ are the integrated orbit conditions and $\rho_o, z_o, \dot{\rho}_o, \dot{z}_o$ are the desired orbit conditions. The angle variation produces a controlling acceleration calculated using Eq (2.53).

2.4.6.2 Root locus method

Solar sail pitch angle variation could be achieved via two methods. Reflective tip-vanes at the corners of the sail could be used to generate a torque which rotates the solar sail about the centre of mass. Alternatively, a centre of mass/pressure offset could be generated to produce a torque using a gimbaled boom to displace the position of the payload.

Figure 2-33 shows the root locus plots for a non-Keplerian orbit displaced 60 L from the central body with radius 20 L. Following the same procedure as the area controller in Section 2.4.5, gains are selected resulting in poles which lie in the left quadrants of the root-locus diagrams. Each of the subplots correspond to pole trajectories for the gains associated with the position and velocity components highlighted in Eq (2.57) where 'Gain1' - ρ , 'Gain2' - z , 'Gain 3' - $\dot{\rho}$ and 'Gain 4' - \dot{z} . The respective gains are represented by the notation (G_1, G_2, G_3, G_4).

Table 2-5 contains the four transfer function numerators and their common denominator. As the order of the denominator is 4, each root locus plot has 4 branches. The maximum acceleration is directed along the e_p axis when the sail pitch angle is 35.7° . The control signal should maintain a pitch angle below this critical value. Suitable values for the gain were selected as $G = [0.2 \ 0.15 \ 49.1 \ 100]$.

	s^4	s^3	s^2	s^1	s^0
N(s) 1	0	0	0.2372	0	-1.5938×10^{-6}
N(s) 2	0	0	0	0	8.4375×10^{-7}
N(s) 3	0	0.2372	0	1.5938×10^{-6}	0
N(s) 4	0	0	0	8.4375×10^{-7}	0
D(s)	1	0	7.9057×10^{-6}	0	1.1094×10^{-10}

Table 2-5 Numerator/Denominator Polynomials in terms of s

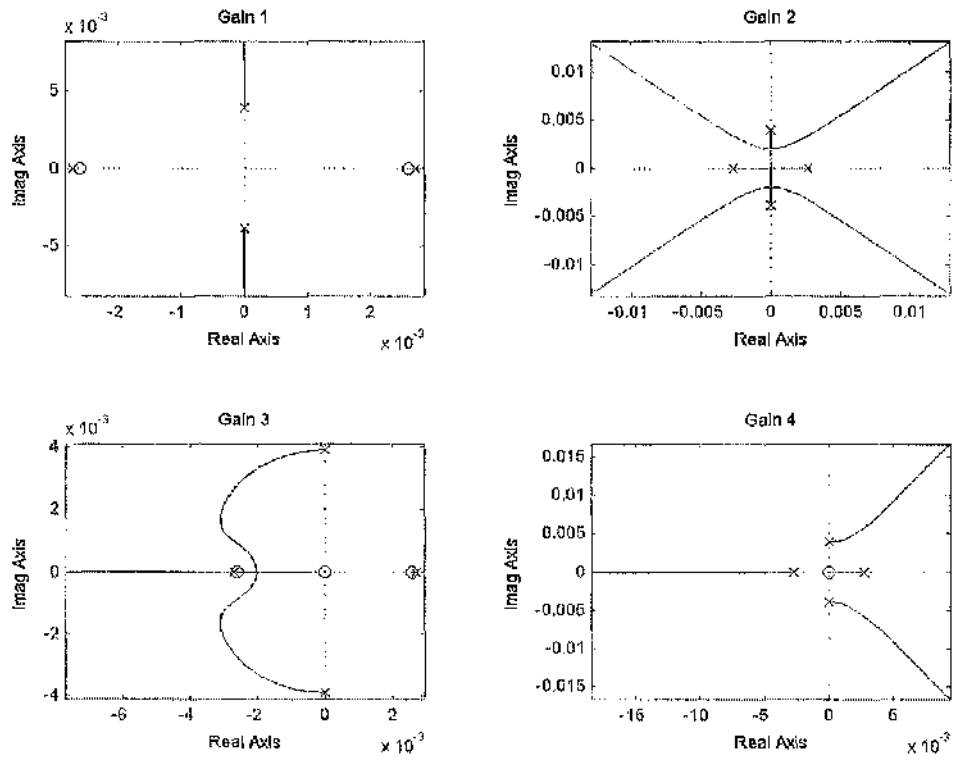


Figure 2-33 Root-locus plot for pitch angle variation control

$$\rho_o = 20L, z_o = 60L, \kappa = 2.3480 \times 10^{-4}, \Delta = 0.01$$

Identical insertion conditions are used as those in Section 2.4.5 located 1.71 L from the central body. Figure 2-34 shows an orbit controlled using the pitch angle controller with the gains selected using root locus plots. The controlling pitch angle is shown in Fig 2-35 with a variation between 0.13° and -15.21° . A negative angle means the sail normal vector is pointing downwards toward the sun-line. This example meets the requirement that the reflecting side of the sail always faces sunward. The resulting acceleration directed along the ρ - and z - axes is provided in Fig 2-36. The acceleration components are normalized with respect to the nominal acceleration, κ_o .

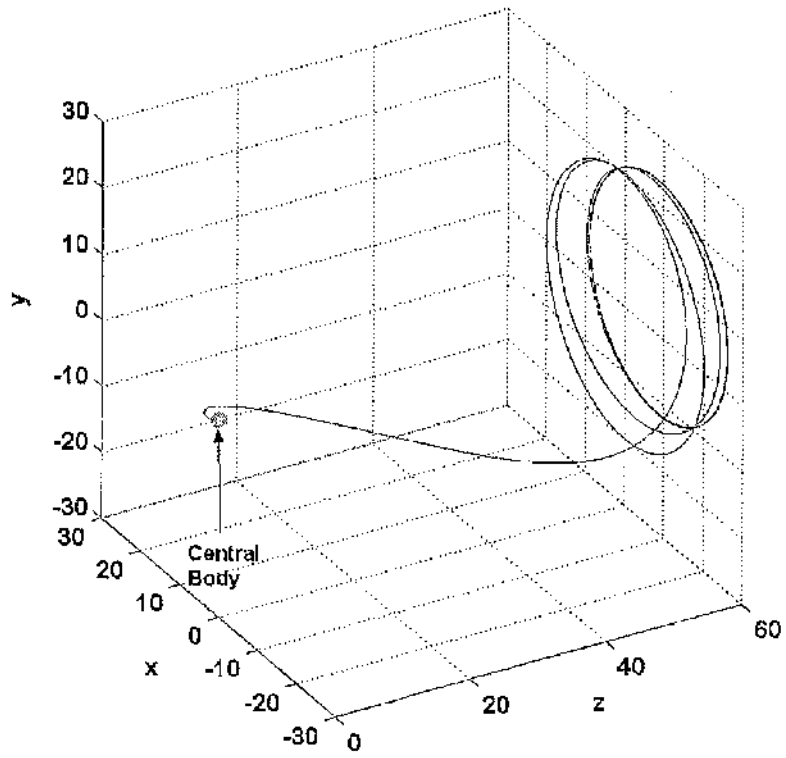


Figure 2-34 Orbit insertion with linear pitch angle control

$$\rho_0 = 60 L, z_0 = 20 L, \kappa = 2.3717 \times 10^{-4}$$

$$G_1 = 0.2 \quad G_2 = 0.15 \quad G_3 = 49.1 \quad G_4 = 100$$

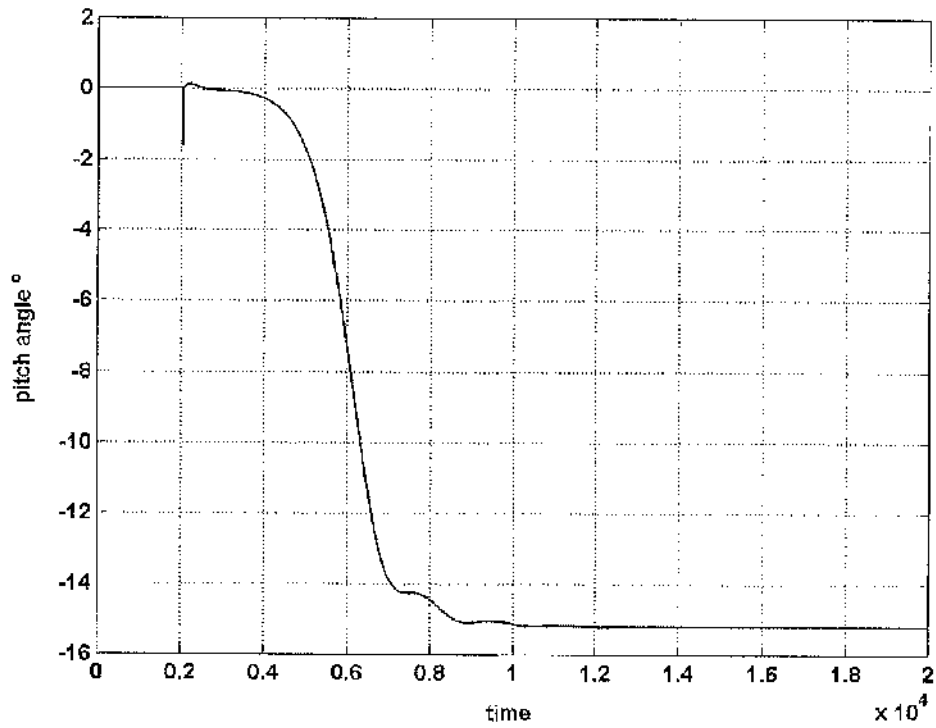


Figure 2-35 Pitch angle variation required to control orbit

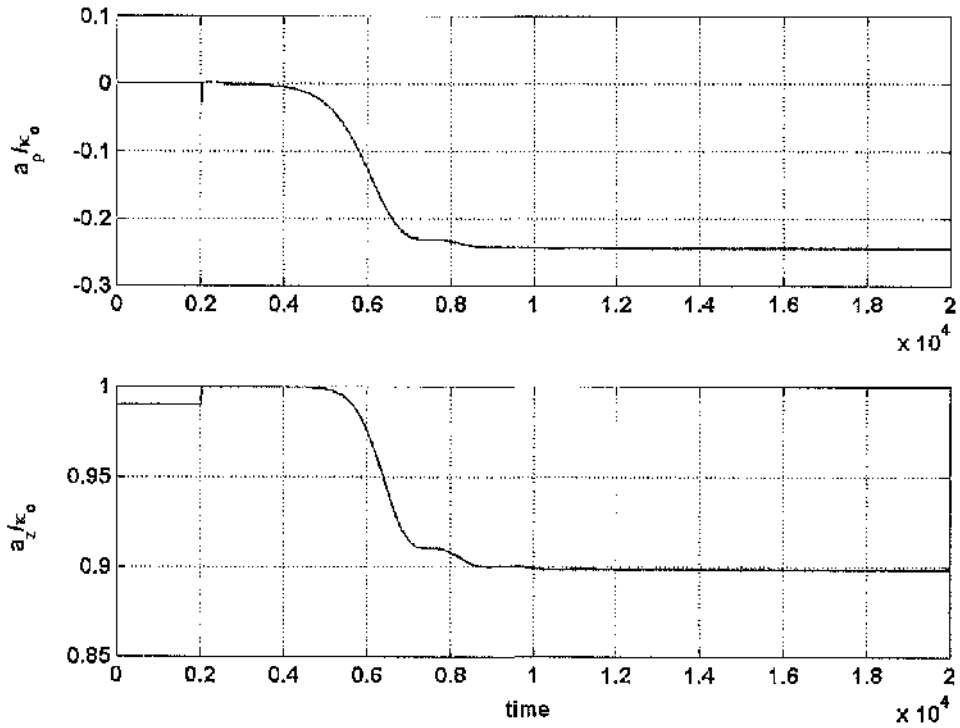


Figure 2-36 Acceleration directed along e_p and e_z axes normalized with respect to κ_0

2.4.6.3 Optimal control method

Using the performance criterion provided in Eq (2.50), optimal gains can be selected which improve the response time of the controller and limits the size of the control signal. Suitable gains were obtained using a state cost function $Q = 100I_{4 \times 4}$ and a control cost function $N = 1 \times 10^4$.

The resulting trajectory is provided in Fig 2-37. The pitch angle variation required to control this orbit, shown in Fig 2-38, was between 0.14° and -2.25° . The controller quickly dampens the instabilities so as only minute angle variations are required to control the orbit. The corresponding acceleration components are provided in Fig 2-39.

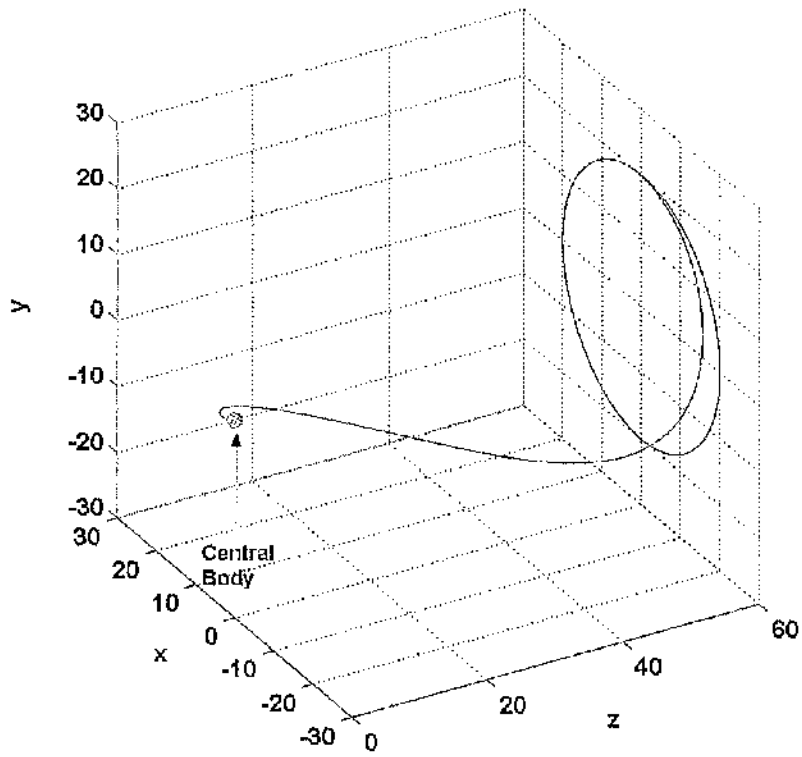


Figure 2-37 Orbit insertion with optimal linear pitch angle control

$$\rho_o = 60 L, z_o = 20 L, \kappa = 2.3717 \times 10^{-4}$$

$$G_1 = 0.06291 \quad G_2 = 0.3818 \quad G_3 = 23.0328 \quad G_4 = 141.3835$$

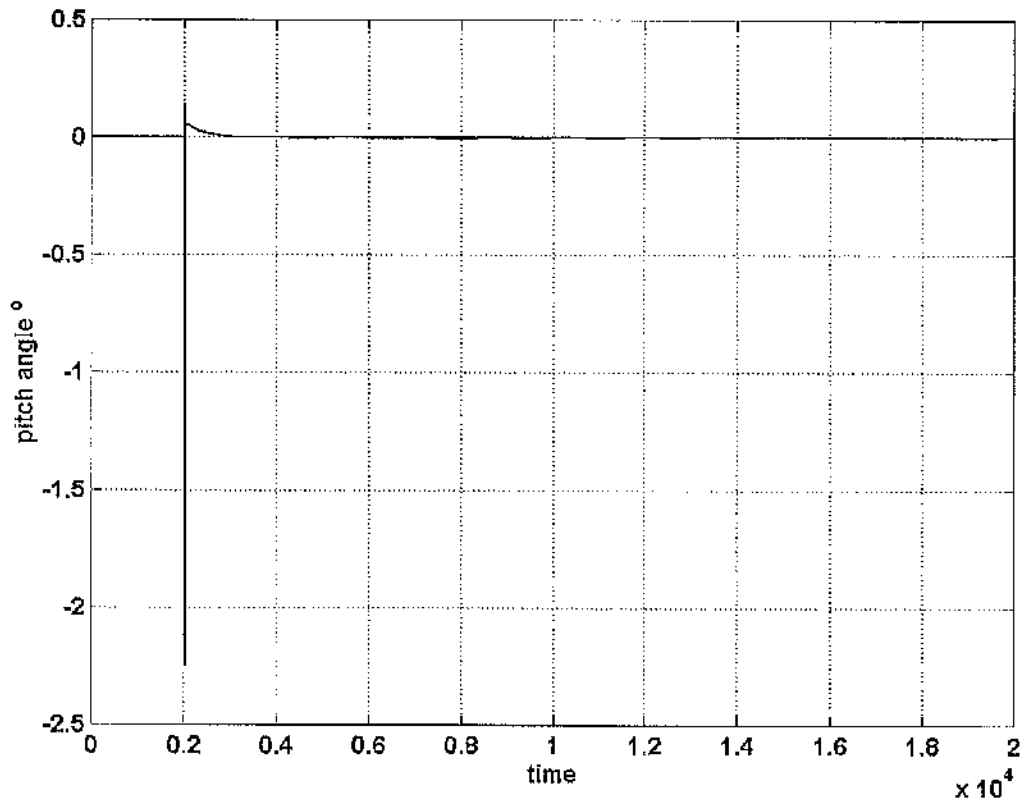


Figure 2-38 Pitch angle variation achieved using an optimal controller

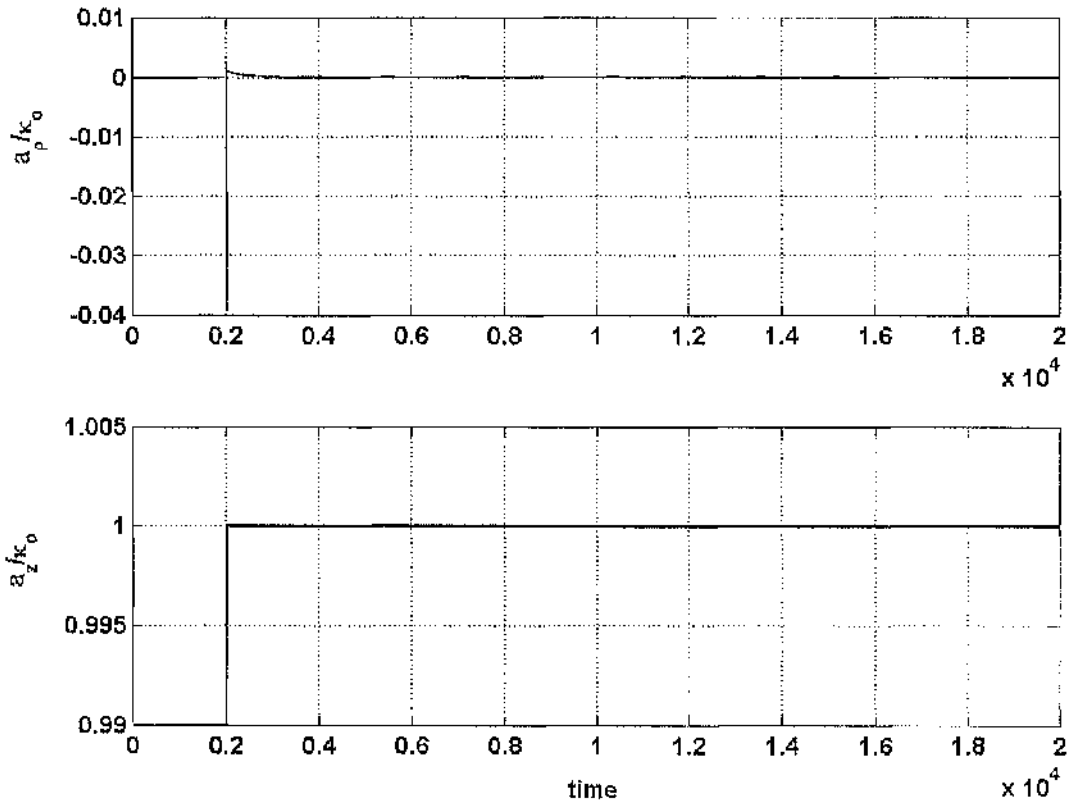


Figure 2-39 Acceleration directed along e_p and e_z axes normalized with respect to κ_0

In a two-body context, the most suitable control method is pitch-angle variation, as varying the sail pitch angle over a few degrees poses less risk to the sail structure than varying the reflecting surface area. Tip vanes could be used to produce unbalanced net forces at the sail edges thus generating small torques [Wie, 2002]. Alternatively steering can be achieved using a gimbaled boom which can be moved to alter the centre of mass relative to the centre of pressure producing a torque. It is clear from Fig 2-38, that control is possible using an angle variation of about 2 degrees using the linear quadratic regulator to select optimal gains.

2.5 Conclusions

This chapter has considered circular displaced non-Keplerian orbits in a two-body context. The stability condition was derived using linear and non-linear approximation methods. Orbit bounding surfaces were identified using a conservation of energy method and an explicit solution identified using parabolic coordinates. A family of homoclinic manifolds were identified which provide a set of transfer trajectories to deliver the solar sail to a circular displaced orbit from near to the central body. It was demonstrated that the homoclinic manifolds are bound to a paraboloid energy surface enabling the closest approach distance to the central body to be determined explicitly.

Stable manifolds which pass near the central body were found to wind onto an unstable circular displaced orbit, defined using the stability condition. Solar sail control techniques were investigated to prevent escape after insertion to a nominal orbit. Applying trims to the solar sail surface area or pitch angle can be used to modulate the sail acceleration. The solar sail controllers were developed using both a root locus method and linear quadratic regulator to select gains. The optimal control method was found to identify gains which minimize the controller response time and control signal amplitude. In the two body case, applying the pitch angle control method seems to be the most suitable control method not requiring large modulation of the sail surface area which poses a risk of damaging the solar sail surface.

The next chapter will consider circular displaced orbits in a three-body context. Hill's approximation of the three-body problem will be used to represent the dynamics of a solar sail including acceleration due to solar radiation pressure. As demonstrated in Chapter 1, including the gravitational influence of the Sun acting on the solar sail and the centripetal force of the Earth revolving around the Sun, limits the regions where artificial libration points can be generated. The two-body controller will be applied to demonstrate control of circular displaced orbits in the three-body problem.

Hill's approximation

3.1 Hill's approximation of the three-body problem

The dynamics of a solar sail will be modelled using Hill's approximation to the three-body problem. These equations represent a case where the smaller bodies, M_2 and M_3 are relatively close to each other and orbit a larger mass M_1 , where the general hierarchy of the masses is $M_1 \gg M_2 > M_3$. A planet centred, rotating frame of reference is adopted. The circular restriction is also applied assuming the separation between the planet and the Sun, R , is constant. This problem models the dynamics of a solar sail non-Keplerian orbit in the vicinity of a planet where the system is revolving around the Sun with angular velocity Ω [Hénon and Petit, 1986; Scheeres and Bellerose, 2005], as shown in Fig 3-1.

The solar sail is located at position $\mathbf{r} = x\mathbf{i} + y\mathbf{j} + z\mathbf{k}$ relative to the planet where $(\mathbf{i}, \mathbf{j}, \mathbf{k})$ are unit vectors along the planet centred axes (x,y,z) . The planet and Sun are located on the x -axis. The vector between the planet and Sun $\mathbf{R} = R\mathbf{i}$. The approximation states that $|\mathbf{R}| \gg |\mathbf{r}|$, thus it is convenient to envisage Hill's problem as a perturbed two-body model including the effects of solar gravity.

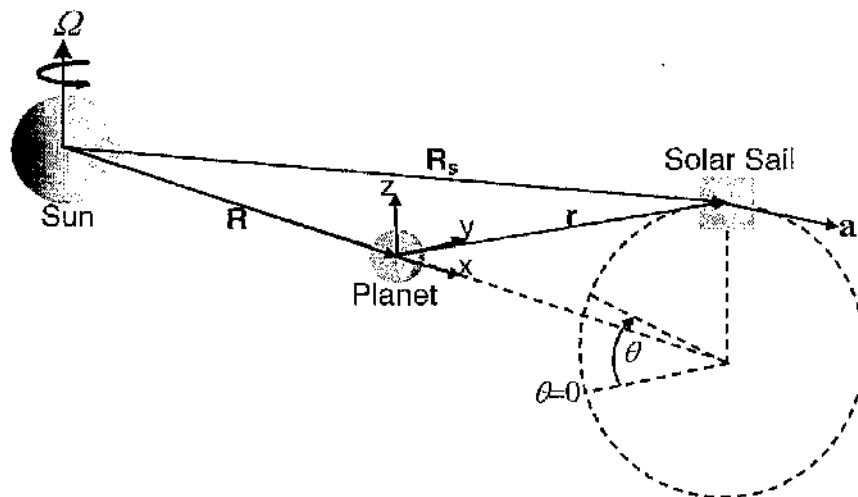


Figure 3-1 Schematic of Hill's problem with displaced solar sail orbit

The two body dynamics for a non-Keplerian orbit have been thoroughly investigated in Chapter 2. The solar sail equation of motion, with respect to the planet, has the form $\ddot{\mathbf{r}} = -\mu\mathbf{r}/|\mathbf{r}|^3 + \mathbf{a}$, where μ is the planet gravitational parameter and \mathbf{a} represents the solar sail acceleration. A rotating frame of reference is chosen to include the dynamics of the planet-sail system orbiting the Sun. The subscripts 'I' and 'R' refer to the inertial and rotating frames respectively. The 1st order derivative of \mathbf{r} relative to the inertial frame produces

$$\left[\frac{d\mathbf{r}}{dt}\right]_I = \left[\frac{d\mathbf{r}}{dt}\right]_R + \boldsymbol{\Omega} \times (\mathbf{r} + \mathbf{R}) \quad (3.1)$$

The second order derivative can be obtained from Eq (3.1) after grouping like-terms as

$$\left[\frac{d^2\mathbf{r}}{dt^2}\right]_I = \left[\frac{d^2\mathbf{r}}{dt^2}\right]_R + \frac{d\boldsymbol{\Omega}}{dt} \times \mathbf{r} + 2\boldsymbol{\Omega} \times \left[\frac{d\mathbf{r}}{dt}\right]_R + \boldsymbol{\Omega} \times \boldsymbol{\Omega} \times (\mathbf{r} + \mathbf{R}) \quad (3.2)$$

As the angular velocity is assumed constant, $d\boldsymbol{\Omega}/dt = 0$ which removes the 2nd term on the right-hand side. The equation of motion representing the solar sail dynamics in the vicinity of the planet can then be extended to a frame of reference rotating with angular velocity $\boldsymbol{\Omega}$ as

$$\ddot{\mathbf{r}} + 2\boldsymbol{\Omega} \times \dot{\mathbf{r}} + \boldsymbol{\Omega} \times \boldsymbol{\Omega} \times \mathbf{r} = -\frac{\mu\mathbf{r}}{|\mathbf{r}|^3} + \mathbf{a}\mathbf{n} \quad (3.3)$$

The final aspect to consider is the gravitational influence of the Sun on the solar sail. Consider the vector, $\mathbf{R}_s = \mathbf{R} + \mathbf{r}$ which represents the position of the solar sail relative to the Sun. The Sun exerts a gravitational acceleration of $-\mu_s\mathbf{R}_s/|\mathbf{R}_s|^3$, where $\mu_s = 1.334 \times 10^{20} \text{ m}^3\text{s}^{-2}$ is the solar gravitational parameter. Substituting $\mathbf{R}_s = \mathbf{R} + \mathbf{r}$, the denominator can be expanded as

$$|\mathbf{R} + \mathbf{r}|^{-3} = [(\mathbf{R} + \mathbf{r})(\mathbf{R} + \mathbf{r})]^{-3/2} = [r^2 + 2\mathbf{r} \cdot \mathbf{R} + R^2]^{-3/2} \quad (3.4)$$

where $r^2 \equiv \mathbf{r} \cdot \mathbf{r}$ and $R^2 \equiv \mathbf{R} \cdot \mathbf{R}$.

Equation (3.4) can then be expressed as

$$|\mathbf{R} + \mathbf{r}|^{-3} = \mathbf{R}^{-3} \left[\left(1 + \frac{2\mathbf{R} \cdot \mathbf{r}}{R^2} + \left(\frac{r}{R} \right)^2 \right) \right]^{-3/2} \quad (3.5)$$

which can be expanded using the binomial theorem to obtain

$$\left[\left(1 + \frac{2\mathbf{R} \cdot \mathbf{r}}{R^2} + \left(\frac{r}{R} \right)^2 \right) \right]^{-3/2} = 1 - \frac{3\mathbf{R} \cdot \mathbf{r}}{R^2} - \frac{3r^2}{2R^2} \quad (3.6)$$

Hill's approximation assumes that $|\mathbf{R}| \gg |\mathbf{r}|$, therefore the third term on the right-hand side of Eqn (3.6) can be ignored. Since $\mathbf{R} = R\mathbf{i}$, the dot product $\mathbf{R} \cdot \mathbf{r} = Rx$. Therefore $|\mathbf{R} + \mathbf{r}|^{-3/2} = R^{-3}(1 - 3x/R)$ ignoring higher order terms. As the angular velocity $\Omega^2 = \mu_s / R^3$ and $(\mathbf{R} + \mathbf{r}) = (R + x)\mathbf{i} + y\mathbf{j} + z\mathbf{k}$ the solar tide components can be expressed as

$$-\mu_s \frac{(\mathbf{R} + \mathbf{r})}{|\mathbf{R} + \mathbf{r}|^3} = -\Omega^2 \left[1 - 3\frac{x}{R} \right] ((x + R)\mathbf{i} + y\mathbf{j} + z\mathbf{k}) \quad (3.7)$$

The solar-tide terms are introduced to the right-hand side of Eq (3.3) to obtain the complete Hill's equations of motion [Morrow, 2001]. The terms can be further simplified by noting that $xy/R \ll 1$, $xz/R \ll 1$ and $x(x + R)/R \approx x$. Evaluating the coriolis and centripetal acceleration cross-products gives

$$\ddot{x} - 2\Omega\dot{y} = -\frac{\mu x}{|\mathbf{r}|^3} + 3\Omega^2 x + a_x \quad (3.8.1)$$

$$\ddot{y} + 2\Omega\dot{x} = -\frac{\mu y}{|\mathbf{r}|^3} + a_y \quad (3.8.2)$$

$$\ddot{z} = -\frac{\mu z}{|\mathbf{r}|^3} - \Omega^2 z + a_z \quad (3.8.3)$$

The equations of motion can be non-dimensionalised with characteristic length L and characteristic time τ , where $\bar{x} = x/L$, $\bar{y} = y/L$, $\bar{z} = z/L$, $\bar{\mathbf{r}} = \mathbf{r}/L$ and $\bar{t} = t/\tau$. Equations (3.8) can then be re-written as

$$\frac{L}{\tau^2} \frac{d^2 \bar{x}}{d\bar{t}^2} - 2\Omega \frac{L}{\tau} \frac{d\bar{y}}{d\bar{t}} = -\frac{1}{L^2} \frac{\bar{x}\mu}{|\bar{\mathbf{r}}|^3} + 3\Omega^2 L\bar{x} + a_x \quad (3.9.1)$$

$$\frac{L}{\tau^2} \frac{d^2 \bar{y}}{d\bar{t}^2} + 2\Omega \frac{L}{\tau} \frac{d\bar{x}}{d\bar{t}} = -\frac{1}{L^2} \frac{\bar{y}\mu}{|\bar{\mathbf{r}}|^3} + a_y \quad (3.9.2)$$

$$\frac{L}{\tau^2} \frac{d^2 \bar{z}}{d\bar{t}^2} = -\frac{1}{L^2} \frac{\bar{z}\mu}{|\bar{\mathbf{r}}|^3} - \Omega^2 L\bar{z} + a_z \quad (3.9.3)$$

Selecting $\Omega^2 \tau^2 = 1$ and $L = (\tau^2 \mu)^{1/3}$ the angular velocity and planet gravitational parameter can be removed from the equations to obtain

$$\frac{d^2 \bar{x}}{d\bar{t}^2} - 2 \frac{d\bar{y}}{d\bar{t}} = -\frac{\bar{x}}{|\bar{\mathbf{r}}|^3} + 3\bar{x} + \kappa_x \quad (3.10.1)$$

$$\frac{d^2 \bar{y}}{d\bar{t}^2} + 2 \frac{d\bar{x}}{d\bar{t}} = -\frac{\bar{y}}{|\bar{\mathbf{r}}|^3} + \kappa_y \quad (3.10.2)$$

$$\frac{d^2 \bar{z}}{d\bar{t}^2} = -\frac{\bar{z}}{|\bar{\mathbf{r}}|^3} - \bar{z} + \kappa_z \quad (3.10.3)$$

where $(\kappa_x, \kappa_y, \kappa_z)$ are the non-dimensionalised acceleration components such that $\boldsymbol{\kappa} = \kappa_x \mathbf{i} + \kappa_y \mathbf{j} + \kappa_z \mathbf{k}$. Table 3-1 provides the characteristic length and characteristic time parameters for a variety of planets.

Name	R, $\times 10^6$ km	μ , $\times 10^{-6}$ km ³ s ⁻²	Ω , s ⁻¹	L, $\times 10^6$ km	τ , days
Mercury	57.91	0.02203	8.788×10^{-7}	0.3177	13.97
Venus	108.21	0.3249	3.2447×10^{-7}	1.4559	35.67
Earth	149.60	0.3986	1.9961×10^{-7}	2.1547	57.98
Mars	227.92	0.04283	1.0615×10^{-7}	1.5607	109.04
Jupiter	778.57	126.686	1.6812×10^{-8}	76.5283	688.42

Table 3-1 Parameters for selection of planets [Williams, 2001]

3.2 Libration points

3.2.1 On-axis libration points

Libration points can be identified by setting the acceleration and velocity components $\ddot{x} = \dot{x} = \ddot{y} = \dot{y} = \ddot{z} = \dot{z} = 0$. Hill's approximation yields two libration points for the ballistic case ($\kappa=0$). These libration points are labeled L_1 and L_2 , which are located symmetrically on the negative and positive side of the x -axis respectively. Setting the acceleration and velocity components equal to zero in Eqn (3.10) and applying the on Sun-line condition $y = z = 0$ yields

$$-\frac{x_o}{|x_o|^3} + 3x_o = 0 \quad (3.11)$$

Solving for x_o gives the location of the two libration points $x_o = \pm(3)^{-1/3} = \pm 0.69336$. Table 3-2 provides the location of these libration points for various planets orbiting the Sun.

For the non-ballistic case ($\kappa > 0$), a continuum of libration points can be generated planetward of L_2 and sunward of L_1 . To generate a libration point at x_o , the required acceleration is determined as

$$\kappa = \frac{x_o}{|x_o|^3} - 3x_o \quad (3.12)$$

Figure 3-2 shows a plot of the non-dimensional acceleration required to generate an on-axis libration point. Assuming $\kappa \geq 0$, no solutions exist beyond L_2 in the anti-Sun direction or between L_1 and the central body.

Name	L_1 , km	L_2 , km
Mercury	-2.2028×10^5	2.2028×10^5
Venus	-1.0095×10^5	1.0095×10^5
Earth	-1.4940×10^6	1.4940×10^6
Mars	-1.0821×10^6	1.0821×10^6
Jupiter	-5.3062×10^7	5.3062×10^7

Table 3-2 Location of L_1 and L_2 for various planets in the solar system

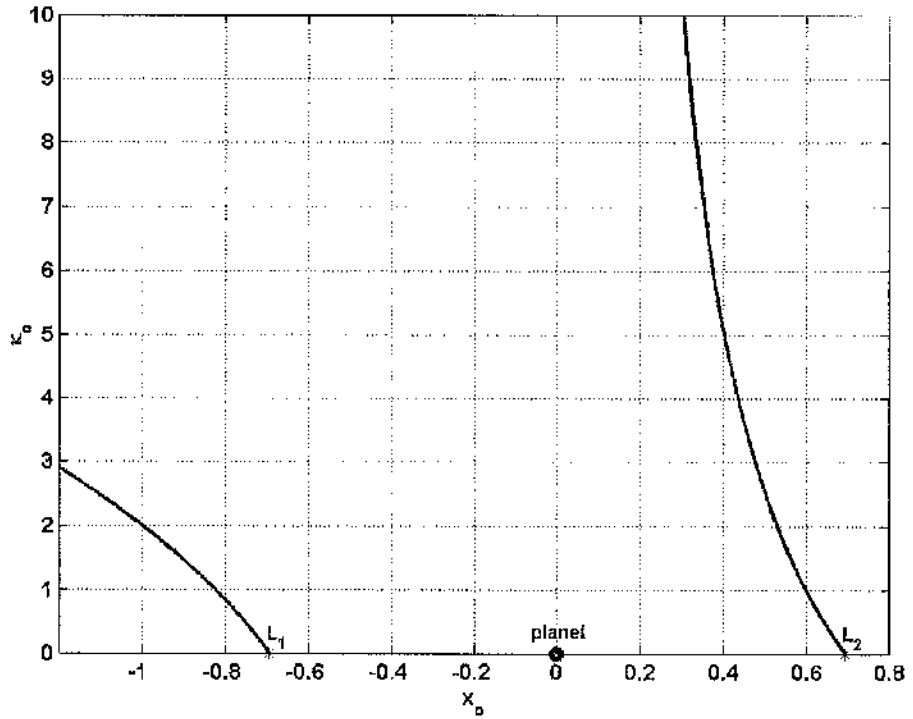


Figure 3-2 Artificial libration points generated using solar sail acceleration

3.2.2 Jacobi integral

The Jacobi Integral and Hill's surfaces have been described in detail by many authors [Marchal, 1990; Szehebel, 1967; Wie, 1998]. The integral provides a useful method for investigating bound motion given a set of initial orbit conditions. One technique for deriving the integral involves multiplying the equations of motion by the respective velocity components and summing them together as follows

$$\dot{x}\ddot{x} + \dot{y}\ddot{y} + \dot{z}\ddot{z} = -\left(\frac{x\dot{x}}{|\mathbf{r}|^3} + \frac{y\dot{y}}{|\mathbf{r}|^3} + \frac{z\dot{z}}{|\mathbf{r}|^3}\right) + 3x\dot{x} - z\dot{z} + \kappa_x\dot{x} + \kappa_y\dot{y} + \kappa_z\dot{z} \quad (3.13)$$

Re-arranging yields

$$\frac{d}{dt}\left[\frac{1}{2}v^2 - \frac{1}{|\mathbf{r}|} - \frac{3}{2}x^2 + \frac{1}{2}z^2 - \boldsymbol{\kappa}\cdot\mathbf{r}\right] = 0 \quad (3.14)$$

As the time derivative is zero, the expression in the brackets is a constant. Integrating with respect to time yields the Jacobi integral

$$v^2 - \frac{2}{|\mathbf{r}|} - 3x^2 + z^2 - 2\boldsymbol{\kappa}\cdot\mathbf{r} = C \quad (3.15)$$

where $v^2 = \dot{x}^2 + \dot{y}^2 + \dot{z}^2$ and the constant of integration, C , is known as the Jacobi constant.

The Jacobi constant can be evaluated at the Lagrange points by substituting $x_0 = \pm 3^{-1/3}$, $y_0 = 0$ and $z_0 = 0$ into Eqn (3.15) and setting $v = 0$. The resulting Jacobi constant is $C = -(9)^{2/3} = -4.3267$ [Villac, 2001]. Figure 3-3 shows a zero-velocity surface evaluated for constant C . It is evident that the surface closes symmetrically at the Lagrange points.

Artificial libration points are generated using the solar sail acceleration $\boldsymbol{\kappa}$. Figure 3-3 also shows a set of zero-velocity surfaces produced at artificial libration points sunward of L_2 . Figure 3-4 shows a set of zero-velocity surfaces produced at artificial libration points sunwards of L_1 . The Jacobi constants, libration point position and required solar sail acceleration for each of the zero-velocity surfaces are provided in Table 3-3.

As in the case of the Lagrange points, the zero-velocity surface is closed when evaluated at the artificial libration point. Therefore the Jacobi constant evaluated at a libration point represents a critical value, C_{crit} , above which the surface will be open. As the acceleration is applied in the anti-Sun direction, the energy for libration points sunward of L_2 is less than $C=-4.3267$. Artificial libration points sunward of L_1 have greater critical energies. The curve is open on the anti-Sun side indicating unbound motion for trajectories corresponding to this energy.

As the Jacobi constant is analogous to the total energy, it is clear from Eq (3.15) that the pseudo-potential function, $U(x,y,z)$, can be expressed as

$$U(x, y, z) = \frac{1}{|r|} + \frac{3}{2}x^2 - \frac{1}{2}z^2 + \kappa r \quad (3.16)$$

The energy surfaces produced by evaluating the Jacobi integral at $v=0$ are equivalent to evaluating the pseudo-potential function at the libration point. Similar to the non-linear stability analysis performed in Chapter 2, it is clear from Fig 3-3 and Fig 3-4 that a local saddle point of the pseudo-potential function exists at each of the on-axis libration points. This graphically indicates that the on-axis libration points are likely to be unstable. An analysis of the eigenvalues of the linearised system will be performed to determine the libration point stability.

Surface	C_{crit}	x_0	κ
1	-4.3267	0.6934	0
2	-4.8863	0.65	0.4169
3	-5.5867	0.6	0.9778
4	-6.3652	0.55	1.6558
5	-7.25	0.5	2.5
6	-4.2443	-0.7	0.0592
7	-3.0800	-0.8	0.8375
8	-2.0144	-0.9	1.4654

Table 3-3 Jacobi constants at the Lagrange point (1) and a series of artificial libration points (2-8)

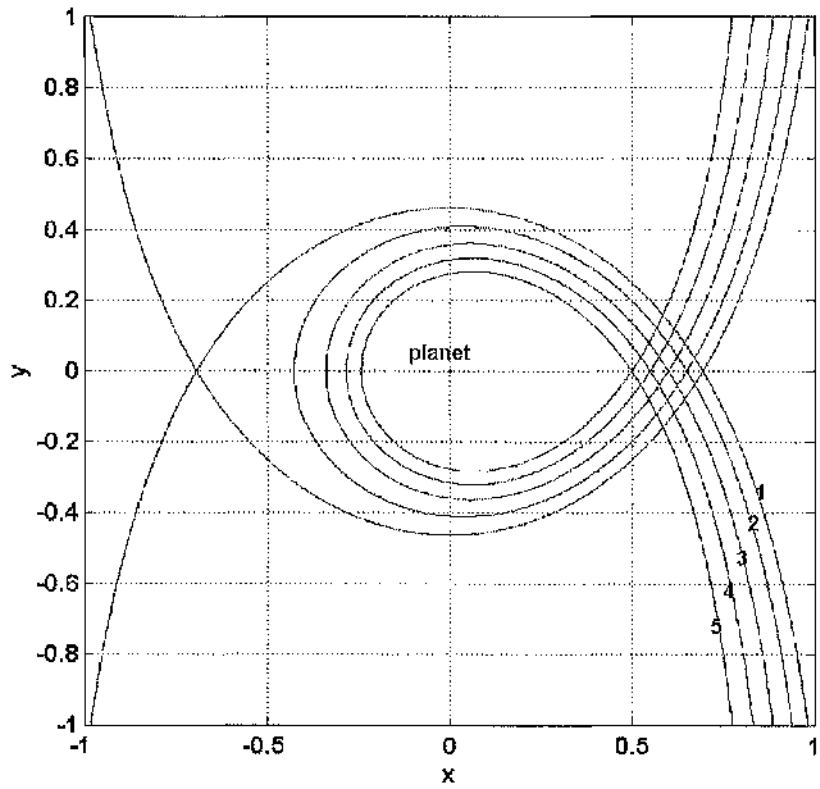


Figure 3-3 Constant energy surfaces corresponding to libration points sunward of L_2

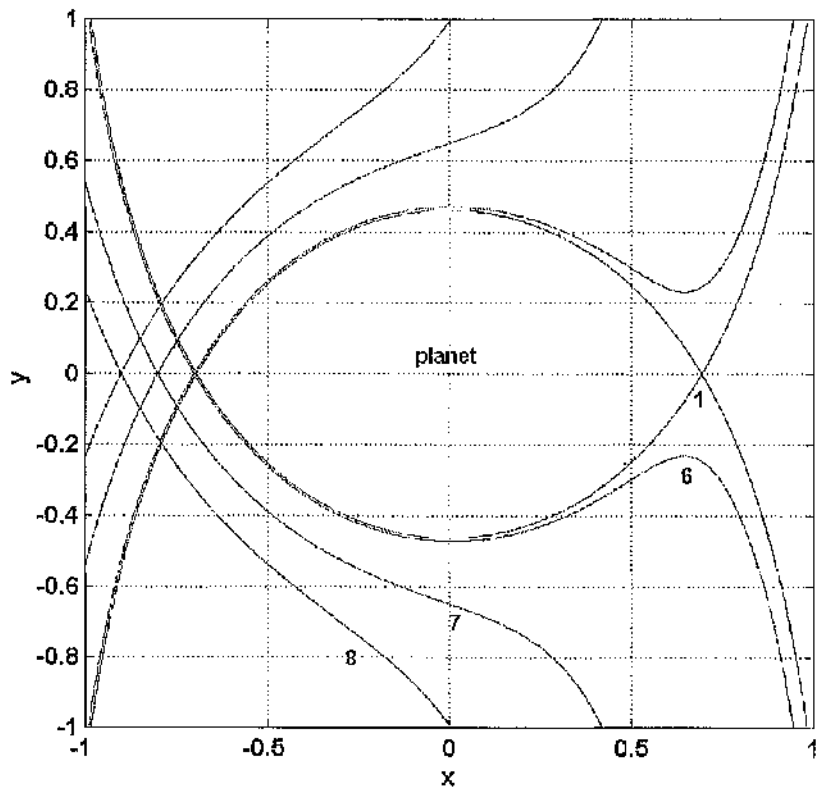


Figure 3-4 Constant energy surfaces corresponding to libration points sunward of L_1

There are four regions of the zero-velocity surface. The region within the vicinity of the central body is referred to as the capture region. A closed curve means that an orbit bound within the capture region is trapped. The exterior region is located on the anti-Sun side of the zero-velocity surface and the interior region exists sunward of the surface [Koon et al, 2002]. These regions are highlighted in Fig 3-5.

Figure 3-5 represents a series of Hill's surfaces in the ballistic case ($\kappa=0$) for a range of Jacobi constant values $4.2 \leq C \leq 4.45$. If the energy for a set of initial conditions corresponds to $C > C_{crit}$, then the energy surface will be open enabling escape from the capture region. In the ballistic case, the zero-velocity surface is symmetric about the y -axis, opening around L_1 and L_2 simultaneously.

Figure 3-6 shows an orbit bound within a closed zero-velocity surface with initial conditions $x_o=0.4934$, $y_o=0$, $\dot{x}_o=0$ and $\dot{y}_o=0.5$. These initial conditions correspond to a Jacobi constant $C=-4.5340$. Figure 3-7 demonstrates a transfer between the exterior and interior region. These initial conditions correspond to a Jacobi constant $C=-4.2375$.

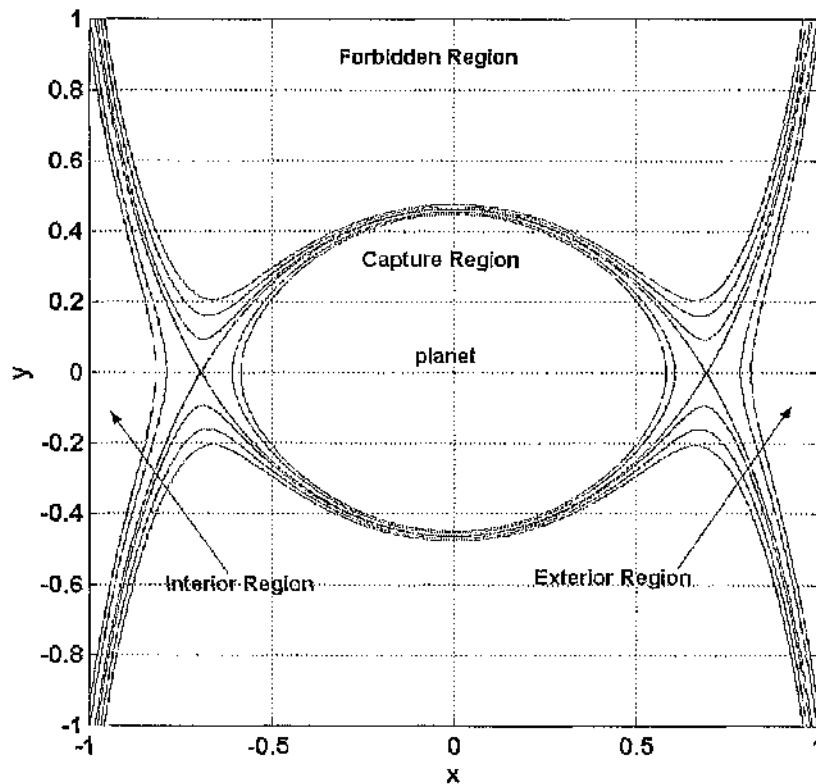


Figure 3-5 Series of zero-velocity surfaces for the ballistic case ($\kappa=0$)

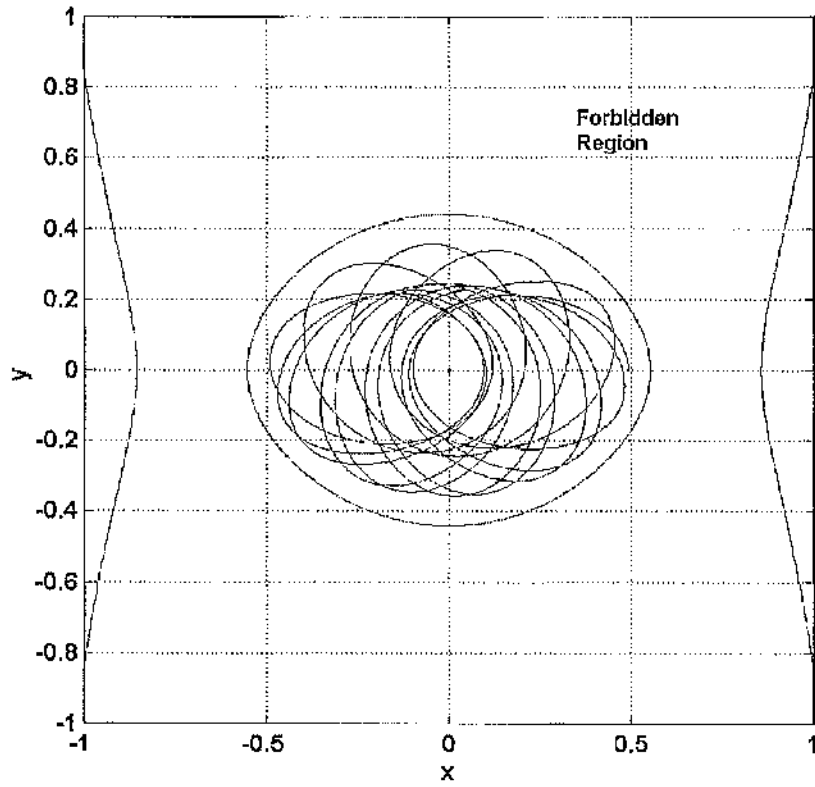


Figure 3-6 Trajectory bound within zero-velocity surface

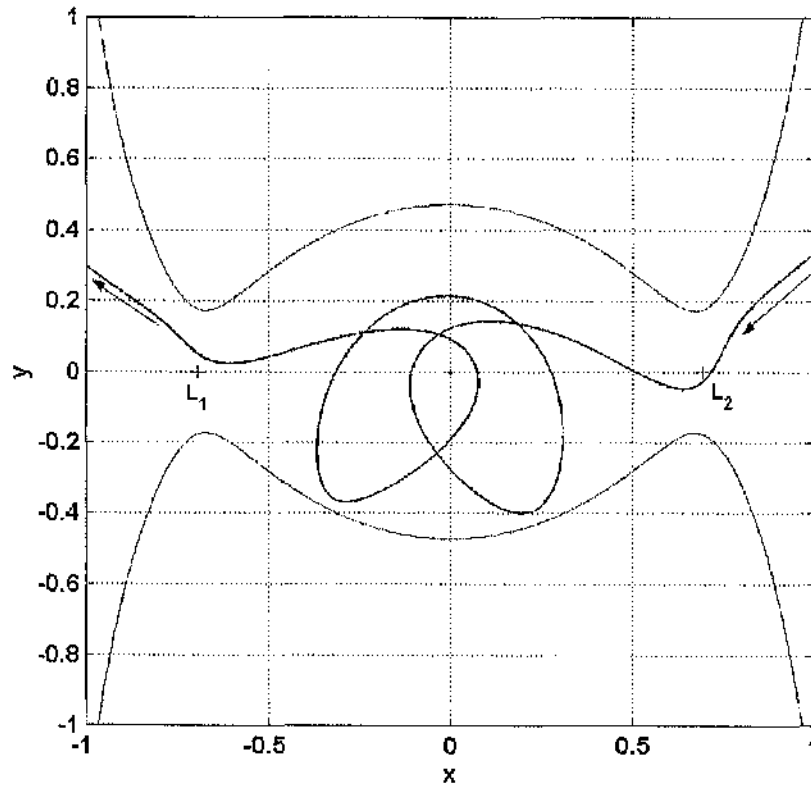


Figure 3-7 Transfer from exterior region to interior region via gap in zero-velocity surface

Similarly, a gap opens in the zero-velocity surface around an artificial libration point. Figure 3-8 shows a series of surfaces for increasing energy where $C_{crit}=-7.25$. The Jacobi constants of the Hill's surfaces range between $-7.75 \leq C \leq -6.75$. There is no gap present on the sunward side of the surface for the applied acceleration, $\kappa=2.5$. As the acceleration is applied in the anti-Sun direction, the energy required to achieve an open surface on the anti-Sun side is reduced. As the acceleration is increased, the achievable libration point position moves closer to the planet and the value of C_{crit} decreases.

Figure 3-9 shows a series of surfaces for a libration point located sunward of L_1 , $x_0=-0.7$. The critical energy, $C_{crit}=-4.2443$ and the Jacobi constants range between $-4.5 \leq C \leq -4$. As the energy is increased, a gap clearly opens around the libration point. Escape in the anti-Sun direction is possible via this opening in the Hill's surface.

It will now be shown that it is possible to generate non-Keplerian orbits around these libration points. Two types of non-Keplerian orbits will be demonstrated, including the displaced circular orbits investigated in the two-body problem and quasi-periodic Lissajous trajectories. Stable manifolds will then be investigated which pass near to the central body and wind onto the desired orbits, particularly useful in the Sun-Earth system for near-Earth orbit insertions.

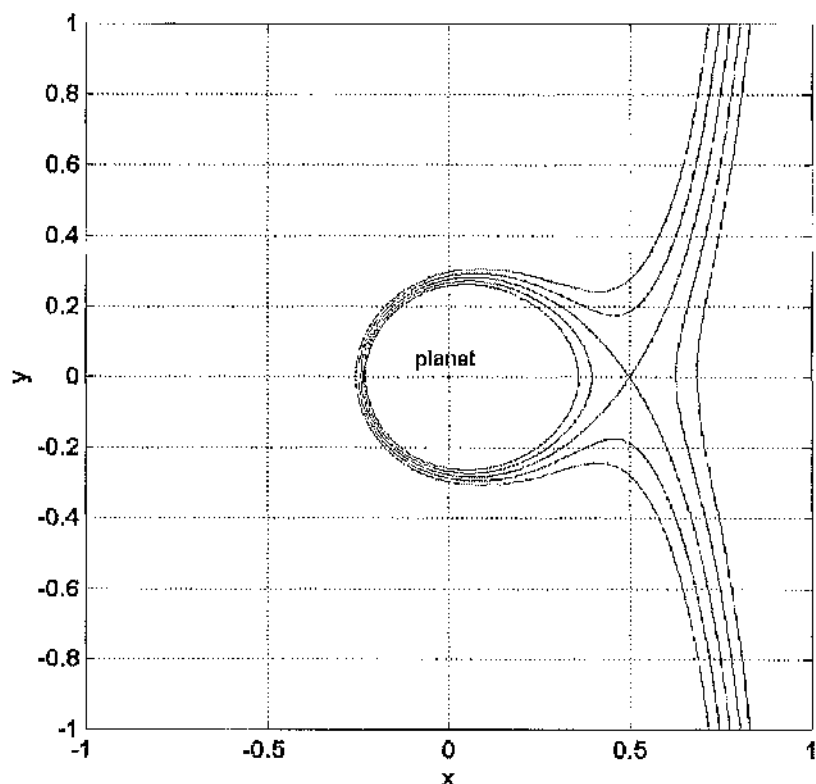


Figure 3-8 Series of zero-velocity surfaces of increasing energy for $\kappa=2.5$

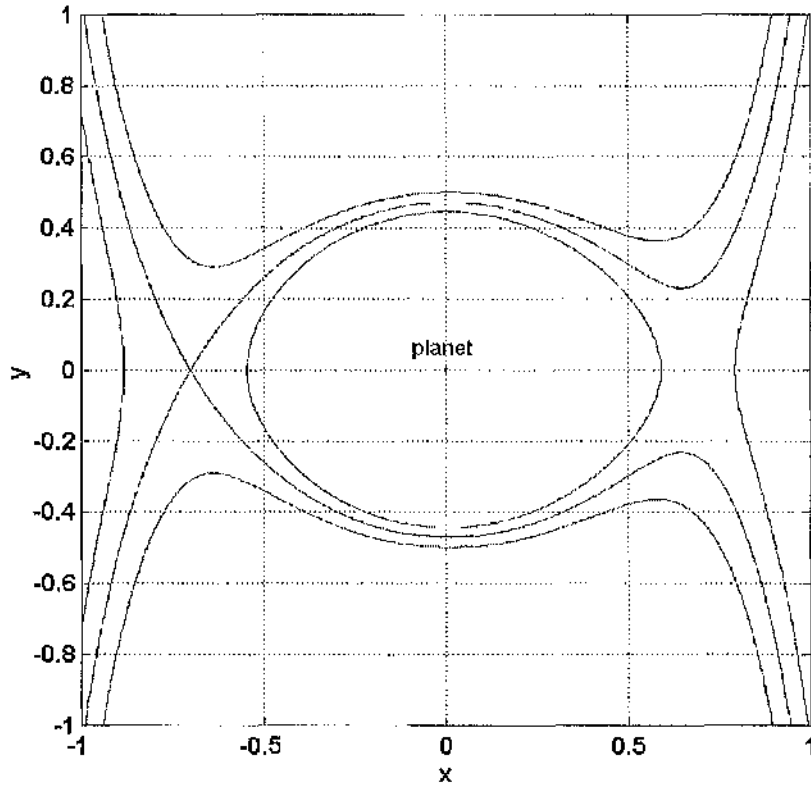


Figure 3-9 Series of zero-velocity surfaces of increasing energy for $\kappa=0.0592$

3.3 Circular displaced non-Keplerian orbit

3.3.1 Planet dependant acceleration perturbation

In Chapter 2, it was demonstrated that by orientating the solar sail normal to the Sun-line, a circular orbit can be displaced in the anti-Sun direction, so that the orbit plane no longer intersects the central body. From the two-body problem discussed in Chapter 2, a circular displaced orbit can be produced by selecting an appropriate initial orbit radius ρ_o and angular velocity $\omega = \sqrt{1/|r|^3}$. Treating Hill's approximation as a perturbed two-body model, a possible solution is assumed with $z_o = \rho_o \cos \theta$ and $y_o = \rho_o \sin \theta$. Evaluating at $\theta=0$ gives the initial position $(x_o, 0, z_o)$ and velocity $(0, \omega z_o, 0)$ where the required acceleration is given by Eq (3.12).

While the solar sail normal is directed in the anti-Sun direction, the acceleration due to solar radiation pressure is related to the lightness number, β , as $\kappa = \beta \mu_s / R_s^2$ where μ_s is

the solar gravitational parameter and R_s is the separation between the solar sail and the Sun. From Fig 3-1, the separation between the solar sail and the Sun at the nominal orbit is defined as $R_o = |\mathbf{R} + \mathbf{r}_o|$, where \mathbf{r}_o represents the nominal distance between the sail and the planet. The acceleration can be evaluated at the nominal orbit conditions for any planet such that $\kappa_o = \beta\mu_s / R_o^2$. For a solar sail with constant surface area, the sail acceleration variation is dependant on time varying distance between the Sun and sail such that $R_s(t) = |\mathbf{R} + \mathbf{r}(t)|$. The time dependant acceleration relative to the nominal acceleration can be expressed as $\kappa(t) = (R_o / R_s(t))^2 \kappa_o$.

Including the acceleration variation due to relative distance from the Sun means the non-dimensionalised Hill's equations can no longer be scaled to any planet, as the resulting trajectory is planet dependent. This section will focus on orbits where the Earth is the central body. The results will be scaled to use Earth radii (R_E) as a suitable scale length.

3.3.2 Stability of circular displaced non-Keplerian orbit

The two-body stability criteria can be examined using Hill's approximation and is valid provided the orbit is within a reasonable distance of the Earth. Figure 3-10 shows a non-Keplerian orbit with nominal radius $50 R_E$ displaced $15 R_E$ from the Earth, requiring an acceleration $\kappa_o = 1.0238 \text{ mms}^{-2}$. This orbit can be described as stable when compared to the two-body stability condition, $\rho_o > 2\sqrt{2}x_o$, where ρ_o represents the nominal radius. The nominal orbit period is $T = 22.1 \text{ days}$. The trajectory exhibits a large deviation from the nominal displacement distance, between $7.95 R_E$ and $24.76 R_E$, but clearly does not escape.

An orbit classed as unstable compared to the two-body stability condition is shown in Fig 3-11. This nominal orbit has a radius of $50 R_E$ and is displaced $20 R_E$ from the Earth, requiring an acceleration $\kappa_o = 1.242 \times 10^{-3} \text{ ms}^{-2}$. The nominal orbit period is 23.15 days . Escape from the nominal orbit occurs within 20 days.

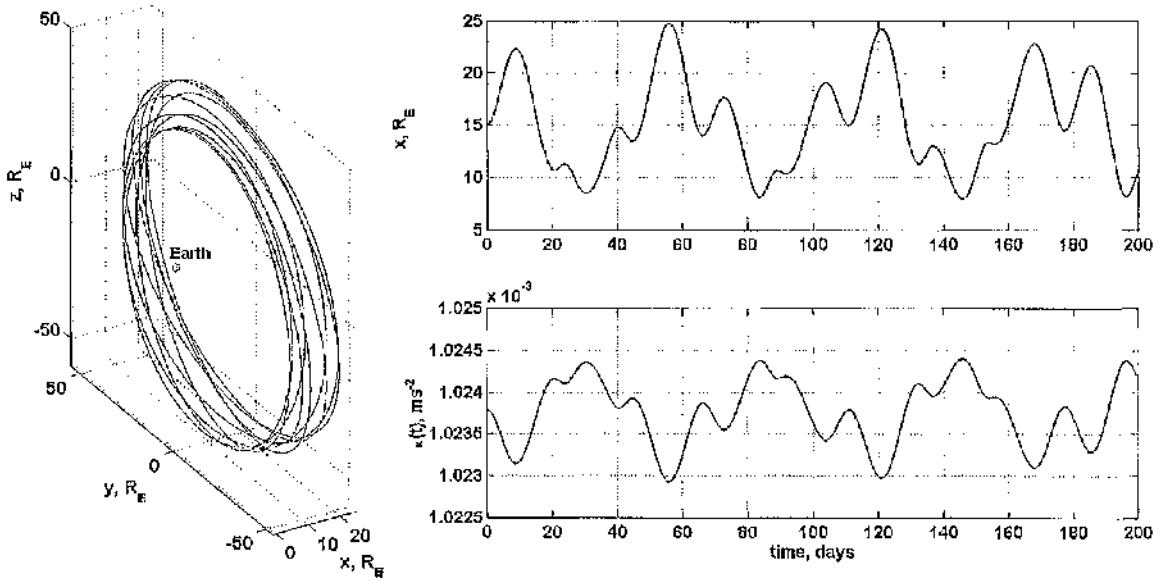


Figure 3-10 Stable circular displaced orbit computed using Hill's equations

$$x_o=15R_E, \rho_o=50 R_E, \dot{y}_o=1.04852 \times 10^3 \text{ ms}^{-1}, \kappa_o=1.0238 \times 10^{-3} \text{ ms}^{-2}$$

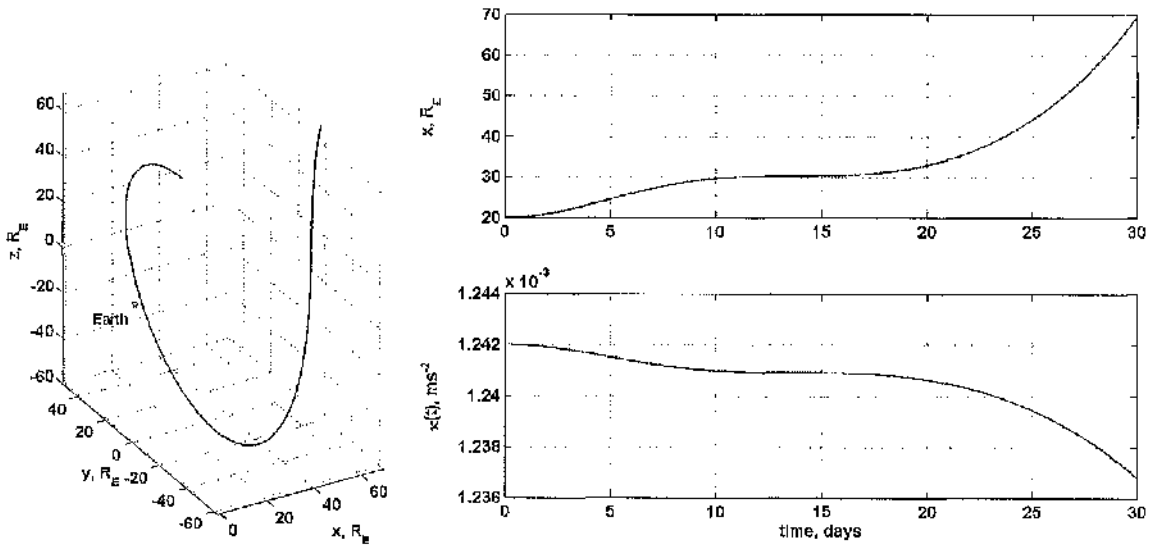


Figure 3-11 Unstable circular displaced orbit computed using Hill's equations

$$x_o=20 R_E, \rho_o=50 R_E, \dot{y}_o=1.0007 \times 10^3 \text{ ms}^{-1}, \kappa_o=1.242 \times 10^{-3} \text{ ms}^{-2}$$

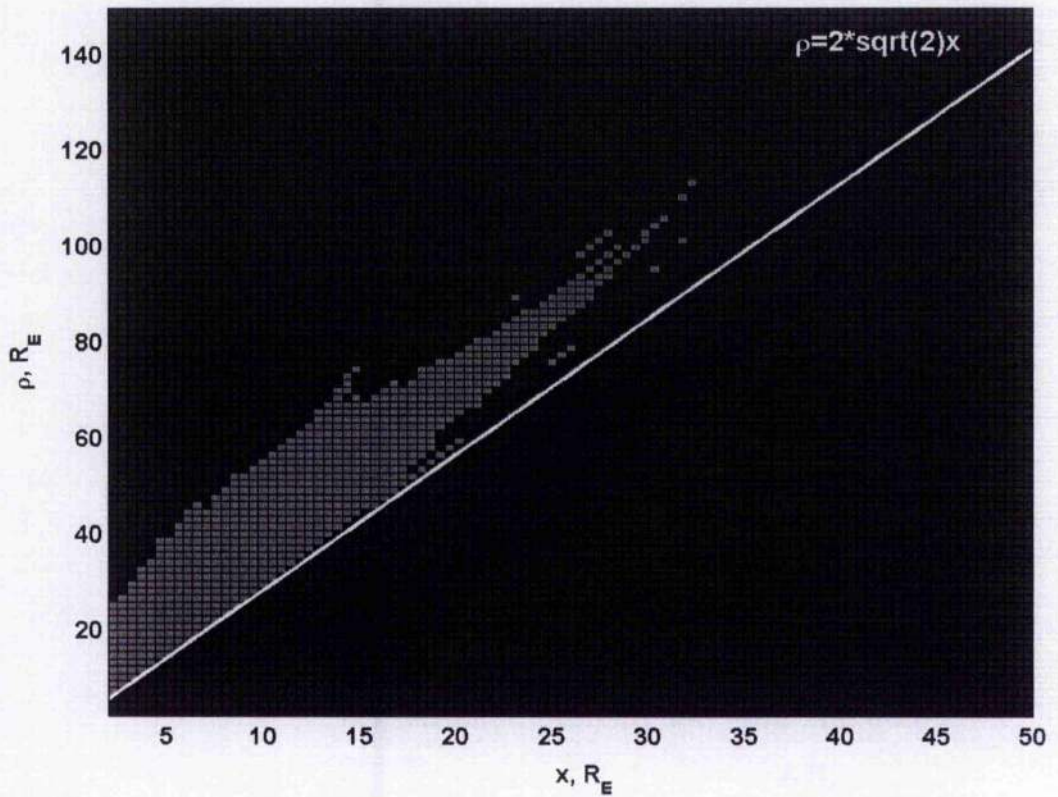


Figure 3-12 Stability of circular displaced Hills orbits
{Dark Region – Unstable; Light Region – Stable}

The stability of circular displaced orbits was computed over a nominal displacement range of $2 \rightarrow 50 R_E$ and radii range $2 \rightarrow 150 R_E$. Using an iterative process, Hill's equations were numerically integrated for each set of initial conditions. An orbit was defined as stable provided after 10 orbit periods the maximum displacement distance remained within an arbitrary distance, $3x_o$, of the Earth. The results are shown in Fig 3-12, where the light and dark regions correspond to stable and unstable orbits respectively.

The line representing the two-body stability criteria, $\rho_o > 2\sqrt{2}x_o$ is included for comparison. Hill's problem shows agreement with the two-body stability criteria provided the radial distance is near to the central body. The orbit displaced furthest from the central body, which can still be classed as stable, has initial conditions $x_o = 32.06 R_E$ and radius $\rho_o = 112.63 R_E$. This orbit was found to be highly perturbed and perform large excursions across the x -axis, frequently passing sunwards of the Earth ($x < 0$).

3.3.3 Periodic looping trajectories

The periodic looping trajectories identified in the two-body study can also be generated in Hill's problem. This family of orbits is obtained by perturbing the required acceleration. Figure 3-13 shows a stable orbit with the acceleration perturbed by $\Delta=0.05$, where $\kappa = \kappa_0(1-\Delta)$. Comparing this to the unperturbed stable orbit provided in Fig 3-10, the acceleration perturbation increases the x -axis oscillation amplitude with a x -displacement range spanning between $x=23.28 R_E$ and $x=3.63 R_E$.

Figure 3-14 shows the effect of perturbing the acceleration with $\Delta=0.05$ for the same initial conditions as the unstable orbit shown in Fig 3-11. In this case, the trajectory does not escape from the nominal orbit in the anti-Sun direction. Instead the orbit oscillates along the x -axis with x -displacement range between $x=26.48 R_E$ and $x=4.49 R_E$.

The periodic looping trajectories provide a series of manifolds which wind-off (unstable) and wind onto (stable) the nominal orbit. Figure 3-15 shows a looping trajectory which passes within $1.52 R_E$ of the Earth before returning to the nominal orbit. Orbit insertion conditions can be determined by numerically integrating the trajectory to obtain the position and velocity coordinates at the minimum distance from the Earth. The unstable manifold eventually intersects a stable manifold near to the central body which winds back onto the nominal orbit. This enables the minimum x -displacement conditions to be applied directly to define a transfer trajectory between the Earth and the nominal orbit.

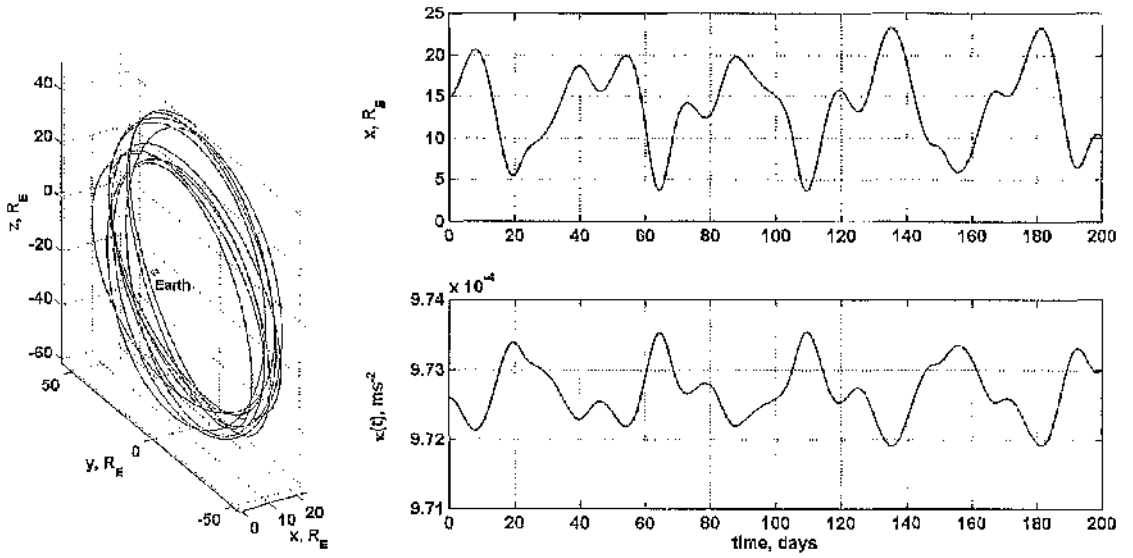


Figure 3-13 Stable orbit with perturbed acceleration computed using Hill's equations
 $x_0=15 R_E$, $z_0=50 R_E$, $\dot{y}_0=1.04852 \times 10^3 \text{ ms}^{-1}$, $\kappa=9.72593 \times 10^{-4} \text{ ms}^{-2}$, $\Delta=0.05$

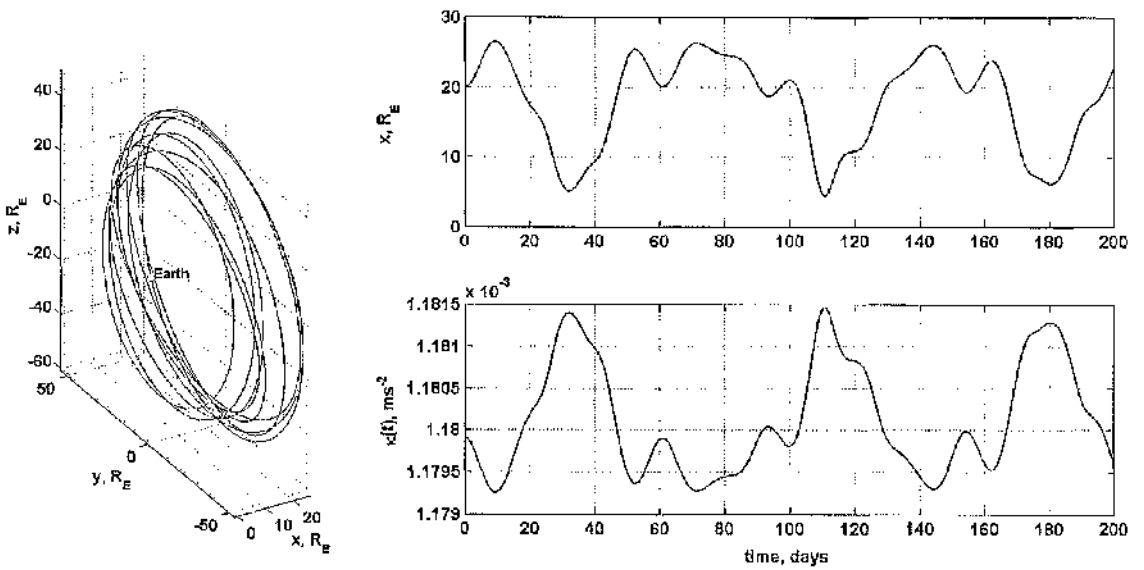


Figure 3-14 Unstable orbit with perturbed acceleration computed using Hill's equations
 $x_0=20 R_E$, $z_0=50 R_E$, $\dot{y}_0=1.0007 \times 10^3 \text{ ms}^{-1}$, $\kappa=1.17991 \times 10^{-3} \text{ ms}^{-2}$, $\Delta=0.05$

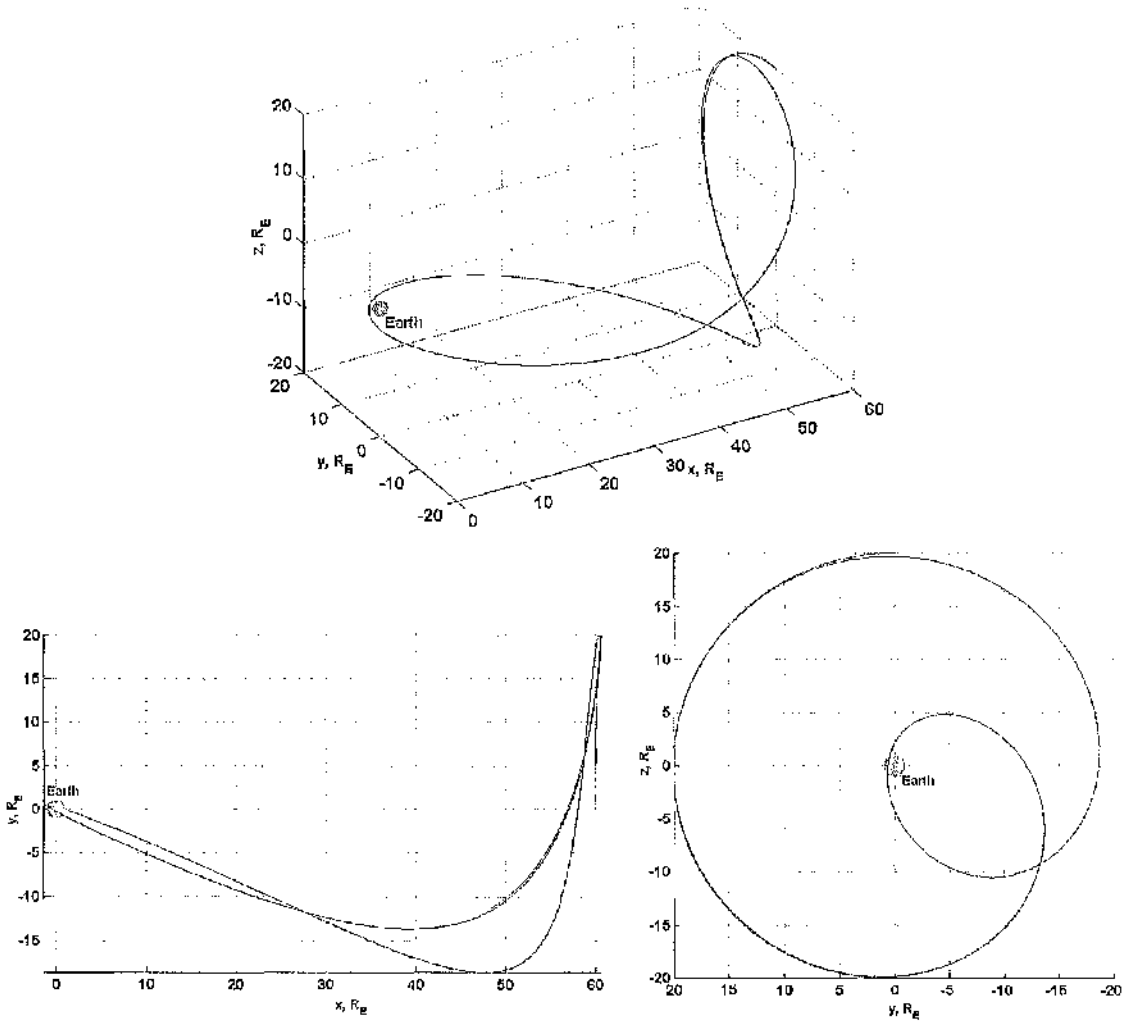


Figure 3-15 Periodic looping trajectory computed using Hill's equations

$$x_o=60 R_E, z_o=20 R_E, \dot{y}_o=314.496 \text{ ms}^{-1}, \kappa=2.19134 \times 10^{-3} \text{ ms}^{-2}, \Delta=0.04$$

Alternatively, the mirror image theorem can be applied which takes advantage of the symmetry of trajectories in the three-body problem [Brouke, 1979; Miele, 1960]. Symmetry about the x - z plane can be achieved by transforming the initial conditions using

$$(x \ y \ z \ \dot{x} \ \dot{y} \ \dot{z}, \ t) \rightarrow (x \ -y \ z \ -\dot{x} \ \dot{y} \ -\dot{z}, \ -t) \quad (3.17)$$

This can be verified by substituting the transformed conditions into Eqns (3.10) to yield

$$\frac{d^2(x)}{d(-t)^2} + 2 \frac{d(-y)}{d(-t)} = -\frac{(x)}{|\mathbf{r}|^3} + 3(x) + \kappa_x \quad (3.18.1)$$

$$-\frac{d^2(-y)}{d(-t)^2} - 2 \frac{d(x)}{d(-t)} = -\frac{(-y)}{|\mathbf{r}|^3} \quad (3.18.2)$$

$$\frac{d^2 z}{d(-t)^2} = -\frac{z}{|\mathbf{r}|^3} - z \quad (3.18.3)$$

Comparing the resulting equations to Eqns (3.10) verifies that the y -axis direction has been reversed but the x - and z -axis remain unaltered when the mirror image conditions are applied. This corresponds to a mirror image of the trajectory reflected about the x - z plane, which means the conditions obtained by integrating forward along the unstable manifold will now wind onto the nominal orbit. Reversing the integration time transforms the unstable manifold into a stable manifold [Koon et al, 1999].

For Hill's approximation, other symmetries exist as outlined by Scheeres and Villac [2003]. For the ballistic case ($\kappa=0$) several symmetries exist including reflections about all the axial planes x - z , x - y and y - z . The other symmetries are obtained by combining the transforms required for plane symmetric trajectories.

The transforms for symmetry about the y - z and x - y planes are

$$(x \ y \ z \ \dot{x} \ \dot{y} \ \dot{z}, \ t) \rightarrow (-x \ y \ z \ \dot{x} \ -\dot{y} \ -\dot{z}, \ -t) \quad (3.19)$$

$$(x \ y \ z \ \dot{x} \ \dot{y} \ \dot{z}, \ t) \rightarrow (x \ y \ -z \ \dot{x} \ \dot{y} \ -\dot{z}, \ t) \quad (3.20)$$

In the case of an artificial libration point, the acceleration term is always positive with the implication that the symmetry about the y - z axis does not exist as the x -axis direction is reversed. This can be verified when the transformed parameters from Eq (3.18.1) are substituted into Eq (3.10.1) to obtain

$$\frac{d^2(-x)}{d(-t)^2} - 2\frac{dy}{d(-t)} = -\frac{(-x)}{|\mathbf{r}|^3} + 3(-x) + \kappa_x \quad (3.21.1)$$

$$-\frac{dx}{dt^2} + 2\frac{dy}{dt} = \frac{x}{|\mathbf{r}|^3} - 3x + \kappa_x \quad (3.21.2)$$

The direction represented by the x -axis equation has been reversed except for the acceleration. This symmetry is only valid when $\kappa=0$. In total there are three possible symmetries in the non-ballistic case. The third possible symmetry is obtained by combining the x - y and x - z transforms to yield

$$(x \ y \ z \ \dot{x} \ \dot{y} \ \dot{z}, \ t) \rightarrow (x \ -y \ -z \ -\dot{x} \ \dot{y} \ \dot{z}, \ -t) \quad (3.22)$$

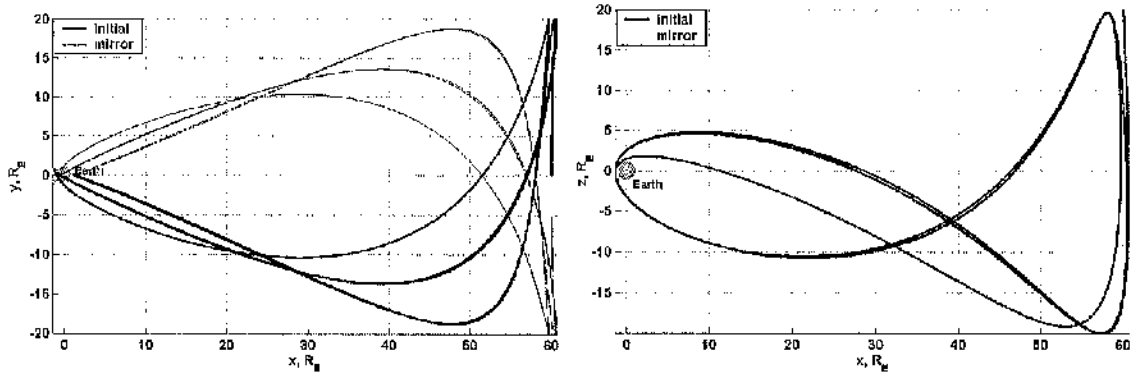
Figure 3-16 (a) represents the initial conditions transformed using Eq (3.17). As the time is negative for this transform, the trajectory is reversed when forward integration is applied i.e. unstable manifolds become stable manifolds. The transformed conditions are identified by integrating the nominal orbit conditions forward for 3 orbit periods. The transformed conditions produce the time reversed orbit, which is inverted in the x - z plane.

Figure 3-16 (b) shows the resulting orbit when the initial conditions are transformed using Eq (3.22). Again, time is negative so the reverse of the original orbit is produced using the transformed conditions. These are obtained after three periodic loops of the original orbit conditions. It is clear that this transformed orbit is inverted in both the x - y and x - z plane.

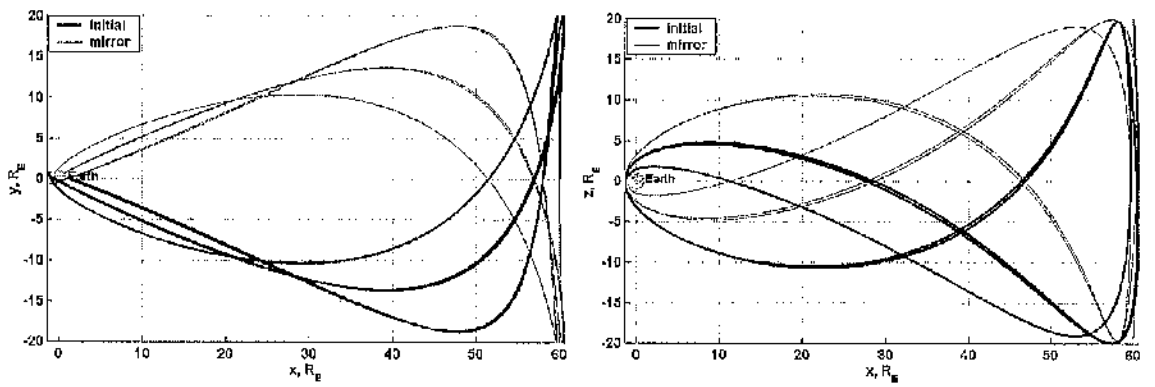
Figure 3-16 (c) is computed using the transform provided in Eq (3.20). For this transform, the time t is positive so integration is forward. The initial conditions are determined by first integrating the nominal orbit conditions forward for 1 periodic loop and selecting conditions which correspond to the minimum x -axis distance from the central body. The initial plot represents the trajectory obtained using these conditions. The transformed conditions produce an inverted trajectory in the x - y plane.

Orbit insertion can be achieved by identifying initial conditions near to the central body which wind onto the desired orbit. As the manifolds can be described as homoclinic, the solar sail will eventually return to the central body via the unstable manifold. Station-keeping strategies have to be employed to prevent the solar sail leaving the nominal orbit after insertion.

(a)



(b)



(c)

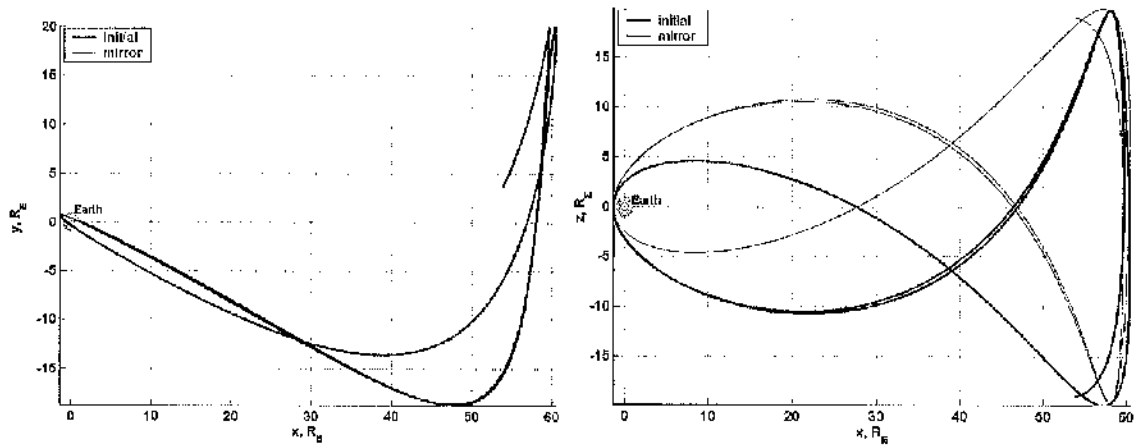


Figure 3-16 Trajectories generated using mirror image theorem

3.3.4 Optimal control of circular displaced orbits

The two solar sail station-keeping techniques examined in Chapter 2, were sail pitch angle variation and sail surface area variation. The optimal controller developed in the two-body case can be used to control circular displaced orbits generated using Hill's equations, which can be considered as a perturbed two-body model provided the orbit is relatively near to the central body ($x_o < 160 R_E$).

3.3.4.1 Hill's sail area controller

The two-body optimal sail area controller is outlined in Section 2.4. For a desired orbit, insertion trajectories are determined by perturbing the acceleration sufficiently to generate a set of periodic looping manifolds. The minimum x -axis turning point is determined and the insertion conditions at this point may either be applied directly or by using the mirror image transforms, as discussed previously.

Area variation directly controls the acceleration of the solar sail. The gains (G_1, G_2, G_3, G_4) are obtained using the Ricatti equation, discussed in Section (2.4.4). The acceleration variation necessary to maintain station-keeping at the desired orbit with displacement x_o and radius ρ_o can be modelled using the linear control law

$$\delta k = -(G_1(\rho - \rho_o) + G_2(x - x_o) + G_3(\dot{\rho} - \dot{\rho}_o) + G_4(\dot{x} - \dot{x}_o)) \quad (3.23)$$

where δk represents the acceleration variation directed along the sun-line, $(\rho, x, \dot{\rho}, \dot{x})$ are the integrated orbit conditions and $(\rho_o, x_o, \dot{\rho}_o, \dot{x}_o)$ are the desired orbit conditions. As the x -axis represents the Sun-line, the orbit radius $\rho = \sqrt{y^2 + z^2}$. The radial velocity can be determined using $\dot{\rho} = (y\dot{y} + z\dot{z})/\rho$.

For a circular orbit displaced a constant distance from the central body $\dot{\rho}_o = 0$ and $\dot{x}_o = 0$, which enables $\delta\kappa$ to be continuously calculated during trajectory integration to provide a control signal. Initially, the controller is inactive while the solar sail traverses the stable manifold which winds onto the nominal orbit. Once the solar sail has arrived at the nominal orbit displacement distance, the controller is activated to prevent the sail winding off the orbit via the unstable manifold.

Figure 3-17 shows an orbit controlled using sail area variation with insertion at a distance of $1.55 R_E$ from the Earth. This corresponds to an insertion starting point approximately 3500 km above the Earth's surface. The nominal acceleration $\kappa_o = 2.2826 \text{ mms}^{-2}$ with a reduction corresponding to $\Delta = 0.04$. The solar sail winds onto the nominal orbit with radius $20 R_E$ displaced $60 R_E$ from the Earth within 13.5 days.

Figure 3-18 shows the acceleration variation for a control period of 200 days. The acceleration varies between 2.4286 mms^{-2} and 2.1198 mms^{-2} . The corresponding area variation for a 500 kg sail and payload mass is between $1.3332 \times 10^5 \text{ m}^2$ and $1.1638 \times 10^5 \text{ m}^2$. Using a sail assembly with loading $\sigma = 3 \text{ gm}^{-2}$ would require a total sail mass of 400 kg, enabling control of a 100 kg payload at this orbit.

As the sail acceleration is linearly dependant on sail mass, the gradient of payload mass against sail area is determined as $1.3328 \times 10^3 \text{ m}^2 \text{ kg}^{-1}$. A small 10 kg payload could be controlled at the nominal orbit using a solar sail of area $13,328 \text{ m}^2$, or a larger 500 kg payload could be controlled with a sail area of $6.6642 \times 10^5 \text{ m}^2$.

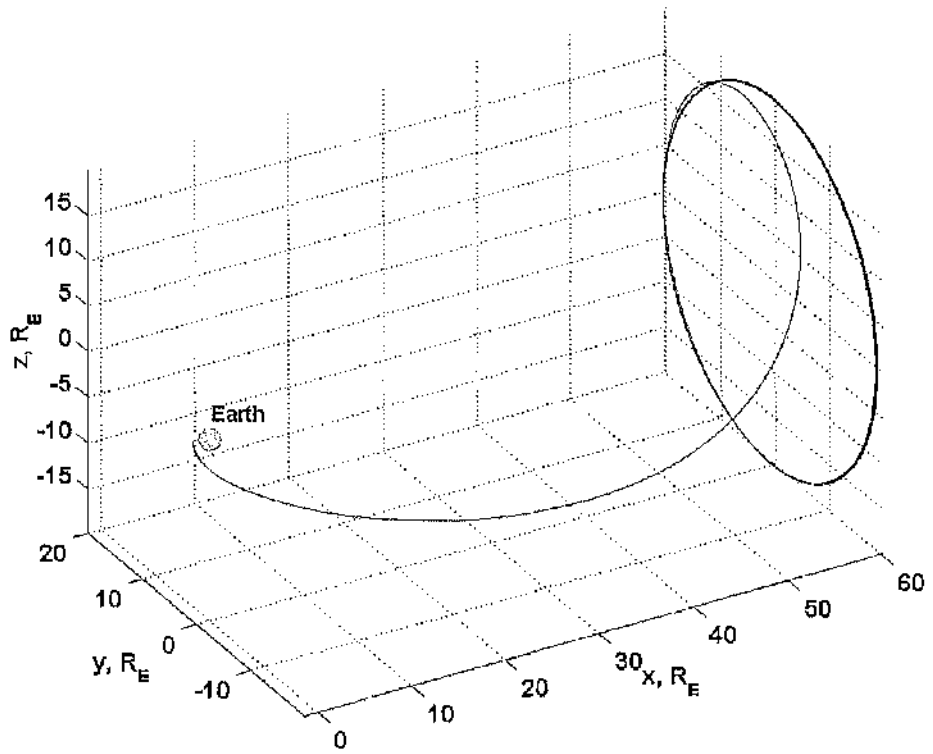


Figure 3-17 Circular planet displaced orbit achieved using sail area control

$$\rho_o = 20 R_E, z_o = 60 R_E, Q = 1000(I_{4 \times 4}) N = 3 \times 10^{11}$$

$$G = [-3.0769 \times 10^{-5} \ 7.4970 \times 10^{-5} \ 0.012174 \ 0.012245]$$

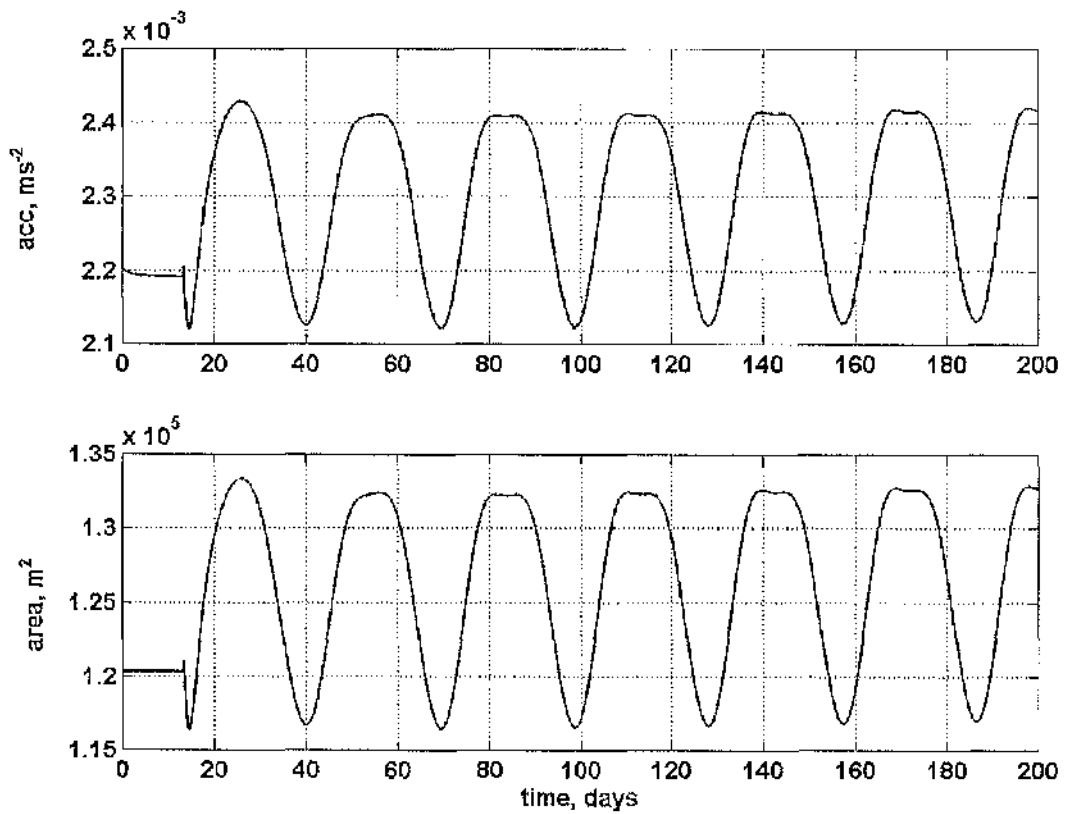


Figure 3-18 Solar sail acceleration and area variation required to control orbit

3.3.4.2 Sail pitch and yaw controller

The two-body pitch angle controller uses the linearised two-body equations represented using cylindrical polar coordinates. The control angles must be transformed into a Cartesian pitch and yaw angles (ϕ, ψ) determined from the cylindrical polar roll and pitch angle, (φ, α) . From Fig 3-19, the components for the unit vector \mathbf{n} can be expressed using cylindrical polar pitch and roll angles as

$$n_x = n \cos \alpha \quad (3.24.1)$$

$$n_y = n \sin \alpha \sin \varphi \quad (3.24.2)$$

$$n_z = n \sin \alpha \cos \varphi \quad (3.24.3)$$

and using Cartesian pitch and yaw angles as

$$n_x = n \cos \phi \cos \psi \quad (3.25.1)$$

$$n_y = n \cos \phi \sin \psi \quad (3.25.2)$$

$$n_z = n \sin \phi \quad (3.25.3)$$

From Eq (3.25.1) and Eq (3.25.2), $n_y/n_x = \tan \psi$ which can be compared to Eq (3.24.1) and Eq (3.24.2) to obtain the relationship for yaw angle as

$$\psi = \tan^{-1}(\tan \alpha \sin \varphi) \quad (3.26.1)$$

Similarly, comparing Eq (3.25.3) to Eq (3.24.3), the Cartesian pitch angle can be determined from

$$\phi = \sin^{-1}(\sin \alpha \cos \varphi) \quad (3.26.2)$$

The acceleration can be expressed including the dependency on the sail pitch and yaw angle as $\kappa(t) = \kappa_o [R_o/R(t)]^2 \cos^2 \phi \cos^2 \psi \mathbf{n}$. Using the Cartesian representation of unit vector, \mathbf{n} , from Eq (3.25), the resulting acceleration components can be expressed as

$$\kappa_x(t) = \kappa_o [R_o/R(t)]^2 \cos^3 \phi \cos^3 \psi \quad (3.27.1)$$

$$\kappa_y(t) = \kappa_o [R_o/R(t)]^2 \cos^3 \phi \cos^2 \psi \sin \psi \quad (3.27.2)$$

$$\kappa_z(t) = \kappa_o [R_o/R(t)]^2 \cos^2 \phi \cos^2 \psi \sin \phi \quad (3.27.3)$$

During numerical integration of Hill's equations, the polar coordinate angular position can be determined as $\theta = \tan^{-1}(y/z)$. The pitch angle variation is determined using the linear control law

$$\delta\alpha = -(G_1(\rho - \rho_o) + G_2(x - x_o) + G_3(\dot{\rho} - \dot{\rho}_o) + G_4(\dot{x} - \dot{x}_o)) \quad (3.28)$$

which is converted to Cartesian pitch and yaw angle variations $\delta\phi$ and $\delta\psi$.

Figure 3-20 shows an orbit controlled using pitch and yaw angle variation with radius $20 R_E$, displaced $60 R_E$ from the Earth. The same insertion conditions are employed as those used in the sail area variation case starting at a distance of $1.55 R_E$ from the Earth. The controller is inactive until the solar sail arrives at the nominal orbit. The solar sail acceleration is boosted to $1.05\kappa_o$ when the controller is activated to compensate for the reduction in the acceleration directed along the x -axis when the sail is pitched.

The pitch and yaw angle variation required to control this orbit is shown in Fig 3-21. Figure 3-22 shows the yaw and pitch angle which demonstrates the periodic nature of the control signal.

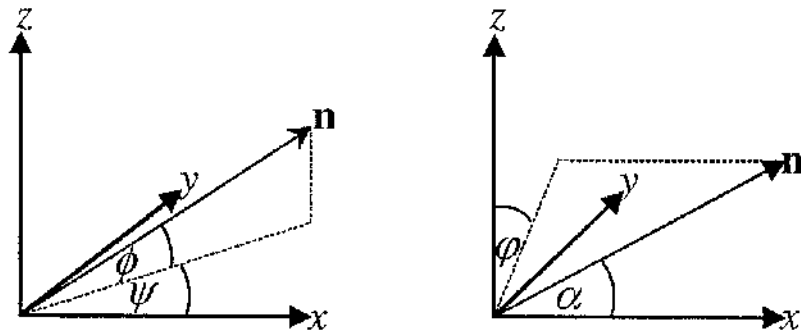


Figure 3-19 Converting cylindrical polar pitch and roll angles into corresponding Cartesian pitch and yaw angles

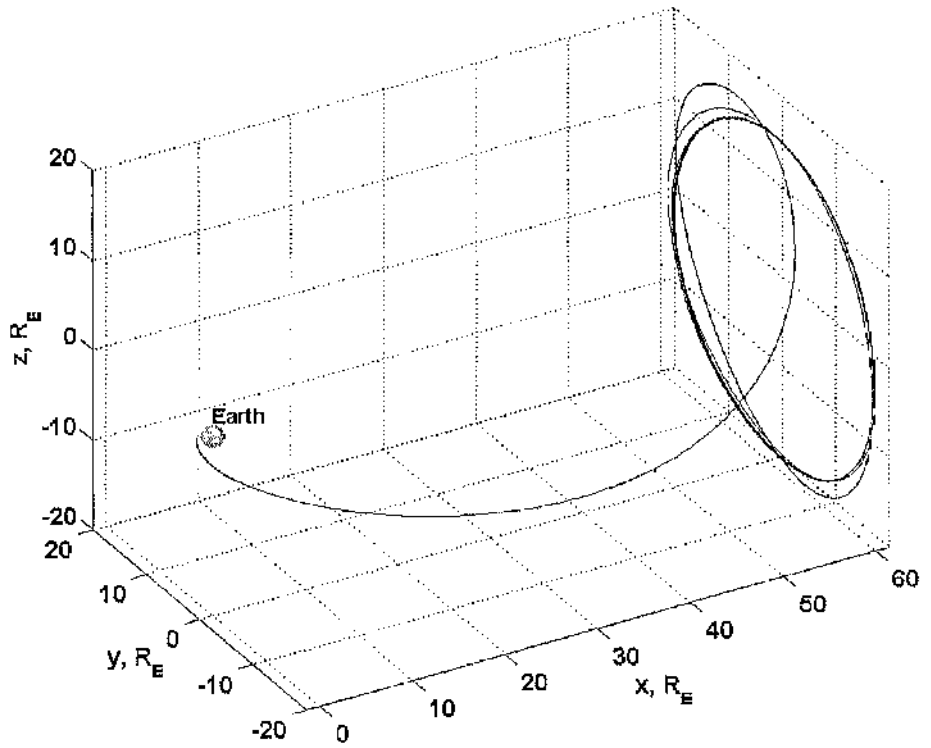


Figure 3-20 Circular Earth displaced orbit achieved using sail pitch and yaw angle control

$$\rho_0 = 20 L, z_0 = 60 L, Q = 100 (I_{4 \times 4}) N = 1 \times 10^4$$

$$G = [0.2302098 \ 0.81155271 \ 43.426737 \ 304.96421]$$

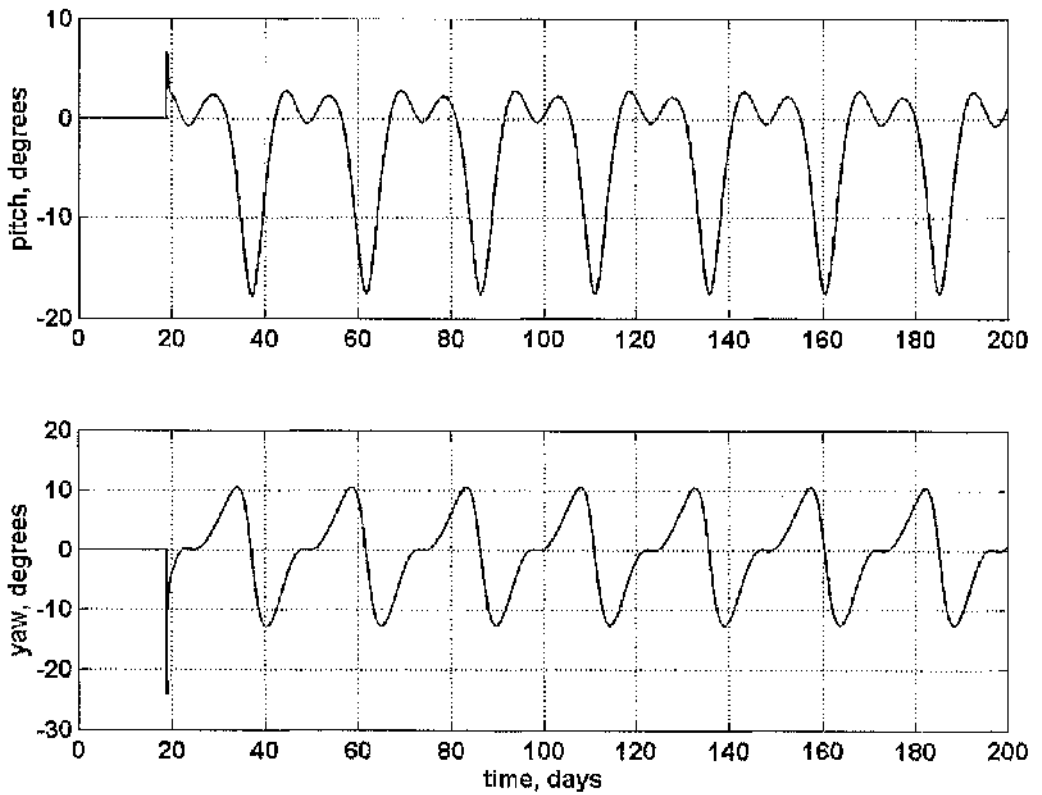


Figure 3-21 Pitch and yaw angle variation required to control orbit

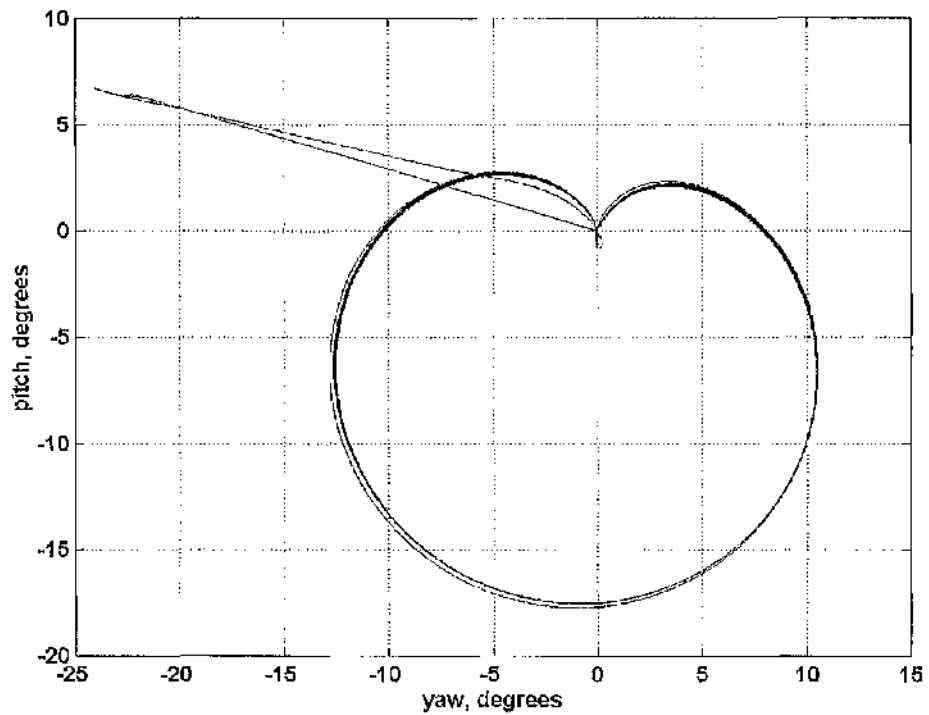


Figure 3-22 Yaw against pitch angle representing motion of the solar sail normal

The solar sail requires a continuous acceleration of 2.3968 mms^{-2} during the control phase. The gradient of payload mass against sail area is 1.2528×10^3 . A payload mass of 10 kg could be controlled using a $12,528 \text{ m}^2$ sail. This represents an 800 m^2 sail area reduction compared to that required using the area variation controller. A larger 500 kg payload could be controlled using a $6.2641 \times 10^5 \text{ m}^2$ sail, which represents an area reduction of $40,000 \text{ m}^2$. In this case, use of a pitch angle controller greatly reduces the required sail area for larger payloads.

3.4 Non-Keplerian orbit dynamics far from the central-body

3.4.1 Linear solution to Hill's approximation

Periodic orbits around the natural and artificial Lagrange points can be generated by selecting initial conditions which suppress divergent modes. In order to identify periodic solutions, Hill's equations are linearised at the desired Lagrange point (x_o, y_o, z_o) using new coordinates $x = x_o + \delta x$, $y = y_o + \delta y$ and $z = z_o + \delta z$. The ballistic Lagrange points lead to initial conditions $x_o = \pm(1/3)^{1/3}$, $y_o=0$ and $z_o=0$. Using Taylor's theorem, the linearised Hill's equations have the form

$$\ddot{x} - 2\dot{y} = \left[\frac{\partial f_x}{\partial x} \right]_o \delta x + \left[\frac{\partial f_x}{\partial y} \right]_o \delta y + \left[\frac{\partial f_x}{\partial z} \right]_o \delta z \quad (3.29.1)$$

$$\dot{y} + 2\dot{x} = \left[\frac{\partial f_y}{\partial x} \right]_o \delta x + \left[\frac{\partial f_y}{\partial y} \right]_o \delta y + \left[\frac{\partial f_y}{\partial z} \right]_o \delta z \quad (3.29.2)$$

$$\ddot{z} = \left[\frac{\partial f_z}{\partial x} \right]_o \delta x + \left[\frac{\partial f_z}{\partial y} \right]_o \delta y + \left[\frac{\partial f_z}{\partial z} \right]_o \delta z \quad (3.29.3)$$

where the partial derivatives are evaluated at the nominal conditions (indicated by the subscript 'o'). The functions $f_x = -x/|\mathbf{r}|^3 + 3x$, $f_y = -y/|\mathbf{r}|^3$ and $f_z = -z/|\mathbf{r}|^3 - z$ and the partial derivatives can be obtained as

$$\begin{aligned} f_{xx} &= \frac{3x^2}{|\mathbf{r}|^5} - \frac{1}{|\mathbf{r}|^3} + 3 & f_{yy} &= \frac{3xy}{|\mathbf{r}|^5} = f_{yx} & f_{xz} &= \frac{3xz}{|\mathbf{r}|^5} = f_{zx} \\ f_{yy} &= \frac{3y^2}{|\mathbf{r}|^5} - \frac{1}{|\mathbf{r}|^3} & f_{yz} &= \frac{3yz}{|\mathbf{r}|^5} = f_{zy} & f_{zz} &= \frac{3z^2}{|\mathbf{r}|^5} - \frac{1}{|\mathbf{r}|^3} - 1 \end{aligned} \quad (3.30)$$

Evaluating these at the classical Lagrange point yields $f_{xx} = 9$, $f_{yy} = -3$, $f_{zz} = -4$ and $f_{xy} = f_{yz} = f_{xz} = 0$.

The eigenvalues of the linearised Hill's equations can be determined by forming a state-space equation with the form $\dot{\mathbf{x}} = A\mathbf{x}$, where A is the linear coefficient matrix and the state vector $\mathbf{x} = [\delta x \quad \delta y \quad \delta z \quad \delta \dot{x} \quad \delta \dot{y} \quad \delta \dot{z}]^T$. The linear coefficient matrix $A = \begin{bmatrix} \bar{0} & I \\ U & \Omega \end{bmatrix}$ which contains four 3x3 sub-matrices

$$\begin{aligned} \bar{0} &= \begin{bmatrix} 0 & 0 & 0 \\ 0 & 0 & 0 \\ 0 & 0 & 0 \end{bmatrix} & I &= \begin{bmatrix} 1 & 0 & 0 \\ 0 & 1 & 0 \\ 0 & 0 & 1 \end{bmatrix} \\ U &= \begin{bmatrix} f_{xx} & f_{xy} & f_{xz} \\ f_{yx} & f_{yy} & f_{yz} \\ f_{zx} & f_{zy} & f_{zz} \end{bmatrix} & \Omega &= \begin{bmatrix} 0 & 2 & 0 \\ -2 & 0 & 0 \\ 0 & 0 & 0 \end{bmatrix} \end{aligned} \quad (3.31)$$

The 6 eigenvalues, λ_n , and corresponding eigenvectors can be extracted from the matrix to obtain a set of solutions

$$\begin{aligned} x &= \sum_{n=1}^6 \alpha_n \xi_n \exp(\lambda_n t) & \dot{x} &= \sum_{n=1}^6 \alpha_n \xi_n \lambda_n \exp(\lambda_n t) \\ y &= \sum_{n=1}^6 \alpha_n \eta_n \exp(\lambda_n t) & \dot{y} &= \sum_{n=1}^6 \alpha_n \eta_n \lambda_n \exp(\lambda_n t) \\ z &= \sum_{n=1}^6 \alpha_n \zeta_n \exp(\lambda_n t) & \dot{z} &= \sum_{n=1}^6 \alpha_n \zeta_n \lambda_n \exp(\lambda_n t) \end{aligned} \quad (3.32)$$

where ξ, η and ζ represent the eigenvectors and α_n are constants determined from the initial conditions.

It is apparent from the linear coefficient matrix that z is linearly independent of x and y . The four in-plane (x - y plane) eigenvalues can be determined from the characteristic equation

$$\lambda^2 = \frac{1}{2} \left((-4 + f_{xx} + f_{yy}) \pm \sqrt{(4 - f_{xx} - f_{yy})^2 - 4(f_{xx}f_{yy} - f_{xy}^2)} \right) \quad (3.33)$$

Substituting the values for f_{xx} , f_{yy} and f_{xy} into Eq (3.33) leads to the expression $\lambda^2 = (1 \pm 2\sqrt{7})$. This yields two real eigenvalues, $\lambda_{1,2} = \pm\sqrt{1+2\sqrt{7}}$ and two imaginary eigenvalues $\lambda_{3,4} = \pm\sqrt{1-2\sqrt{7}}$. The eigenvalues of the independent variable z , can be determined as $\lambda^2 = f_{zz}$. Substituting the value of f_{zz} obtains two imaginary eigenvalues, $\lambda_{5,6} = \pm i2$.

Consider only the dependant variables, x and y . The eigenvectors $v = [v_1 \ v_2 \ v_3 \ v_4]^T$, can be evaluated for each eigenvalue by forming the matrix $(\lambda I - A)v = 0$, ignoring the z and \dot{z} rows as

$$\begin{bmatrix} \lambda & 0 & -1 & 0 \\ 0 & \lambda & 0 & -1 \\ -9 & 0 & \lambda & -2 \\ 0 & 3 & 2 & \lambda \end{bmatrix} \begin{bmatrix} v_1 \\ v_2 \\ v_3 \\ v_4 \end{bmatrix} = 0 \quad (3.34)$$

Evaluating the rows for each eigenvalue obtains $v_3 = \lambda v_1$, $v_4 = \lambda v_2$, $v_1 = -\frac{(\lambda^2 + 3)}{2\lambda} v_2$.

The eigenvectors for the independant variable can be evaluated by forming a 2x2 determinant from the rows of matrix A which contain z and \dot{z} as

$$\begin{bmatrix} \lambda & -1 \\ -f_{zz} & \lambda \end{bmatrix} \begin{bmatrix} e_1 \\ e_2 \end{bmatrix} = 0 \quad (3.35)$$

where the eigenvectors here are represented as $e = [e_1 \ e_2]^T$. Evaluating the rows leads to the expression $e_2 = \lambda e_1$. It is convenient to select $e_1=1$ which yields $e_2 = \lambda_{5,6}$.

Selecting an arbitrary value of $v_2=1$, the values of $v_1 = \mp 0.3117171i$ corresponding to eigenvalues $\lambda_{3,4} = \pm 3.33142637 \times 10^{-4}i$. For a periodic orbit, the positive real exponents must be suppressed to prevent asymptotic escape. This can be achieved by setting constants $\alpha_1 = \alpha_2 = 0$. The solutions for x , y and z have the form

$$x = -\alpha_3 i \bar{v} \exp(i\lambda_{xy}t) + \alpha_4 i \bar{v} \exp(-i\lambda_{xy}t) \quad (3.36.1)$$

$$y = \alpha_3 \exp(i\lambda_{xy}t) + \alpha_4 \exp(-i\lambda_{xy}t) \quad (3.36.2)$$

$$z = \alpha_5 \exp(i\lambda_z t) + \alpha_6 \exp(-i\lambda_z t) \quad (3.36.3)$$

where $\bar{v} \equiv \text{Im}\{\nu_1\}$, $\lambda_{xy} = \text{Im}\{\lambda_{3,4}\}$ and $\lambda_z = \text{Im}\{\lambda_{5,6}\}$. Setting the constants $\alpha_3 = \alpha_4 = A_y$ and $\alpha_5 = \alpha_6 = A_z$ these expressions can be re-written in trigonometric terms using $\exp(i\theta) = \cos\theta + i\sin\theta$ as

$$x = -A_y \bar{v} (i \cos(\lambda_{xy}t) - \sin(\lambda_{xy}t)) + A_y \bar{v} (i \cos(\lambda_{xy}t) + \sin(\lambda_{xy}t)) \quad (3.37.1)$$

$$y = A_y (\cos(\lambda_{xy}t) + i \sin(\lambda_{xy}t)) + A_y (\cos(\lambda_{xy}t) - i \sin(\lambda_{xy}t)) \quad (3.37.2)$$

$$z = A_z (\cos(\lambda_z t) + i \sin(\lambda_z t)) + A_z (\cos(\lambda_z t) - i \sin(\lambda_z t)) \quad (3.37.3)$$

The expressions can be reduced to $x = A_y \bar{v} \sin(\lambda_{xy}t)$, $y = A_y \cos(\lambda_{xy}t)$ and $z = A_z \cos(\lambda_z t + \varphi)$ where φ represents the phase change of z . For a circular orbit in the y - z plane, it is required that z is $\pi/2$ out of phase with y . This leads to the following initial conditions $x = 0$, $\dot{x} = A_y \bar{v} \lambda_{xy}$, $y = A_y$, $\dot{y} = 0$, $z = 0$ and $\dot{z} = A_z \lambda_z$ [Cielaszyk and Wie, 1996].

Figure 3-23 shows the quasi-periodic trajectory evaluated using the linear solution of Hill's equations. This trajectory is a result of the in-plane and out of plane frequency ratio, λ_{xy}/λ_z , being non-rational [Howell and Pernicka, 1993; Cobos and Masdemont, 2002; Roberts, 2004].

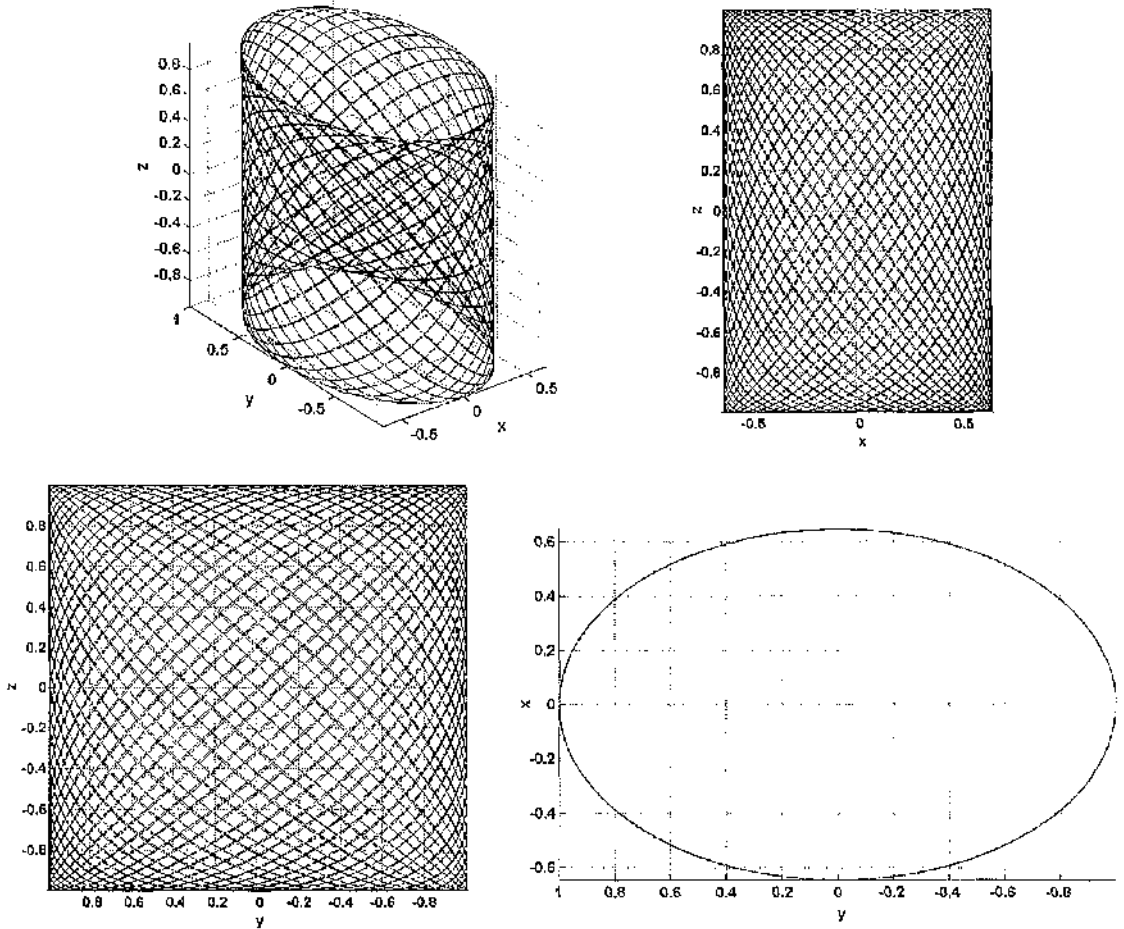


Figure 3-23 Quasi-periodic Lissajous trajectory

3.4.2 Lissajous orbits using Hill's equations

Due to the orbit instability, escape still occurs from the Lissajous orbit during numerical integration. Figure 3-24 shows a Lissajous orbit around the L_2 point with y -axis amplitude $A_y=5 R_H$. This orbit is generated by numerically integrating the linearised Hill's equations, provided in Eq (3.29). Escape occurs in the anti-Sun direction after $4.5T$, where the orbit period $T= 175.87$ days.

Figure 3-25 shows a series of Lissajous orbits around L_2 computed using numerical integration of the nonlinear Hill's equations, provided in Eqns (3.10). The initial conditions for each orbit are provided in Table 3-4.

The initial conditions in Table 3-4 are determined using the linear solution, provided in Eq (3.37), evaluated at time $t=0$. Comparing the trajectory computed using the linearised Hill's equations, Fig 3-24, to those computed using the non-linear Hill's equations,

Fig 3-25, it is clear that divergence from the nominal orbit occurs much sooner for the latter case. This is due to the presence of nonlinear terms which are ignored in the linear solution.

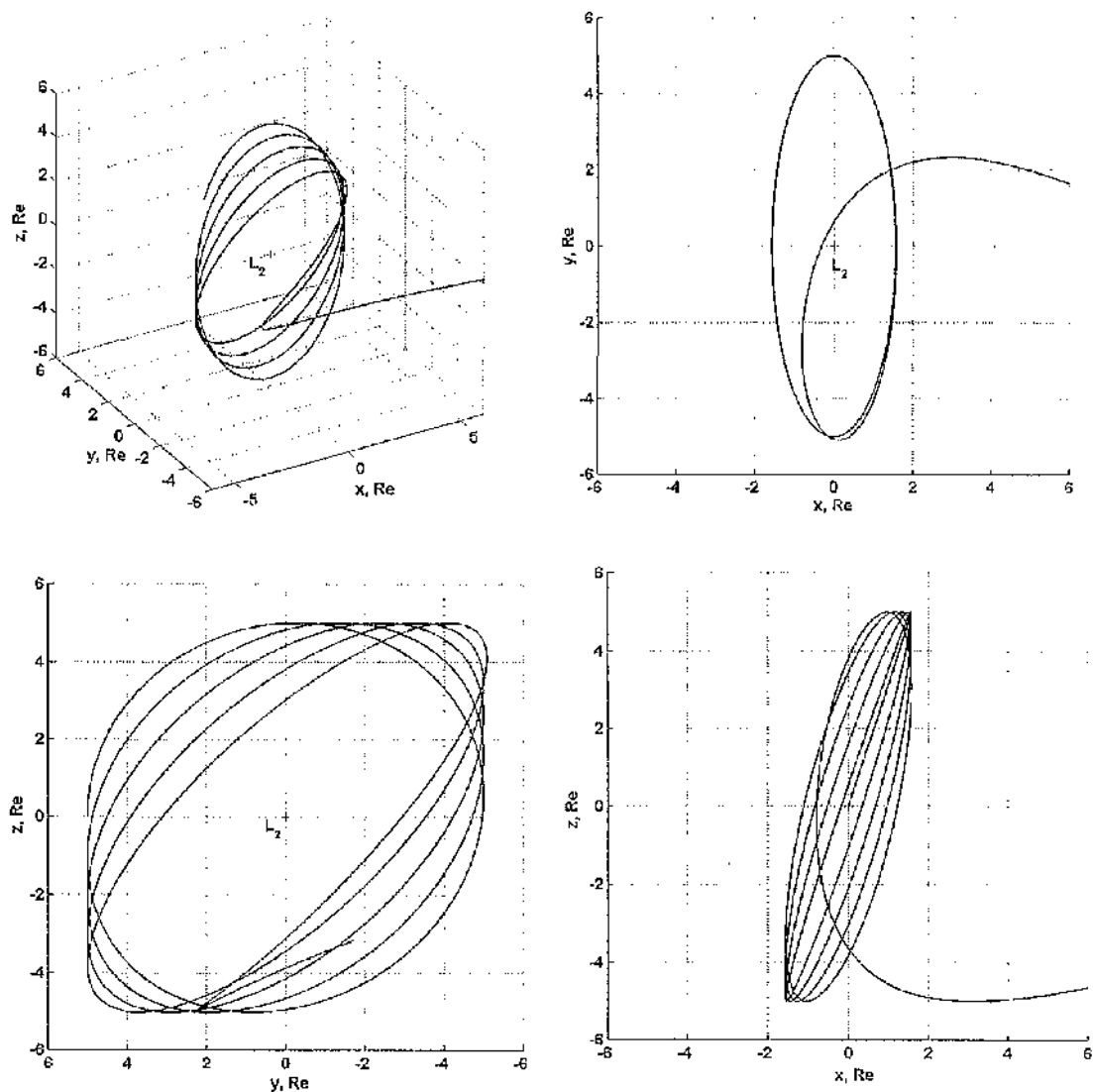


Figure 3-24 Lissajous trajectory generated by integrating linearised Hills equations about L_2

Orbit	A_y	A_z	\dot{x}_0	\dot{z}_0
1	1 Re	1 Re	1.0384625×10^{-4}	3.2162924×10^{-4}
2	2 Re	2 Re	2.0769250×10^{-4}	6.4325848×10^{-4}
3	3 Re	3 Re	3.1153875×10^{-4}	9.6488772×10^{-4}
4	4 Re	4 Re	4.1538501×10^{-4}	1.2865170×10^{-3}
5	5 Re	5 Re	5.1923126×10^{-4}	1.6081462×10^{-3}

Table 3-4 Lissajous trajectory initial conditions for contours 1-5

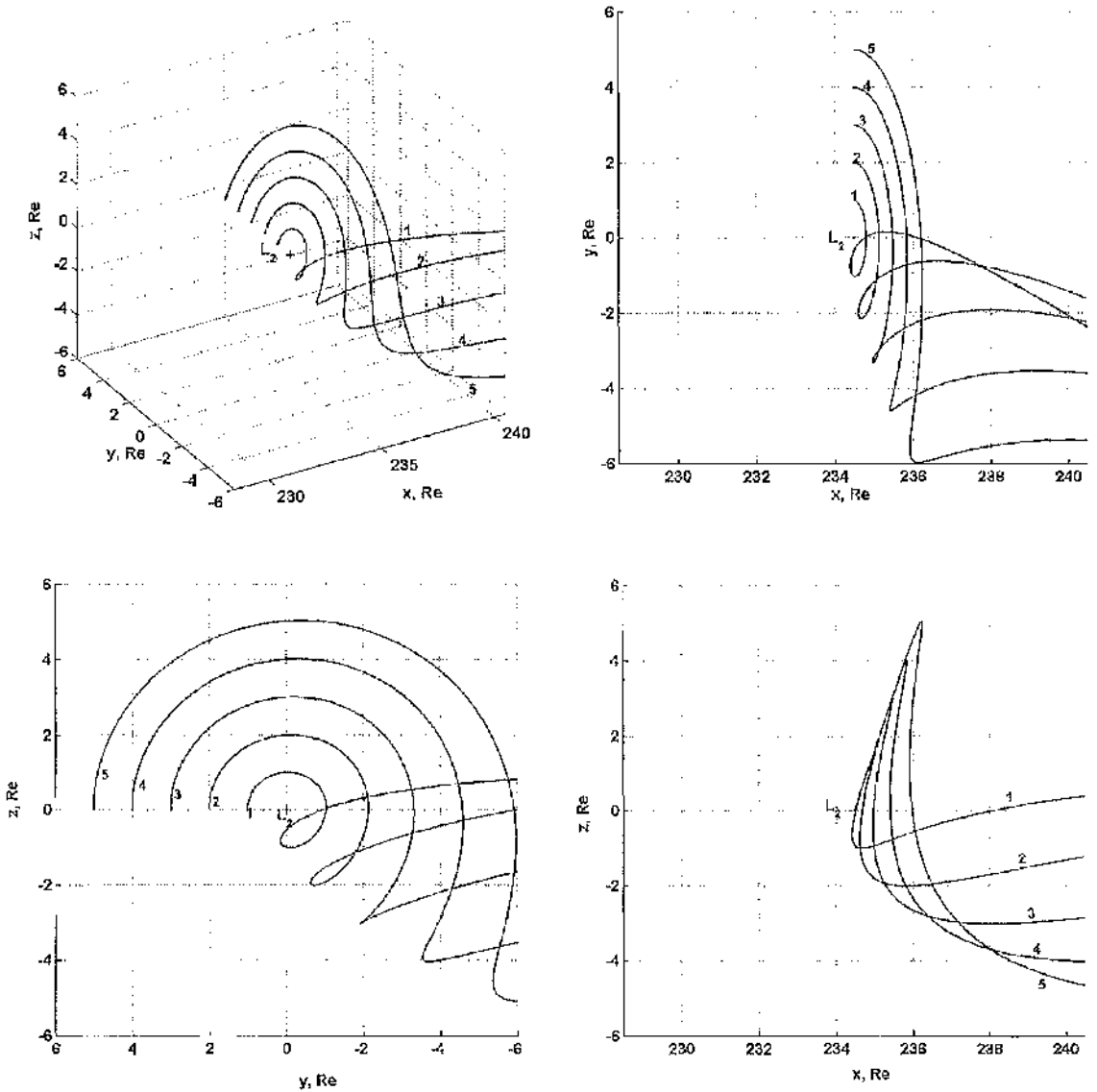


Figure 3-25 Lissajous trajectories around L_2 for A_y amplitude equal to orbit number

Using an iterative method, the \dot{x}_o component can be corrected using $\dot{\tilde{x}}_o = \dot{x}_o + \delta\dot{x}$ to improve the precision of the initial conditions which converges the trajectory towards the nominal Lissajous orbit. For an orbit around the L_2 point with y -axis amplitude, $A_y=20 R_E$, the correction factor $\delta\dot{x}=4.914954741 \times 10^{-4}$ is applied improving precision to order 1×10^{-13} . The corrected initial conditions lead to the improved orbit shown in Fig 3-26. Escape occurs after 4 orbit periods where $T=175$ days. Increasing the convergence accuracy for the solar sail trajectory reduces the amount of station-keeping required to control the orbit.

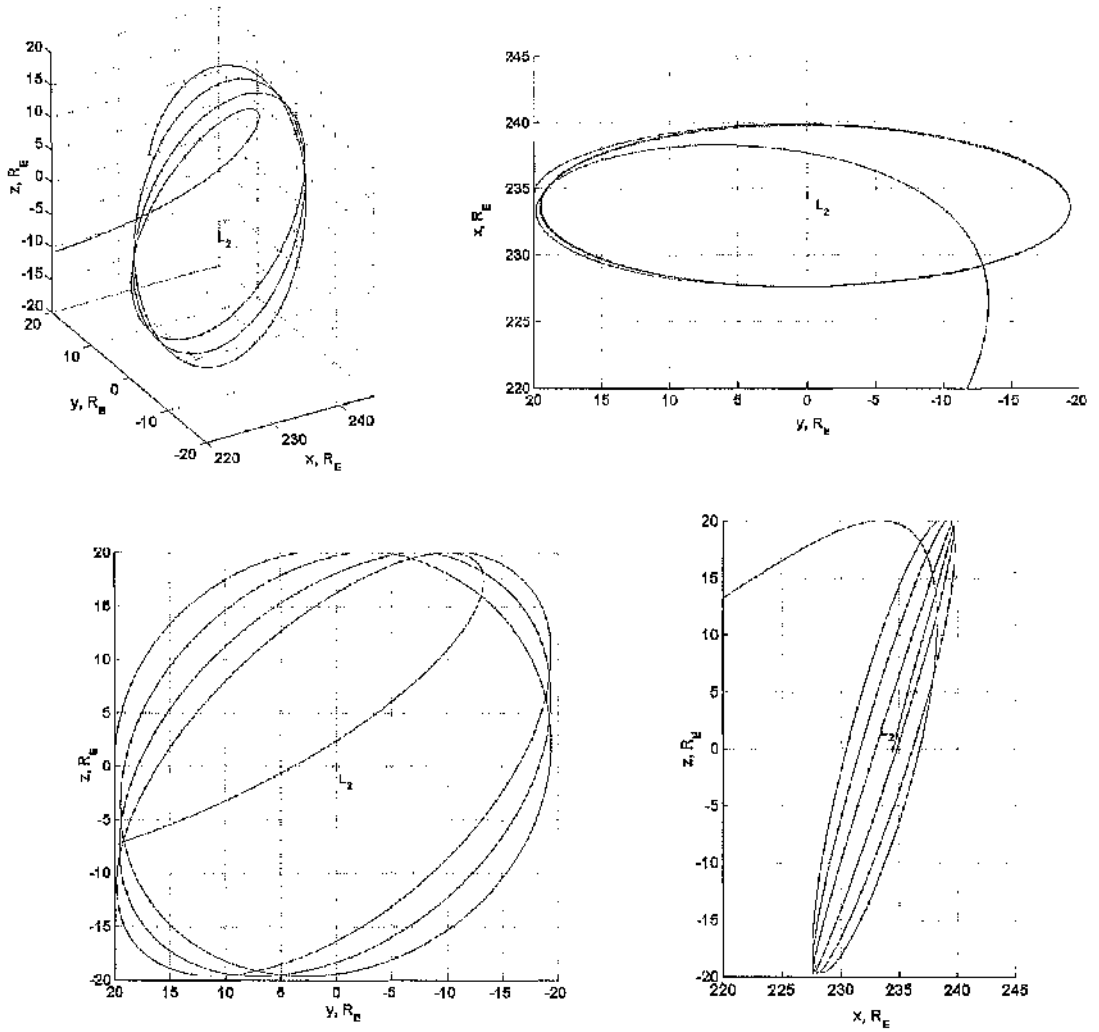


Figure 3-26 Lissajous trajectory around L_2 computed using corrected initial conditions

3.4.3 Optimal controller for Lissajous orbits

3.4.3.1 Solar sail area control

An optimal controller can be developed using Hill's equations linearised at the libration point. As stated in Section 3.4.1, the linear coefficient matrix $A = \begin{bmatrix} \bar{0} & \mathbf{I} \\ \mathbf{U} & \mathbf{\Omega} \end{bmatrix}$, where the sub-matrices are defined in Eq (3.31). The control matrix is developed using the partial derivatives of Eqns (3.27) with respect to the acceleration $\kappa(t)$ where

$$\frac{\partial \kappa_x}{\partial \kappa(t)} = \cos^3 \alpha \cos^3 \phi \tag{3.38.1}$$

$$\frac{\partial \kappa_y}{\partial \kappa(t)} = \cos^3 \alpha \cos^2 \phi \sin \phi \quad (3.38.2)$$

$$\frac{\partial \kappa_z}{\partial \kappa(t)} = \cos^2 \alpha \cos^2 \phi \sin \alpha \quad (3.38.3)$$

For area variation control, the control matrix has the form

$$B = \begin{bmatrix} 0 & 0 & 0 & \frac{\partial \kappa_x}{\partial \kappa(t)} & \frac{\partial \kappa_y}{\partial \kappa(t)} & \frac{\partial \kappa_z}{\partial \kappa(t)} \end{bmatrix}^T \quad (3.39)$$

Evaluating the partial derivatives at the nominal orbit conditions, $\alpha=0$ and $\phi=0$, obtains the control matrix $B = [0 \ 0 \ 0 \ 1 \ 0 \ 0]^T$. The output matrix C is a 6x6 identity matrix $I_{6 \times 6}$.

Using the optimal control laws developed in Section 2.4, a gain matrix can be derived using the state-weighting matrix Q and the control-weighting matrix, N . The solution leads to a 6 element gain matrix which can be used to determine the required acceleration variation

$$\delta \kappa_x = G_1 \delta \xi + G_2 \delta \eta + G_3 \delta \zeta + G_4 \delta \dot{\xi} + G_5 \delta \dot{\eta} + G_6 \delta \dot{\zeta} \quad (3.40)$$

where the difference between the desired and actual position is calculated using

$$\delta \xi = \xi - A_y v \sin(\lambda_{xy} \tau) \quad (3.41.1)$$

$$\delta \eta = \eta - A_y \cos(\lambda_{xy} \tau) \quad (3.41.2)$$

$$\delta \zeta = \zeta - A_y \sin(\lambda_z \tau) \quad (3.41.3)$$

$$\delta \dot{\xi} = \dot{\xi} - A_y v \lambda_{xy} \cos(\lambda_{xy} \tau) \quad (3.41.4)$$

$$\delta \dot{\eta} = \dot{\eta} + A_y \lambda_{xy} \sin(\lambda_{xy} \tau) \quad (3.41.5)$$

$$\delta \dot{\zeta} = \dot{\zeta} - A_y \lambda_z \cos(\lambda_z \tau) \quad (3.41.6)$$

Selecting suitable values for the state and control weighting matrices minimizes the magnitude of $\delta \kappa$.

3.4.3.2 Solar sail pitch and yaw control

A similar design can be used to develop a pitch and yaw angle controller by linearising Hill's equations at the libration point. The linear coefficient matrix has the same form as the area variation case. The control matrix has the form

$$B = \begin{bmatrix} 0 & 0 & 0 & \frac{\partial \kappa_x}{\partial \alpha} & \frac{\partial \kappa_y}{\partial \alpha} & \frac{\partial \kappa_z}{\partial \alpha} \\ 0 & 0 & 0 & \frac{\partial \kappa_x}{\partial \phi} & \frac{\partial \kappa_y}{\partial \phi} & \frac{\partial \kappa_z}{\partial \phi} \end{bmatrix}^T \quad (3.42)$$

where the partial derivatives of Eqns (3.27), with respect to sail pitch and yaw angle, are expressed as

$$\frac{\partial \kappa_x}{\partial \alpha} = -3\kappa(t) \cos^2 \alpha \sin \alpha \cos^3 \phi \quad (3.43.1)$$

$$\frac{\partial \kappa_y}{\partial \alpha} = -3\kappa(t) \cos^2 \alpha \sin \alpha \cos^2 \phi \sin \phi \quad (3.43.2)$$

$$\frac{\partial \kappa_z}{\partial \alpha} = \kappa(t) \cos^3 \alpha \cos^2 \phi (1 - 2 \tan^2 \alpha) \quad (3.43.3)$$

$$\frac{\partial \kappa_x}{\partial \phi} = -3\kappa(t) \cos^3 \alpha \cos^2 \phi \sin \phi \quad (3.43.4)$$

$$\frac{\partial \kappa_y}{\partial \phi} = \kappa(t) \cos^3 \phi \cos^3 \alpha (1 - 2 \tan^2 \phi) \quad (3.43.5)$$

$$\frac{\partial \kappa_z}{\partial \phi} = -2\kappa(t) \cos^2 \alpha \sin \alpha \cos \phi \sin \phi \quad (3.43.6)$$

Evaluating at the nominal orbit conditions $\kappa(0) \equiv \kappa_o$, $\alpha=0$ and $\phi=0$, obtains the control matrix

$$B = \begin{bmatrix} 0 & 0 & 0 & 0 & 0 & \kappa_o \\ 0 & 0 & 0 & 0 & \kappa_o & 0 \end{bmatrix}^T \quad (3.42)$$

This control matrix produces a 6x2 gain matrix. The pitch angle variation required to control the orbit is determined using

$$\delta\alpha = G_{11}\delta\dot{\zeta} + G_{12}\delta\dot{\eta} + G_{13}\delta\dot{\zeta} + G_{14}\delta\dot{\zeta} + G_{15}\delta\dot{\eta} + G_{16}\delta\dot{\zeta} \quad (3.43.1)$$

and the yaw angle variation using

$$\delta\phi = G_{21}\delta\dot{\zeta} + G_{22}\delta\dot{\eta} + G_{23}\delta\dot{\zeta} + G_{24}\delta\dot{\zeta} + G_{25}\delta\dot{\eta} + G_{26}\delta\dot{\zeta} \quad (3.43.2)$$

where gain element G_{ij} refers to value located at the j^{th} column of the i^{th} row in the gain matrix. The difference between the actual and desired position is provided in Eqns (3.41).

3.4.4 Lissajous orbit control near L_1 and L_2

Both optimal controllers developed in the previous section will be demonstrated for control of a Lissajous orbit near the natural Lagrange points. This control method offers a near-term application for solar sails as the required sail area is much smaller than cases examined for circular displaced orbits. Current technology could provide the necessary acceleration to enable orbit control near the L_1 and L_2 points [Farquhar, 1970b; Bookless and McInnes, 2005].

3.4.4.1 Solar sail control near L_2

Selecting appropriate gains, solar sail control techniques can be applied to control an orbit near L_2 . An insertion manifold was selected with a closest Earth approach of 19.1 R_E . The zero velocity surface which bounds the orbit is provided in Fig 3.27 with Jacobi constant $C=-0.0131$. After delivery to the insertion manifold, the solar sail is deployed and it winds onto the nominal orbit within 91 days. The nominal orbit is located at $x_0=230 R_E$ with y -axis amplitude $A_y=20 R_E$. The solar sail controller is activated upon approach to the nominal orbit at $x > 0.99x_0$. The nominal acceleration required to generate this libration point is $\kappa_0=0.00831 \text{ mms}^{-2}$.

Figure 3-28 shows the insertion to the orbit via the stable manifold and control for a period of 15 years. An enlarged view of the Lissajous orbit around the libration point at $x_0=230 R_E$ is provided in Fig 3-29. The acceleration and corresponding area variation required to control this orbit for a 200 kg total payload and sail mass is provided in Fig 3-30.

The acceleration varies between 0.00682 mms^{-2} and 0.0114 mms^{-2} , which corresponds to an area variation between 152 m^2 and 254 m^2 for a 200 kg total mass. For solar sail loading parameter $\sigma=12 \text{ gm}^{-2}$, the sail mass is approximately 3 kg enabling a 197 kg payload to be controlled at this Lissajous orbit.

The gradient of payload mass against sail surface area is 1.2917 for loading $\sigma=12 \text{ gm}^{-2}$. A relatively small payload of 100 kg could be controlled using a 129 m^2 solar sail or a large 2000 kg payload could be controlled with a 2583 m^2 sail. Area variation could be achieved using four reflective tip-vanes attached to the payload.

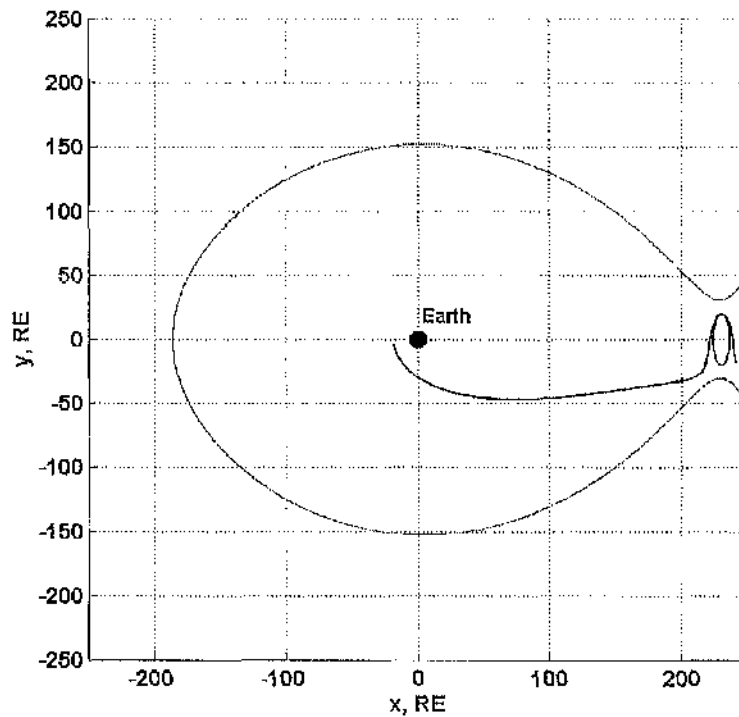


Figure 3-27 Hill's surface bounding insertion conditions to Lissajous orbit near L_2

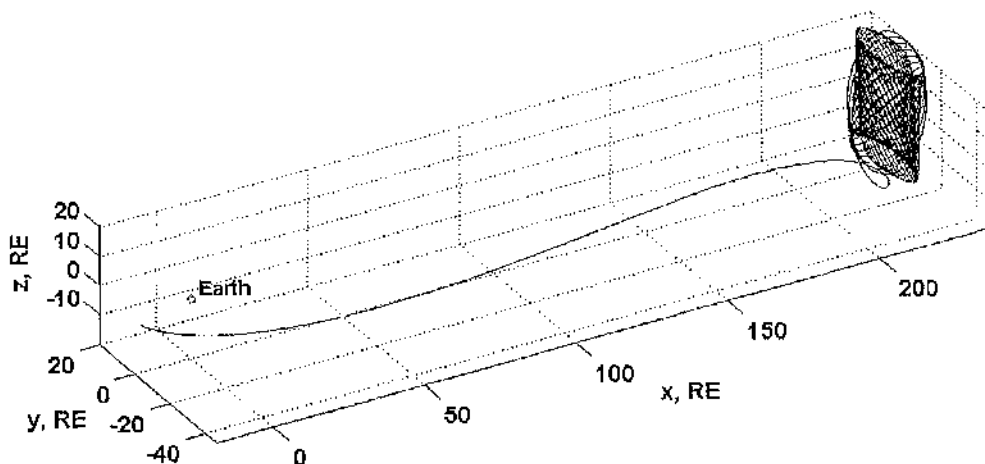


Figure 3-28 Insertion to Lissajous orbit around $x_0=230 R_E$ controlled using sail area variation

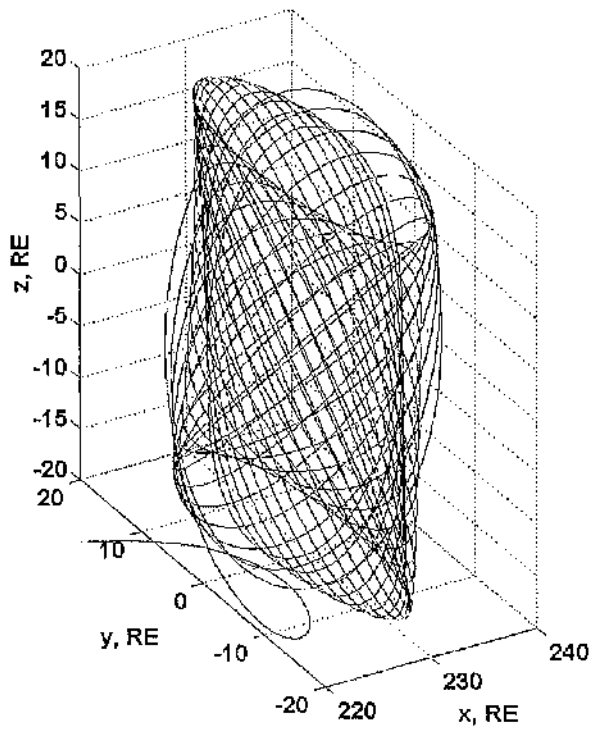


Figure 3-29 Enlarged view of Lissajous orbit around $x_0=230 R_E$

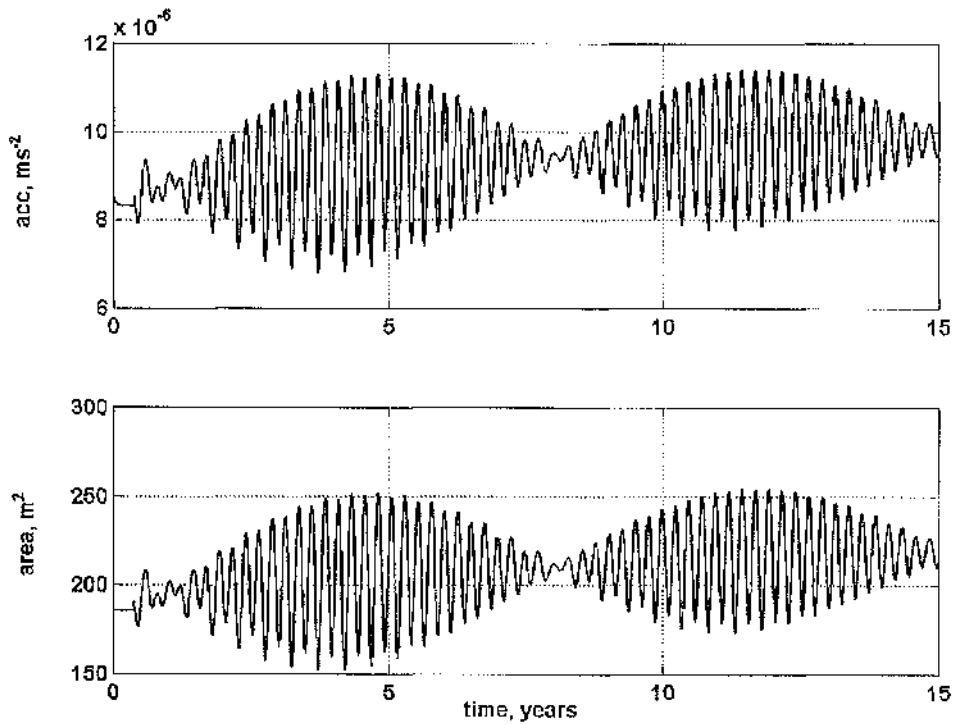


Figure 3-30 Acceleration and area variation required to control Lissajous orbit

Gains: $G_1=4.839 \times 10^{-7}$ $G_2=-8.630 \times 10^{-8}$ $G_3=1.485 \times 10^{-15}$ $G_4=8.295 \times 10^{-4}$ $G_5=4.394 \times 10^{-4}$ $G_6=-4.048 \times 10^{-12}$

Solar sail pitch and yaw angle variation can also be used to control a Lissajous orbit around the libration point. Using the same insertion manifold, the optimal controller is activated upon arrival at the nominal orbit. When the controller is activated the sail is fully deployed to provide an acceleration of $1.05\kappa_0$. The increase in nominal acceleration is required to prevent the solar sail escaping towards the Earth as pitching the sail reduces the acceleration component directed along the x -axis. Figure 3-31 shows the orbit insertion and control for 15 years duration. An enlarged view of this orbit is provided in Fig 3-32.

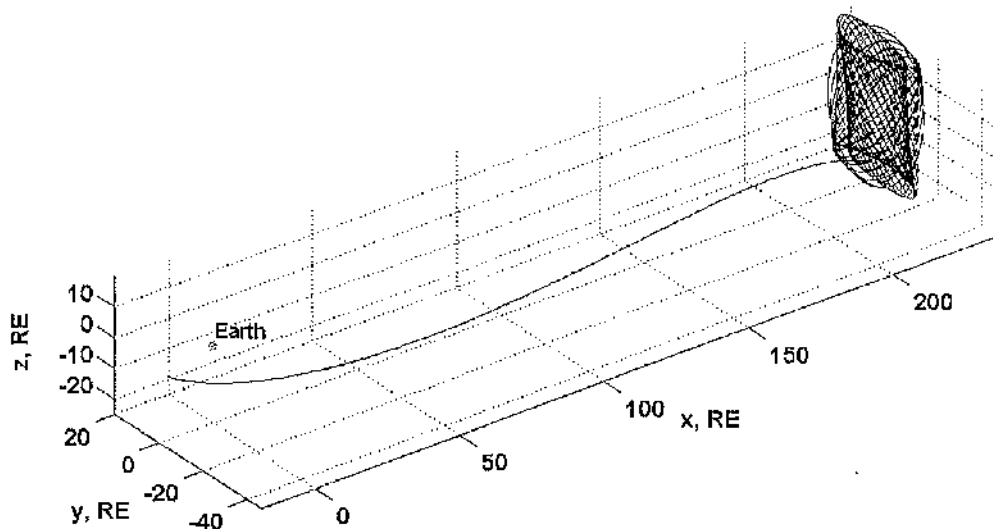


Figure 3-31 Insertion to Lissajous orbit around $x_0=230R_E$ controlled using pitch and yaw angle variation

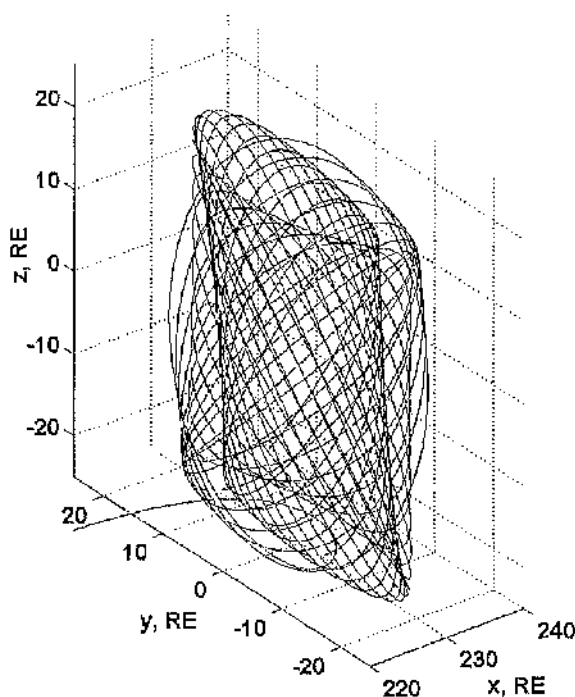


Figure 3-32 Enlarged view of Lissajous orbit around $x_0=230R_E$

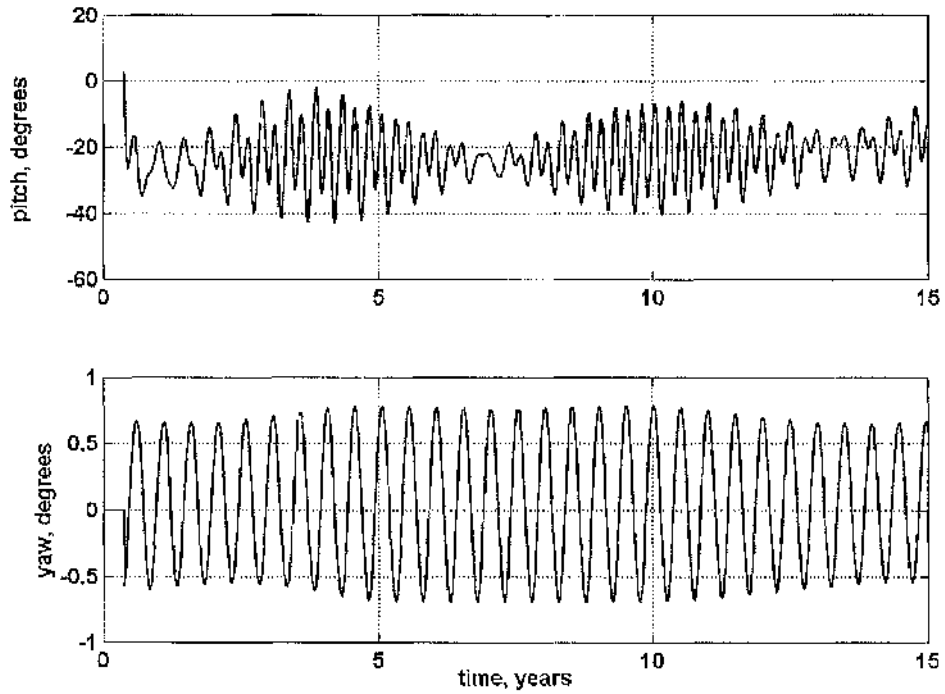


Figure 3-33 Pitch and Yaw angle variation required to control Lissajous orbit

$$\text{Gain } \phi: G_1 = -5.157 \times 10^{-14} \quad G_2 = 9.628 \times 10^{-15} \quad G_3 = 1.568 \times 10^{-6} \quad G_4 = -8.788 \times 10^{-11} \quad G_5 = -4.631 \times 10^{-11} \quad G_6 = 1.7564$$

$$\text{Gain } \alpha: G_1 = 0.9103 \quad G_2 = -0.1618 \quad G_3 = 4.032 \times 10^{-14} \quad G_4 = 1560.8995 \quad G_5 = 818.3383 \quad G_6 = -4.631 \times 10^{-11}$$

Figure 3-33 shows the pitch and yaw angle variation required to control the orbit around the artificial libration point. The pitch angle varies between -42.9° and 2.9° . The yaw angle varies between -0.69° and 0.78° . For a 200 kg total sail and payload mass, the constant area of this sail is 222 m^2 . The required sail area is approximately 30 m^2 less than that required for sail area variation control. The gradient of payload mass against sail area is 1.1268. An angle variation controller slightly reduces the required sail area by 13% compared to the area variation controller.

3.4.4.2 Solar sail control near L_1

Insertion to an orbit sunward of L_1 can also be achieved. Direct insertion of a deployed sail is demonstrated which requires an increased Δv compared to a ballistic insertion to L_1 . A Lissajous orbit is generated around the artificial libration point $x_0 = -240 R_E$ with y -axis amplitude $A_y = 20 R_E$. The nominal acceleration required to generate the artificial libration point $\kappa_0 = 0.0141 \text{ mms}^{-1}$.

A stable manifold which winds onto the desired orbit is identified by perturbing the \dot{x}_0 value slightly so the solar sail escapes from the nominal orbit in the anti-Sun direction. The zero-velocity surface bounding this orbit is shown in Fig 3-34, with Jacobi constant $C=-0.01205$. The Hill's surface is open on the anti-Sun side of the Earth at this energy. As the libration point position is moved sunward, the energy required for insertion to a Lissajous orbit increases, resulting in a larger gap in the zero-velocity surface on the anti-Sun side of the Earth. It becomes increasingly difficult to identify manifolds which pass near to the Earth as the larger gap in the zero-velocity surface allows escape from the capture region into the exterior region.

Using the stable manifold, the solar sail arrives at the nominal orbit within 320 days. Figure 3-35 shows the insertion and control of a solar sail at the Lissajous orbit for 15 years duration. An enlarged view of the Lissajous orbit is provided in Fig 3-36. Figure 3-37 shows the acceleration variation and corresponding area variation for a 200 kg total sail and payload mass.

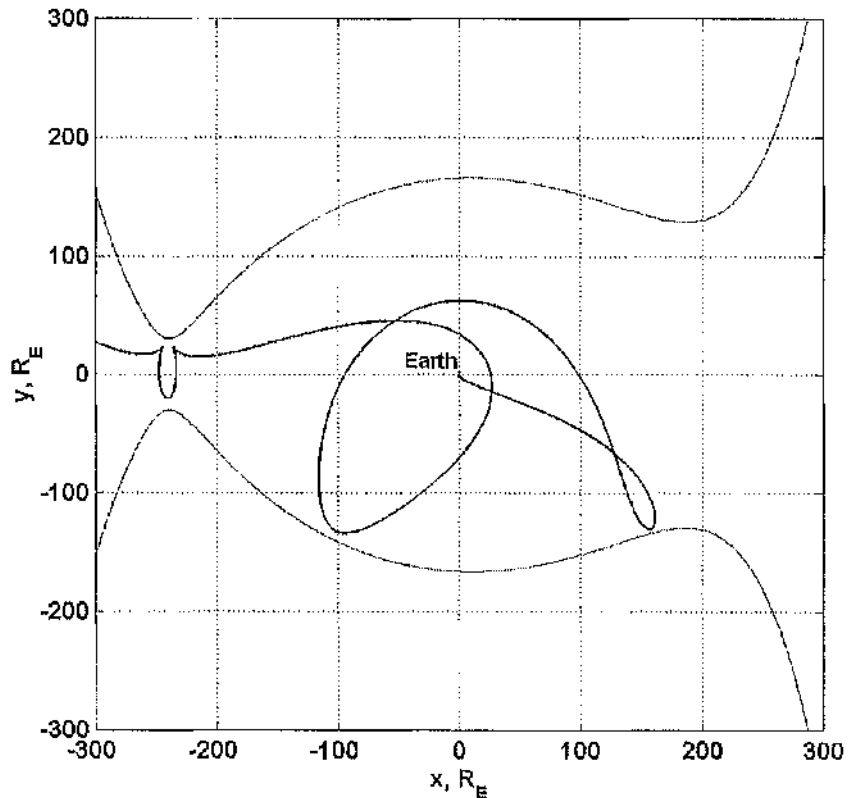


Figure 3-34 Hill's surface bounding insertion conditions to Lissajous orbit near L_1

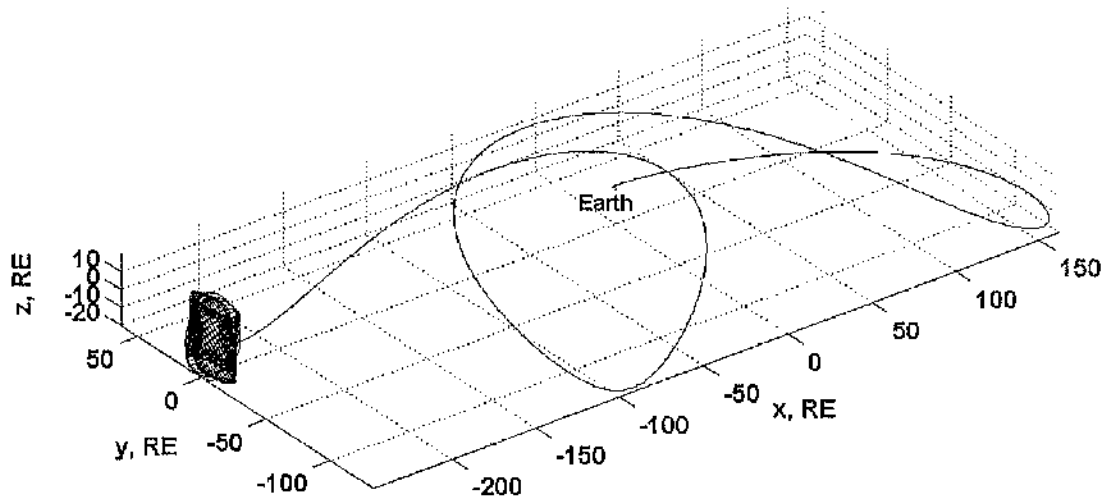


Figure 3-35 Insertion to Lissajous orbit around $x_0 = -240 R_E$ controlled using sail area variation

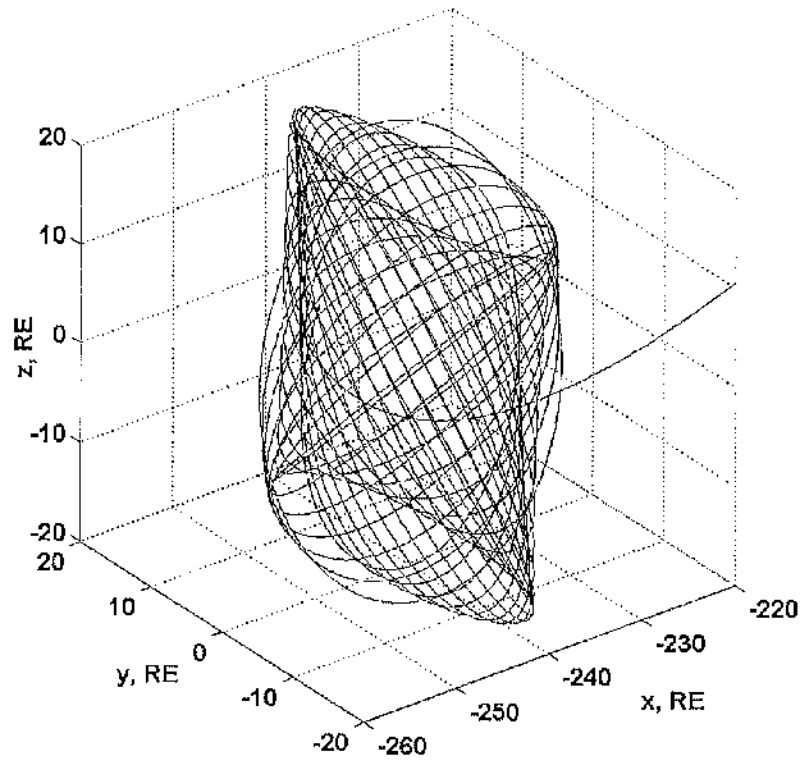


Figure 3-36 Enlarged view of Lissajous orbit around $x_0 = -240 R_E$

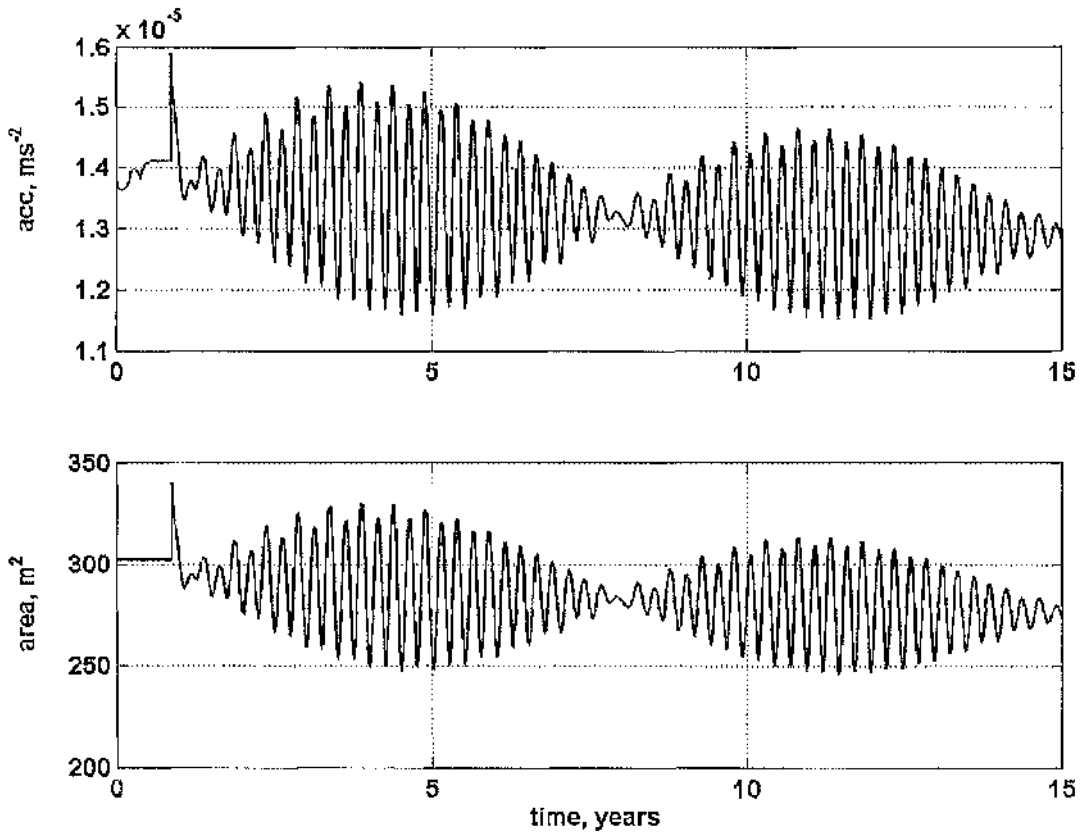


Figure 3-37 Acceleration and area variation required to control Lissajous orbit

Gains: $G_1=4.655 \times 10^{-7}$ $G_2=-8.379 \times 10^{-8}$ $G_3=1.4 \times 10^{-16}$ $G_4=8.068 \times 10^{-4}$ $G_5=4.355 \times 10^{-4}$ $G_6=2.345 \times 10^{-12}$

The acceleration required to control the orbit varies between 0.0115 mms^{-2} and 0.0159 mms^{-2} . For a 200 kg total mass, this corresponds to an area variation between 246 m^2 and 340 m^2 . For sail loading $\sigma=12 \text{ gm}^{-2}$, the sail mass is 4 kg enabling control of a 196 kg payload around this libration point.

Spacecraft orbiting on-axis libration points sunwards of the Earth require suitable y - and z -axis amplitudes to avoid telemetry interference from the solar radio disk. Farquhar [1977] states that the angular radius of the radio interference disk is 3.5° relative to the Earth. For a Lissajous orbit around the libration point, $x_0=-240 R_E$, the solar radio disk has radius 93,500 km. Throughout the 15 year control period, the solar sail spends approximately $1/4^{\text{th}}$ of the time within the telemetry interference zone.

Solar sail pitch and yaw angle control is also demonstrated using the same insertion conditions. Figure 3-38 shows insertion and control of a Lissajous orbit around the artificial libration point near L_1 . An enlarged view of the Lissajous orbit is provided in Fig 3-39. Upon arrival at the nominal orbit, the solar sail is fully deployed to provide acceleration $\kappa_p=0.0247 \text{ mms}^{-2}$. A total sail and payload mass of 200 kg could be controlled

using a 529 m^2 sail. Figure 3-40 shows the sail pitch and yaw angle variations controlling this orbit.

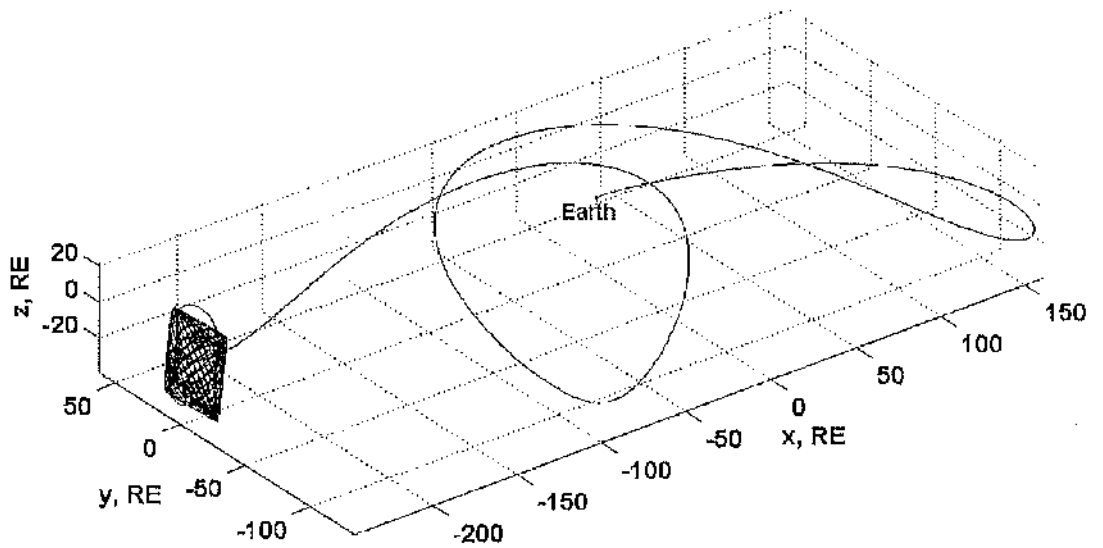


Figure 3-38 Insertion to Lissajous orbit around $x_0 = -240 R_E$ controlled using pitch and yaw angle variation

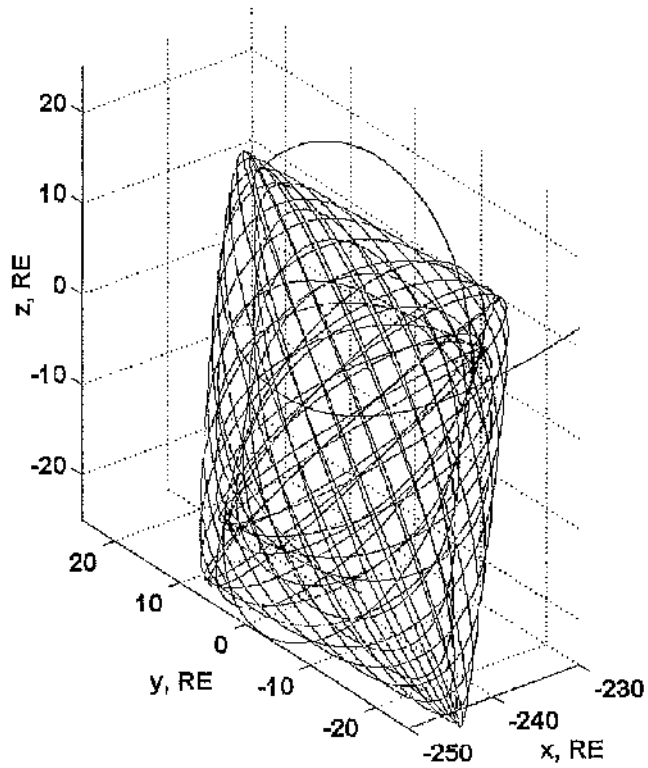


Figure 3-39 Enlarged view of Lissajous orbit around $x_0 = -240 R_E$

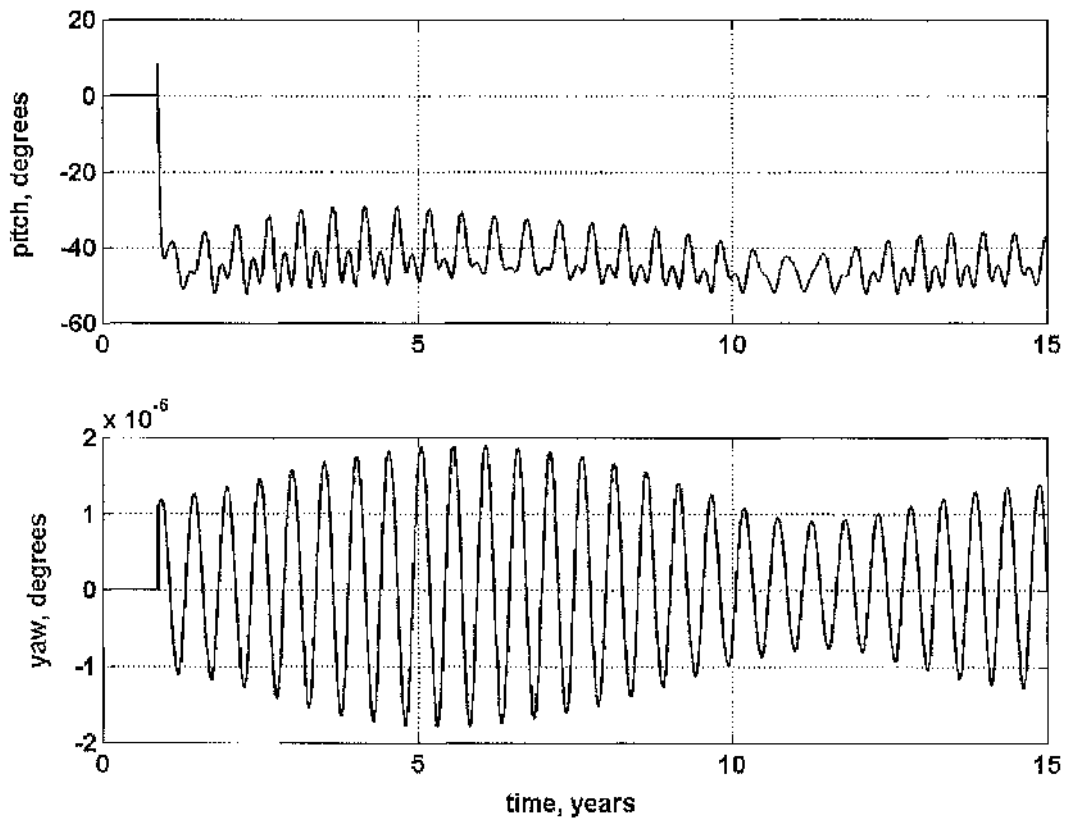


Figure 3-40 Pitch and yaw angle variation required to control Lissajous orbit

$$\text{Gain } \phi: G_1=1.872 \times 10^{-13} \quad G_2=-3.405 \times 10^{-14} \quad G_3=1.283 \times 10^{-17} \quad G_4=-3.295 \times 10^{-10} \quad G_5=1.836 \times 10^{-10} \quad G_6=3.19 \times 10^{-6}$$

$$\text{Gain } \alpha: G_1=0.916 \quad G_2=-0.0575 \quad G_3=-5.666 \times 10^{-14} \quad G_4=554.3190 \quad G_5=309.7840 \quad G_6=1.836 \times 10^{-10}$$

The pitch angle varies between -52.3° and 8.3° . The yaw angle is extremely small varying between $-1.8 \times 10^{-6}^\circ$ and $1.9 \times 10^{-6}^\circ$. Throughout the control period, the solar sail spends $1/5^{\text{th}}$ of the time within the radio exclusion zone. In this case, angle variation decreases the amount of time the payload spends within the solar exclusion zone compared to sail area variation. However, solar sail area variation control requires 64% the total sail surface area required by the pitch and yaw angle controller, in this case, due to the increase in nominal acceleration.

3.5 Conclusions

Circular displaced orbits were investigated using Hill's approximation of the three-body problem. At displacement distances relatively near to the Earth ($x_0 < 160 R_E$) the two-body dynamics provide a reasonable approximation of the solar sail dynamics as the influence of the Earth's gravity on the solar sail is significantly larger than the Sun. A quasi-periodic solution was also derived by linearising Hill's equations at the artificial libration point. The linear solution yields initial conditions which converge toward a Lissajous trajectory. The solar sail area variation and pitch angle variation control techniques were shown to provide linear control for both types of orbit.

Sunward of the Earth, Lissajous orbits have the disadvantage that the trajectory spends part of the time within the telemetry exclusion zone. Richardson [1980a, 1980b] derived a method to obtain matching in-plane and out-of-plane frequencies, thus producing periodic halo orbits. This method will be investigated in Chapter 4 to generate halo orbits around artificial libration points.

Chapter 4 Three body non-Keplerian orbits –

Restricted Problem

4.1 Restricted three-body problem

The study of non-Keplerian orbits will now be taken further using the circular and the elliptical restricted three-body problems. The circular restricted model assumes that the distance between the planet and the Sun is fixed. The elliptic model improves the dynamics by including the orbit eccentricity of the planet which results in the position of the libration points continually oscillating between the planetary apoapsis and periapsis. Richardson's third order approximation will be used to identify initial conditions which converge toward periodic halo orbits around artificial libration points in both restricted problems.

4.1.1 Circular restricted three-body problem

Complete derivations of the equations of motion are provided by Marchal [1990] and Szehebely [1967]. In this case, the relative motion of the two primary bodies is assumed circular. Figure 4-1 provides a schematic of the problem.

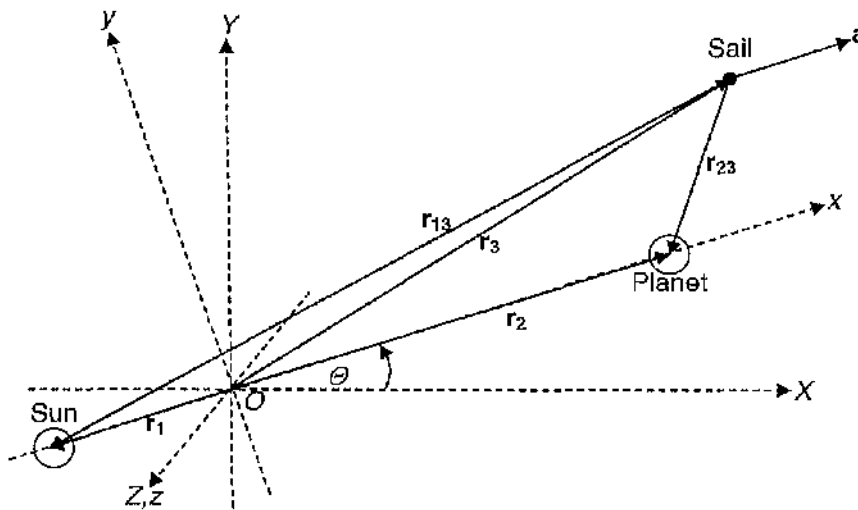


Figure 4-1 Schematic of circular restricted three-body problem

The angle between the inertial (sidereal) coordinate system (X,Y,Z) and the rotating (synodic) coordinate system (x,y,z) is defined as Θ . The constant distance between the Sun and the planet is defined as R . The problem will first be considered in the inertial frame and then the coordinates will be transformed into the rotating frame relative to the barycentre O . In the inertial reference frame, the general form of the gravitational attraction of each body is given by

$$m_k \ddot{\mathbf{r}}_k = G \sum_{j=1, j \neq k}^3 \frac{m_j m_k}{|\mathbf{r}_j - \mathbf{r}_k|^3} (\mathbf{r}_j - \mathbf{r}_k) \quad (4.1)$$

It is assumed that the mass of the solar sail is negligible and therefore does not exert a gravitational influence on the two primary masses. The acceleration of the solar sail in the inertial frame can be written as

$$\frac{d^2 \mathbf{r}_3}{dt^2} = -\frac{GM_1 (\mathbf{r}_3 - \mathbf{r}_1)}{|\mathbf{r}_{13}|^3} - \frac{GM_2 (\mathbf{r}_3 - \mathbf{r}_2)}{|\mathbf{r}_{23}|^3} + \mathbf{a} \quad (4.2)$$

where $\mathbf{r}_{jk} = |\mathbf{r}_j - \mathbf{r}_k|$. In the inertial frame, the solar sail is located at coordinates (X,Y,Z) , the Sun at (X_1, Y_1, Z_1) and the Earth at (X_2, Y_2, Z_2) . The acceleration due to solar radiation pressure has components $\mathbf{a} = a_x \mathbf{i} + a_y \mathbf{j} + a_z \mathbf{k}$. The masses co-rotate around the barycentre with constant angular velocity $\Omega = \dot{\Theta}$. The Sun-Planet and Sun-Sail separation distances are defined as

$$|\mathbf{r}_{13}| = \left((X - X_1)^2 + (Y - Y_1)^2 + (Z - Z_1)^2 \right)^{1/2} \quad (4.3.1)$$

$$|\mathbf{r}_{23}| = \left((X - X_2)^2 + (Y - Y_2)^2 + (Z - Z_2)^2 \right)^{1/2} \quad (4.3.2)$$

Equation (4.2) can be transformed into a rotating system about the z -axis using the following matrix. The motion of the primary masses is assumed to be in the X - Y plane.

$$\begin{bmatrix} X \\ Y \\ Z \end{bmatrix} = \begin{bmatrix} \cos \Omega t & -\sin \Omega t & 0 \\ \sin \Omega t & \cos \Omega t & 0 \\ 0 & 0 & 1 \end{bmatrix} \begin{bmatrix} x \\ y \\ z \end{bmatrix} \quad (4.4)$$

As $|\mathbf{r}_3| = (X^2 + Y^2 + Z^2)^{1/2}$, the 2nd order time derivatives of the transform can be calculated as follows

$$\ddot{X} = (\ddot{x} - 2\Omega\dot{y} - \Omega^2 x) \cos \Omega t - (\ddot{y} + 2\Omega\dot{x} - \Omega^2 y) \sin \Omega t \quad (4.5.1)$$

$$\ddot{Y} = (\ddot{x} - 2\Omega\dot{y} - \Omega^2 x) \sin \Omega t + (\ddot{y} + 2\Omega\dot{x} - \Omega^2 y) \cos \Omega t \quad (4.5.2)$$

From Keplers laws, it is assumed that the angular velocity is constant where $\Omega = \sqrt{G(M_1 + M_2)/R^3}$. These components can be substituted into the Eq (4.2) to obtain the following expressions [Escobal, 1968] after re-arranging and grouping the trigonometric terms

$$A \cos \Omega t - B \sin \Omega t = 0 \quad (4.6.1)$$

$$A \sin \Omega t + B \cos \Omega t = 0 \quad (4.6.2)$$

where

$$A = \ddot{x} - 2\Omega\dot{y} - \Omega^2 x + GM_1 \frac{(x - x_1)}{|\mathbf{r}_{13}|^3} + GM_2 \frac{(x - x_2)}{|\mathbf{r}_{23}|^3} - a_x \quad (4.7.1)$$

$$B = \ddot{y} + 2\Omega\dot{x} - \Omega^2 y + GM_1 \frac{(y - y_1)}{|\mathbf{r}_{13}|^3} + GM_2 \frac{(y - y_2)}{|\mathbf{r}_{23}|^3} - a_y \quad (4.7.2)$$

Equations (4.6) require that variables $A=B=0$ so these conditions are true for all t . In the rotating frame, the location of the Sun is defined by coordinates (x_1, y_1, z_1) and of the planet (x_2, y_2, z_2) . Equation (4.7) can be further simplified by re-writing the expression in non-dimensional coordinates. The characteristic mass of the planet can be expressed as $\mu = M_2/M$ where the total mass of the primaries $M = M_1 + M_2$. The mass of the Sun is therefore $(1-\mu)$.

The coordinate system is chosen such that the Sun and planet are co-axial, located on the synodic x -axis. The barycentre is located at the centre of mass of the two primaries. The characteristic length is selected as the separation distance between the two primaries. It can be demonstrated that the Sun is located at $(-\mu, 0, 0)$ and the planet at $(1-\mu, 0, 0)$.

The angular velocity and the gravitational constant terms can be removed from the equations using characteristic time, τ . The non-dimensionalised time derivatives, denoted

by $*$, are equivalent to $d/dt = \tau^{-1} d^*/dt$. The gravitational constant $G = \Omega^2 R^3 / (M_1 + M_2)$ where the non-dimensionalised total mass $(M_1 + M_2)/M = 1$. Substitution into Eq (4.7) results in the following equations of motion

$$\frac{R}{\tau^2} \frac{d^2 x^*}{dt^2} - 2\Omega \frac{R}{\tau} \frac{dy^*}{dt} - \Omega^2 R x = -\Omega^2 R \frac{(1-\mu)(x+\mu)}{|\mathbf{r}_{13}|^3} - \Omega^2 R \frac{\mu(x-1+\mu)}{|\mathbf{r}_{23}|^3} + a_x \quad (4.8.1)$$

$$\frac{R}{\tau^2} \frac{d^2 y^*}{dt^2} + 2\Omega \frac{R}{\tau} \frac{dy^*}{dt} - \Omega^2 R y = -\Omega^2 R \frac{(1-\mu)y}{|\mathbf{r}_{13}|^3} - \Omega^2 R \frac{\mu y}{|\mathbf{r}_{23}|^3} + a_y \quad (4.8.2)$$

$$\frac{R}{\tau^2} \frac{d^2 z^*}{dt^2} = -\Omega^2 R \frac{(1-\mu)z}{|\mathbf{r}_{13}|^3} - \Omega^2 R \frac{\mu z}{|\mathbf{r}_{23}|^3} + a_z \quad (4.8.3)$$

The angular velocity can be removed by setting $\tau\Omega = 1$ which requires that the characteristic time $\tau = \sqrt{R^3/G(M_1 + M_2)}$. Dropping the $*$ notation from the expressions, the final non-dimensionalised equations can be expressed as

$$\frac{d^2 x}{dt^2} - 2 \frac{dy}{dt} - x = -\frac{(1-\mu)(x+\mu)}{|\mathbf{r}_{13}|^3} - \frac{\mu(x-1+\mu)}{|\mathbf{r}_{23}|^3} + \kappa_x \quad (4.9.1)$$

$$\frac{d^2 y}{dt^2} + 2 \frac{dx}{dt} - y = -\frac{(1-\mu)y}{|\mathbf{r}_{13}|^3} - \frac{\mu y}{|\mathbf{r}_{23}|^3} + \kappa_y \quad (4.9.2)$$

$$\frac{d^2 z}{dt^2} = -\frac{(1-\mu)z}{|\mathbf{r}_{13}|^3} - \frac{\mu z}{|\mathbf{r}_{23}|^3} + \kappa_z \quad (4.9.3)$$

where $(\kappa_x, \kappa_y, \kappa_z)$ represent the non-dimensionalised acceleration components due to solar radiation pressure and the Sun-sail and Earth-Sail distances are defined as $|\mathbf{r}_{13}| = \sqrt{(x+\mu)^2 + y^2 + z^2}$ and $|\mathbf{r}_{23}| = \sqrt{(x-1+\mu)^2 + y^2 + z^2}$ respectively.

The coordinate system is easily transformed to obtain planet centred equations by substituting $x = (\tilde{x} - 1 + \mu)$, where \tilde{x} denotes the x -axis position relative to the planet.

Therefore, the Sun-sail distance $|\tilde{\mathbf{r}}_{13}| = \sqrt{(\tilde{x}+1)^2 + y^2 + z^2}$ and the planet-sail distance $|\tilde{\mathbf{r}}_{23}| = \sqrt{\tilde{x}^2 + y^2 + z^2}$ relative to the planet. Equation (4.9) can finally be expressed in planet centred coordinates as

$$\frac{d^2\tilde{x}}{dt^2} - 2\frac{dy}{dt} - \tilde{x} = -\frac{(1-\mu)(\tilde{x}+1)}{|\tilde{\mathbf{r}}_{13}|^3} - \frac{\mu\tilde{x}}{|\tilde{\mathbf{r}}_{23}|^3} + (1-\mu) + \kappa_x \quad (4.10.1)$$

$$\frac{d^2y}{dt^2} + 2\frac{d\tilde{x}}{dt} - y = -\frac{(1-\mu)y}{|\tilde{\mathbf{r}}_{13}|^3} - \frac{\mu y}{|\tilde{\mathbf{r}}_{23}|^3} + \kappa_y \quad (4.10.2)$$

$$\frac{d^2z}{dt^2} = -\frac{(1-\mu)z}{|\tilde{\mathbf{r}}_{13}|^3} - \frac{\mu z}{|\tilde{\mathbf{r}}_{23}|^3} + \kappa_z \quad (4.10.3)$$

The resulting Lagrange points obtained will be compared to those of the planet centered Hill's approximation.

4.1.2 Elliptical restricted three-body problem

An extension to the circular restricted problem is to include the elliptical nature of the planets orbit around the Sun. The derivation is similar to the circular restricted problem derived previously. However, the angular velocity $\dot{\Theta}$ and separation distance R of the two primaries can no longer be assumed constant.

A suitable method to represent the variation of the angular velocity and separation distance is to define both as an eccentricity power series. This method is adopted by both Farquhar [1970a] and Wie [1998], and is valid provided the eccentricity is relatively small. The separation distance, R , between two masses is determined by

$$R = \frac{a(1-e^2)}{1+e \cos \Theta} \quad (4.11)$$

where a is the length of the semi-major axis, e is the orbit eccentricity and Θ represents the true-anomaly. Figure 4.2 shows a schematic of an ellipse with each of these parameters outlined.

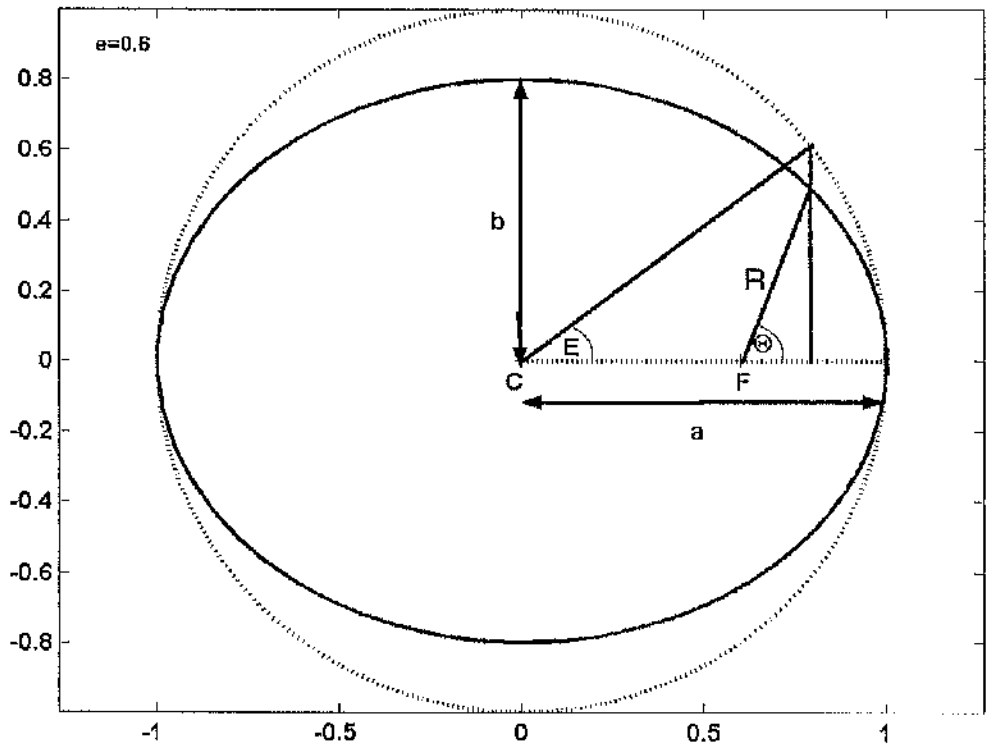


Figure 4-2 Schematic of elliptical orbit where eccentricity $e = 0.6$

The eccentric anomaly, E , is related to the true anomaly by the equation

$$\tan \frac{\Theta}{2} = \left(\frac{1+e}{1-e} \right)^{1/2} \tan \frac{E}{2} \quad (4.12)$$

A thorough derivation is provided by Smart [1953] outlining how the true-anomaly and radial separation distance are expanded in terms of the eccentric anomaly using Bessel functions of the first kind.

The mean anomaly, $M = \nu(t - \tau)$, where the orbit frequency $\nu = 2\pi/T$, t is the current time, τ is time elapsed at periapsis and T is the orbit period. The mean anomaly is related to the eccentric anomaly by the equation

$$M = E - e \sin E \quad (4.13)$$

Using the methodology of Smart [1953], the relationship between true anomaly and eccentric anomaly provided in Eq (4.12) can be represented by the series

$$\Theta = E + 2 \sum_{n=1}^{\infty} \frac{\beta^n}{n} \sin nE \quad (4.14)$$

where β^n contains powers of eccentricity and is equivalent to

$$\beta^n = \left(\frac{e}{2}\right)^n \left\{ 1 + n \sum_{m=1}^{\infty} \frac{(2m+n-1)!}{m!(n+m)!} \left(\frac{e}{2}\right)^{2m} \right\} \quad (4.15)$$

where n and m are integers.

The eccentric anomaly can be expressed as a power series of mean anomaly

$$\sin nE = \sum_{k=1}^{\infty} \frac{n}{k} [J_{k+n}(ke) + J_{k-n}(ke)] \sin kM \quad (4.16)$$

where $J_n(x)$ is a Bessel function of the first kind. The Bessel function has the form

$$J_n(x) = \sum_{k=0}^{\infty} \frac{(-1)^k (x/2)^{2k+n}}{k! \Gamma(k+n+1)} \quad (4.17)$$

which has the property $J_{-n}(x) = (-1)^n J_n(x)$. The series representing true anomaly, Eq (4.14), can be represented in terms of the mean anomaly by re-arranging Eq (4.13) to obtain $E = M + e \sin E$.

Using the series from Eq (4.16) the true anomaly can be expressed as

$$\Theta = M + 2 \sum_{n=1}^{\infty} \frac{1}{n} J_n(ne) \sin nM + 2 \sum_{n=1}^{\infty} \frac{\beta^n}{n} \sum_{k=1}^{\infty} \frac{n}{k} [J_{k+n}(ke) + J_{k-n}(ke)] \sin kM \quad (4.18)$$

Similarly, the radial distance can also be expressed in terms of eccentricity and mean anomaly. The term $\cos E$ can be expressed as a series in terms of the mean anomaly where

$$\cos E = -\frac{1}{2}e + \sum_{n=1}^{\infty} \frac{2}{n^2} \frac{d}{de} \{J_n(ne)\} \cos nM \quad (4.19)$$

It can be shown that the radial distance $R = a(1 - e \cos E)$ which can be expressed as

$$\bar{R} = 1 + \frac{e^2}{2} - 2e \sum_{n=1}^{\infty} \frac{1}{n^2} \frac{d}{de} \{J_n(ne)\} \cos nM \quad (4.20)$$

This is non-dimensionalised with respect to the semi-major axis length where $\bar{R} = R/a$.

The non-dimensionalised power series for true-anomaly and radial distance is outlined to the 7th power of e in Wie [1998]. Both series can be expressed as follows

$$\begin{aligned} \bar{R} = 1 + \frac{1}{2}e^2 + \left(-e + \frac{3}{8}e^3 - \frac{5}{192}e^5 + \frac{7}{9216}e^7\right) \cos M + \left(-\frac{1}{2}e^2 + \frac{1}{3}e^4 - \frac{1}{16}e^6\right) \cos 2M \\ + \left(-\frac{3}{8}e^3 + \frac{45}{128}e^5 - \frac{567}{5120}e^7\right) \cos 3M + \left(-\frac{1}{3}e^4 + \frac{2}{5}e^6\right) \cos 4M \\ + \left(-\frac{125}{384}e^5 + \frac{4375}{9216}e^7\right) \cos 5M - \frac{27}{80}e^6 \cos 6M - \frac{16807}{46080}e^7 \cos 7M \end{aligned} \quad (4.21.1)$$

$$\begin{aligned} \Theta = M + \left(2e - \frac{1}{4}e^3 + \frac{5}{96}e^5 + \frac{107}{4608}e^7\right) \sin M + \left(\frac{5}{4}e^2 - \frac{11}{24}e^4 + \frac{17}{192}e^6\right) \sin 2M \\ + \left(\frac{13}{12}e^3 - \frac{43}{64}e^5 + \frac{95}{512}e^7\right) \sin 3M + \left(\frac{103}{96}e^4 - \frac{451}{480}e^6\right) \cos 4M \\ + \left(\frac{1097}{960}e^5 - \frac{5957}{4608}e^7\right) \cos 5M + \frac{1223}{960}e^6 \cos 6M + \frac{47273}{32256}e^7 \cos 7M \end{aligned} \quad (4.21.2)$$

The mean anomaly represents the non-dimensionalised time with units $1/\nu$. The expansions for \bar{R} and Θ are convergent provided $e < 0.6627$.

The elliptical three-body problem including solar radiation pressure is represented by the same schematic as the circular restricted case, Fig 4-1. The equations of motion for the solar sail will be constructed relative to the planet where $\mathbf{r}_{13} = \mathbf{r}_3 - \mathbf{r}_2$.

Relative to the barycentre

$$\ddot{\mathbf{r}}_3 = -\left(\frac{GM_1}{|\mathbf{r}_{13}|^3}\right)\mathbf{r}_{13} - \left(\frac{GM_2}{|\mathbf{r}_{23}|^3}\right)\mathbf{r}_{23} + \kappa\mathbf{n} \quad (4.22.1)$$

$$\ddot{\mathbf{r}}_2 = \left(\frac{Gm}{|\mathbf{r}_{23}|^3}\right)\mathbf{r}_{23} - \left(\frac{GM_1}{|\mathbf{r}_{12}|^3}\right)\mathbf{r}_{12} \quad (4.22.2)$$

where M_1 , M_2 and m are the mass of the Sun, planet and sail respectively. The motion of the solar sail relative to the planet can therefore be expressed as

$$\ddot{\mathbf{r}}_{23} = -G(M_2 + m)\frac{\mathbf{r}_{23}}{|\mathbf{r}_{23}|^3} - GM_1\left(\frac{\mathbf{r}_{13}}{|\mathbf{r}_{13}|^3} - \frac{\mathbf{r}_{12}}{|\mathbf{r}_{12}|^3}\right) + \kappa\mathbf{n} \quad (4.23)$$

The mass of the solar sail $m \ll M_2$ thus, can be neglected from the first term. Using the non-dimensionalised mass $\mu = M_2/(M_1 + M_2)$ and $(1 - \mu) = M_1/(M_1 + M_2)$, the expression can be re-written as

$$\ddot{\mathbf{r}}_{23} = -\mu\frac{\mathbf{r}_{23}}{|\mathbf{r}_{23}|^3} - (1 - \mu)\left(\frac{\mathbf{r}_{13}}{|\mathbf{r}_{13}|^3} - \frac{\mathbf{r}_{12}}{|\mathbf{r}_{12}|^3}\right) + \kappa\mathbf{n} \quad (4.24)$$

The vector representing motion of the solar sail relative to the planet $\mathbf{r}_{23} = x\mathbf{i} + y\mathbf{j} + z\mathbf{k}$ and the motion of the planet relative to the Sun is described by the expansion provided in Eq (4.21.1), such that $\mathbf{r}_{12} = \bar{R}\mathbf{i}$. The motion of the solar sail relative to the Sun $\mathbf{r}_{13} = (x + \bar{R})\mathbf{i} + y\mathbf{j} + z\mathbf{k}$.

The motion of the solar sail in the rotating frame is determined using the rotational matrix

$$\begin{bmatrix} X \\ Y \\ Z \end{bmatrix} = \begin{bmatrix} \cos \Theta & -\sin \Theta & 0 \\ \sin \Theta & \cos \Theta & 0 \\ 0 & 0 & 1 \end{bmatrix} \begin{bmatrix} x \\ y \\ z \end{bmatrix} \quad (4.25)$$

which has second order time derivatives

$$\ddot{X} = (\ddot{x} - x\dot{\Theta}^2 - 2y\dot{\Theta} - y\ddot{\Theta}) \cos \Theta + (-\ddot{y} + y\dot{\Theta}^2 - 2x\dot{\Theta} - x\ddot{\Theta}) \sin \Theta \quad (4.26.1)$$

$$\ddot{Y} = (\ddot{y} - y\dot{\Theta}^2 + 2x\dot{\Theta} + x\ddot{\Theta}) \cos \Theta + (\ddot{x} - x\dot{\Theta}^2 - 2y\dot{\Theta} - y\ddot{\Theta}) \sin \Theta \quad (4.26.2)$$

$$\ddot{Z} = \ddot{z} \quad (4.26.3)$$

Substituting these expressions into Eq (4.24), the non-dimensionalised equations of motion can be expressed as

$$\ddot{x} - 2y\dot{\Theta} - y\ddot{\Theta} = \dot{\Theta}^2 x - \frac{\mu x}{|\mathbf{r}_{23}|^3} - (1 - \mu) \left(\frac{x + \bar{R}}{|\mathbf{r}_{13}|^3} - \frac{1}{\bar{R}^2} \right) + \kappa_x \quad (4.27.1)$$

$$\ddot{y} - \dot{\Theta}^2 y + x\ddot{\Theta} = -2x\dot{\Theta} - \frac{\mu y}{|\mathbf{r}_{23}|^3} - (1 - \mu) \frac{y}{|\mathbf{r}_{13}|^3} + \kappa_y \quad (4.27.2)$$

$$\ddot{z} = -\frac{\mu z}{|\mathbf{r}_{23}|^3} - (1 - \mu) \frac{z}{|\mathbf{r}_{13}|^3} + \kappa_z \quad (4.27.3)$$

These equations are time dependant due to the variation of the separation distance \bar{R} and the variation of the true-anomaly derivatives $\dot{\Theta}$ and $\ddot{\Theta}$. The elliptical three-body problem will be used to examine the perturbations due to orbit eccentricity of the primary masses.

4.2 Ballistic and artificial Lagrange points

4.2.1 Classical Lagrange points

In the circular restricted three-body problem there exists five naturally occurring Lagrange points. Figure 4-3 provides a schematic indicating the location of the Lagrange points. The three co-linear points (L_1, L_2, L_3) were identified by Euler and the triangular points (L_4, L_5) by Lagrange [Lo, 2001].

The location of the co-linear points can be solved by forming a quintic equation and calculating the real roots [Farquhar, 1970a]. As the libration points lie on the x -axis, $y=z=0$ and as they are stationary points $\dot{x} = \ddot{x} = \dot{y} = \ddot{y} = \dot{z} = \ddot{z} = 0$ in the synodic coordinate system, the location of the L_1 and L_2 Lagrange points, relative to the planet, are determined by solving Eq (4.28.1) for x

$$x^5 + (3 - \mu)x^4 + (3 - 2\mu)x^3 \pm \mu x^2 \pm 2\mu x \pm \mu = 0 \quad (4.28.1)$$

where the upper sign corresponds to L_1 and the lower sign to L_2 . The L_3 Lagrange point, located on the opposite side of the Sun, can be determined by solving Eq (4.28.2) for x

$$x^5 + (3 - \mu)x^4 + (3 - 2\mu)x^3 + 2x^2 + 2\mu x - \mu = 0 \quad (4.28.2)$$

Given a system mass ratio for the primaries, $\mu = M_2 / (M_1 + M_2)$ it is possible to locate the co-linear lagrange points of the system. In the case of the Sun-Earth-Sail system the mass ratio is defined as $\mu = 3.00373 \times 10^{-6}$. The locations of the co-linear Lagrange points are provided in Table 4-1.

The triangular Lagrange points, L_4 and L_5 , are located at the apex of an equilateral triangle where $|\mathbf{r}_{13}|=1$, $|\mathbf{r}_{23}|=1$ and $|\mathbf{r}_{12}|=1$. This can be verified by evaluating the x and y components of motion at the stationary point. Simultaneous equations can be found which yield $x = -1/2$ and $y = \pm\sqrt{3}/2$. The positions of L_4 and L_5 relative to the Earth in the Sun-Earth system are also provided in Table 4-1.

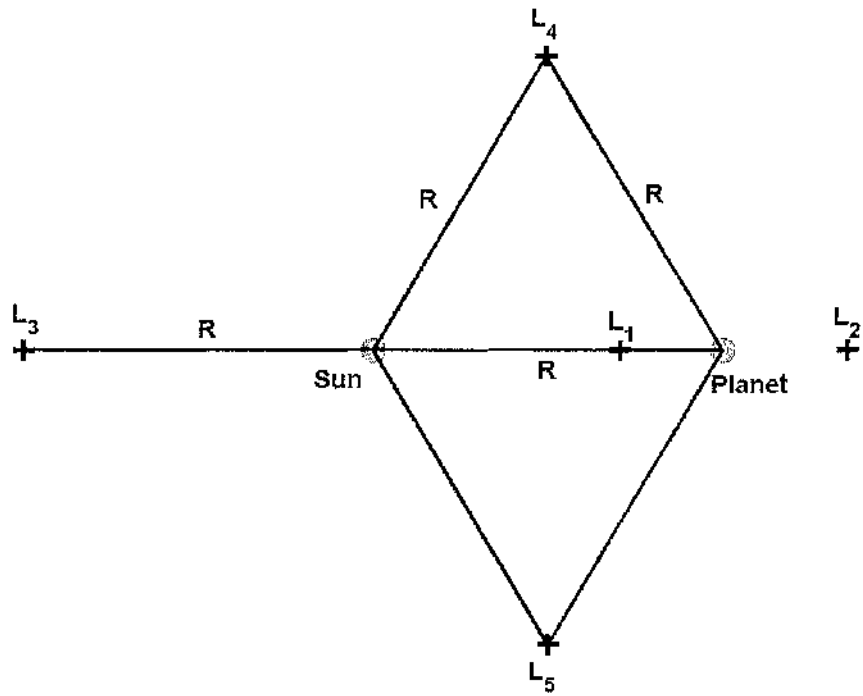


Figure 4-3 Schematic of Lagrange points in the circular restricted problem

Lagrange Point	Position in x-y plane	
L ₁	x=-0.0099707	y=0
L ₂	x=0.01003740	y=0
L ₃	x=-2.0	y=0
L ₄	x=-0.5	y=0.8660
L ₅	x=-0.5	y=-0.8660

Table 4-1 Location of Lagrange points in ballistic case ($\kappa=0$)

4.2.2 Artificial libration points

Artificial libration points can be generated using a solar sail to produce an additional uniform acceleration which yields artificial stationary points. A complete stability analysis of the on-axis case will be investigated in the circular restricted problem. The solar sail is orientated such that the thrust vector is directed along the x -axis which generates a constant axial acceleration with magnitude determined by

$$\kappa_x = \frac{(1-\mu)}{(x+1)^2} \pm \frac{\mu}{x^2} - x - (1-\mu) \quad (4.29)$$

where the upper sign corresponds to a libration point sunward of L_2 and the lower sign corresponds to a libration point sunward of L_1 .

Figure 4-4 shows the acceleration required to generate such artificial libration points. The stability of these libration points can be determined from the eigenvalues of the linearised equations of motion. As the solar sail acceleration can only be directed in the anti-Sun direction ($\kappa_x > 0$), there are no on-axis libration points beyond L_2 or between the planet and L_1 .

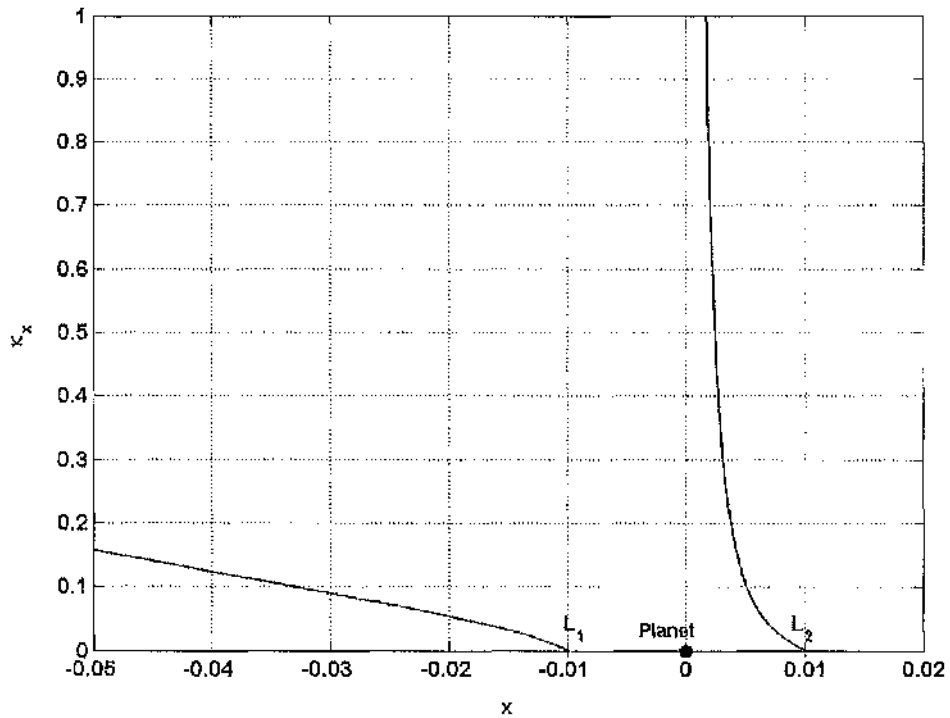


Figure 4-4 Artificial libration points generated using solar sail acceleration

4.2.3 Libration points in the elliptical restricted problem

In the case of the elliptical restricted problem, the distance between the Sun and the planet pulsates. As a result, the libration point position also varies. The symbols, l_2 and l_1 denote the distance between the planet and the Lagrange points, L_2 and L_1 , respectively. The ratio, l_1/\bar{R} and l_2/\bar{R} remain constant as the separation distance between the two primaries varies due to the eccentricity of the orbit [Wie, 1998].

The variation of the L_2 position can be determined by setting the velocity and acceleration components equal to zero in Eq (4.27). The resulting quintic expression can be solved to find the location of the on-axis libration point relative to the planet. For libration points Sunward of L_2 , the expression has the form

$$\begin{aligned} \dot{\Theta}^2 \bar{R}^2 x^5 + (2\dot{\Theta}^2 \bar{R}^3 + 1 - \mu + \kappa)x^4 + (\dot{\Theta}^2 \bar{R}^4 + 2(1 - \mu + \kappa)\bar{R})x^3 \\ - (\mu - \kappa)\bar{R}^2 x^2 - 2\mu\bar{R}^3 x - \mu\bar{R}^4 = 0 \end{aligned} \quad (4.30.1)$$

The quintic expression for libration points sunward of L_1 has the form

$$\begin{aligned} \dot{\Theta}^2 \bar{R}^2 x^5 + (2\dot{\Theta}^2 \bar{R}^3 + 1 - \mu + \kappa)x^4 + (\dot{\Theta}^2 \bar{R}^4 + 2(1 - \mu + \kappa)\bar{R})x^3 \\ + (\mu + \kappa)\bar{R}^2 x^2 + 2\mu\bar{R}^3 x + \mu\bar{R}^4 = 0 \end{aligned} \quad (4.30.2)$$

When the orbit eccentricity $e=0$, the angular velocity $\dot{\Theta} = 1$ and separation distance $\bar{R} = 1$, the quintic expressions representing libration points in the circular restricted case are recovered.

Table 4-2 contains the distance of the Lagrange points relative to a selection of planets at apoapsis and periapsis, evaluated at $\kappa=0$. In the case of the Earth, this motion corresponds to a displacement greater than 50,000 km throughout the year.

The acceleration required to generate an artificial libration point can be calculated using Eq (4.29). Figure 4-5 shows the position variation of artificial libration points generated using constant acceleration due to the eccentric motion of the planet around the Sun.

The further the libration point is located from the planet, the larger the position variation. Orbits near the L_2 Lagrange points will be more noticeably affected by the elliptical motion than orbits located near to the planet. Similarly, the position fluctuation is larger for orbits around libration points displaced sunwards of L_1 than for libration points near to L_1 .

Planet	Eccentricity E	μ ($\times 10^{-6}$)	semi-major axis a ($\times 10^6$ km)	L_1 Location		L_2 Location	
				Apoapsis	Periapsis	Apoapsis	Periapsis
Mercury	0.2056	0.1660	57.91	-0.00466	-0.00299	0.004675	0.002993
Venus	0.0067	2.4476	108.21	-0.00938	-0.00925	0.009302	0.009442
Earth	0.0168	3.00373	149.60	-0.01016	-0.00979	0.010224	0.009852
Mars	0.0935	0.3227	227.92	-0.00524	-0.00427	0.005255	0.004283
Jupiter	0.0489	953.59	778.57	-0.07024	-0.06314	0.073590	0.066013

Table 4-2 Position of Lagrange points relative to planet at periapsis and apoapsis

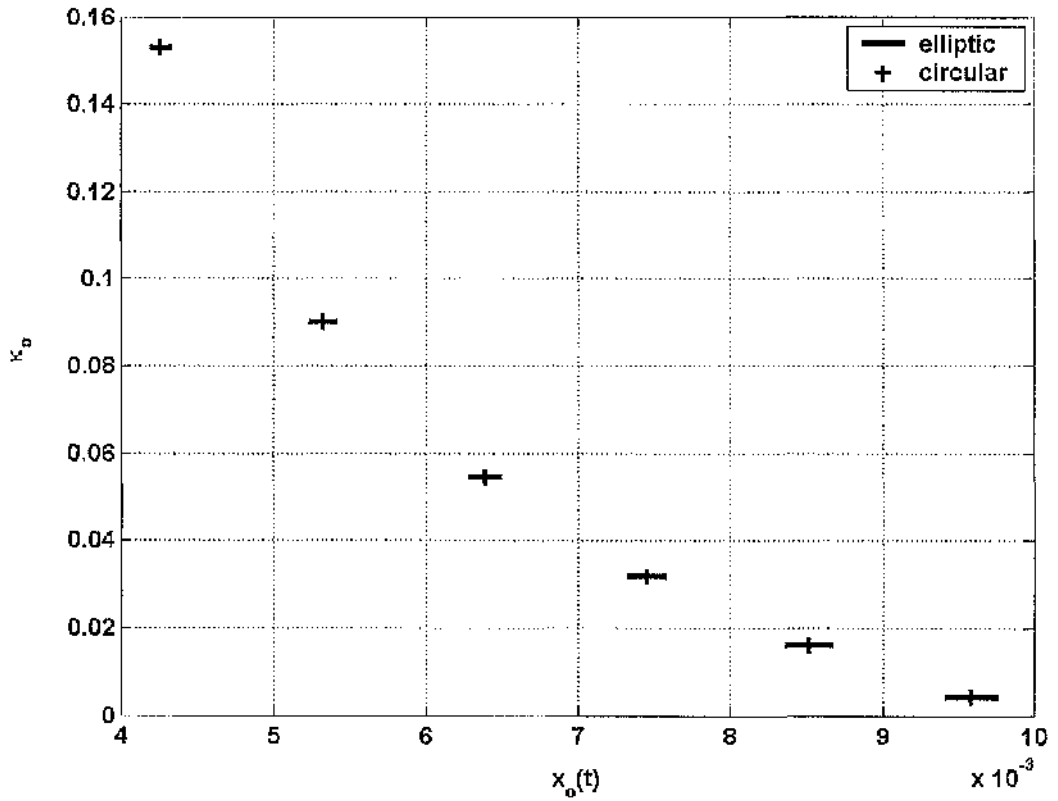


Figure 4-5 Variation of artificial libration point position for eccentric orbit

4.3 Jacobi integral

4.3.1 Jacobi integral of the circular restricted problem

The Jacobi Integral and Hill's surfaces provide a useful method for investigating bound motion given the initial orbit conditions. From Eqns (4.10) it can be seen that

$$\ddot{x}\ddot{x} + \ddot{y}\ddot{y} + \ddot{z}\ddot{z} = x\dot{x} + y\dot{y} - \frac{(1-\mu)}{|\mathbf{r}_1|^3}[(x+1)\dot{x} + y\dot{y} + z\dot{z}] - \frac{\mu}{|\mathbf{r}_2|^3}[x\dot{x} + y\dot{y} + z\dot{z}] + (1-\mu)\dot{x} + \boldsymbol{\kappa} \cdot \dot{\mathbf{r}} \quad (4.31)$$

Factoring a time derivative from the above expression gives the integral

$$\frac{d}{dt} \left[\frac{1}{2} v^2 - \frac{(x^2 + y^2)}{2} - \frac{(1-\mu)}{|\mathbf{r}_1|} - \frac{\mu}{|\mathbf{r}_2|} - (1-\mu)x - \boldsymbol{\kappa} \cdot \mathbf{r} \right] = 0 \quad (4.32)$$

where $v^2 = \dot{x}^2 + \dot{y}^2 + \dot{z}^2$.

Integrating with respect to time gives the Jacobi integral for the circular restricted problem including the effects of solar radiation pressure as

$$v^2 - (x^2 + y^2) - \frac{2(1-\mu)}{|\mathbf{r}_1|} - \frac{2\mu}{|\mathbf{r}_2|} - (1-\mu)x - 2\kappa \cdot \mathbf{r} = C \quad (4.33)$$

where C is a constant, known as the Jacobi constant which is analogous to the total orbit energy E ($C \equiv 2E$). Zero velocity surfaces are calculated by first evaluating C at a set of initial conditions and then generating a surface for constant C in the x - y plane when velocity $v=0$.

4.3.2 Zero-velocity surfaces of the Lagrange points

The Jacobi constants evaluated at the L_1 and L_2 Lagrange points are $C_{L_1} = -2.00089675$ and $C_{L_2} = -2.00089275$ respectively. Figure 4-6 shows the Hill's surfaces generated for these energies. It is evident that the zero-velocity surfaces surrounding the Earth are closed when the Jacobi constant $C \leq C_{L_1}$. As energy is increased, the zero-velocity surface opens around the Lagrange points. In the case of the surface $C = C_{L_2}$, there is a gap in the surface around L_1 . Unlike the Hill's approximation, the surfaces are not symmetric and open around L_1 at a slightly lower energy than at L_2 .

As the Jacobi constant is analogous to the total energy, evaluating a zero-velocity surface at a libration point produces a surface equivalent to the pseudo-potential function. A local saddle point of the pseudo-potential function clearly exists at the libration points suggesting that the on-axis libration points are likely to be unstable. This will be confirmed using eigenvalue analysis as in the case of Hill's approximation.

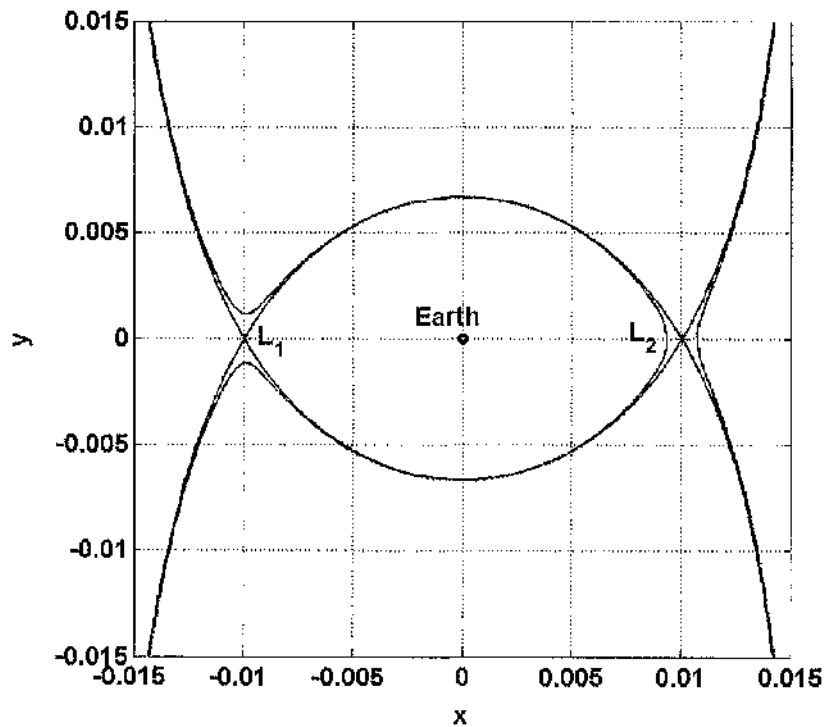


Figure 4-6 Zero-velocity surfaces in vicinity of Earth for $C=C_{L1}$ and $C=C_{L2}$

4.3.3 Zero-velocity surfaces of artificial libration points

Including the affects of acceleration due to solar radiation pressure alters the shape of the zero-velocity surface. A series of zero-velocity surfaces generated at artificial libration points sunward of L_1 and L_2 are provided in Fig 4-7. The accelerations required to generate these libration points are calculated using Eq (4.29). The values of Jacobi constant for each surface is provided in Table 4-3.

In the case of artificial libration points between L_2 and the Earth, there is no gap in the surface sunward of the Earth. However, for libration points generated sunward of L_1 there is a gap in the zero-velocity surface around L_2 . This can be attributed to the solar sail acceleration reducing the energy required for escape in the anti-Sun direction.

Time is explicitly present in the elliptical restricted problem thus no Jacobi integral can be derived [Broucke, 1969]. However, surfaces of zero-velocity exist instantaneously resulting in time dependant capture regions which pulsate periodically as the planet orbits the Sun [Astakhov and Farrelly, 2004].

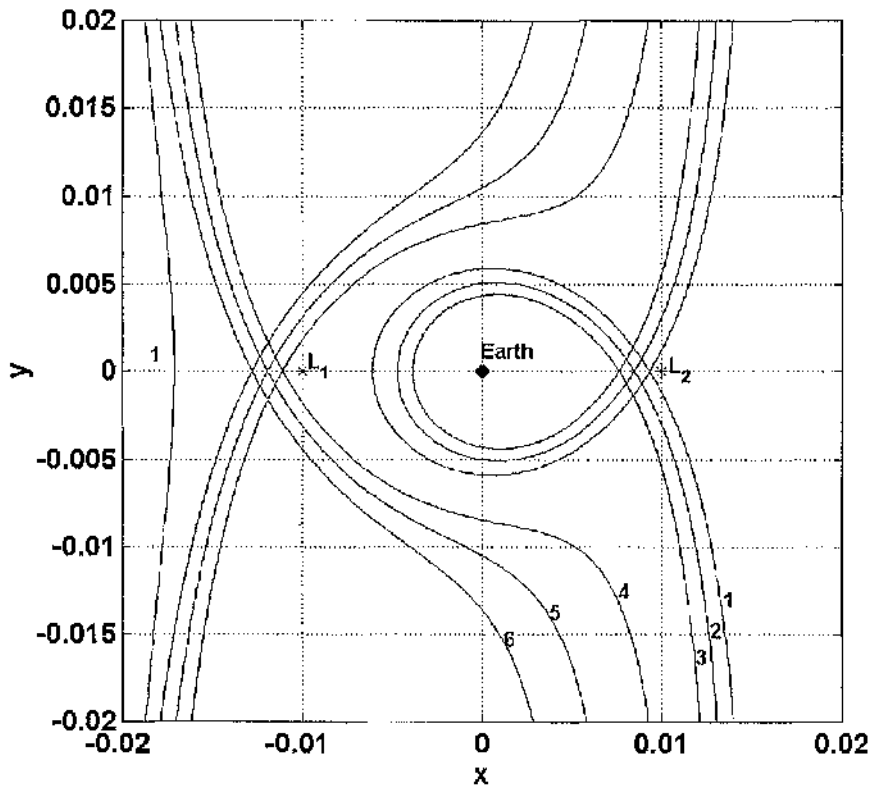


Figure 4-7 Zero-velocity surfaces for series of artificial libration points sunward of L_1 and L_2

Surface	Libration point x_0, R_E	Acceleration κ, mms^{-2}	Jacobi Constant C
1	220	0.0379	-2.001016
2	200	0.0957	-2.0011891
3	180	0.1685	-2.0013866
4	-260	0.0543	-2.0007055
5	-280	0.0900	-2.0005678
6	-300	0.1218	-2.0004359

Table 4-3 Parameters for zero-velocity surfaces evaluated at artificial libration

4.4 Periodic halo orbits

4.4.1 Richardson's method

An approximation of the circular restricted three-body problem can be derived which enables initial conditions to be identified that lead to periodic solutions. A linear approximation of the equations provides a crude estimate of initial conditions which lead to halo or Lissajous trajectories but for more accurate solutions, which require less station-keeping after orbit insertion, several higher order non-linear terms must also be considered. The problem of identifying an analytical solution which yields accurate initial conditions has been studied extensively by Farquhar and Kamel [1973], and Richardson [1980a; 1980b].

Richardson developed a method for representing the three-body equations as a series expansion using Legendre polynomials [Richardson, 1980a; 1980b]. This method involves expressing the Lagrangian in terms of gravitational disturbing functions representing the gravity of the two primaries. Figure 4-8 shows a schematic of the three-body problem.

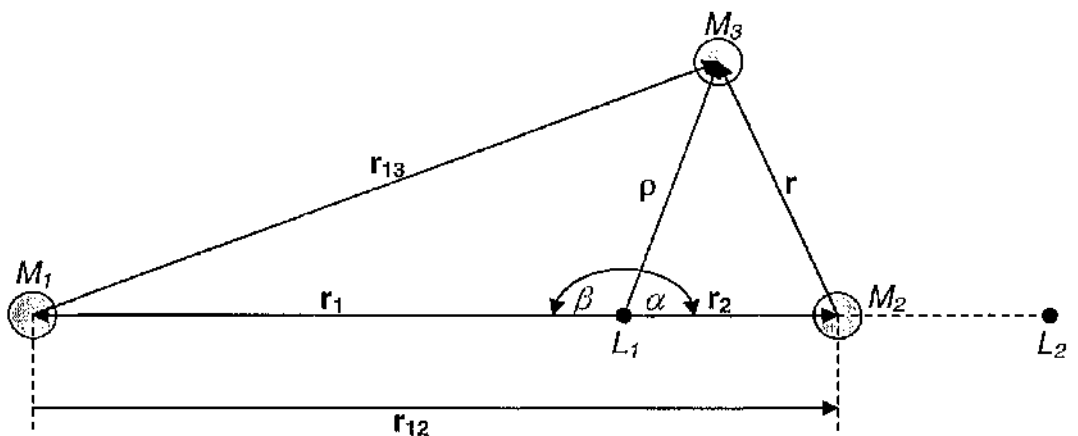


Figure 4-8 Schematic of three-body system with motion of M_3 derived relative to L_1

The vector position of mass M_3 relative to M_2 , \mathbf{r} , can be expressed as

$$\ddot{\mathbf{r}} = \mu \frac{\mathbf{r}}{|\mathbf{r}|^3} - (1 - \mu) \left(\frac{\mathbf{r}_{13}}{|\mathbf{r}_{13}|^3} - \frac{\mathbf{r}_{12}}{|\mathbf{r}_{12}|^3} \right) \quad (4.34)$$

where the expression is non-dimensionalised with mass ratio $\mu = M_2 / (M_1 + M_2)$ and $(1 - \mu) = M_1 / (M_1 + M_2)$. The characteristic length is selected as the separation distance between the two primaries $|\mathbf{r}_{12}|$ and the characteristic time is equivalent to $\tau = \Omega t$.

As $\ddot{\mathbf{r}} = -\nabla V$, where V is the potential function, the Lagrangian can be represented in terms of \mathbf{r} as

$$L = \frac{1}{2} (\dot{\mathbf{r}} \cdot \dot{\mathbf{r}}) + \frac{\mu}{\mathbf{r}} + (1 - \mu) \left(\frac{1}{|\mathbf{r}_{12} + \mathbf{r}|} + \frac{\mathbf{r}_{12} \cdot \mathbf{r}}{|\mathbf{r}_{12}|^3} \right) \quad (4.35)$$

where $\mathbf{r}_{13} = \mathbf{r}_{12} + \mathbf{r}$ and for the circular restricted case, $|\mathbf{r}_{12}|$ is constant.

The third right-hand term represents the disturbing function, perturbing the motion of M_3 relative to M_1 . By changing the coordinate system relative to the Lagrange points, it is possible to express the second right-hand term in a similar form. The vector, $\boldsymbol{\rho}$, represents the position of M_3 relative to L_1 , such that $\mathbf{r} = \boldsymbol{\rho} - \mathbf{r}_2$, which can be substituted into Eq (4.35) to obtain

$$L = \frac{1}{2} (\dot{\boldsymbol{\rho}} \cdot \dot{\boldsymbol{\rho}}) - \dot{\mathbf{r}}_2 \cdot \dot{\boldsymbol{\rho}} + \frac{1}{2} (\dot{\mathbf{r}}_2 \cdot \dot{\mathbf{r}}_2) + \frac{\mu}{|\boldsymbol{\rho} - \mathbf{r}_2|} + (1 - \mu) \left(\frac{1}{|\boldsymbol{\rho} - \mathbf{r}_1|} + \frac{\mathbf{r}_{12}}{|\mathbf{r}_{12}|^3} \cdot (\boldsymbol{\rho} - \mathbf{r}_2) \right) \quad (4.36)$$

where $\mathbf{r}_{12} + \mathbf{r} = \boldsymbol{\rho} - \mathbf{r}_1$ since $\mathbf{r}_{12} = \mathbf{r}_2 - \mathbf{r}_1$.

To remove the term $\mathbf{r}_{12} / |\mathbf{r}_{12}|^3$, the motion of M_2 relative to L_1 is expressed as

$$\ddot{\mathbf{r}}_2 = -(1 - \mu) \left(\frac{\mathbf{r}_{12}}{|\mathbf{r}_{12}|^3} + \frac{\mathbf{r}_1}{|\mathbf{r}_1|^3} \right) - \mu \frac{\mathbf{r}_2}{|\mathbf{r}_2|^3} \quad (4.37)$$

Re-arranging the expression and substituting the two-body equation $\ddot{\mathbf{r}}_2 + \mathbf{r}_2/|\mathbf{r}_{12}|^3 = 0$ yields

$$(1-\mu)\frac{\mathbf{r}_{12}}{|\mathbf{r}_{12}|^3} = \frac{\mathbf{r}_2}{|\mathbf{r}_{12}|^3} - (1-\mu)\frac{\mathbf{r}_1}{|\mathbf{r}_1|^3} - \mu\frac{\mathbf{r}_2}{|\mathbf{r}_2|^3} \quad (4.38)$$

This can be substituted into Eq (4.36) to obtain the Lagrangian in the form

$$L = \frac{1}{2}(\dot{\boldsymbol{\rho}} \cdot \dot{\boldsymbol{\rho}}) + \frac{\mathbf{r}_2 \cdot \boldsymbol{\rho}}{|\mathbf{r}_{12}|^3} - \dot{\mathbf{r}}_2 \cdot \dot{\boldsymbol{\rho}} + \mu \left(\frac{1}{|\boldsymbol{\rho} - \mathbf{r}_2|} - \frac{\mathbf{r}_2 \cdot \boldsymbol{\rho}}{|\mathbf{r}_2|^3} \right) + (1-\mu) \left(\frac{1}{|\boldsymbol{\rho} - \mathbf{r}_1|} - \frac{\mathbf{r}_1 \cdot \boldsymbol{\rho}}{|\mathbf{r}_1|^3} \right) + \Gamma \quad (4.39)$$

where Γ contains constant terms of \mathbf{r}_1 , \mathbf{r}_2 and \mathbf{r}_{12} .

The second and third terms in Eq (4.39) can be combined using the identity

$$\frac{\mathbf{r}_2 \cdot \boldsymbol{\rho}}{|\mathbf{r}_{12}|^3} - \dot{\mathbf{r}}_2 \cdot \dot{\boldsymbol{\rho}} = -\frac{d}{dt}(\boldsymbol{\rho} \cdot \dot{\mathbf{r}}_2) \quad (4.40)$$

which allows a new Lagrangian, $L^* = L + \frac{d}{dt}(\boldsymbol{\rho} \cdot \dot{\mathbf{r}}_2)$, to be expressed as

$$L^* = \frac{1}{2}(\dot{\boldsymbol{\rho}} \cdot \dot{\boldsymbol{\rho}}) + \mu \left(\frac{1}{|\boldsymbol{\rho} - \mathbf{r}_2|} - \frac{\mathbf{r}_2 \cdot \boldsymbol{\rho}}{|\mathbf{r}_2|^3} \right) + (1-\mu) \left(\frac{1}{|\boldsymbol{\rho} - \mathbf{r}_1|} - \frac{\mathbf{r}_1 \cdot \boldsymbol{\rho}}{|\mathbf{r}_1|^3} \right) \quad (4.41)$$

ignoring the constant term, Γ .

The scalar products in the second and third terms can be expressed as $\mathbf{r}_2 \cdot \boldsymbol{\rho} = |\mathbf{r}_2||\boldsymbol{\rho}|\cos\alpha$ and $\mathbf{r}_1 \cdot \boldsymbol{\rho} = |\mathbf{r}_1||\boldsymbol{\rho}|\cos\beta$, where α is the angle between $\boldsymbol{\rho}$ and \mathbf{r}_2 , and β is the angle between $\boldsymbol{\rho}$ and \mathbf{r}_1 . The Lagrangian can be expressed as

$$L^* = \frac{1}{2}(\dot{\boldsymbol{\rho}} \cdot \dot{\boldsymbol{\rho}}) + \frac{\mu}{|\mathbf{r}_2|} \left(\frac{|\mathbf{r}_2|}{|\boldsymbol{\rho} - \mathbf{r}_2|} - \frac{|\boldsymbol{\rho}|\cos\alpha}{|\mathbf{r}_2|} \right) + \frac{(1-\mu)}{|\mathbf{r}_1|} \left(\frac{|\mathbf{r}_1|}{|\boldsymbol{\rho} - \mathbf{r}_1|} - \frac{|\boldsymbol{\rho}|\cos\beta}{|\mathbf{r}_1|} \right) \quad (4.42)$$

As demonstrated by Thurman and Worfolk [1996], the first terms in either brackets can be written as

$$\frac{|r_2|}{|\rho - r_2|} = \left(1 - 2 \frac{|\rho|}{|r_2|} \cos \alpha + \left(\frac{|\rho|}{|r_2|} \right)^2 \right)^{-1/2} \quad (4.43.1)$$

$$\frac{|r_1|}{|\rho - r_1|} = \left(1 - 2 \frac{|\rho|}{|r_1|} \cos \beta + \left(\frac{|\rho|}{|r_1|} \right)^2 \right)^{-1/2} \quad (4.43.2)$$

Equation (4.43.1) can be expressed as $|r_2|/|\rho - r_1| = (1 + q)^{-1/2}$, where $q = j^2 - 2j \cos \alpha$ and $j = |\rho|/|r_2|$. Expanding using Taylor's formula yields the expression

$$(1 + q)^{-1/2} = \sum_{k \geq 0} (-1)^k \frac{(2k)}{(2^k k!)^2} q^k \quad (4.44)$$

Using a binomial expansion of q^k yields

$$q^k = \sum_{l=0}^k \frac{k!}{l!(k-l)!} j^{k+l} (-2)^{k-l} \cos^{k-l} \alpha \quad (4.45)$$

Substituting Eq (4.45) into Eq (4.44) obtains

$$(1 + q)^{-1/2} = \sum_{k \geq 0} \sum_{l=0}^k (-1)^l \frac{(2k)!}{2^{k-l} k!(k-l)!l!} \cos^{k-l} \alpha j^{k+l} \quad (4.46)$$

As demonstrated by Barrabés [2004], the summation index can be replaced by $n = k + l$ to obtain

$$(1 + q)^{-1/2} = \sum_{n \geq 0} \sum_{l=0}^{n/2} (-1)^l \frac{(2n-2l)!}{2^n (n-l)!(n-2l)!l!} \cos^{n-2l} \alpha j^n \quad (4.47)$$

This represents a power series of $j = |\rho|/|r_2|$ with coefficients which are polynomials of $\cos \alpha$. A similar expression can be derived for Eq (4.43.2) where $j = |\rho|/|r_1|$ and the coefficients are polynomials of $\cos \beta$.

Equation (4.47) can be re-written in terms of Legendre polynomials, $P_n(z)$ where

$$P_n(z) = \frac{1}{2^n n!} \frac{d^n}{dz^n} (z^2 - 1)^n \quad (4.48)$$

Using binomial theorem to expand the brackets, the n^{th} derivative can be represented as

$$P_n(z) = \sum_{l=0}^{n/2} (-1)^l \frac{n!}{l!(n-l)!} \frac{(2n-2l)!}{(n-2l)!} z^{n-2l} \quad (4.49)$$

From Eq (4.47), it is clear that z corresponds to $\cos \alpha$ (or $\cos \beta$ in the case of $j = |\mathbf{p}|/|\mathbf{r}_1|$) which yields

$$\frac{r_2}{|\mathbf{p} - \mathbf{r}_2|} = \sum_{n \geq 0} P_n(\cos \alpha) \left(\frac{\mathbf{p}}{r_2} \right)^n \quad (4.50.1)$$

$$\frac{r_1}{|\mathbf{p} - \mathbf{r}_1|} = \sum_{n \geq 0} P_n(\cos \beta) \left(\frac{\mathbf{p}}{r_1} \right)^n \quad (4.50.2)$$

These expressions can be substituted into Eq (4.42) to obtain

$$L^* = \frac{1}{2} (\dot{\mathbf{p}} \cdot \dot{\mathbf{p}}) + \frac{\mu}{|\mathbf{r}_2|} \left(1 + \sum_{n \geq 2} \left(\frac{\mathbf{p}}{r_2} \right)^n P_n(\cos \alpha) \right) + \frac{(1-\mu)}{|\mathbf{r}_1|} \left(1 + \sum_{n \geq 2} \left(\frac{\mathbf{p}}{r_1} \right)^n P_n(\cos \beta) \right) \quad (4.51)$$

It is convenient to normalize the distances so that the separation between the libration point and M_2 , $|\mathbf{r}_2| = 1$. This can be achieved using the dimensionless parameter, $\gamma = r_2/|\mathbf{r}_{21}|$, where $\tilde{\mathbf{p}} = \mathbf{p}/\gamma$ and $\tilde{\mathbf{p}} = \xi \hat{\mathbf{i}} + \eta \hat{\mathbf{j}} + \zeta \hat{\mathbf{k}}$. From Fig 4-8, $\cos \alpha = \xi/|\tilde{\mathbf{p}}|$ and $\cos \beta = -\xi/|\tilde{\mathbf{p}}|$ at L_1 and using the relationship of Legendre polynomials, $P_n(-z) = (-1)^n P_n(z)$, the Lagrangian can be expressed as

$$L^* = \frac{1}{2} (\dot{\tilde{\mathbf{p}}} \cdot \dot{\tilde{\mathbf{p}}}) + \sum_{n \geq 2} c_n |\tilde{\mathbf{p}}|^n P_n \left(\frac{\xi}{|\tilde{\mathbf{p}}|} \right) \quad (4.52)$$

Since $|\mathbf{r}_1| \pm |\mathbf{r}_2| = 1$, the constant c_n is equivalent to

$$c_n = \gamma^{-3} \left((\pm 1)^n \mu + (-1)^n \frac{(1-\mu)\gamma^{n+1}}{(1\mp\gamma)^{n+1}} \right) \quad (4.53)$$

where the upper sign refers to L_1 and the lower sign to L_2 .

The Lagrange equation can be applied to obtain the following equations of motion

$$\ddot{\xi} - 2\dot{\eta} - \xi = \frac{\partial}{\partial \xi} \sum_{n \geq 2} c_n |\tilde{\rho}|^n P_n \left(\frac{\xi}{|\tilde{\rho}|} \right) \quad (4.54.1)$$

$$\ddot{\eta} + 2\dot{\xi} - \eta = \frac{\partial}{\partial \eta} \sum_{n \geq 2} c_n |\tilde{\rho}|^n P_n \left(\frac{\xi}{|\tilde{\rho}|} \right) \quad (4.54.2)$$

$$\dot{\xi} = \frac{\partial}{\partial \xi} \sum_{n \geq 2} c_n |\tilde{\rho}|^n P_n \left(\frac{\xi}{|\tilde{\rho}|} \right) \quad (4.54.3)$$

The Legendre polynomials can be expressed via the recursion relation

$$P_n(z) = \left(\frac{2n-1}{n} z \right) P_{n-1} - \left(\frac{n-1}{n} \right) P_{n-2} \quad (4.55)$$

where $P_0(z) = 1$ and $P_1(z) = z$ [Thurman and Worfolk, 1996]. This enables Eqns (4.54) to be evaluated as a series where by increasing the number of terms improves the accuracy of the approximation.

4.4.2 Approximate periodic solution

The Lindstedt-Poincaré perturbation technique can be applied to find an asymptotic approximation to the periodic solution of Eqns (4.54). This method uses a frequency variation represented by $\omega(\varepsilon) = \omega_0 + \varepsilon\omega_1 + \varepsilon^2\omega_2$ to remove secular terms from the solution where the linear system frequency $\omega_0=1$ [Nayfeh, 1973]. Secular terms are unbounded, growing over time resulting in eventual escape from the periodic orbit. These terms include those where the time variable appears as a coefficient or those which result in groups of trigonometric terms in the solution causing unbounded motion.

Using a time variable $\bar{\tau} = \omega(\varepsilon)\tau$, the time derivative can be represented as $(\)' = \omega d/d\bar{\tau}$. Equations (4.54) can be expanded to the third order as

$$\omega^2 \xi'' - 2\omega \eta' - (1 + 2c_2)\xi = \frac{3}{2}c_3(2\xi^2 - \eta^2 - \zeta^2) + 2c_4\xi(2\xi^2 - 3\eta^2 - 3\zeta^2) \quad (4.56.1)$$

$$\omega^2 \eta'' + 2\omega \xi' + (c_2 - 1)\eta = -3c_3\xi\eta - \frac{3}{2}c_4\eta(4\xi^2 - \eta^2 - \zeta^2) \quad (4.56.2)$$

$$\omega^2 \zeta'' + \lambda^2 \zeta = -3c_3\xi\eta - \frac{3}{2}c_4\eta(4\xi^2 - \eta^2 - \zeta^2) + \Delta \zeta \quad (4.56.3)$$

The correction term, Δ , is assumed to have order of magnitude $\Delta(\varepsilon^2)$, where $\Delta = \lambda^2 - c_2$. The correction term is required to ensure the ratio of in-plane and out-of-plane frequencies is rational, producing periodic orbits as opposed to the quasi-periodic trajectories demonstrated in Hill's approximation.

The position coordinates can similarly be represented as $\xi(\varepsilon) = \varepsilon\xi_1 + \varepsilon^2\xi_2 + \varepsilon^3\xi_3$, $\eta(\varepsilon) = \varepsilon\eta_1 + \varepsilon^2\eta_2 + \varepsilon^3\eta_3$ and $\zeta(\varepsilon) = \varepsilon\zeta_1 + \varepsilon^2\zeta_2 + \varepsilon^3\zeta_3$. A general solution can be derived by substituting the power series representing frequency and position into Eqns (4.56). This can be achieved by evaluating particular integrals at each of the powers of the perturbing parameter ε . Richardson [1980a; 1980b] derived a solution up to order, ε^3 , using the frequency constants to remove secular terms leading to a periodic solution. The technique which results in Richardson's solution is outlined below.

4.4.2.1 Linear solution

Grouping terms which contain a perturbing parameter of order ε , yields the linear equations

$$\xi_1'' - 2\eta_1' - (1 + 2c_2)\xi_1 = 0 \quad (4.57.1)$$

$$\eta_1'' + 2\xi_1' + (c_2 - 1)\eta_1 = 0 \quad (4.57.2)$$

$$\zeta_1'' + \lambda^2 \zeta_1 = 0 \quad (4.57.3)$$

A solution to the linear equations can be obtained by forming a matrix and extracting the eigenvalues and corresponding eigenvectors. For the in-plane case, a 2x2 matrix is formed using the vector $\mathbf{Q} = [\xi \quad \eta]^T$ as

$$\begin{bmatrix} 1 & 0 \\ 0 & 1 \end{bmatrix} \mathbf{Q}'' + \begin{bmatrix} 0 & -2 \\ 2 & 0 \end{bmatrix} \mathbf{Q}' + \begin{bmatrix} -(1+2c_2) & 0 \\ 0 & (c_2-1) \end{bmatrix} \mathbf{Q} = 0 \quad (4.58)$$

Assuming that $\mathbf{Q} = \mathbf{Q}_0 \exp(\lambda \tilde{\tau})$, the resulting characteristic equation can be expressed as

$$\lambda^4 + (2 - c_2)\lambda^2 - 2c_2^2 + c_2 + 1 \quad (4.59)$$

Equation (4.59) yields two real and two imaginary eigenvalues as demonstrated in previous examples. The eigenvalues have the form

$$\lambda_{1,2} = \sqrt{\frac{(c_2 - 2) + \sqrt{9c_2^2 - 8c_2}}{2}} \quad (4.60.1)$$

$$\lambda_{3,4} = \sqrt{\frac{(c_2 - 2) - \sqrt{9c_2^2 - 8c_2}}{2}} \quad (4.60.2)$$

where $\lambda_{1,2}$ are real eigenvalues and $\lambda_{3,4}$ are imaginary eigenvalues. As the linear equations contain both oscillatory and divergent modes, this confirms that the on-axis libration points are unstable.

The corresponding eigenvectors relating ξ to η can be expressed as

$$v_{\eta i} = \frac{-2\lambda_i}{\lambda_i^2 + c_2 - 1} v_{\xi i} \quad (4.61)$$

where the index $i=(1,2,3,4)$. Eigenvectors $v_{\eta i}$ and $v_{\xi i}$ correspond to the ξ - and η - axis respectively. The solution to the linear equations can be expressed in terms of the eigenvalues and eigenvectors as

$$\xi(\tilde{\tau}) = \sum_{i=1}^4 a_i v_{\xi i} \exp(\lambda_i \tilde{\tau}) \quad (4.62.1)$$

$$\eta(\tilde{\tau}) = \sum_{i=1}^4 a_i \nu_{\eta i} \exp(\lambda_i \tilde{\tau}) \quad (4.62.2)$$

where a represents a constant matrix. The real eigenvalues, $\lambda_{1,2}$, result in asymptotically increasing terms and can be suppressed by setting $a_1=a_2=0$, as demonstrated in Chapter 3. The oscillatory terms containing imaginary eigenvalues can be expressed as

$$\xi_1(\tilde{\tau}) = -A_x \cos(\lambda \tilde{\tau} + \phi) \quad (4.63.1)$$

$$\eta_1(\tilde{\tau}) = kA_x \sin(\lambda \tilde{\tau} + \phi) \quad (4.63.2)$$

where A_x denotes the x -axis amplitude and ϕ represents the phase angle.

The imaginary part of eigenvalues $\lambda_{3,4}$ is represented by λ where k represents the relationship between the ξ - and η -axis evaluated at λ . These terms can be expressed as

$$\lambda = \sqrt{-\frac{(c_2 - 2) - \sqrt{9c_2^2 - 8c_2}}{2}} \quad (4.64.1)$$

$$k = \frac{2\lambda}{\lambda + 1 - c_2} \quad (4.64.2)$$

To ensure the orbit is periodic, the solution for the out-of-plane motion is required to be

$$\zeta_1(\tilde{\tau}) = A_z \sin(\lambda \tilde{\tau} + \phi) \quad (4.65)$$

where A_z is the z -axis amplitude and ϕ represents the phase angle. These expressions represent the 1st order solution which can be used to evaluate higher order expressions. Following the notation used by Thurman and Worfolk [1996], the frequency terms will be represented by $\tau_1 = \lambda \tilde{\tau} + \phi$ and $\tau_2 = \lambda \tilde{\tau} + \phi$.

4.4.2.2 Second order solution

The second order solution is evaluated by collecting perturbing parameter terms of order ϵ^2 , which yields the equations

$$\xi_2'' - 2\eta_2' - (1 + 2c_2)\xi_2 = -2\omega_1(\xi_1'' - \eta_1') + \frac{3}{2}c_3(2\xi_1^2 - \eta_1^2 - \zeta_1^2) \quad (4.66.1)$$

$$\eta_2'' + 2\xi_2' + (c_2 - 1)\eta_2 = -2\omega_1(\eta_1'' + \xi_1') - 3c_3\xi_1\eta_1 \quad (4.66.2)$$

$$\zeta_2'' + \lambda^2\zeta_2 = -2\omega_1\zeta_1'' - 3c_3\xi_1\zeta_1 \quad (4.66.3)$$

The solution to the 1st order terms ξ_1 , η_1 and ζ_1 have been obtained previously and can be substituted into these equations to obtain

$$\xi_2'' - 2\eta_2' - (1 + 2c_2)\xi_2 = 2\omega_1 A_x \lambda (k - \lambda) \cos \tau_1 + 3c_3 A_x^2 \cos^2 \tau_1 - \frac{3}{2}c_3 (k^2 A_x^2 \sin^2 \tau_1 + A_z^2 \sin^2 \tau_2) \quad (4.67.1)$$

$$\eta_2'' + 2\xi_2' + (c_2 - 1)\eta_2 = 2\omega_1 A_x \lambda (k\lambda - 1) \sin \tau_1 + 3c_3 k A_x^2 \cos \tau_1 \sin \tau_1 \quad (4.67.2)$$

$$\zeta_2'' + \lambda^2\zeta_2 = 2\omega_1 A_z \lambda^2 \cos \tau_2 + 3c_3 A_x A_z \cos \tau_1 \sin \tau_2 \quad (4.67.3)$$

The equations can be reduced by substituting the trigonometric relationships

$$2 \cos^2 \tau_1 = \cos 2\tau_1 + 1 \quad (4.68.1)$$

$$2 \sin^2 \tau_1 = -\cos 2\tau_1 + 1 \quad (4.68.2)$$

$$2 \cos \tau_1 \sin \tau_2 = \sin(\tau_1 + \tau_2) + \sin(\tau_2 - \tau_1) \quad (4.68.3)$$

$$2 \cos \tau_1 \sin \tau_1 = \sin 2\tau_1 \quad (4.68.4)$$

The secular terms present in Eq (4.67.1) and (4.67.2) contain $\cos \tau_1$ and $\sin \tau_1$. The coefficients for these terms are $2\omega_1 A_x \lambda (k - \lambda)$ and $2\omega_1 A_x \lambda (k\lambda - 1)$ respectively and can be easily removed by setting $\omega_1 = 0$. The equations can then be re-written in the form

$$\xi_2'' - 2\eta_2' - (1 + 2c_2)\xi_2 = \alpha_{20} + \alpha_{21} \cos 2\tau_1 + \alpha_{22} \cos 2\tau_2 \quad (4.69.1)$$

$$\eta_2'' + 2\xi_2' + (c_2 - 1)\eta_2 = \beta_{21} \sin 2\tau_1 \quad (4.69.2)$$

$$\zeta_2'' + \lambda^2\zeta_2 = \gamma_{21} \sin(\tau_1 + \tau_2) + \gamma_{22} \sin(\tau_2 - \tau_1) \quad (4.69.3)$$

where the coefficients are provided in Appendix 1. To solve these equations for ξ_2 , η_2 and ζ_2 it can be assumed that the solutions have the form

$$\xi_2(\tilde{\tau}) = \rho_{20} + \rho_{21} \cos 2\tau_1 + \rho_{22} \cos 2\tau_2 \quad (4.70.1)$$

$$\eta_2(\tilde{\tau}) = \sigma_{21} \sin 2\tau_1 + \sigma_{22} \sin 2\tau_2 \quad (4.70.2)$$

$$\zeta_2(\tilde{\tau}) = \delta_{21} \sin(\tau_1 + \tau_2) + \delta_{22} \sin(\tau_2 - \tau_1) \quad (4.70.3)$$

The coefficients are determined by substituting these solutions into Eqns (4.69) and grouping the trigonometric terms. The time derivatives are evaluated as

$$\xi_2'(\tilde{\tau}) = -2\lambda\rho_{21} \sin 2\tau_1 - 2\lambda\rho_{22} \sin 2\tau_2 \quad (4.71.1)$$

$$\xi_2''(\tilde{\tau}) = -4\lambda^2\rho_{21} \cos 2\tau_1 - 4\lambda^2\rho_{22} \cos 2\tau_2 \quad (4.71.2)$$

$$\eta_2'(\tilde{\tau}) = 2\lambda\sigma_{21} \cos 2\tau_1 + 2\lambda\sigma_{22} \cos 2\tau_2 \quad (4.71.3)$$

$$\eta_2''(\tilde{\tau}) = -4\lambda^2\sigma_{21} \sin 2\tau_1 - 4\lambda^2\sigma_{22} \sin 2\tau_2 \quad (4.71.4)$$

$$\zeta_2'(\tilde{\tau}) = 2\delta_{21}\lambda \cos(\tau_1 + \tau_2) \quad (4.71.5)$$

$$\zeta_2''(\tilde{\tau}) = -4\delta_{21}\lambda^2 \sin(\tau_1 + \tau_2) \quad (4.71.6)$$

Firstly, the constant terms can be equated to obtain the coefficient

$$\rho_{20} = \frac{-\alpha_{20}}{(1 + 2c_2)} \quad (4.72)$$

Grouping the corresponding trigonometric terms yields the following systems of equations which are used to identify the remaining coefficients for the dependant variables

$$(-4\lambda^2 + c_2 - 1)\sigma_{21} - 4\lambda\rho_{21} = \beta_{21} \quad (4.73.1)$$

$$(-4\lambda^2 - 1 - 2c_2)\rho_{21} - 4\lambda\sigma_{21} = \alpha_{21} \quad (4.73.2)$$

$$(-4\lambda^2 + c_2 - 1)\sigma_{22} - 4\lambda\rho_{22} = 0 \quad (4.73.3)$$

$$(-4\lambda^2 - 1 - 2c_2)\rho_{22} - 4\lambda\sigma_{22} = \alpha_{22} \quad (4.73.4)$$

The coefficients σ_{21} , σ_{22} , ρ_{21} , ρ_{22} are evaluated in terms of λ , c_2 , β_{21} , α_{21} and α_{22} . The resulting expression are provided in Appendix 1.

In the case of the dependant variable, ζ_2 , the derivatives represented by Eq (4.71.5) and Eq (4.71.6) are substituted into Eq (4.69.3) to obtain

$$-4\delta_{21}\lambda^2 \sin(\tau_1 + \tau_2) + \lambda^2 \delta_{21} \sin(\tau_1 + \tau_2) + \lambda^2 \delta_{22} \sin(\tau_2 - \tau_1) = \gamma_{21} \sin(\tau_1 + \tau_2) + \gamma_{22} \sin(\tau_2 - \tau_1) \quad (4.74)$$

Again, grouping the $\sin(\tau_1 + \tau_2)$ and $\sin(\tau_2 - \tau_1)$ terms and solving for δ_{21} and δ_{22} leads to the coefficients

$$\delta_{21} = -\frac{\gamma_{21}}{3\lambda} \quad (4.75.1)$$

$$\delta_{22} = \frac{\gamma_{22}}{\lambda} \quad (4.75.2)$$

Having obtained the expressions for the coefficients, Eqns (4.70) now represent particular solutions of the second order equations. This can be used to evaluate the coefficients in the third order approximation.

4.4.2.3 Third order solution

The third order solution is evaluated by collecting perturbing parameter terms of order ε^3 and noting that $\omega_1 = 0$ from the second order solution, which yields the equations

$$\begin{aligned} \xi_3'' - 2\eta_3' - (1 + 2c_2)\xi_3 = -2\omega_2(\xi_1'' - \eta_1') + \frac{3}{2}c_3(2\xi_1\xi_2 - \eta_1\eta_2 - \zeta_1\zeta_2) \\ + 2c_4\xi_1(2\xi_1^2 - 3\eta_1^2 - 3\zeta_1^2) \end{aligned} \quad (4.76.1)$$

$$\begin{aligned} \eta_2'' + 2\xi_2' + (c_2 - 1)\eta_2 = -2\omega_2(\eta_1' + \xi_1') - 3c_3(\xi_1\eta_2 + \xi_2\eta_1) \\ - \frac{3}{2}c_4\eta_1(4\xi_1^2 - \eta_1^2 - \zeta_1^2) \end{aligned} \quad (4.76.2)$$

$$\zeta_2'' + \lambda^2\zeta_2 = -2\omega_2\zeta_1'' - 3c_3(\xi_1\zeta_2 + \xi_2\zeta_1) - \frac{3}{2}c_4\zeta_1(4\xi_1^2 - \eta_1^2 - \zeta_1^2) + \Delta\zeta_1 \quad (4.76.3)$$

The previously obtained solutions to the linear and second order terms can be substituted into these expressions which can be solved for third order terms ξ_3 , η_3 and ζ_3 . Richardson noted that after substitution, the expressions can be reduced to the following form

$$\begin{aligned} \xi_3'' - 2\eta_3 - (1 + 2c_2)\xi_3 = & [\alpha_{31} + 2\omega_2 A_x \lambda(k - \lambda)] \cos \tau_1 + \alpha_{32} \cos 3\tau_1 \\ & + \alpha_{33} \cos(\tau_1 + 2\tau_2) + \alpha_{34} \cos(2\tau_2 - \tau_1) \end{aligned} \quad (4.77.1)$$

$$\begin{aligned} \eta_3'' + 2\xi_3' - (1 - c_2)\eta_3 = & [\beta_{31} + 2\omega_2 A_z \lambda(k\lambda - 1)] \sin \tau_1 + \beta_{32} \sin 3\tau_1 \\ & + \beta_{33} \sin(\tau_1 + 2\tau_2) + \beta_{34} \cos(2\tau_2 - \tau_1) \end{aligned} \quad (4.77.2)$$

$$\begin{aligned} \zeta_3'' + \lambda^2 \zeta_3 = & [\gamma_{31} + A_z (2\omega_2 \lambda^2 + \Delta)] \sin \tau_2 + \gamma_{32} \sin 3\tau_2 \\ & + \gamma_{33} \sin(2\tau_1 + \tau_2) + \gamma_{34} \sin(2\tau_2 - \tau_1) \end{aligned} \quad (4.77.3)$$

where the coefficients are provided in Appendix 1 [Kim and Hall, 2001; Thurman and Worfolk, 1996].

The secular terms in Eq (4.77.3) are $\sin(2\tau_1 - \tau_2)$ and $\sin \tau_2$. These terms are removed by adjusting the phase angles such that $\phi = \varphi + n\pi/2$, where integer $n=0,1,2,3$. The term $\sin(2\tau_1 - \tau_2) = \sin \tau_2$ if the value of $n=0,2$ and $\sin(2\tau_1 - \tau_2) = -\sin \tau_2$ if $n=1,3$. Combining the $\sin \tau_2$ expressions, it is clear that removal of secular terms from Eq (4.77.3) is achieved provided

$$\gamma_{31} + A_z (2\omega_2 \lambda^2 + \Delta) + (-1)^n \gamma_{34} = 0 \quad (4.78)$$

To remove secular terms from Eq (4.77.1) and Eq (4.77.2), the constraint derived by Richardson [1980a] is defined as

$$\omega_2 = s_1 A_x^2 + s_2 A_z^2 \quad (4.79)$$

where s_1 and s_2 are provided in Appendix 1. Substituting into the constraint defined in Eq (4.78) leads to the expression

$$l_1 A_x^2 + l_2 A_z^2 + \Delta = 0 \quad (4.80)$$

This expression imposes a constraining relationship between the in-plane and out-of-plane amplitudes, A_x and A_z , to ensure removal of secular terms from the solution. A complete third order solution after removal of the secular terms is provided by Thurman and Worfolk [1996].

The final solution obtained by Richardson [1980a] is provided below

$$\xi(\tau_1) = a_{21}A_x^2 + a_{22}A_z^2 - A_x \cos \tau_1 + (a_{23}A_x^2 - a_{24}A_z^2) \cos 2\tau_1 + (a_{31}A_x^3 - a_{32}A_xA_z^2) \cos 3\tau_1 \quad (4.81.1)$$

$$\eta(\tau_1) = kA_x \sin \tau_1 + (b_{21}A_x^2 - b_{22}A_z^2) \sin 2\tau_1 + (b_{31}A_x^3 - b_{32}A_xA_z^2) \sin 3\tau_1 \quad (4.81.2)$$

$$\zeta(\tau_1) = \begin{cases} +A_z \cos \tau_1 + d_{21}A_xA_z(\cos 2\tau_1 - 3) + (d_{32}A_zA_x^2 - d_{31}A_z^3) \cos 3\tau_1 & n=0,2 \\ -A_z \cos \tau_1 - d_{21}A_xA_z(\cos 2\tau_1 - 3) - (d_{32}A_zA_x^2 - d_{31}A_z^3) \cos 3\tau_1 & n=1,3 \end{cases} \quad (4.81.3)$$

This solution is achieved by adding the particular solutions calculated at each order of perturbing parameter, ε . They are expressed in terms of the in-plane and out-of-plane amplitudes, A_x and A_z , which are constrained by Eq (4.80). As a consequence of the phase constraint $\phi = \varphi + n\pi/2$, two equations are obtained for the out-of-plane solution, $\zeta(\tau_1)$. Farquhar and Kamel [1973] demonstrated that this constraint leads to two different classes of orbit, shown in Fig 4-9. Class I occurs for $n=0,2$ and Class II occurs when $n=1,3$.

These solutions define a nominal halo orbit in the three-body problem where the ratio of the in-plane and out-of-plane frequency is rational. Evaluating this expression at $\tilde{\tau} = 0$ yields initial conditions which converge toward halo orbits around the libration points. Several authors have investigated halo orbits around the collinear Lagrange points of the three-body problem [Farquhar, 1970a; 1973; Breakwell and Brown, 1979; Richardson, 1980a; 1980b; 1980c; Howell, 1984]. It will be demonstrated that similar methods can be applied to generate halo orbits around an artificial libration point using a solar sail.

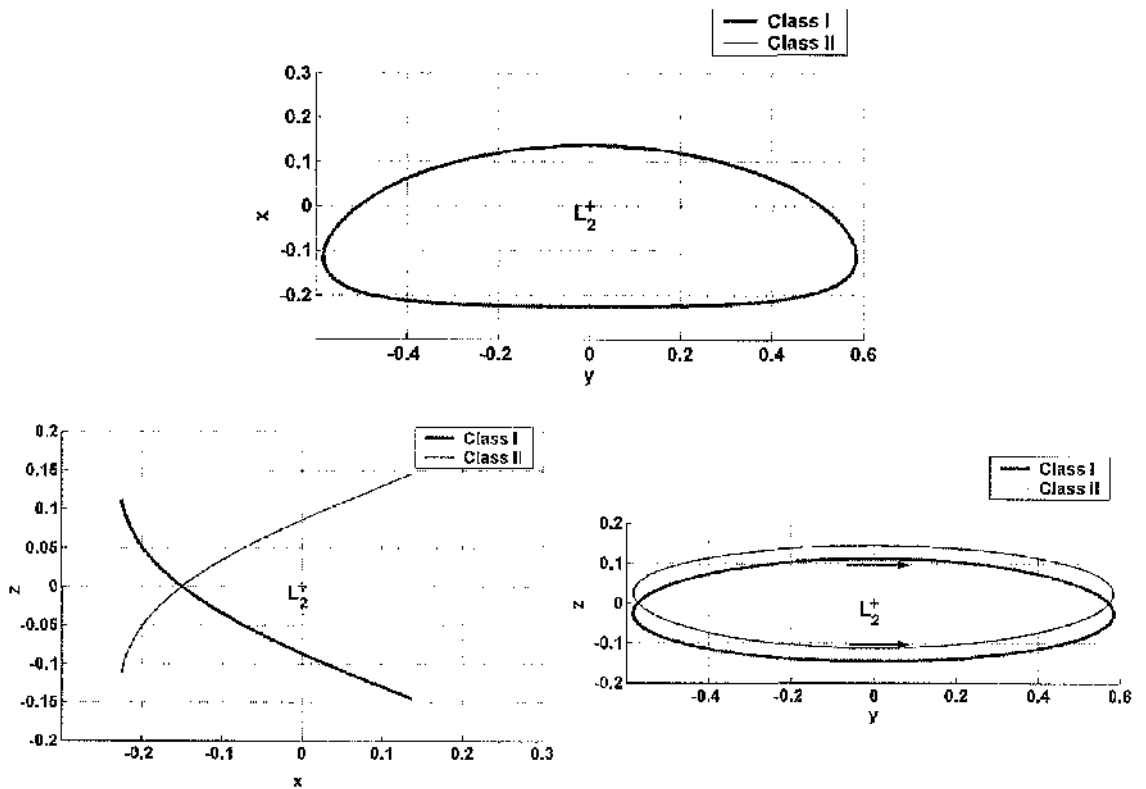


Figure 4-9 Class I and Class II halo orbits around L_2 of Sun-Earth system ($A_x=280,000\text{km}$)

4.4.3 Halo orbits around artificial libration points

4.4.3.1 Differential correction methods

The coefficients of the third order solution, provided in Appendix 1, are evaluated at the artificial libration point. For a required z-axis amplitude, A_z , Eq (4.80) can be solved to determine a value of x-axis amplitude, A_x , which suppresses divergent terms. The amplitudes and evaluated coefficients can then be substituted into Eq (4.81), and evaluating at time $\tau_f=0$ yields a set of initial position conditions. The 1st order derivatives, with respect to time, of Eq (4.81) can also be determined to yield a set of initial velocity conditions. These conditions do not immediately produce periodic halo-orbits within the non-linear three-body equations but do provide a solution which converges toward a periodic halo orbit after applying a differential correction method.

A numerical method is developed similar to that used by Breakwell and Brown [1979], and Howell [1984]. This method uses the Matlab 5th order Runge-Kutta integrator to numerically integrate a periodic orbit with period T starting at the initial conditions $\mathbf{x}_0 = [x_0 \ 0 \ z_0 \ 0 \ \dot{y}_0 \ 0]^T$ and integrating until time $T/2$. The integration time of $T/2$ is

indicated when $|y| < 1 \times 10^{-11}$, at which point the time and orbit conditions are stored. To achieve this precision requires the integrator to step forward until $y < 0$. The step-size is then reduced and the integration is repeated starting at conditions near $T/2$. In this way, precision is improved without greatly increasing the integration time.

The linearised equations can be represented in the form of a state equation $\dot{\mathbf{x}} = \mathbf{A}\mathbf{x}$, where the state vector $\mathbf{x} = [x \ y \ z \ \dot{x} \ \dot{y} \ \dot{z}]^T$ and the linear coefficient matrix is defined as

$$\mathbf{A} = \begin{bmatrix} 0 & 0 & 0 & 1 & 0 & 0 \\ 0 & 0 & 0 & 0 & 1 & 0 \\ 0 & 0 & 0 & 0 & 0 & 1 \\ U_{xx} & U_{xy} & U_{xz} & 0 & 2 & 0 \\ U_{yx} & U_{yy} & U_{yz} & -2 & 0 & 0 \\ U_{zx} & U_{zx} & U_{zz} & 0 & 0 & 0 \end{bmatrix} \quad (4.82)$$

where the partial derivatives of the pseudo-potential

$$U = \frac{1}{2}(x^2 + y^2) + \frac{(1-\mu)}{|\mathbf{r}_1|} + \frac{\mu}{|\mathbf{r}_2|} \quad (4.83)$$

are represented as U_{ij} for $i, j = \{x, y, z\}$. These derivatives are evaluated at the on-axis libration point where $x_o = \gamma$, $y_o = 0$ and $z_o = 0$.

The eigenvalues and eigenvectors of the linear coefficient matrix \mathbf{A} can be used to form a fundamental solution matrix $\Phi(t)$ with solution $\mathbf{x}(t) = \Phi(t)\mathbf{x}_o$. The solution of the linear state equation can be expressed as $\mathbf{x}(t) = \exp(t\mathbf{A})\mathbf{x}_o$, which suggests $\Phi(t) = \exp(t\mathbf{A})$. The eigenvalues and eigenvectors of the linear coefficient matrix are represented by matrices Λ and P respectively, where $\mathbf{A}P = \Lambda P$. As demonstrated by Glendinning [1994], the transform $\mathbf{x} = P\mathbf{y}$ can be applied to form a fundamental matrix using the eigenvalues and eigenvectors Λ and P .

It follows that $\mathbf{y} = P^{-1}\mathbf{x}$ which has time derivative $\dot{\mathbf{y}} = P^{-1}\dot{\mathbf{x}}$. Substituting the state equation gives $\dot{\mathbf{y}} = P^{-1}\mathbf{A}\mathbf{x} = P^{-1}\mathbf{A}P\mathbf{y}$. The relationship between the eigenvalues and eigenvectors can be re-arranged as $\Lambda = P^{-1}\mathbf{A}P$ which obtains the state equation $\dot{\mathbf{y}} = \Lambda\mathbf{y}$.

This state equation has the solution $\mathbf{y}(t) = \exp(t\Lambda)\mathbf{y}_0$ and further substitution obtains the expression $\mathbf{x}(t) = P \exp(t\Lambda)P^{-1}\mathbf{x}_0$. Comparing the solutions for $\mathbf{x}(t)$ proves that $\Phi(t) = \exp(tA) = P \exp(t\Lambda)P^{-1}$, where Λ is a diagonal matrix of eigenvalues. The fundamental matrix evaluated at $t=0$ is equivalent to a 6x6 identity matrix, $\Phi(0) = I_{6 \times 6}$.

The required variation of the initial conditions, $\delta\mathbf{x}$, is calculated using the relationship

$$\delta\mathbf{x} \approx \Phi(T/2, 0)\delta\mathbf{x}_0 + \frac{\partial\mathbf{x}}{\partial t}\delta(T/2) \quad (4.84)$$

where $\Phi(T/2, 0)$ is the fundamental matrix evaluated at time $T/2$ [Breakwell and Brown, 1979; Howell, 1984].

For a periodic orbit at time $T/2$, $\delta\mathbf{y} = 0$ and as the initial conditions $\delta\dot{\mathbf{x}} = \delta\dot{\mathbf{z}} = 0$, Eq (4.84) leads to the expression

$$\phi_{21}\delta x_o + \phi_{23}\delta z_o + \phi_{25}\delta y_o + \dot{y}\delta(T/2) = 0 \quad (4.85)$$

where ϕ_{ij} represents elements of the fundamental matrix $\Phi(T/2, 0)$. Re-arranging Eq (4.85) enables the time variation $\delta(T/2)$ to be evaluated as

$$\delta(T/2) = -\frac{1}{\dot{y}}(\phi_{21}\delta x_o + \phi_{23}\delta z_o + \phi_{25}y_o) \quad (4.86)$$

The aim of this method is to alter the initial conditions to obtain $\delta\dot{\mathbf{x}} = \delta\dot{\mathbf{z}} = 0$ at time $T/2$. Varying two of the initial conditions is sufficient to provide orbit correction. Keeping the value of x_o fixed, such that $\delta x_o = 0$, leads to the expression

$$\begin{bmatrix} \delta\dot{x} \\ \delta\dot{z} \end{bmatrix} = \begin{bmatrix} \phi_{43} & \phi_{45} \\ \phi_{63} & \phi_{65} \end{bmatrix} \begin{bmatrix} \delta z_o \\ \delta y_o \end{bmatrix} + \begin{bmatrix} \ddot{x} \\ \ddot{z} \end{bmatrix} \delta(T/2) \quad (4.87)$$

Substituting the expression for $\delta(T/2)$ derived in Eq (4.86), into Eq (4.87) gives the correction expression used by Breakwell and Brown [1979], and Howell [1984] as

$$\begin{bmatrix} \delta\dot{x} \\ \delta\dot{z} \end{bmatrix} = \begin{bmatrix} \phi_{43} & \phi_{45} \\ \phi_{63} & \phi_{65} \end{bmatrix} \begin{bmatrix} \delta z_o \\ \delta y_o \end{bmatrix} - \frac{1}{\dot{y}} \begin{bmatrix} \ddot{x} \\ \ddot{z} \end{bmatrix} \begin{bmatrix} \phi_{23} & \phi_{25} \end{bmatrix} \begin{bmatrix} \delta z_o \\ \delta y_o \end{bmatrix} \quad (4.88)$$

The required change in the initial conditions δz_o and δy_o is calculated from the required change to the velocities at $T/2$, $-\delta\dot{x}$ and $-\delta\dot{z}$. Through an iterative process of numerical integration and correction, the initial conditions obtained from Richardson's third order approximation converge toward a periodic halo orbit. This correction method will be demonstrated for periodic halo orbits around the L_1 and L_2 Lagrange points.

Figure 4-10 demonstrates the effectiveness of the differential correction method. The trajectory produced by the initial conditions obtained by Richardson's theorem winds off the nominal orbit escaping in the anti-Sun direction. The correction method gradually improves the resulting trajectory by varying the initial z_o and y_o conditions in order to force the conditions at time $T/2$ towards that required for a periodic orbit. Trajectory 6 represents the periodic halo orbit achieved after 6 iterations. At each stage of correction, the resulting trajectory converges comparably closer to the nominal orbit.

The initial conditions obtained using the differential correction method are provided in Table 4-4. The correction method required 6 iterations to obtain suitable values of $\dot{x} = -3.515 \times 10^{-6}$ and $\dot{z} = 5.792 \times 10^{-5}$ at time $T/2 = 90.7$ days.. The in-plane and out-of-plane amplitudes correspond to $A_x = 40.26 R_E$ and $A_z = 20 R_E$. The initial conditions yielded from Richardson's approximation are converted to a planet centred coordinate system for use in the non-linear equations derived in Section 4.1.

Figure 4-11 demonstrates the iterative correction process which converges toward a periodic halo orbit around the L_1 Lagrange point after 12 iterations. The in-plane and out-of-plane amplitudes are defined as $A_z = 20 R_E$ and $A_x = 38.9 R_E$. Table 4-5 provides the corrected initial conditions for each iteration of the correction method. After 12 iterations suitable values of $\dot{x} = -9.180 \times 10^{-6}$ and $\dot{z} = 7.455 \times 10^{-5}$ were obtained at time $T/2 = 89.5$ days.

It was found that the correction method can 'overshoot' the desired orbit if the calculated change in initial conditions, δz_o and δy_o are applied directly. To improve the accuracy of the convergence method, a coefficient n was introduced such that the initial conditions are

altered by a factor $n\delta y_o$ and $n\delta z_o$. The value of n was selected arbitrarily between the limits $0.1 \leq n \leq 0.5$ providing a trade-off between accuracy and efficiency.

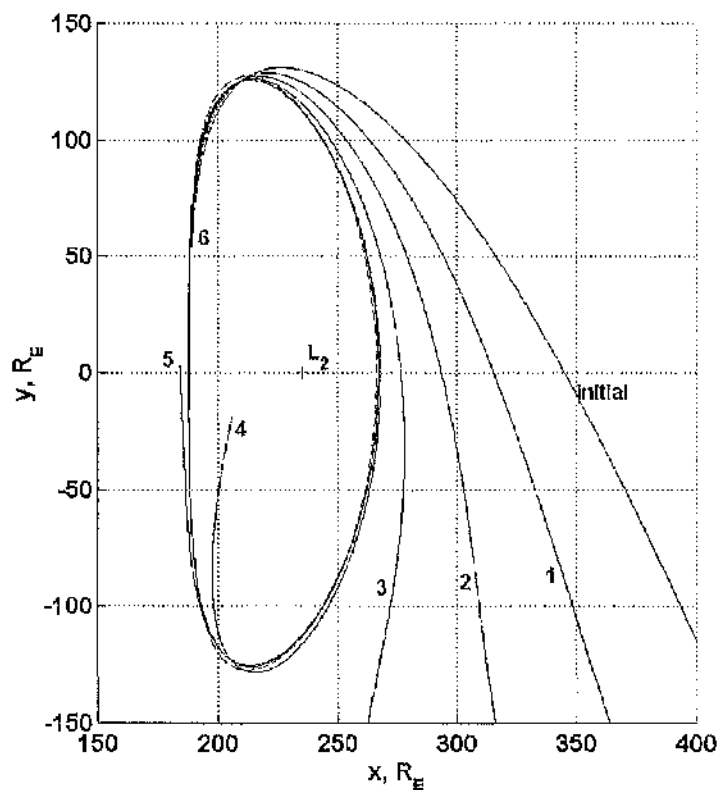


Figure 4-10 Iterative method improving initial conditions towards a periodic halo orbit around L_2

	x_o	y_o	z_o	\dot{x}_o	\dot{y}_o	\dot{z}_o
Initial	0.00799589840	0	0.00075906746	0	0.01237406764	0
1 st Iteration	0.00799589840	0	0.00072933473	0	0.01209224716	0
2 nd Iteration	0.00799589840	0	0.00070939306	0	0.01191541801	0
3 rd Iteration	0.00799589840	0	0.00069750983	0	0.01179636391	0
4 th Iteration	0.00799589840	0	0.00069294029	0	0.01174034054	0
5 th Iteration	0.00799589840	0	0.00069282234	0	0.01173611718	0
Corrected	0.00799589840	0	0.00069307255	0	0.01173670786	0

Table 4-4 Initial conditions yielded from the third order approximation and the corrected conditions of L_2 orbit

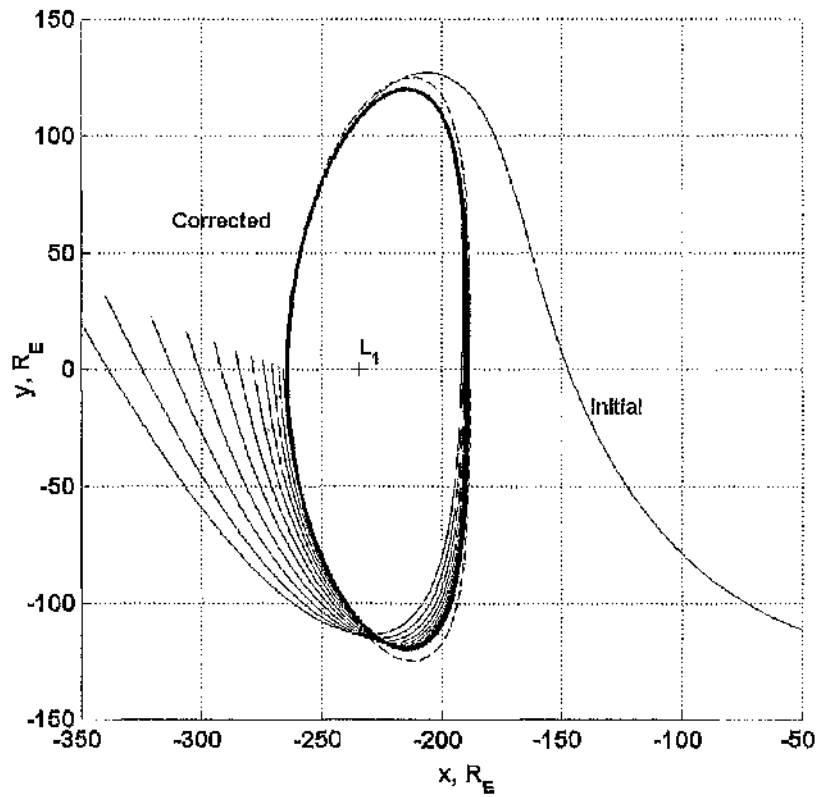


Figure 4-11 Iterative method improving initial conditions towards a periodic halo orbit around L_1

	x_0	y_0	z_0	\dot{x}_0	\dot{y}_0	\dot{z}_0
Initial	-	0	0.00095934221	0	0.01107461150	0
1 st Iteration	-	0	0.00107262323	0	0.01010643172	0
2 nd Iteration	-	0	0.00106617368	0	0.01011405614	0
3 rd Iteration	-	0	0.00106119927	0	0.01012023328	0
4 th Iteration	-	0	0.00105738480	0	0.01012507391	0
5 th Iteration	-	0	0.00105446338	0	0.01012876494	0
6 th Iteration	-	0	0.00105221807	0	0.01013151518	0
7 th Iteration	-	0	0.00105047797	0	0.01013352251	0
8 th Iteration	-	0	0.00104911165	0	0.01013495810	0
9 th Iteration	-	0	0.00104801980	0	0.01013596183	0
10 th Iteration	-	0	0.00104712841	0	0.01013664373	0
11 th Iteration	-	0	0.00104638282	0	0.01013708815	0
Corrected	-	0	0.00104574299	0	0.01013735855	0

Table 4-5 Initial conditions yielded from the third order approximation and the corrected conditions of L_1 orbit

4.4.3.2 Halo orbits sunward of L_2

A solar sail can be used to generate an artificial libration point sunwards of L_2 . Richardson's third order approximation can be used to identify periodic halo orbits around an artificial libration point. Figure 4-12 shows a family of periodic orbits around an on-axis artificial libration point at $x_0=150 R_E$. The constant acceleration required to generate these orbits is 0.323 mms^{-2} .

The constraint imposed by Eq (4.80) on the A_x amplitude, to achieve periodic halo orbit, decreases as the orbit is displaced closer to the central body. Figure 4-13 shows the minimum A_x amplitude and corresponding kA_x calculated for $A_z=0$ at a range of libration point distances sunward of L_2 . The y -axis amplitude is approximately equivalent to kA_x . It is clear that the minimum x -axis and y -axis amplitude decrease asymptotically toward $y=0$ as the libration point is displaced towards the Earth.

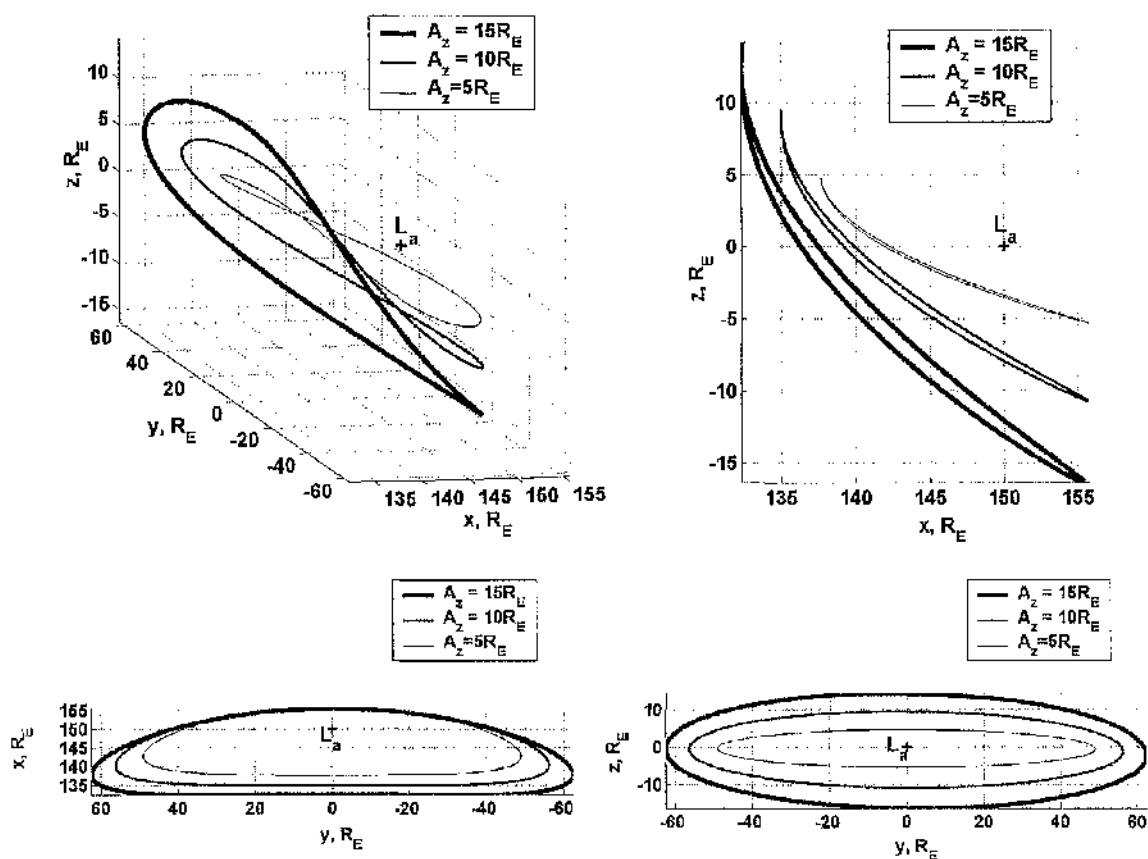


Figure 4-12 Family of periodic halo orbits around artificial libration sunward of L_2 ($150R_E$ from Earth)

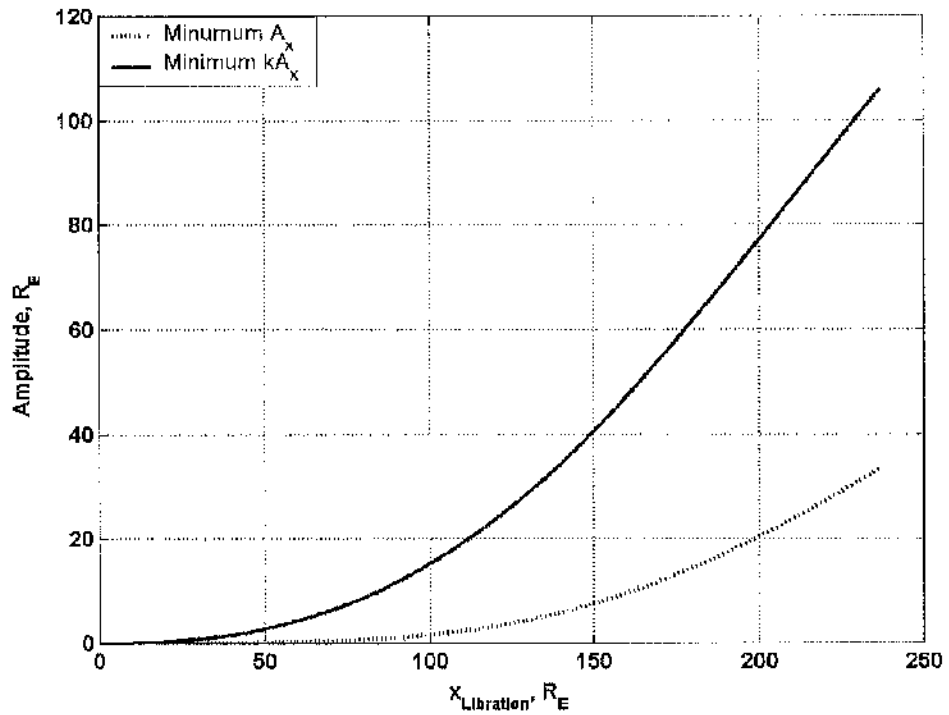


Figure 4-13 Minimum y-axis and x-axis amplitude for periodic halo orbit sunward of L_2 ($A_z=0$)

4.4.3.3 Halo orbits sunward of L_1

Similarly, an artificial libration point can be generated sunward of L_1 and Richardson's approximation applied to identify periodic halo orbits. Figure 4-14 shows a family of halo orbits around an artificial libration point generated sunward of L_1 at $x=-300 R_E$. The constant acceleration required to generate this libration point is 0.12 mms^{-2} . Comparing these halo orbits to the example of a libration point sunward of L_2 , the y-axis and x-axis amplitudes are much larger for the same out-of-plane amplitude, A_z .

Figure 4-15 shows the minimum A_x and kA_x values for libration points sunward of L_1 extending to 0.02 AU from the Earth. The values of A_x and kA_x linearly increase becoming very large as the libration point is displaced further sunward of L_1 .

Although the nominal orbit defines a periodic halo orbit, numerical integration of the non-linear circular three-body equations results in a gradual escape due to limited precision of the $|\dot{x}|$ and $|\dot{z}|$ values at $T/2$. Including the effects of the Earth's eccentricity and solar sail acceleration variation leads to perturbations, which result in gradual escape from the nominal orbit. Solar sail control laws will be developed which damp these perturbations.

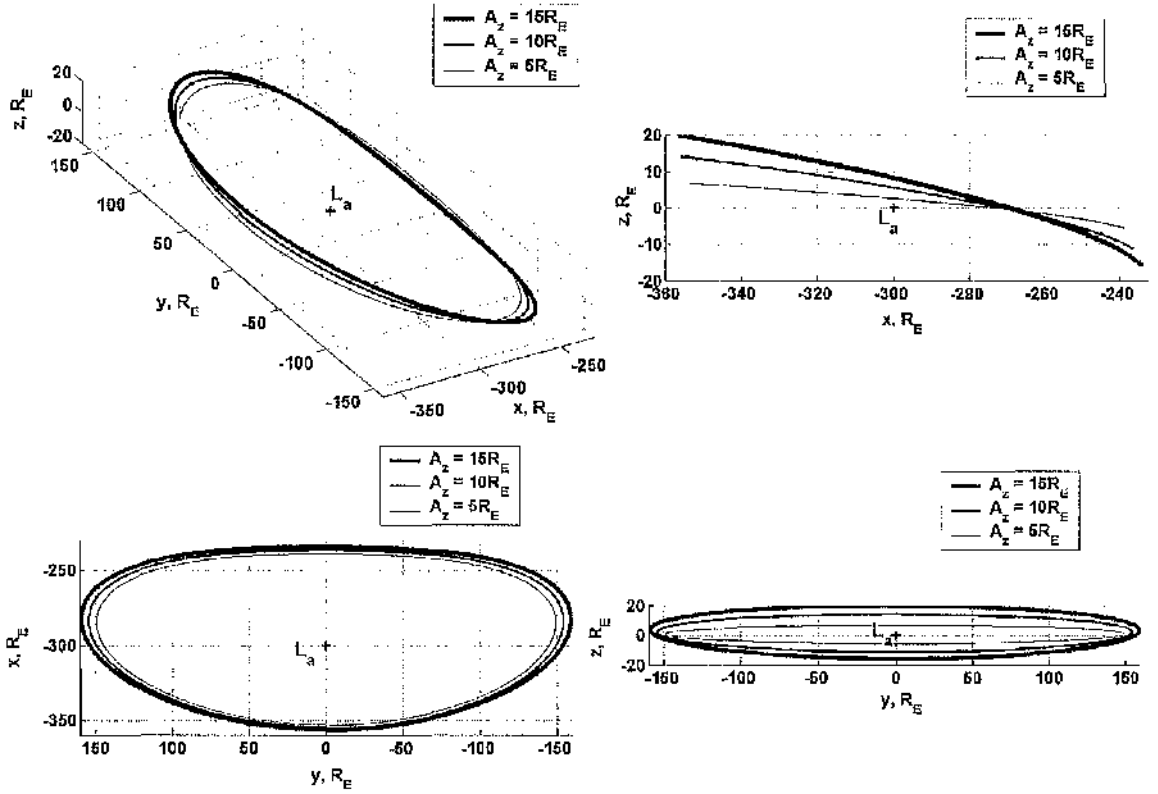


Figure 4-14 Family of periodic halo orbits around artificial libration sunward of L_1 ($-300R_E$ from Earth)

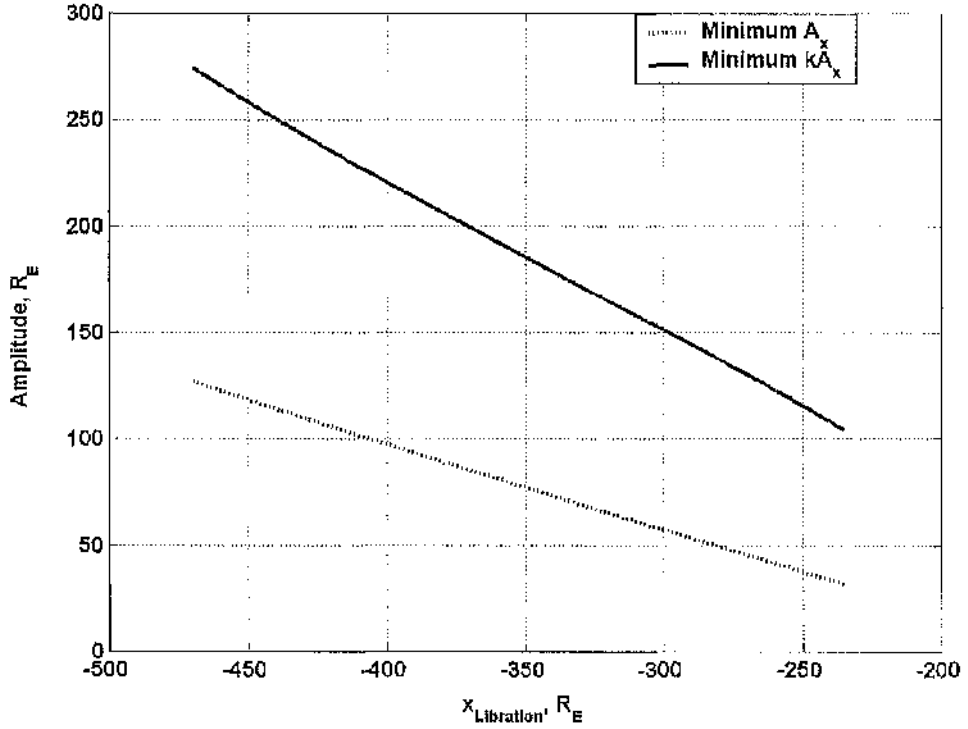


Figure 4-15 Minimum y -axis and x -axis amplitude for periodic halo orbit sunward of L_1 ($A_z=0$)

4.4.4 Control of periodic halo orbits using solar sail control laws

4.4.4.1 Three-axis controller design

The solar sail diverges rapidly from the nominal periodic halo orbit if the trajectory varies slightly from the nominal path. Control techniques were developed for the ISEE-3 (International Sun Earth Explorer) mission launched into a halo orbit around L_1 in 1978. To prevent escape from the nominal orbit after insertion, stationkeeping techniques were applied which used hydrazine thrusters to track a reference trajectory. The trajectory was optimised requiring an annual Δv of 10-15 ms^{-1} for orbit control [Farquhar et al, 1980].

The SOHO mission, launched in 1995, also followed a periodic halo trajectory around L_1 with a y -axis amplitude of 600,000 km. SOHO performs thrust maneuvers every 8 to 12 weeks ensuring the spacecraft remains within the vicinity of the nominal orbit and with the correct attitude relative to the Sun [Beckman, 2002].

An orbit controller was developed which tracks the nominal trajectory produced by the differential correction method. The corrected initial conditions were used to numerically generate one complete orbit with a maximum time step of $10^{-3}\tau$. This resulted in approximately 1×10^5 data points representing the desired position and velocity around the nominal orbit, $\mathbf{x}_d = [x_d \quad y_d \quad z_d \quad \dot{x}_d \quad \dot{y}_d \quad \dot{z}_d]$. The angular position relative to the libration point in the x - y plane was calculated using $\theta_d = \tan(y_d/x_d)$.

The difference between the actual and desired position and velocity was determined as $\delta\mathbf{x} = \mathbf{x} - \mathbf{x}_d$. The angle $\theta = \tan(y/x)$ was calculated for each point during numerical integration of the actual trajectory. Using a look-up table method, this angle was compared to the desired orbit angle, θ_d to identify the value closest to angle θ . The corresponding position and velocity values were used as the desired conditions. By storing the location in the table of the previous value, the next value could be found much quicker as the angle θ only changes gradually with each iteration. This technique was found to greatly improve the numerical integration rate during orbit control.

The control gains were selected using optimal methods similar to those applied for the solar sail area and angle variation controller. Unlike these cases, 3-axis control was enabled providing full controllability in the three-body problem. The control matrix has the form

$$B = \begin{bmatrix} O_{3 \times 3} \\ I_{3 \times 3} \end{bmatrix} \quad (4.89)$$

where $O_{3 \times 3}$ and $I_{3 \times 3}$ represent 3×3 zero and identity matrices respectively. As before, the state equation has the form

$$\dot{\mathbf{x}} = A\mathbf{x} + B\mathbf{u} \quad (4.90.1)$$

$$\mathbf{y} = C\mathbf{x} \quad (4.90.2)$$

where the linear coefficient A is provided in Eq (4.82), C represents the output matrix, \mathbf{u} is the control vector and \mathbf{y} is the output vector. The controllability matrix was found to be full-rank, indicating that this control method provides total three-axis control in the three-body problem.

As demonstrated in Section 3.4.4, the state weighting matrix, N , and the control weighting matrix Q can be used to construct a 3×6 optimal gain matrix, G . This gain matrix is used to calculate the required acceleration directed along each axis as

$$\delta\kappa_x = G_{1,1}\delta x + G_{1,2}\delta y + G_{1,3}\delta z + G_{1,4}\delta \dot{x} + G_{1,5}\delta \dot{y} + G_{1,6}\delta \dot{z} \quad (4.91.1)$$

$$\delta\kappa_y = G_{2,1}\delta x + G_{2,2}\delta y + G_{2,3}\delta z + G_{2,4}\delta \dot{x} + G_{2,5}\delta \dot{y} + G_{2,6}\delta \dot{z} \quad (4.91.2)$$

$$\delta\kappa_z = G_{3,1}\delta x + G_{3,2}\delta y + G_{3,3}\delta z + G_{3,4}\delta \dot{x} + G_{3,5}\delta \dot{y} + G_{3,6}\delta \dot{z} \quad (4.91.3)$$

where N and Q are selected so as to minimise the required acceleration. The state weighting matrix $N = \nu I_{6 \times 6}$ where ν is a constant factor selected to minimise the deviation from the nominal orbit and the control weighting matrix, Q , has the form

$$Q = \begin{bmatrix} q_x & 0 & 0 \\ 0 & q_y & 0 \\ 0 & 0 & q_z \end{bmatrix} \quad (4.92)$$

where (q_x, q_y, q_z) are parameters selected to minimise the required control signals.

The solar sail could achieve three-axis control by combining variation of the reflecting sail surface area with variation of the sail pitch and yaw angle to ensure the required thrust orientation and magnitude is achieved. The effective sail acceleration to control the orbit is determined as

$$\kappa_{eff} = \sqrt{\kappa_x^2 + \kappa_y^2 + \kappa_z^2} \quad (4.93)$$

where κ is the nominal acceleration required to generate an artificial libration point, $\kappa_x = \kappa + \delta\kappa_x$, $\kappa_y = \delta\kappa_y$ and $\kappa_z = \delta\kappa_z$. The sail pitch and yaw angles can be calculated as $\alpha = \sin^{-1}(\delta\kappa_z/\kappa_{eff})$ and $\phi = \tan^{-1}(\kappa_y/\kappa_x)$ respectively.

Pitching the sail reduces the effective acceleration, therefore the actual sail acceleration must be increased accordingly such that

$$\kappa_{actual} = \frac{\kappa_{eff}}{\cos^2 \alpha \cos^2 \phi} \quad (4.94)$$

The effective sail acceleration also varies as the solar sail distance relative to the Sun changes. The solar sail area can also be varied accordingly to achieve the required acceleration as

$$A_{sail} = \frac{2\pi c m \kappa_{actual} R(t)^2}{L_s} \quad (4.95)$$

where c is the speed of light, L_s is the solar luminosity, m is the solar sail mass and $R(t)$ is the distance between the solar sail and the Sun at time t . Orbit control in the circular and elliptical three-body problem will now be demonstrated using this control method.

4.4.4.2 Control of periodic halo orbit sunward of L_2

A periodic halo orbit was generated around a libration point sunward of L_2 using the developed control method. A libration point generated 200 R_E from the Earth can be achieved with solar sail acceleration $\kappa=0.0095 \text{ mms}^{-2}$. The z -axis amplitude was selected as $A_z=10 R_E$ which requires in-plane amplitudes $A_x=23.83 R_E$ and $A_y=90.42 R_E$. The controller gains were selected using state weighting factor $\nu=1$ and control weighting elements $q_1=1$, $q_2=1$ and $q_3=0.5$.

Figure 4-16 shows the resulting orbit controlled for a period of 2 years in the circular restricted problem. The orbit period is 148 days giving approximately five controlled periods. Figure 4-17 provides the acceleration and corresponding area variation required to control this orbit for a 100 kg sail and payload mass. The acceleration varies between 0.099 mms^{-2} and 0.094 mm^{-2} which corresponds to an area variation of between 1093 m^2 and 1043 m^2 . Figure 4-18 shows the required solar sail pitch and yaw angle variation over the 2 year control period.

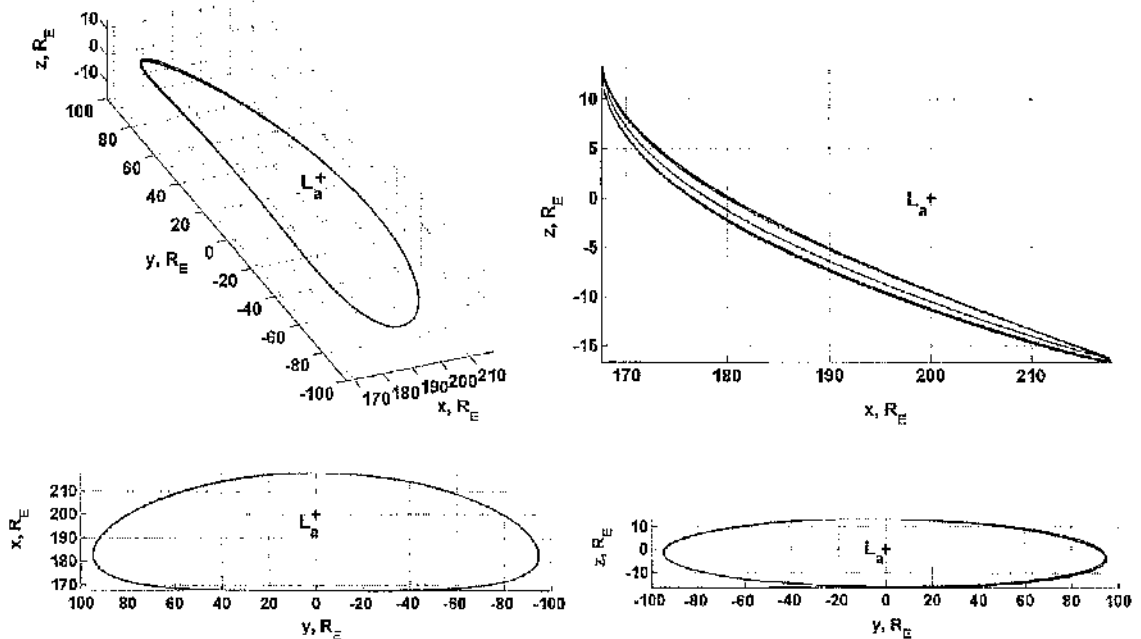


Figure 4-16 Controlled periodic halo orbit around artificial libration point in the circular restricted problem

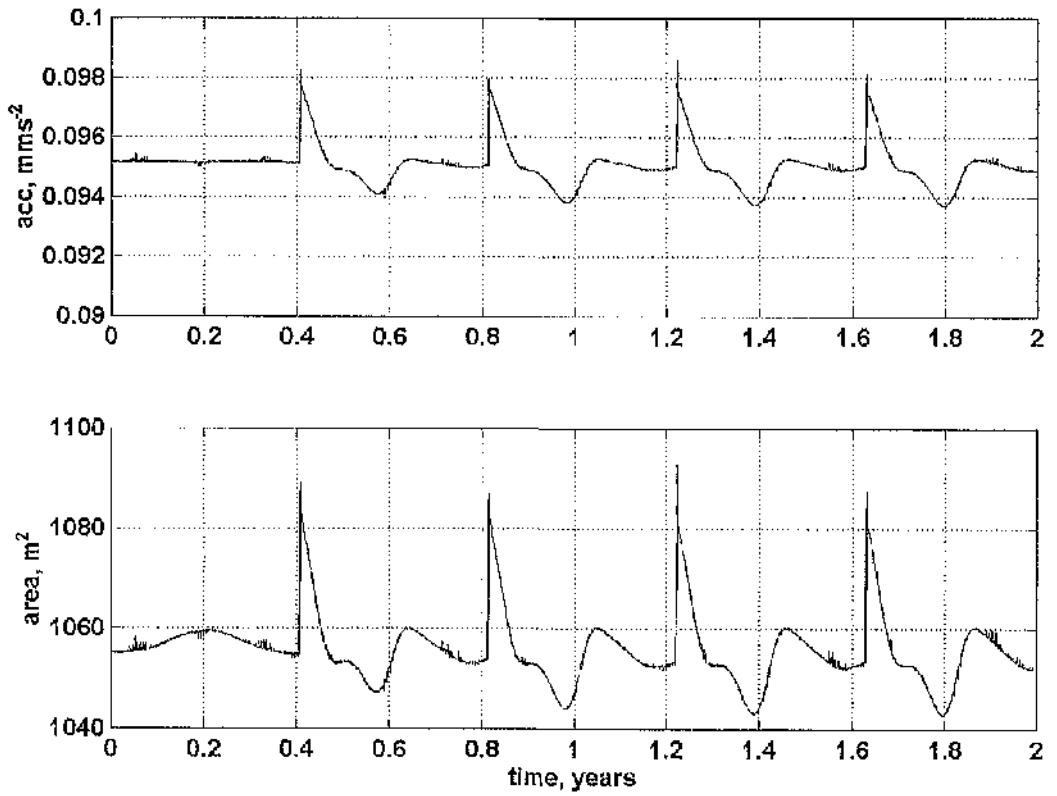


Figure 4-17 Solar sail acceleration and corresponding area variation required to control halo orbit

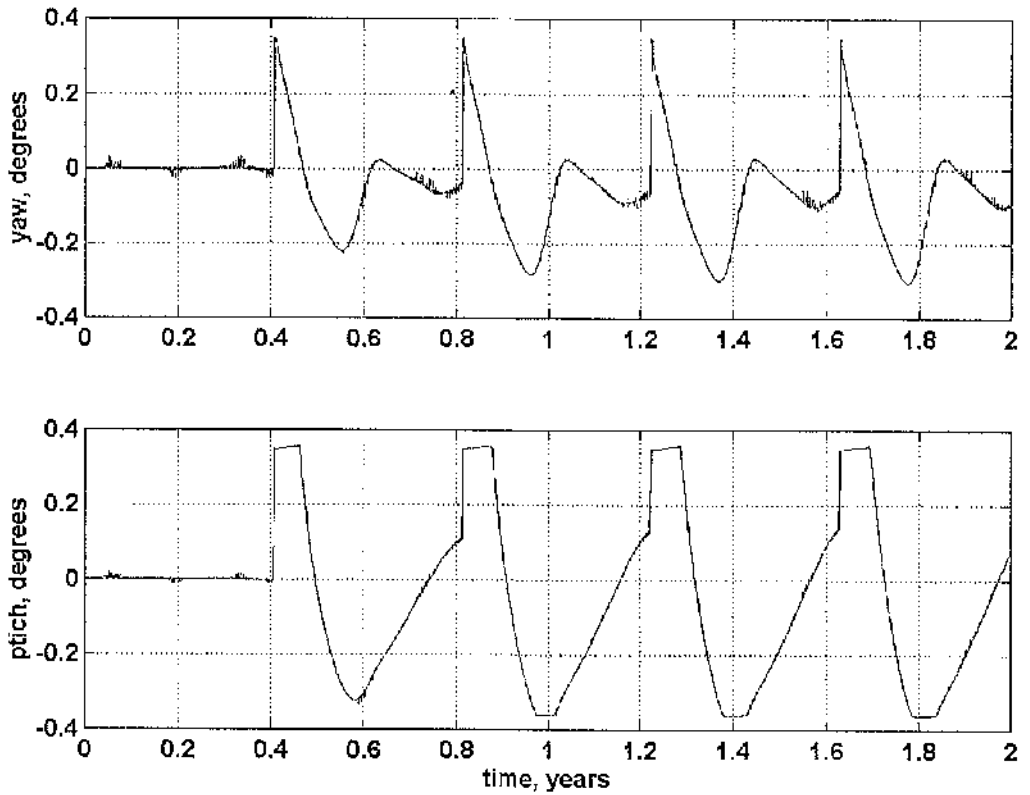


Figure 4-18 Solar sail pitch and yaw angle variation required to control halo orbit

Similarly, orbit control can be achieved in the elliptical three body problem using this solar sail control method. Figure 4-19 shows the controlled orbit around a libration point $200 R_E$ from the Earth with the same amplitudes as investigated in the circular restricted case. The eccentricity of the Earth's orbit $e=0.0167$ means the actual position of the libration point fluctuates throughout the year between $196 R_E$ and $204 R_E$.

The controller gains were selected using state weighting factor $v=20$ and control weighting elements $q_1=0.01$, $q_2=0.1$ and $q_3=0.05$. These differ from those selected in the circular restricted case as the control signal is required to be larger in order to dampen the perturbations introduced by the elliptical motion of the Earth. Figure 4-20 shows the acceleration and corresponding sail area variation for a 100 kg sail and payload mass. The acceleration varies between 0.177 mms^{-2} and 0.077 mms^{-2} resulting in sail area variation between 2026 m^2 and 822 m^2 . This is over a wider range than exhibited in the circular restricted problem. Figure 4-21 shows the sail pitch and yaw angle variation required to control the solar sail at the nominal orbit.

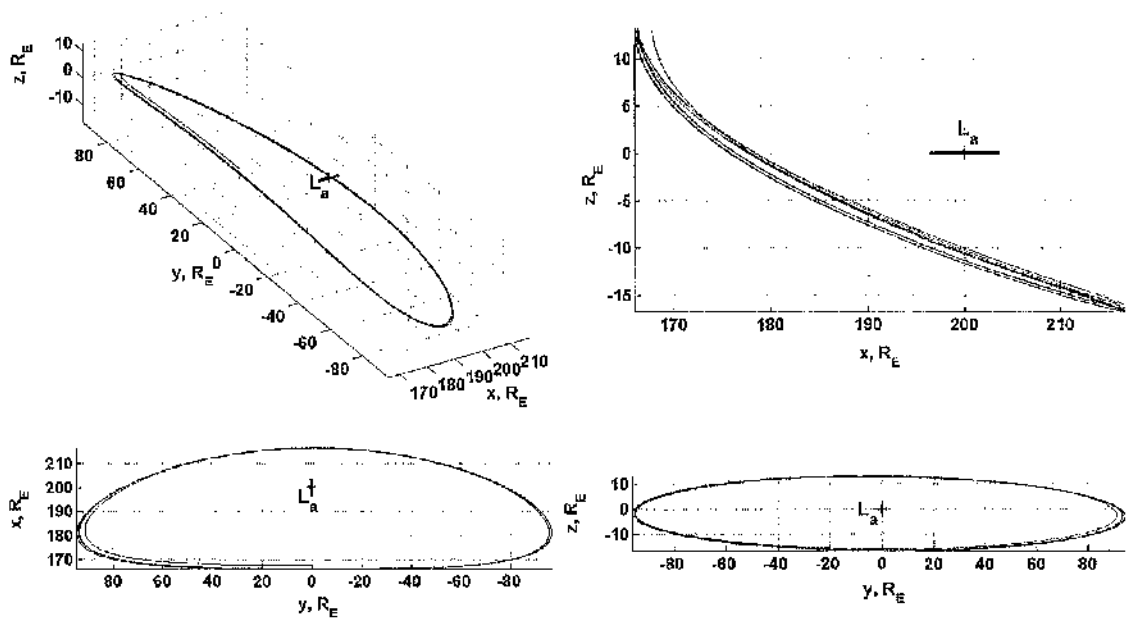


Figure 4-19 Controlled periodic halo orbit around artificial libration point in the elliptical restricted problem

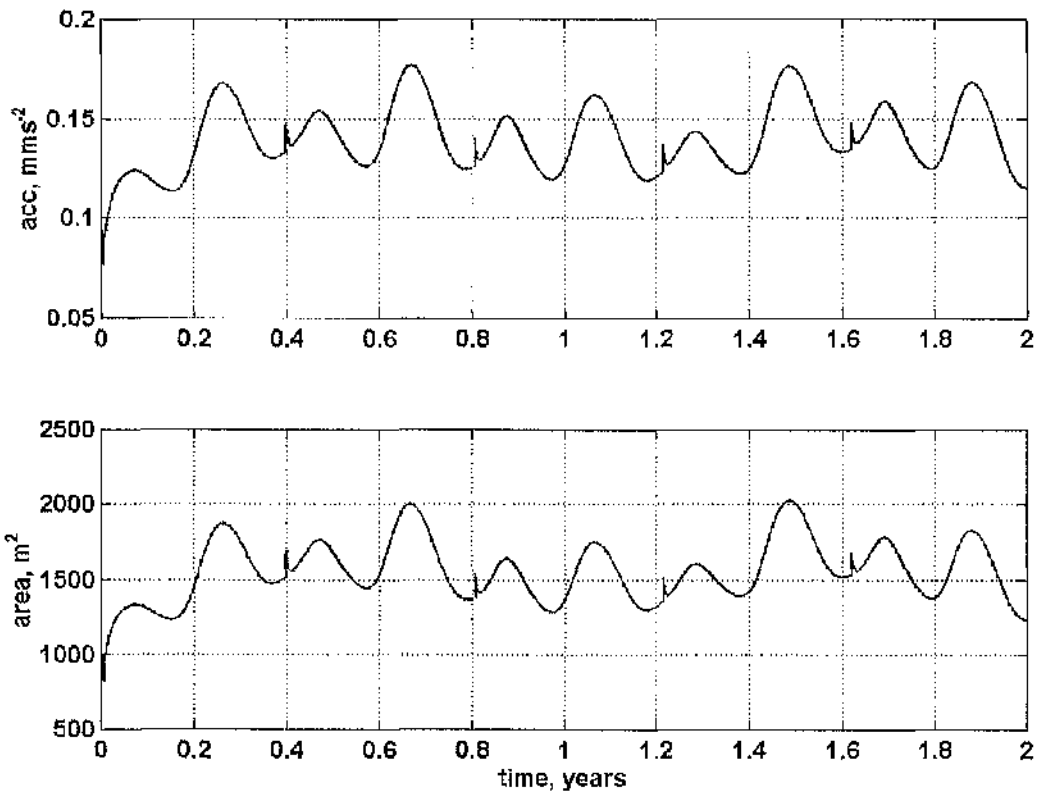


Figure 4-20 Solar sail acceleration and corresponding area variation required to control halo orbit

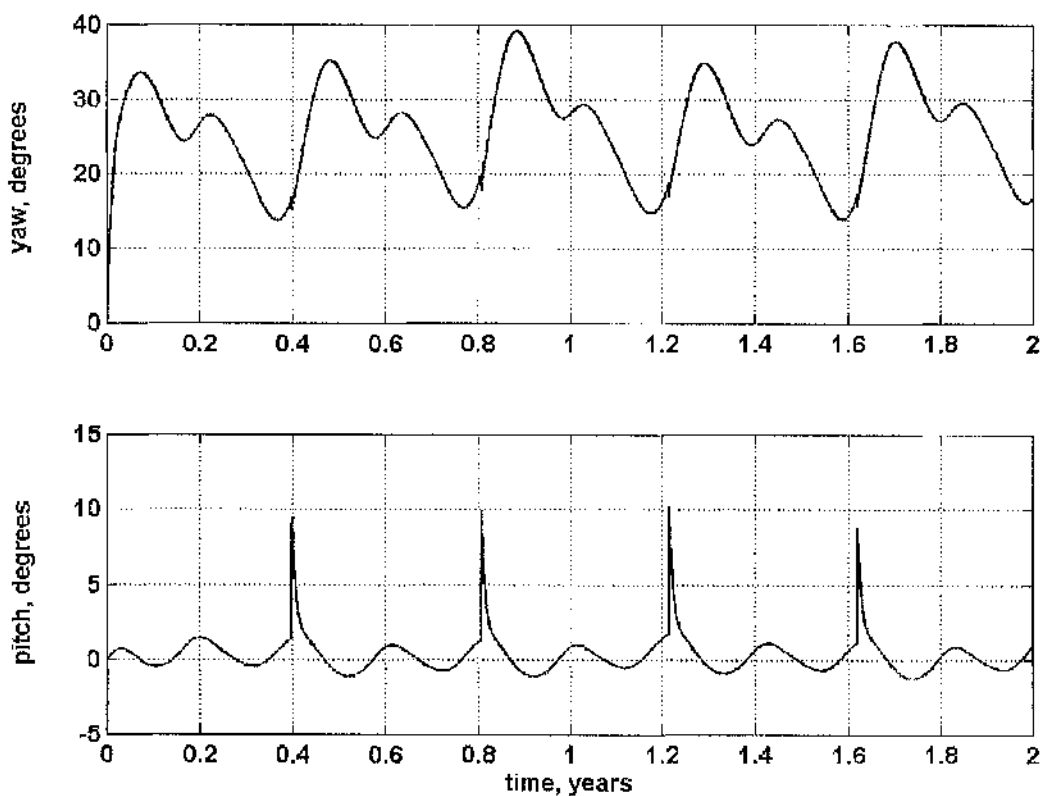


Figure 4-21 Solar sail pitch and yaw angle variation required to control halo orbit

4.4.4.3 Control of periodic halo orbit sunward of L_1

The orbit controller can also be used to control an orbit Sunward of L_1 , see Figure 4-22. The nominal orbit was selected with z -axis amplitude $A_z=20 R_E$ with corresponding in-plane amplitudes $A_x=53 R_E$ and $A_y=151 R_E$. The artificial libration point is located $270 R_E$ sunwards of the Earth requiring a solar sail acceleration of $\kappa=0.072 \text{ mms}^{-2}$. The controller gains were selected using state weighting factor $\nu=1$ and control weighting elements $q_1=5$, $q_2=5$ and $q_3=0.01$.

The acceleration and corresponding sail area variation for a 100 kg sail and payload mass are provided in Fig 4-23. The acceleration varies between 0.073 mms^{-2} and 0.059 mms^{-2} which corresponds to an area variation 805 m^2 and 695 m^2 . The pitch and yaw angle variation is provided in Fig 4-24. The 'spikes' in the plot occurring once every orbit period are a result of the deviation between the starting and end conditions of the reference orbit. By improving the precision of the differential correction method used to generate the reference orbit, these 'spikes' could be reduced.

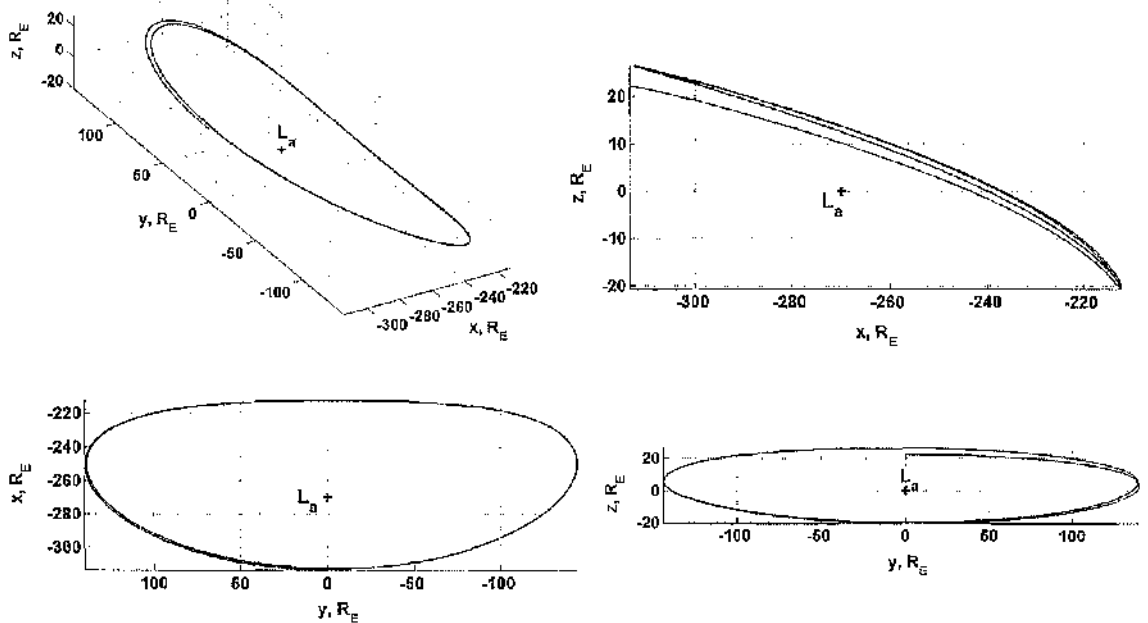


Figure 4-22 Controlled periodic halo orbit around artificial libration point in the circular restricted problem

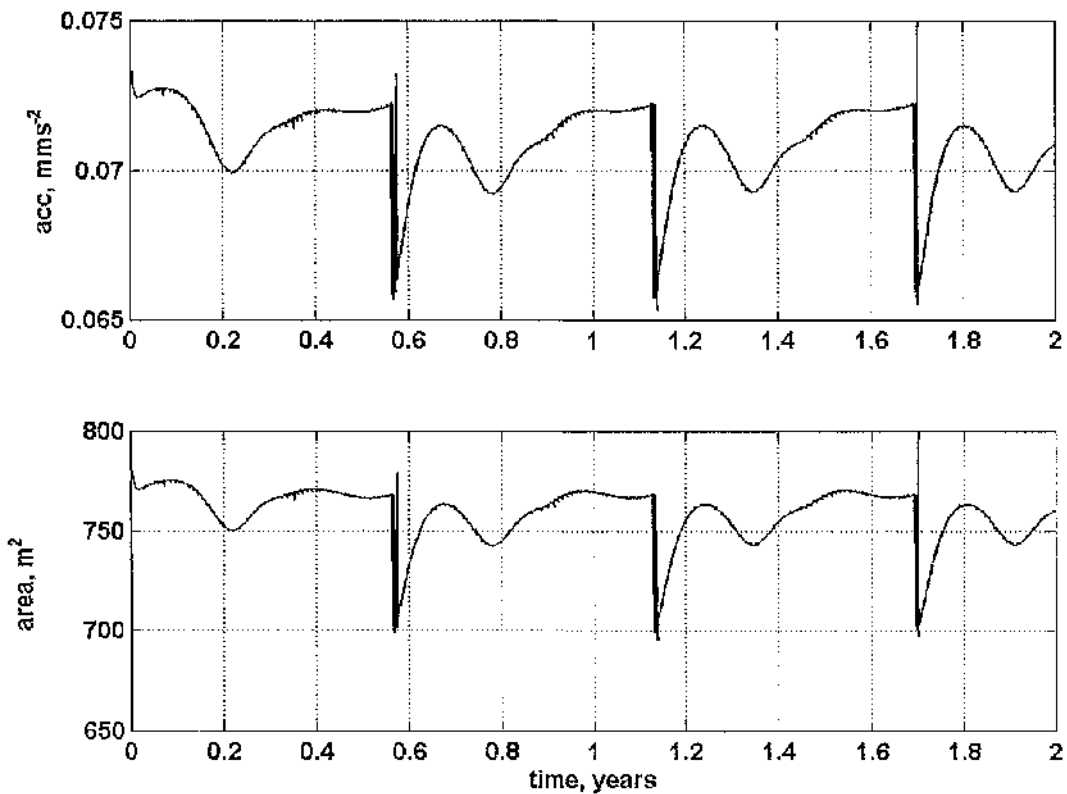


Figure 4-23 Solar sail acceleration and corresponding area variation required to control halo orbit

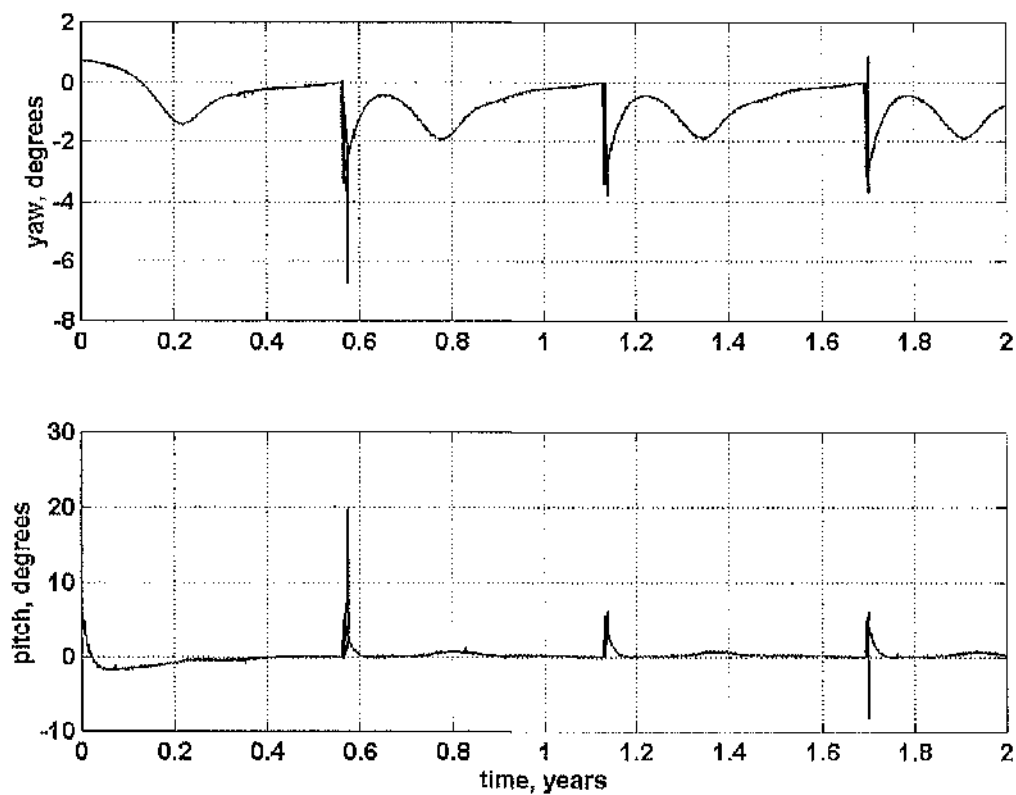


Figure 4-24 Solar sail pitch and yaw angle variation required to control halo orbit

Orbit control is now demonstrated including the perturbations due to the elliptical motion of the Earth orbiting the Sun. Figure 4-25 shows a controlled orbit around an artificial libration $270 R_E$ sunwards of the Earth with the same amplitudes as investigated in the circular restricted case. Due to the eccentric motion of the Earth, the libration point oscillates between $-275 R_E$ and $-265 R_E$.

This example highlights a possible problem with the solar sail control method in the elliptical three-body problem when it is used to control an orbit around a libration point displaced far from the Earth. The oscillations in the libration point position combined with the large x - and y -axis amplitudes requires large control accelerations directed along the y -axis. When a small acceleration is required along the x -axis but large acceleration directed along the y -axis, the sail yaw angle tends toward $\pi/2$ and the required sail area becomes unbound.

Figure 4-26 shows the acceleration required to provide control at this orbit. It is apparent that the magnitude of κ_y is comparable to the magnitude of κ_x . Occasionally, as $\kappa_x \rightarrow 0$ the value of $\kappa_y \gg \kappa_x$ which results in unrealistic sail area requirements of order $1 \times 10^5 \text{ m}^2$. For short intervals during control of this orbit, the acceleration directed along the x -axis $\kappa_x < 0$. A constraint imposed on the solar sail acceleration requires that it is always directed in the anti-Sun direction. Applying the constraint $\kappa_x \geq 0$, would result in the solar sail escaping toward the Earth meaning the control method is not suitable for control of this orbit.

The annual Δv requirement for control in the elliptical three-body problem was analysed at this orbit. The x -axis control requires a total annual Δv of 2.73 kms^{-1} and control in the y - z plane requires an annual Δv of 162 ms^{-1} . Comparing these requirements to other conventional propulsion methods excludes the feasibility of using chemical propulsion, however, the Δv could be achievable using solar electric propulsion with the longevity of stored reaction mass limiting the mission duration.

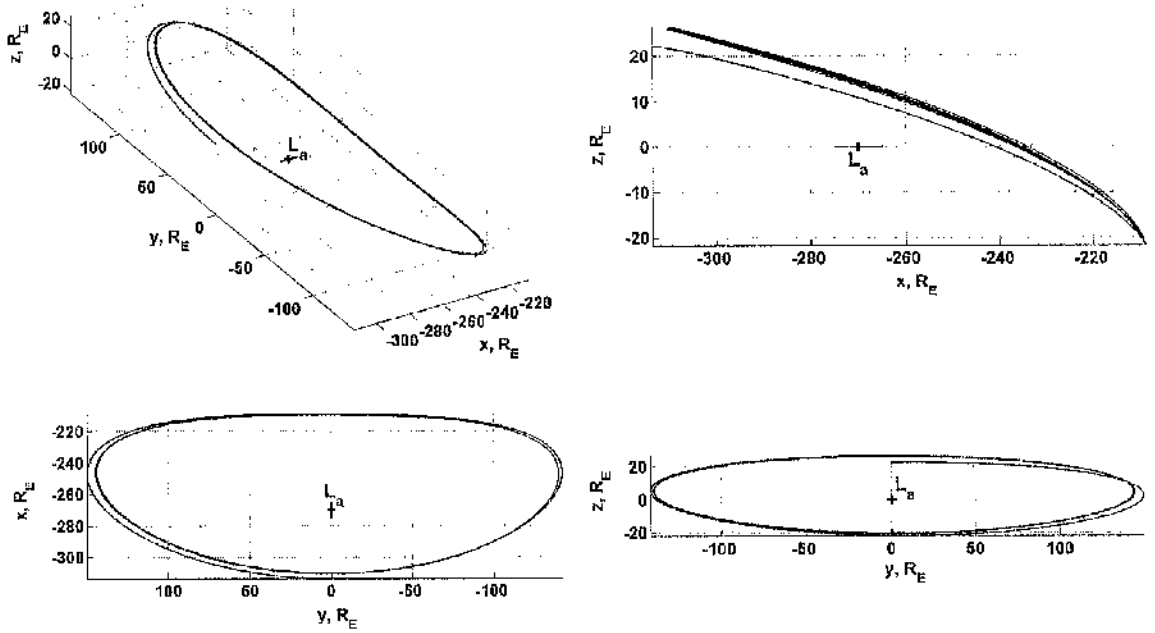


Figure 4-25 Controlled periodic halo orbit around artificial libration point in the elliptical restricted problem

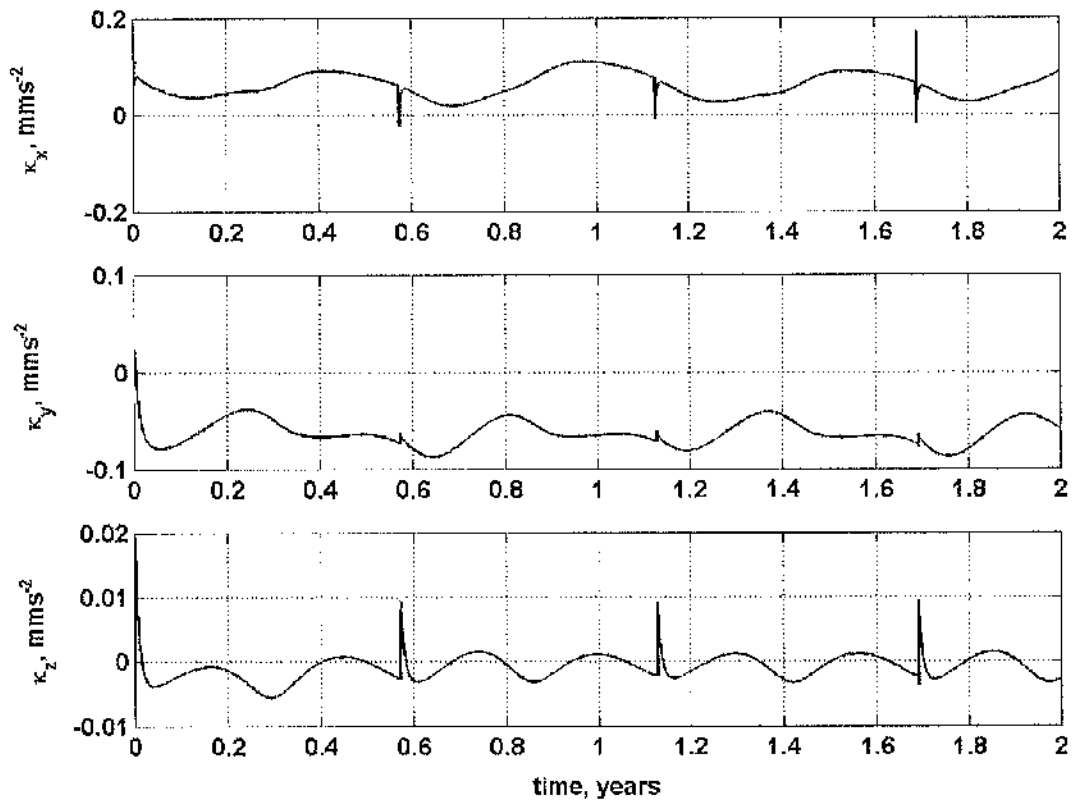


Figure 4-26 Acceleration components for orbit control at orbit sunward of L_1

Unrealistic sail area requirements occurring when the yaw angle tends toward $\pi/2$ can be avoided by generating a periodic halo orbit around a libration point displaced further from L_1 . This requires a larger nominal acceleration, κ , which prevents the acceleration, κ_x , tending toward zero. Figure 4-27 shows a periodic halo orbit controlled around a libration point 350 R_E sunward of the Earth. The dynamics are modeled using the elliptical restricted three-body problem and the resulting libration point oscillates between -343 R_E and -357 R_E . The nominal acceleration $\kappa=0.189 \text{ mms}^{-2}$, the orbit out of plane amplitude $A_z=30 R_E$ and corresponding in-plane amplitudes $A_x=89 R_E$ and $A_y=213 R_E$.

Figure 4-28 shows the required sail acceleration and area variation required to provide station-keeping at the nominal orbit for the duration of 2 years. The controller gains were selected using state weighting factor $\nu=20$ and control weighting elements $q_1=0.1$, $q_2=0.05$ and $q_3=0.05$. During orbit control, the sail acceleration varies between 0.17 mms^{-2} and 0.3 mms^{-2} with corresponding area variation between 1886 m^2 and 3092 m^2 for a 100 kg sail and payload mass.

The pitch and yaw angle variation is provided in Figure 4-29. The yaw angle varies between -40.7° and -0.6° , and the pitch angle varies between -1.3° and 3.2° . Although the nominal acceleration is larger than for artificial libration points near L_1 , the yaw angle does not tend toward $\pi/2$ enabling full orbit controllability using a reasonable sail area.

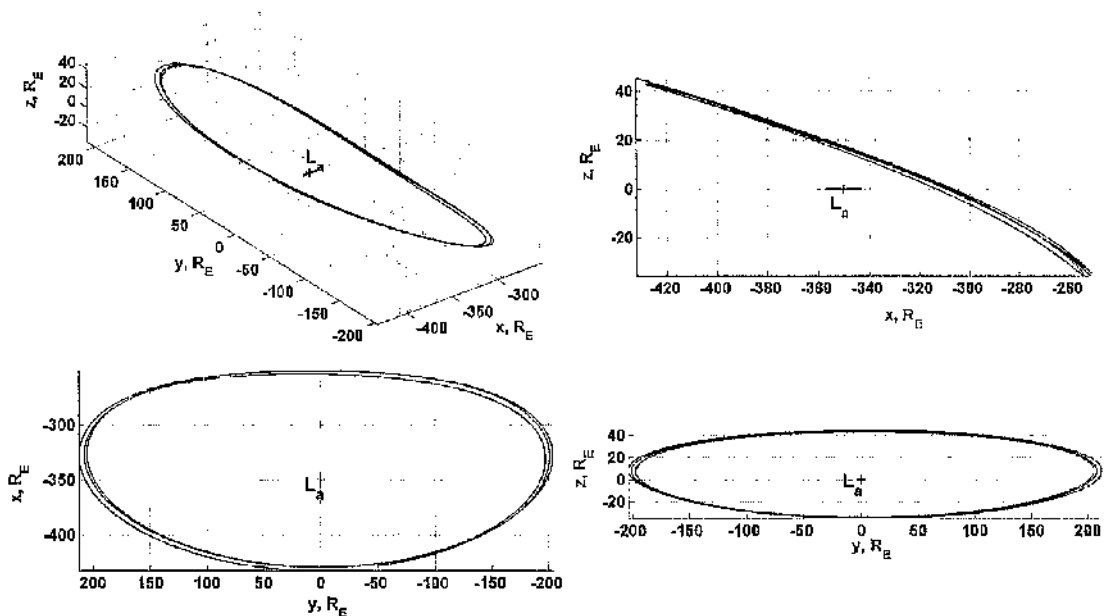


Figure 4-27 Controlled periodic halo orbit around artificial libration point in the elliptical restricted problem

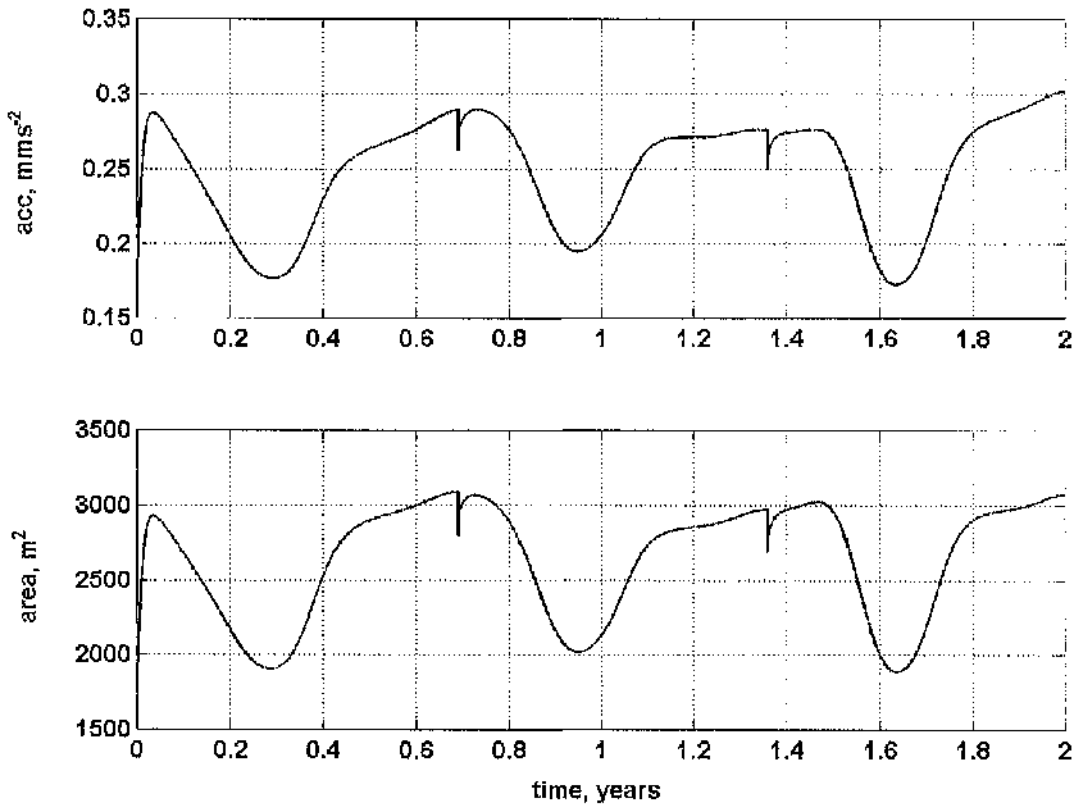


Figure 4-28 Solar sail acceleration and corresponding area variation required to control halo orbit

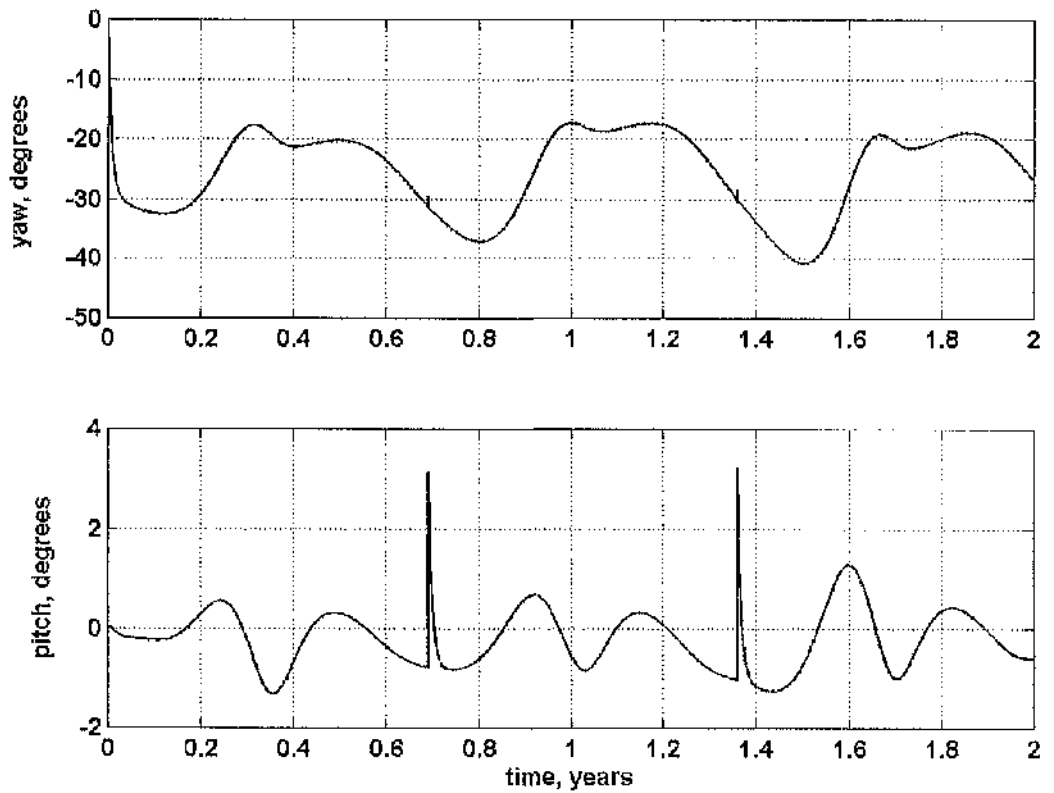


Figure 4-29 Solar sail pitch and yaw angle variation required to control halo orbit

4.5 Conclusions

Periodic halo orbits have been investigated in the circular and elliptical restricted three-body problem. Initial conditions which lead to these orbits were identified using Richardson's approximation method. A differential correction method was applied and provided reasonable convergence toward a periodic halo orbit. Precision errors lead to eventual escape from the nominal orbit and optimal control techniques were employed to provide orbit control.

The orbit control method was demonstrated for periodic halo orbits around libration points sunwards of L_1 and L_2 . A possible three-axis solar sail control method was investigated using a combination of sail area variation and sail pitch and yaw angle variation to control both the thrust direction and magnitude. This method was found to work well in the circular restricted case providing accurate orbit control for achievable sail surface areas. Perturbations due to the elliptical motion of the Earth required an increased acceleration directed along the y -axis to achieve control.

In the elliptical problem, the libration point position oscillates throughout the year where the size of oscillation is larger for libration points displaced further from the Earth. In the case of orbits sunwards of L_1 , the perturbations were found to be more significant. Due to the dependency of sail acceleration on $\cos^2 \alpha \cos^2 \phi$, as the pitch and yaw angle tend towards $\pi/2$, the required sail area becomes unbound in order to generate the necessary sail acceleration for orbit control. It was shown that selecting a libration point at a greater distance from L_1 increases the x -axis acceleration but reduces the sail yaw angle variation required to control the orbit.

The next chapter will investigate periodic orbits around possible interstellar libration points. The stability of such orbits will be examined in order to determine if interstellar matter can become temporarily trapped at these orbits. The two-centre approximation will be used to model the gravitational dynamics assuming, over a short timescale, the stars are fixed relative to each other.

5.1 Gravitational two-centre problem**5.1.1 Gravitational two-centre equations of motion**

The problem of two fixed centres was first investigated by Euler as a restriction of the three-body equations of motion. It considers a non-rotating system where a particle of negligible mass is moving under the gravitational influence of two fixed masses (or electrostatic influence if fixed charges are considered) [Howard and Wilkerson, 1995b].

Figure 5-1 provides a schematic of the two-centre problem where the two fixed masses, M_1 and M_2 , are positioned on the z -axis separated by a distance R . The centre of mass is located at position C . A point mass, m , is located a distance ρ from the z -axis. The separation distance between the point mass and the primary bodies is r_1 and r_2 respectively, where $|\mathbf{r}_1| = \sqrt{\rho^2 + z^2}$ and $|\mathbf{r}_2| = \sqrt{\rho^2 + (R - z)^2}$. The angular position θ is orientated around the z -axis.

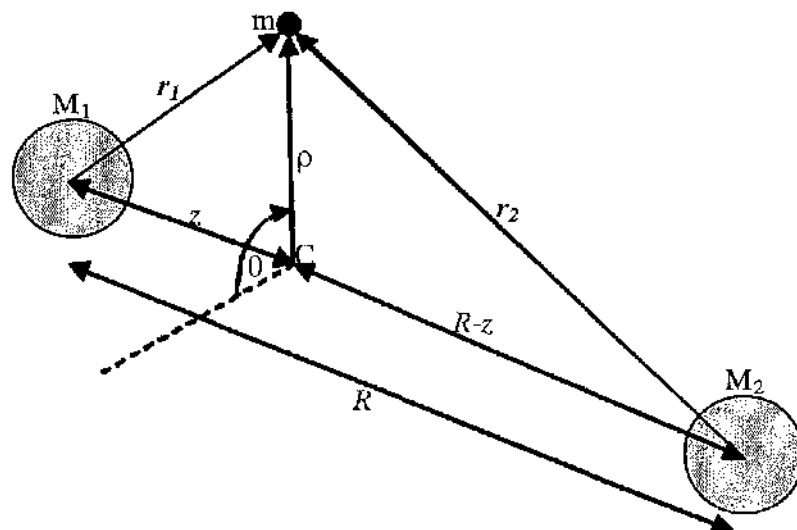


Figure 5-1 Schematic of two-centre problem with fixed masses M_1 and M_2

Similar to the derivation of the two-body problem, provided in Section 2.1, the equations of motion can be obtained from the Hamiltonian. The two-centre kinetic energy, T , can be defined using polar coordinates as

$$T = \frac{1}{2}m(\dot{z}^2 + \dot{\rho}^2 + \rho^2\dot{\theta}^2) \quad (5.1)$$

and the two-centre potential energy, V , can be defined as

$$V = -\frac{GM_1m}{|\mathbf{r}_1|} + \frac{GM_2m}{|\mathbf{r}_2|} \quad (5.2)$$

where G is the gravitational constant. This gives the Hamiltonian, $H = T + V$ which can be expressed using the momenta terms $P_z = m\dot{z}$, $P_\rho = m\dot{\rho}$ and $P_\theta = m\rho^2\dot{\theta}$ as

$$H = \frac{1}{2m}\left(P_z^2 + P_\rho^2 + \frac{P_\theta^2}{\rho^2}\right) - Gm\left(\frac{M_1}{|\mathbf{r}_1|} - \frac{M_2}{|\mathbf{r}_2|}\right) \quad (5.3)$$

The equations of motion can be obtained from the Hamiltonian using $\partial H/\partial P_q = \dot{q}$ and $\partial H/\partial q = -\dot{P}_q$ where $q = (\rho, \theta, z)$. This obtains the following equations of motion

$$\ddot{\rho} = \rho\dot{\theta}^2 + G\left(-\frac{M_1\rho}{|\mathbf{r}_1|^3} + \frac{M_2\rho}{|\mathbf{r}_2|^3}\right) \quad (5.4.1)$$

$$\ddot{\theta} = -\frac{2\dot{\rho}\dot{\theta}}{\rho} \quad (5.4.2)$$

$$\ddot{z} = -G\left(\frac{M_1z}{|\mathbf{r}_1|^3} + \frac{M_2(R-z)}{|\mathbf{r}_2|^3}\right) \quad (5.4.3)$$

The two-centre equations of motion can be non-dimensionalised using the characteristic length R as the separation between the two primary masses and the characteristic time $\tau = \sqrt{R^3/GM_1}$. From Eq (5.4.2), the z -component of angular momentum can be derived as $h_z = \rho^2\dot{\theta}$. This can be substituted into Eq (5.4.1) to obtain the non-dimensionalised equations as

$$\ddot{\rho} = \frac{h_z^2}{\rho^3} - \frac{\rho}{|\mathbf{r}_1|^3} - \frac{\lambda\rho}{|\mathbf{r}_2|^3} \quad (5.5.1)$$

$$\ddot{z} = -\frac{z}{|\mathbf{r}_1|^3} + \frac{\lambda(1-z)}{|\mathbf{r}_2|^3} \quad (5.5.2)$$

where the constant, λ , is equivalent to the mass ratio M_2/M_1 . For a circular orbit about the z -axis, the acceleration and velocity component $\dot{\rho} = \rho = 0$. From Eq (5.5.1), the required angular velocity for such a circular orbit is given by $\dot{\theta} = \sqrt{|\mathbf{r}_1|^{-3} + \lambda|\mathbf{r}_2|^{-3}}$.

5.1.2 On-axis libration points

Consider a libration point which lies on the z -axis ($\rho=0$) collinear with the two primaries. In this case, the respective distance of the point mass from M_1 and M_2 is $|\mathbf{r}_1| = z$ and $|\mathbf{r}_2| = (R - z)$. Equation (5.5.2) reduces to

$$\ddot{z} = -\frac{1}{z^2} + \frac{\lambda}{(1-z)^2} \quad (5.6)$$

A libration point exists when $\ddot{z} = 0$ and the location depends on the mass ratio, λ . The position of the libration point is given by

$$z = \frac{1 \pm \sqrt{\lambda}}{1 + \lambda} \quad (5.7)$$

which has limits at $\lambda=1$, where the solution no longer has a quadratic form but instead represents a linear equation with solution $z=0.5$. As the libration point is formed by balancing the gravitational forces between the two masses, it is clear that the libration points can only exist for $0 < z < 1$.

The stability of the on-axis libration point can be determined using a 1st order Taylor expansion of Eq (5.6). This gives a state equation with the form $\ddot{z} = [\partial f / \partial z]_0 z$, where the function $f(z)$ is equivalent to

$$f(z) = -\frac{1}{z^2} + \frac{\lambda}{(1-z)^2} \quad (5.8)$$

and the derivative evaluated at the nominal libration point has the form

$$\left[\frac{\partial f}{\partial z} \right]_o = \frac{2}{z_o^3} + \frac{2\lambda}{(1-z_o)^3} \quad (5.9)$$

The eigenvalues for the linear state equation can be determined using a change of variables $z_1 = z$ and $z_2 = \dot{z}$. This state equation can then be expressed in the form

$$\begin{bmatrix} \dot{z}_1 \\ \dot{z}_2 \end{bmatrix} = \begin{bmatrix} 0 & 1 \\ \left[\frac{\partial f}{\partial z} \right]_o & 0 \end{bmatrix} \begin{bmatrix} z_1 \\ z_2 \end{bmatrix} \quad (5.10)$$

Let the symbol, Λ represent the square matrix in Eq (5.10). The eigenvalues, Λ can be calculated using $|\Lambda I - A| = 0$. This leads to the characteristic equation

$$\Lambda^2 - \left(\frac{2}{z_o^3} + \frac{2\lambda}{(1-z_o)^3} \right) = 0 \quad (5.11)$$

For a stable orbit the eigenvalues must be imaginary. Therefore $\Lambda^2 < 0$, which requires the expression in the brackets also to be less than zero. Figure 5-2 demonstrates that between the two masses located at $z=0$ and $z=1$, $\Lambda^2 > 0$ for $\lambda=2.17$. Analytical analysis of Eq (5.11) shows that for $\Lambda^2 > 0$, the inequality condition $(1-z_o)^3 > -\lambda z_o$ must be true. As the mass ratio $\lambda > 0$ and $0 < z_o < 1$, this condition is true for all values of λ . This demonstrates that a saddle point always exists at the on-axis equilibrium point as there is one positive and one negative eigenvalue for all possible mass ratios.

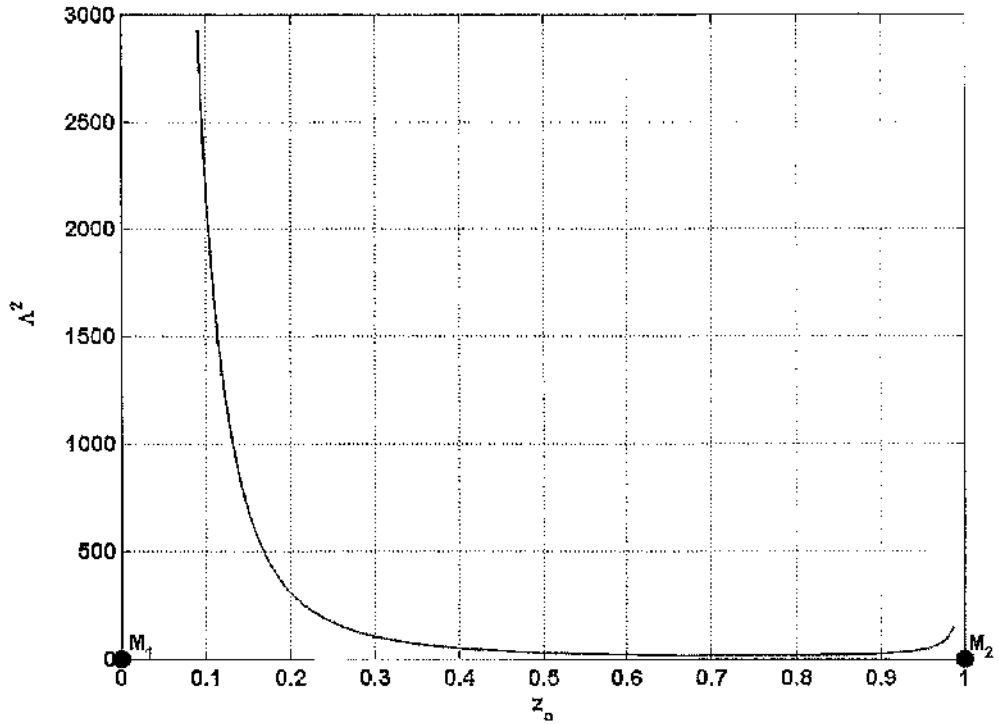


Figure 5-2 Eigenvalues of linearised equations over range of equilibria between $0 < z_0 < 1$

5.1.3 Halo orbits around Libration points

Halo orbits can be identified from Eq (5.5) when the acceleration and velocity components $\dot{\rho} = \dot{z} = 0$ and $\ddot{\rho} = \ddot{z} = 0$. A pseudo-potential function, $U(\rho, z)$ can then be derived as

$$U(\rho, z) = \frac{h_z^2}{2\rho^2} - \frac{1}{|\mathbf{r}_1|} - \frac{\lambda}{|\mathbf{r}_2|} \quad (5.12)$$

which includes the z -component of angular momentum, h_z .

Figure 5-3 shows a contour plot of the potential energy function for a constant value of $h_z=0.4$ and mass ratio $\lambda=0.5$. Figure 5-4 shows a contour plot for the same angular momentum value $h_z=0.4$ but for mass ratio $\lambda=2$. It is clear that there exists three equilibrium points in this system corresponding to circular orbits about the z -axis. The two points (E_1, E_2) nearest M_1 and M_2 are stable, indicated by the local minima of the potential energy function. These are similar to the two-body problem with a uniform axial force displacing the orbit from the central body. The local saddle point indicates that the central libration point (E_3) is unstable.

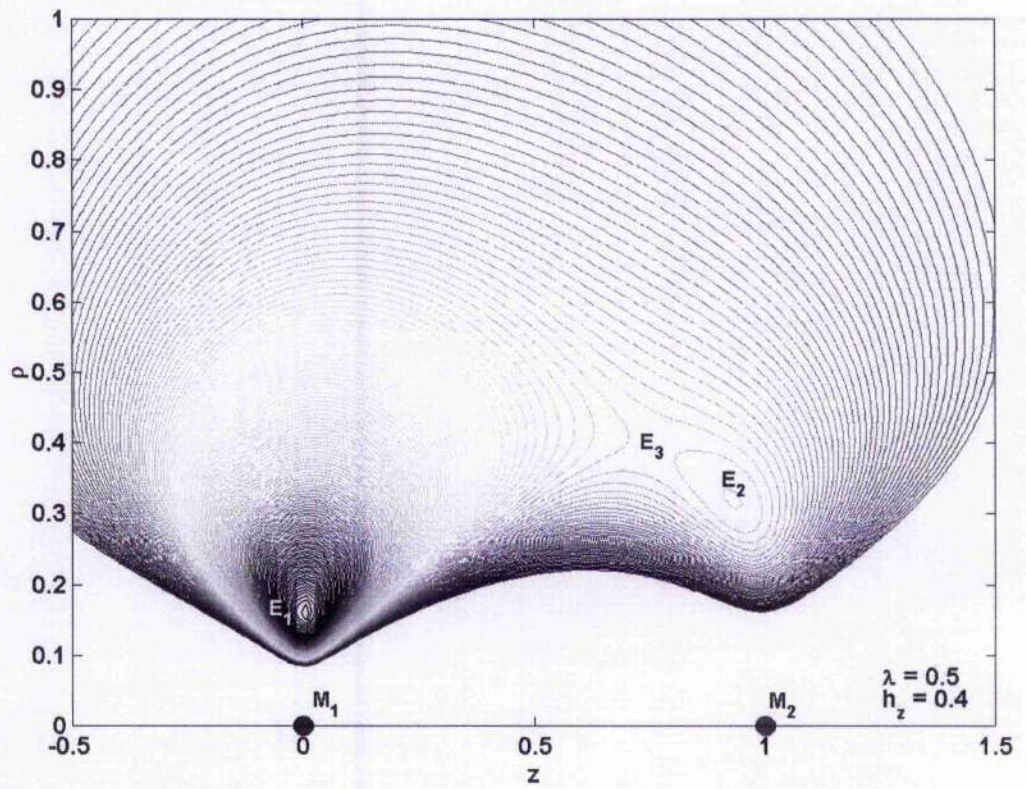


Figure 5-3 Potential energy function $U(\rho, z)$ for rotating frame around z -axis

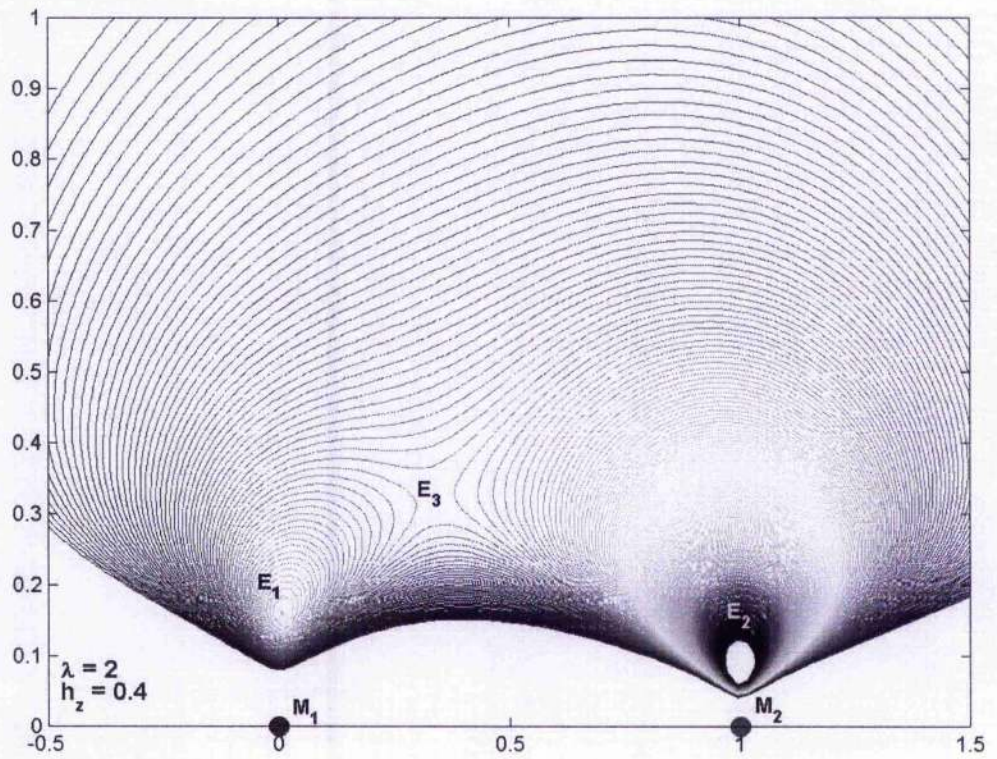


Figure 5-4 Potential energy function $U(\rho, z)$ for rotating frame around z -axis

From Eq (5.5), the angular momentum parameter h_z can be selected such that $\ddot{\rho} = 0$ with the requirement that $\dot{\theta}^2 > 0$. Halo orbit contours representing the initial conditions, ρ_0 and z_0 in the rotating reference frame are provided in Fig 5-5. For any fixed value of $\rho_0 < 0.4$, it is clear that there exists three possible halo orbits, each with a different angular momentum. When $\rho_0 > 0.4$, there exists only one possible halo orbit, which is located nearest to the body of larger mass.

An example of the three possible halo orbits at selected distances along the z -axis is provided in Fig 5-6. These halo orbits correspond to a system with mass ratio $\lambda = 2$. The initial conditions are calculated numerically from the contours provided in Fig 5-5. This is performed by selecting a desired value of z_0 and calculating the corresponding value of ρ_0 which gives $\ddot{z} = 0$. An angular momentum is then calculated which obtains $\ddot{\rho} = 0$ for the necessary value of ρ_0 . Orbit 1 and orbit 3 are stable, and the central orbit 2 is unstable which agrees with the potential energy contours provided in Fig 5-4. The calculated initial conditions for each of these orbits are provided in Table 5-1.

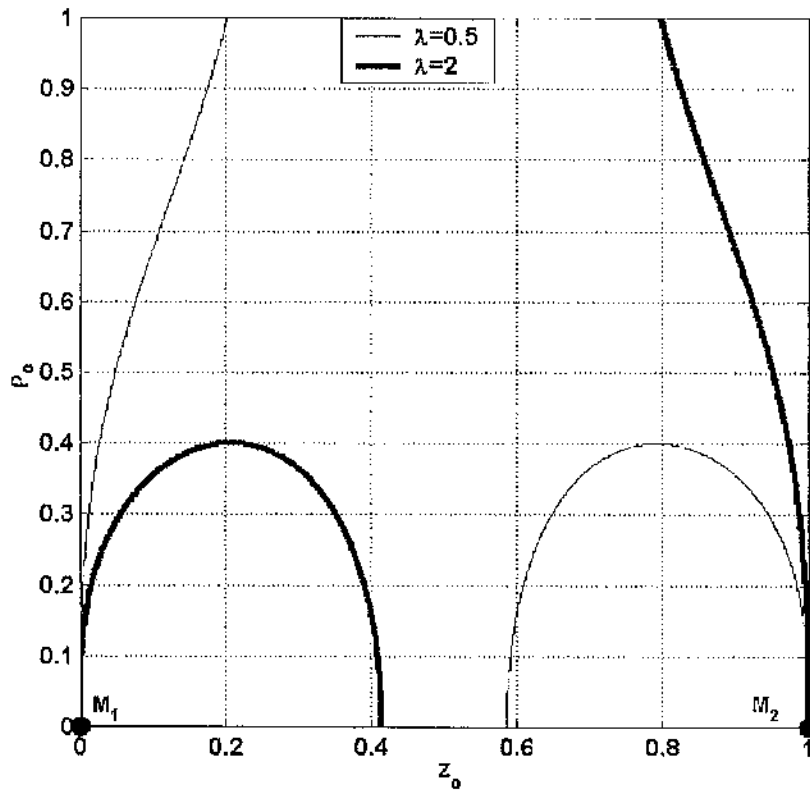


Figure 5-5 Contours represent halo orbit initial conditions for varying h_z

Orbit No.	ρ_0	z_0	h_z
1	0.3554	0.1	0.5935
2	0.2358	0.38	0.2362
3	0.5057	0.95	1.0243

Table 5-1 Numerically calculated initial conditions for two-centre halo orbits ($\lambda=2$)

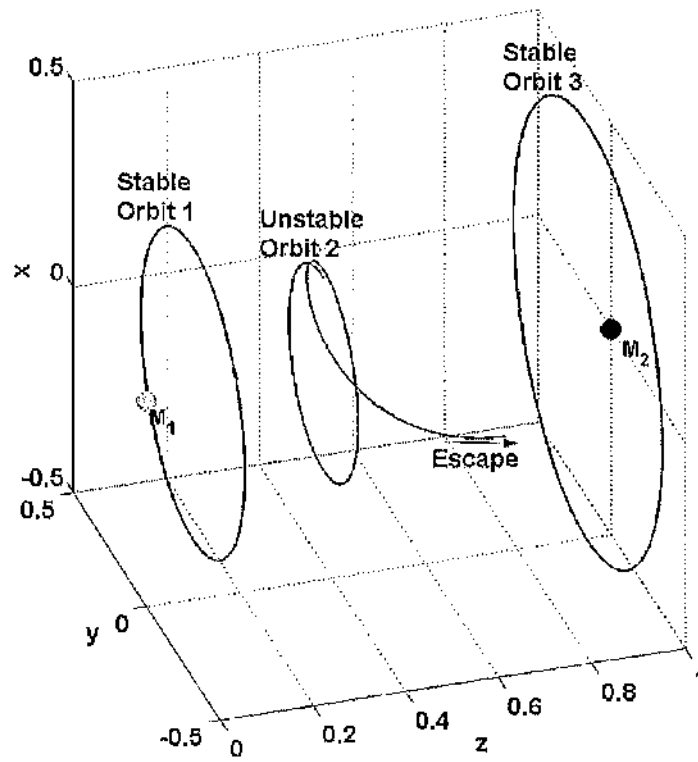


Figure 5-6 Two-centre halo orbits for system with mass ratio $\lambda=2$

5.2 Photo-gravitational two-centre problem

5.2.1 Investigation of interstellar libration points

The two-centre problem could have a possible application for the study of libration points between stars. Investigation of the libration point stability could determine whether interstellar dust can become trapped, at least temporarily, in the vicinity of these libration points. If the relative motion of the stars is negligible compared to the instability timescale of the trapped dust, the two-centre problem could provide a reasonable approximation of the dynamics. A thorough study has been performed by Bookless and McInnes [2004] investigating the possible existence of libration points between the Sun and nearby stars.

The nearest star system to the Sun is α -Centauri separated by a distance of 4.36 ly (light year) where 1 ly is equivalent to 9.4605×10^{15} m. Table 5-2 contains the spectral details of the Sun and the α -Centauri system taken from the Nstars database [1988]. Centauri is a triple star system with components A, B and C. A and B represent a binary system which orbit each other with a period of 80 years. Their separation varies between an apoapsis of 35AU and periapsis of 11AU [Soderblom, 1987]. The third component, α -Centauri C (also known as Proxima Centauri), is a much smaller red-dwarf possibly orbiting the two larger bodies from a much larger distance.

The influence of radiation pressure exerted on the small dust particles will be included in the equations of motion. Only the effects of direct radiation pressure will be considered in this model, ignoring Poynting-Robertson drag [Krivov et al, 1996; Mignard, 1982]. Assuming the dust particles have an absorbing surface, the lightness number is defined as

$$\beta = \frac{L}{4\pi cGM\sigma} \quad (5.13)$$

where L is the stellar luminosity, M is stellar mass and c is the velocity of light. The loading parameter is defined as $\sigma = m/A$ where A is the illuminated surface area and m is the particle mass. The dominant force influencing the dust depends on the value of β . If $\beta > 1$, the force due to stellar radiation pressure is dominant and if $\beta < 1$, the force due to stellar gravity is dominant.

Name	Spectral Class	Absolute Mag	Luminosity (W)
Sun	G2-V	+4.77	3.86×10^{26}
α -Centauri A	G2-V	+4.38	5.58×10^{26}
α -Centauri B	K1-V	+5.71	1.61×10^{26}
Proxima	M5.5-V	+15.49	7.41×10^{15}

Table 5-2 Spectral properties of nearby stars from the NStars database

The luminosity of a star can be calculated from its spectral magnitude. The difference in magnitude of two stars can be determined using

$$m_1 - m_2 = -2.5 \log_{10} \left(\frac{4\pi d_2^2 L_1}{4\pi d_1^2 L_2} \right) \quad (5.14)$$

where m_1 and m_2 are the spectral magnitude of the stars, d_1 and d_2 are the stellar distances and L_1 and L_2 are the stellar luminosities. The absolute magnitude is the magnitude of a star as would be observed from a distance of 10 pc (parsec), where $1 \text{ pc} = 3.0857 \times 10^{16} \text{ m}$. Centauri A and B are of similar magnitude to the Sun and C is a very dim red dwarf. Neglecting C, the luminosities of A and B can be combined to give the overall system luminosity of $7.19 \times 10^{26} \text{ W}$. This is much larger than the Sun's luminosity of $3.86 \times 10^{26} \text{ W}$.

5.2.2 Photo-gravitational two-centre equations of motion

Figure 5-7 represents a schematic of the Sun-Centauri system ignoring the relative stellar motion. The Centauri triple system is located approximately 4.36 ly from the Sun and has a combined mass of $2.17 M_{\odot}$ (solar mass), where $1 M_{\odot} = 1.989 \times 10^{30} \text{ kg}$. The force exerted on the particles by stellar radiation pressure is equivalent to $F_{srp} = \beta \mu / |r|^2$, where r is the distance from the star and μ is the stellar gravitational parameter. The two-centre kinetic energy corresponds to Eq (5.1) and the potential energy can be written as

$$V = -\frac{GM_1 m}{|r_1|} (1 - \beta_1) + \frac{GM_2 m}{|r_2|} (1 - \beta_2) \quad (5.15)$$

where the lightness numbers β_1 and β_2 correspond to the Sun and Centauri system respectively.

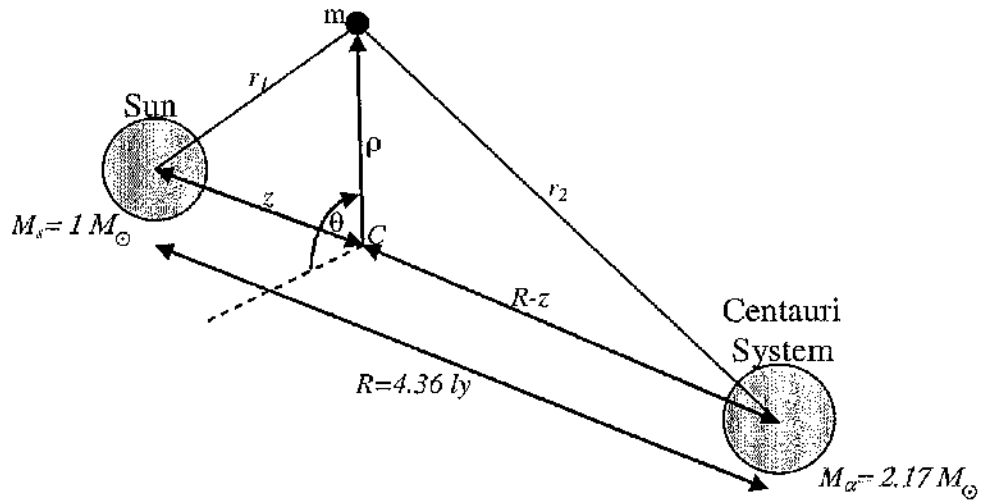


Figure 5-7 Schematic of Sun-Centauri system

The Hamiltonian method is applied to derive the equations of motion where $H = T + V$. The photo-gravitational Hamiltonian has the form

$$H = \frac{1}{2m} \left(P_z^2 + P_\rho^2 + \frac{P_\theta^2}{\rho^2} \right) - Gm \left(\frac{M_1}{|r_1|} (1 - \beta_1) - \frac{M_2}{|r_2|} (1 - \beta_2) \right) \quad (5.16)$$

The equations of motion are derived in polar coordinates (ρ, θ, z) using $\partial H / \partial P_q = \dot{q}$ and $\partial H / \partial q = -\dot{P}_q$, which yields components

$$\ddot{\rho} = \frac{h_z^2}{\rho^3} - \frac{(1 - \beta_1)\rho}{|r_1|^3} - \frac{\lambda(1 - \beta_2)\rho}{|r_2|^3} \quad (5.17.1)$$

$$\ddot{\theta} = -\frac{2\dot{\rho}\dot{\theta}}{\rho} \quad (5.17.2)$$

$$\ddot{z} = -\frac{(1 - \beta_1)z}{|r_1|^3} + \frac{\lambda(1 - \beta_2)(1 - z)}{|r_2|^3} \quad (5.17.3)$$

The equations are non-dimensionalised with the separation distance between the two stars selected as characteristic length $R=4.36$ ly and characteristic time $\tau = \sqrt{R^3/GM_s}$. The system mass ratio is defined as $\lambda=2.17M_0$.

The angular velocity required for a circular orbit ($\ddot{\rho} = 0$) is defined using Eq (5.17.1) as

$$\dot{\theta} = \sqrt{(1 - \beta_1)|r_1|^{-3} + \lambda(1 - \beta_2)|r_2|^{-3}} \quad (5.18)$$

with the condition $\dot{\theta}^2 > 0$ required for a real orbit. It is clear from these equations, if $\beta_1=1$ or $\beta_2=1$, the repulsion force due to stellar radiation pressure balances the gravitational force and the influence of that star on the dust particles is cancelled.

5.2.3 Light extinction

Photons traversing between stars are subject to absorption and scattering by gaseous atoms/ions and dust grains collectively known as interstellar matter. Neutral hydrogen is abundant in the interstellar medium, detectable from Earth as it emits the 21 cm radio line, which can be used to probe the galactic structure. A plethora of molecules exist ranging from basic types such as H_2O , CO , CH_4 and NH_3 to complex carbon structures such as polycyclic aromatic hydrocarbons and spherical fullerenes [Ehrenfreund and Foing, 1996; Salma et al, 1996]. Estimates from the Goddard High Resolution Spectrograph of the Hubble space telescope indicate there are as few as 140 ± 20 ppm (parts per million) carbon atoms present in the interstellar matter [Groth, 2003].

In the galactic plane, the estimated average light extinction value is 1 to 2 magnitudes per 1 kpc (kiloparsec) pathlength [Scheffler and Elsässer, 1988]. Shorter wavelength light intensity is greater reduced by scattering and absorption than longer wavelength light thus there is a reddening of starlight which increases systematically with distance [Bertin, 2000]. For simplicity, the increased extinction at shorter wavelengths or extinction curve structures such as the 2175\AA bump [Massa and Savage, 1998] will be neglected to provide a basic extinction model.

A suitable location to calculate the stellar luminosities is the gravitational on-axis libration point between the two primary masses. This libration point is located 1.763 ly from the Sun and 2.597 ly from α -Centauri evaluated using Eq (5.7). The apparent luminosity of the Sun at this distance is 3.8581×10^{26} W and the combined luminosity of the Centauri system is 7.1848×10^{26} W which represents a reduction of only 0.05% and 0.07% respectively due to light extinction.

5.2.4 Halo orbits around libration points

Including the lightness number terms alters the apparent system mass ratio by a factor $(1 - \beta_2)/(1 - \beta_1)$. Figure 5-8 shows a set of contours representing possible halo orbit initial conditions for a selection of particle loading parameters. These contours are generated in the rotating ρ - z plane where the angular velocity is calculated using Eq (5.18).

The particle loading parameters and corresponding lightness numbers are provided in Table 5-3. The lightness numbers are calculated using Eq (5.13) with the respective luminosities of the Sun and the Centauri system. Consider three cases

$\beta_2 < \beta_1 < 1$: In this case stellar gravity is the dominant potential field. For particles with $\sigma > 3 \text{ gm}^{-2}$, the lightness number values are small and possible orbit conditions, ρ_0 and z_0 , are not displaced significantly from the values calculated when radiation pressure forces are ignored. As σ decreases, the on-axis libration point position moves towards the Sun and the nominal radius at which the three halo orbits bifurcate to just one possible halo orbit decreases until $\sigma < 0.7673 \text{ gm}^{-2}$.

$\beta_2 < 1 < \beta_1$: Between loading values of $0.6584 < \sigma < 0.7673 \text{ gm}^{-2}$ there exists a scenario where there are no possible halo orbits to trap particles between the two stars. In this case the dominant force from the Sun is solar radiation pressure and the dominant force from α -Centauri is gravity.

Contour 2, in Fig 5-8 provides an example of this case. The required angular velocity for a circular halo orbit is imaginary near the Sun thus no possible halo orbits exist. Near α -Centauri, the angular velocity is real, resulting in a contour of possible halo orbit conditions on the opposite side of the Centauri system.

$\beta_1 > \beta_2 > 1$: In this case, the dominant force is radiation pressure and halo-orbits can no longer exist as the combined radiation pressure will push any particles out of the system. Contour 1, in Fig 5-8 provides an example of this case. The on-axis libration point is unstable and any motion off-axis will cause the particle to be swept from the system due to radiation pressure.

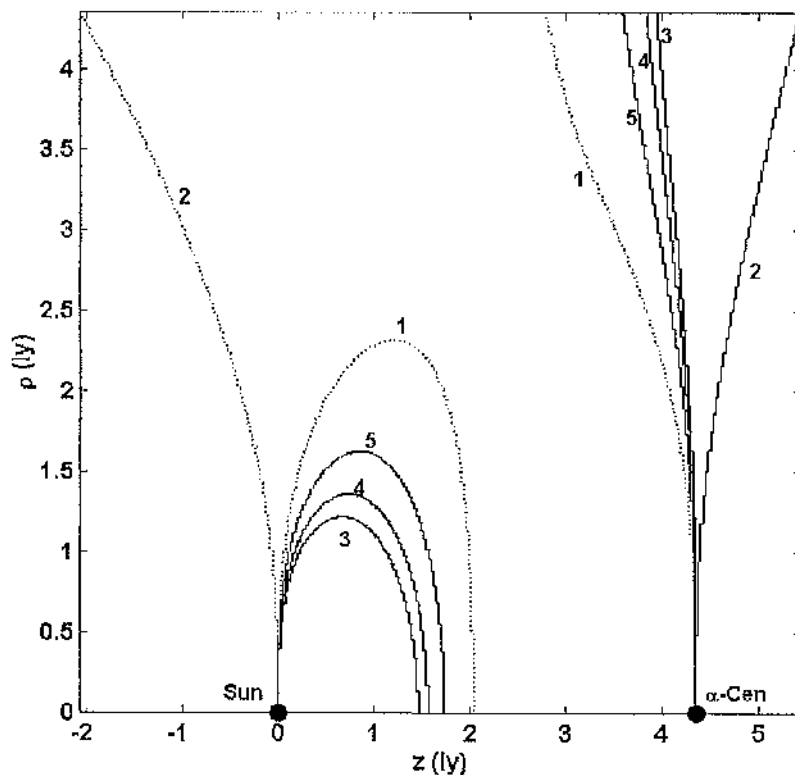


Figure 5-8 Possible halo orbit ρ - z values for different particle loading values

Values of σ (gm^{-2}) contours: **1=0.5 2=0.7 3=0.9 4=1 5=3**

**dotted-line corresponds to imaginary values of $\dot{\theta}$ therefore orbit can not exist*

σ_y (kgm^{-2})	β_1	β_2
3×10^{-3}	0.2558	0.2195
1×10^{-3}	0.7673	0.6584
9×10^{-4}	0.8525	0.7315
7×10^{-4}	1.0961	0.9405
5×10^{-4}	1.5346	1.3167

Table 5-3 Sail loading a corresponding lightness numbers for Sun-Centauri system

Orbit	σ (gm^{-2})	ρ_o (ly)	z_o (ly)	$\dot{\theta}_o$ (πs^{-1})	T (Myr)
1	1	1.2757	0.4360	4.0775×10^{-15}	48.863
2		1.2349	1.0900	3.3075×10^{-15}	60.239
3		1.8742	4.2728	4.2480×10^{-15}	46.901
4	0.7	1.9832	4.5780	1.5615×10^{-15}	127.594

Table 5-4 Halo orbit initial conditions including orbit period

Figure 5-9 shows a set of possible halo orbits for different particle loading parameters corresponding to the first lightness number case where $\beta_2 < \beta_1 < 1$ ($\sigma = 3 \text{ gm}^{-2}$) and second case where $\beta_2 < 1 < \beta_1$ ($\sigma = 0.7 \text{ gm}^{-2}$). The initial conditions for each orbit are provided in Table 5-4.

Orbits 1, 3 and 4 can be described as stable as they are observed to remain within the vicinity of the nominal orbit after applying a small perturbation. This agrees with the potential energy analysis which indicates that local minima exist around the orbit conditions for 1,3 and 4. The orbit period is extremely long, in the order of 10 Myrs (million years). Orbit 2 is unstable with escape occurring rapidly exhibiting homoclinic behaviour [Jordan and Smith, 1999], see Fig 5-10. Escape from the nominal orbit occurs after roughly 60 Myrs and the trajectory performs a loop around the Centauri system 75 Myrs later. The trajectory returns to the nominal orbit 150 Myrs after escape.

The two-centre problem provides a basic model of the dynamics between two stars, ignoring the photo-gravitational influence of other nearby stars and the relative stellar motion. The two-centre equations can be adapted to investigate how these perturbations affect the system dynamics.

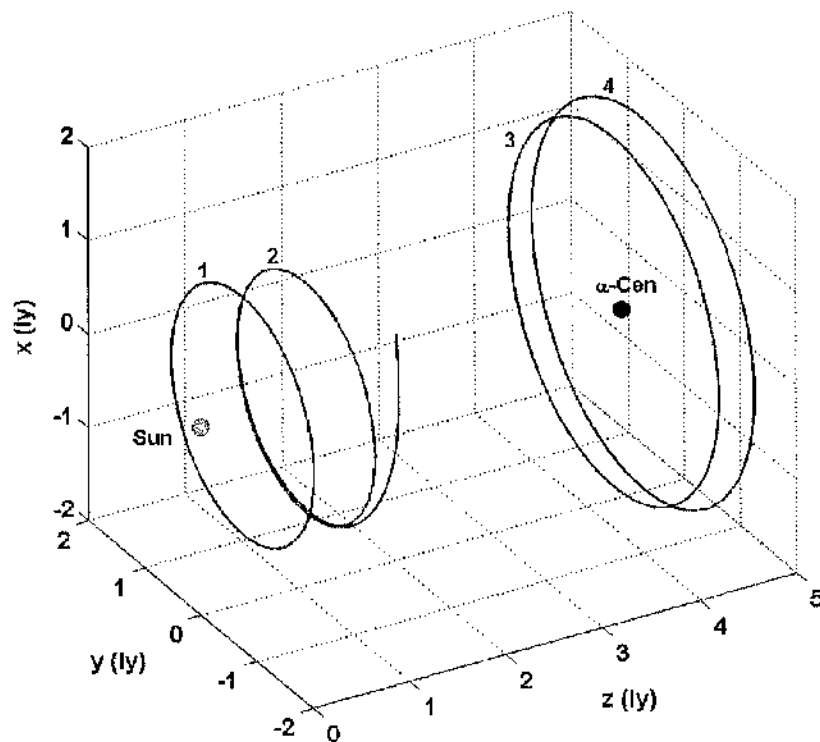


Figure 5-9 Possible halo orbits for particles with loading 3 gm^{-2} (1,2,3) and 0.7 gm^{-2} (4)

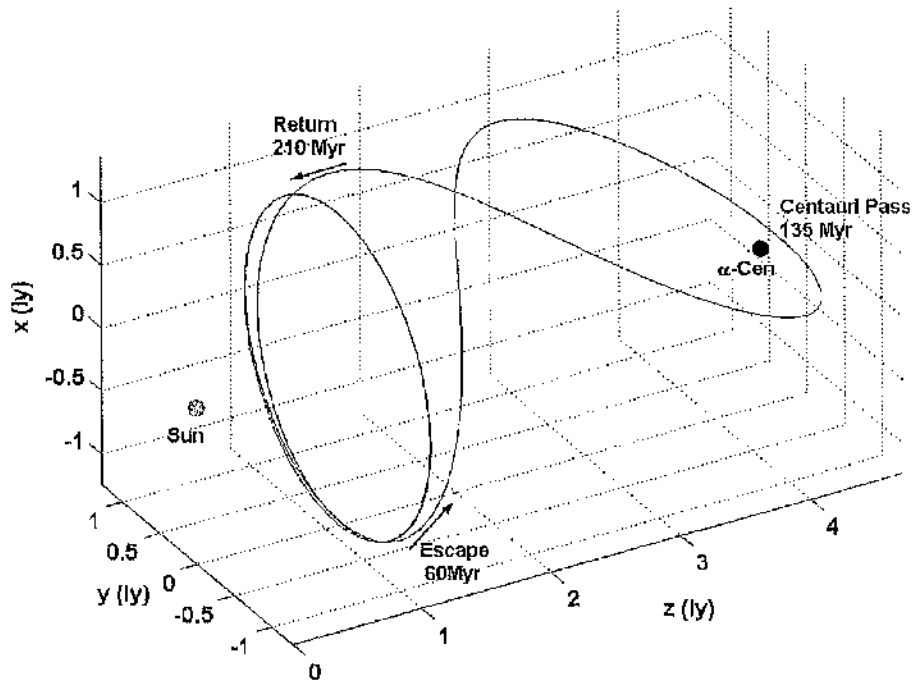


Figure 5-10 'Homoclinic-like' trajectory of unstable halo orbit

5.3 Closed-form solution of the two-centre problem

5.3.1 Derivation using confocal elliptical coordinates

In Chapter 2, it was demonstrated that an explicit solution exists for the two-body problem using parabolic coordinates. The stable and unstable manifolds winding onto/off the circular displaced orbit were shown to be bound within a paraboloid surface. Similarly, a closed-form solution can be derived for the photo-gravitational two-centre problem by transforming Eq (5.5.1) and Eq (5.5.2) into confocal elliptical coordinates [Waalkens et al, 2003].

These equations are represented in a rotating frame with angular momentum h_z . Elliptical coordinates (ξ, η) can be used to express the radial distance from M_1 and M_2 as $|\mathbf{r}_1| = (\xi + \eta)$ and $|\mathbf{r}_2| = (\xi - \eta)$. The polar coordinates can be transformed into elliptical coordinates using $|\mathbf{r}_1| = \sqrt{\rho^2 + z^2}$ and $|\mathbf{r}_2| = \sqrt{\rho^2 + (1-z)^2}$ then solving $|\mathbf{r}_1| - |\mathbf{r}_2|$ for z to obtain

$$z = 2\xi\eta + \frac{1}{2} \quad (5.19.1)$$

$$\rho = \sqrt{\frac{1}{4}(4\xi^2 - 1)(1 - 4\eta^2)} \quad (5.19.2)$$

The time derivatives of ρ and z are obtained as

$$\dot{z} = 2\dot{\xi}\eta + 2\xi\dot{\eta} \quad (5.20.1)$$

$$\dot{\rho} = \frac{\xi\dot{\xi}}{\rho}(1 - 4\eta^2) - \frac{\eta\dot{\eta}}{\rho}(4\xi^2 - 1) \quad (5.20.2)$$

The non-dimensionalised photo-gravitational Hamiltonian can then be written as

$$H = \frac{1}{2}(\dot{\rho}^2 + \dot{z}^2 + \rho^2\dot{\theta}^2) - \frac{(1 - \beta_1)}{|\mathbf{r}_1|} - \frac{\lambda(1 - \beta_2)}{|\mathbf{r}_2|} \quad (5.21)$$

The first term on the right hand side corresponds to the kinetic energy. The ρ - and z -velocity terms can be expanded as

$$\dot{\rho}^2 = 4\xi^2\dot{\xi}^2 \frac{(1 - 4\eta^2)}{(4\xi^2 - 1)} - 8\xi\dot{\xi}\eta\dot{\eta} + 4\eta^2\dot{\eta}^2 \frac{(4\xi^2 - 1)}{(1 - 4\eta^2)} \quad (5.22.1)$$

$$\dot{z}^2 = 4\xi^2\dot{\eta}^2 + 8\xi\dot{\xi}\eta\dot{\eta} + 4\xi^2\dot{\eta}^2 \quad (5.22.2)$$

Substitution of these expressions into Eq (5.21) gives the Hamiltonian in terms of elliptical coordinates

$$H = \frac{1}{2} \left[4\xi^2 \left(\xi^2 \frac{(1 - 4\eta^2)}{(4\xi^2 - 1)} + \eta^2 \right) + 4\eta^2 \left(\eta^2 \frac{(4\xi^2 - 1)}{(1 - 4\eta^2)} + \xi^2 \right) + \frac{1}{4}(4\xi^2 - 1)(1 - 4\eta^2)\dot{\theta}^2 \right] - \frac{(1 - \beta_1)}{(\xi + \eta)} - \frac{\lambda(1 - \beta_2)}{(\xi - \eta)} \quad (5.23)$$

The momenta terms can be identified using $P_\xi = \partial H / \partial \dot{\xi}$, $P_\eta = \partial H / \partial \dot{\eta}$ and $P_\theta = \partial H / \partial \dot{\theta}$ as

$$P_\xi = 4\dot{\xi} \left(\xi^2 \frac{(1-4\eta^2)}{(4\xi^2-1)} + \eta^2 \right) \quad (5.24.1)$$

$$P_\eta = 4\dot{\eta} \left(\eta^2 \frac{(4\xi^2-1)}{(1-4\eta^2)} + \xi^2 \right) \quad (5.24.2)$$

$$P_\theta = \frac{1}{4} (4\xi^2 - 1)(1 - 4\eta^2) \dot{\theta} \quad (5.24.3)$$

These terms can be substituted into the Hamiltonian to obtain

$$H = \frac{1}{2} \left[\frac{P_\xi^2 (4\xi^2 - 1)}{(4\xi^2(1-4\eta^2) + 4\eta^2(4\xi^2 - 1))} + \frac{P_\eta^2 (1-4\eta^2)}{(4\xi^2(1-4\eta^2) + 4\eta^2(4\xi^2 - 1))} + \frac{P_\theta^2}{\rho^2} \right] - \frac{(1-\beta_1)}{(\xi+\eta)} - \frac{\lambda(1-\beta_2)}{(\xi-\eta)} \quad (5.25)$$

A common factor of $1/(4\xi^2 - 4\eta^2)$ can be extracted from the Hamiltonian as follows

$$H = \frac{1}{8(\xi^2 - \eta^2)} \left[P_\xi^2 (4\xi^2 - 1) + P_\eta^2 (1 - 4\eta^2) + 4P_\theta^2 \left(\frac{1}{(4\xi^2 - 1)} + \frac{1}{(1 - 4\eta^2)} \right) \right] + \frac{\eta[(1-\beta_1) - \lambda(1-\beta_2)] - \xi[(1-\beta_1) + \lambda(1-\beta_2)]}{(\xi^2 - \eta^2)} \quad (5.26)$$

The Hamilton-Jacobi method can now be applied to separate the Hamiltonian using the transforming function $S(t, \xi, \eta, \theta)$ [Landau and Lifschitz, 1976; Goldstein, 1959], which is defined as

$$S(t, \xi, \eta, \theta) = -Et + P_\theta \theta + S(\xi) + S(\eta) \quad (5.27)$$

where E represents the total energy. The transforming function is selected to meet the Hamilton-Jacobi condition $\partial S / \partial t + H = 0$. Equation (5.26) can be substituted into this condition to obtain

$$-E + \frac{1}{8(\xi^2 - \eta^2)} \left[P_\xi^2 (4\xi^2 - 1) + P_\eta^2 (1 - 4\eta^2) + 4P_\theta^2 \left(\frac{1}{(4\xi^2 - 1)} + \frac{1}{(1 - 4\eta^2)} \right) \right] + \frac{\eta[(1 - \beta_1) - \lambda(1 - \beta_2)] - \xi[(1 - \beta_1) + \lambda(1 - \beta_2)]}{(\xi^2 - \eta^2)} = 0 \quad (5.28)$$

This expression can be re-arranged to group the separable variables as

$$8E\eta^2 + P_\eta^2 (1 - 4\eta^2) + \frac{4P_\theta^2}{(1 - 4\eta^2)} + 8\eta[(1 - \beta_1) - \lambda(1 - \beta_2)] = 8E\xi^2 - P_\xi^2 (4\xi^2 - 1) - \frac{4P_\theta^2}{(4\xi^2 - 1)} + 8\xi[(1 - \beta_1) + \lambda(1 - \beta_2)] \quad (5.29)$$

The expression on the left-hand side is dependant only on η and the left-hand side dependant on ξ . The expression can be split using the separation constant Φ to obtain

$$P_\xi^2 (4\xi^2 - 1) - 8E\xi^2 + \frac{4P_\theta^2}{(4\xi^2 - 1)} - 8\xi[(1 - \beta_1) + \lambda(1 - \beta_2)] = -\Phi \quad (5.30.1)$$

$$P_\eta^2 (1 - 4\eta^2) + 8E\eta^2 + \frac{4P_\theta^2}{(1 - 4\eta^2)} + 8\eta[(1 - \beta_1) - \lambda(1 - \beta_2)] = \Phi \quad (5.30.2)$$

Elliptical bounding surfaces can then be determined from the initial conditions by evaluating the constants E , Φ and P_θ . The expressions are then solved for ξ and η , with the momenta terms $P_\xi = P_\eta = 0$. The constants $A = [(1 - \beta_1) + \lambda(1 - \beta_2)]$ and $B = [(1 - \beta_1) - \lambda(1 - \beta_2)]$ are used to obtain the following quartic equations

$$8E\xi^4 + 8A\xi^3 - (2E + \Phi)\xi^2 - 2A\xi - P_\theta^2 + \frac{\Phi}{4} = 0 \quad (5.31.1)$$

$$8E\eta^4 + 8B\eta^3 - (2E + \Phi)\eta^2 - 2B\eta - P_\theta^2 + \frac{\Phi}{4} = 0 \quad (5.31.2)$$

Each set of constants gives 4 values of η and of ξ . Each value corresponds to an ellipsoid surface in Cartesian space which bounds the orbit. The initial conditions (ρ_o, z_o) are used to determine the elliptical coordinate ξ_o from

$$4\xi_o^4 - (4(z_o - 1/2)^2 + 4\rho_o^2 + 1)\xi_o^2 + (z_o - 1/2)^2 = 0 \quad (5.32)$$

which can be substituted into $|\mathbf{r}_1| = (\xi + \eta)$ or $|\mathbf{r}_2| = (\xi - \eta)$ to determine the corresponding value of η_0 . The velocity components can be calculated by treating Eq (5.20) as a simultaneous equation problem and solving for $\dot{\xi}$ and $\dot{\eta}$ at the initial conditions. Once the parameters $(\xi, \eta, \dot{\xi}, \dot{\eta})$ are evaluated, the momenta terms can then be calculated using Eq (5.24). These terms are required to calculate the separation constant Φ from Eq (5.30). After evaluating the three constants E , P_θ and Φ , the zero-velocity ellipsoid surfaces are identified by solving Eq (5.31) for ξ and η .

5.3.2 Stable halo orbits bound by elliptical surfaces

In the case of stable halo orbits, 4 bounding surfaces trap the orbit represented by coordinates $(\xi_1, \xi_2, \eta_1, \eta_2)$. Figure 5-11 shows the bounding surfaces for a stable orbit, $\rho_0=0.3367$ and $z_0=0.1$, with particle loading $\sigma=3 \times 10^{-3} \text{ kgm}^{-2}$ where the initial conditions are perturbed slightly by setting $\dot{\rho}_0=-0.1$. A closer view of the bounding surfaces is provided in Fig 5-12. Redundant surfaces have been removed to make the figure easier to view.

The elliptical bounding surfaces for a stable halo orbit near the Centauri system is provided in Fig 5-13. The initial conditions are again perturbed slightly by setting $\dot{\rho}_0=-0.1$. A closer view of the bound orbit is provided in Fig 5-14.

Figure 5-15 shows a stable halo orbit for a particle of loading $\sigma=0.7 \text{ gm}^{-2}$. In this case the dominant force from the Sun is solar radiation pressure which produces a displaced orbit in the anti-Sun direction at Centauri. The initial conditions are again slightly perturbed by setting $\dot{\rho}_0=-0.1$. The elliptic coordinates representing the bounding surfaces for each of these examples are provided in Table 5-5.

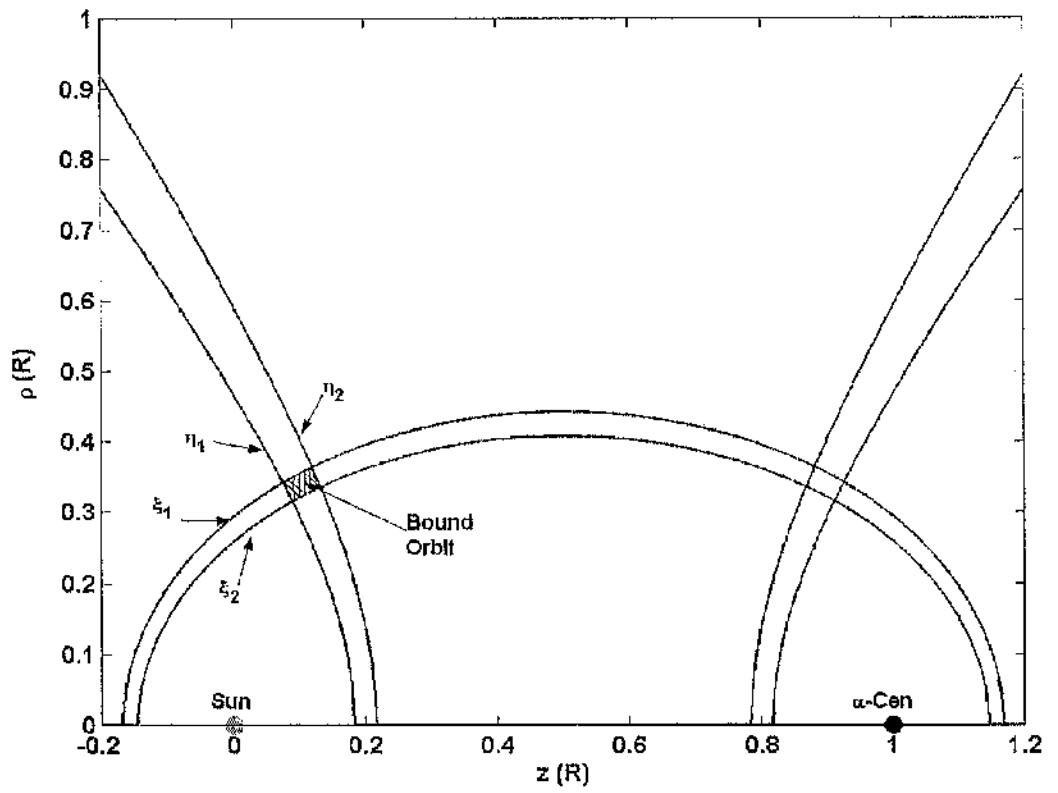


Figure 5-11 Perturbed stable orbit bounded by elliptical surfaces

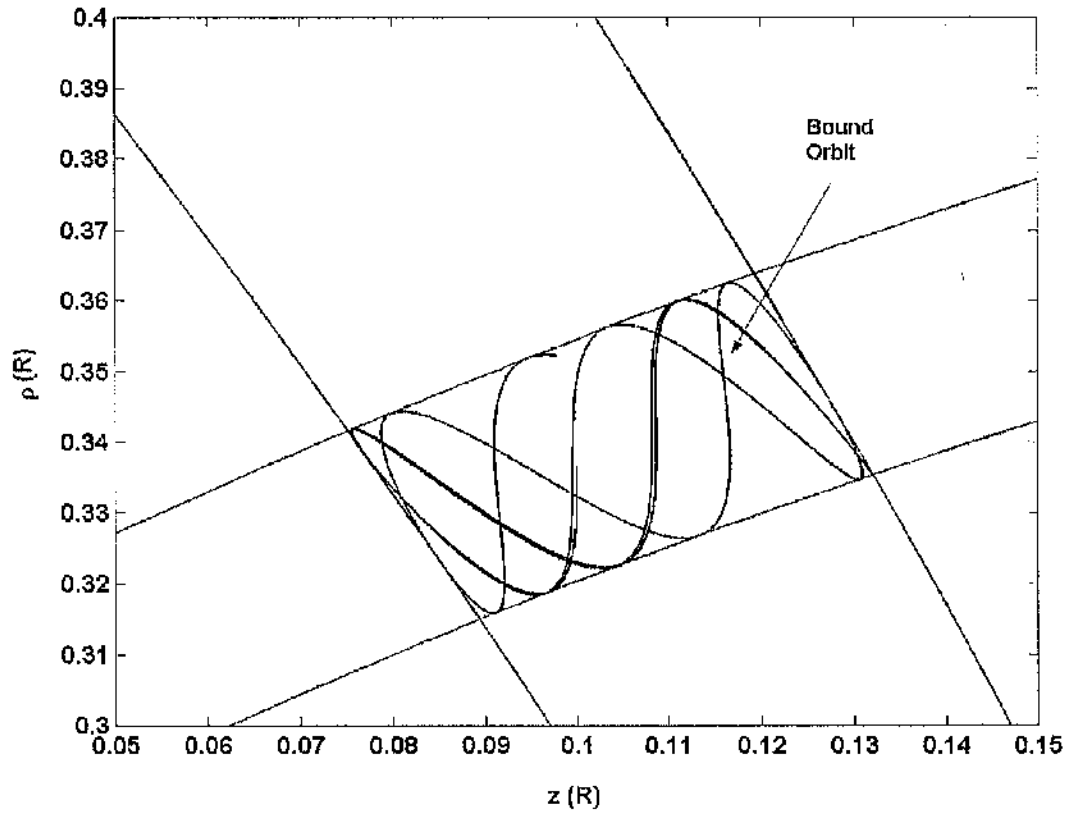


Figure 5-12 Closer view of bounded perturbed stable orbit

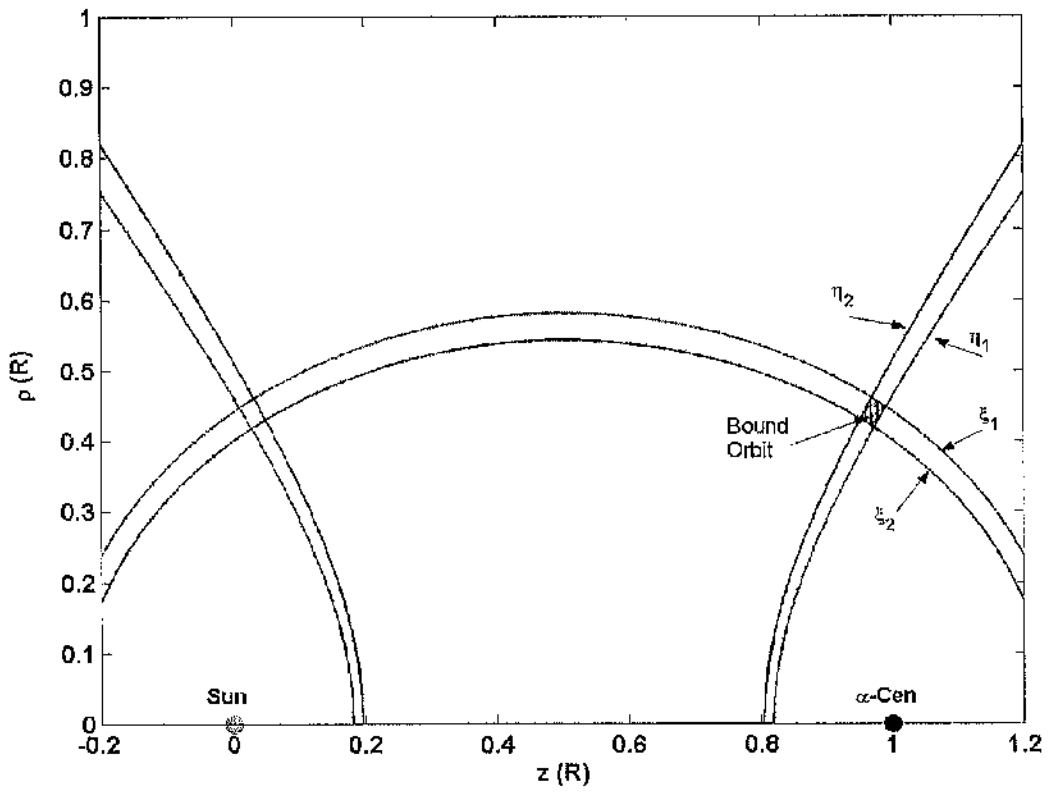


Figure 5-13 Stable Orbit near Centauri bound by elliptical surfaces

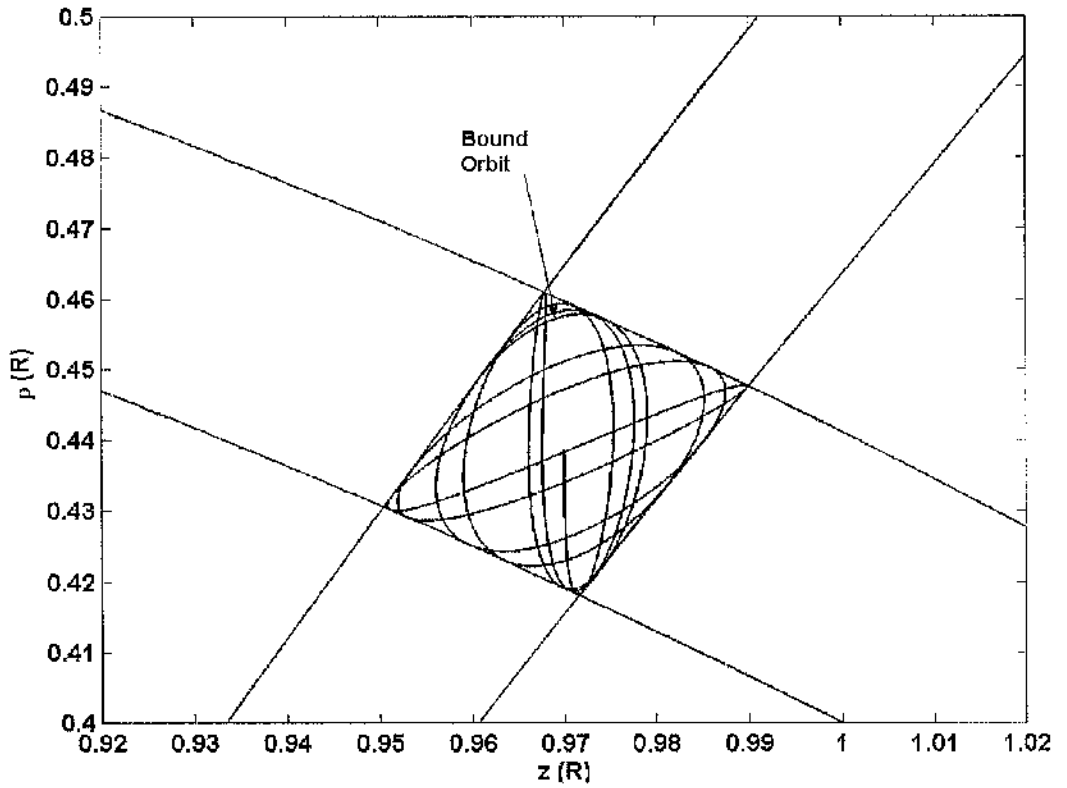


Figure 5-14 Closer view of stable orbit near Centauri

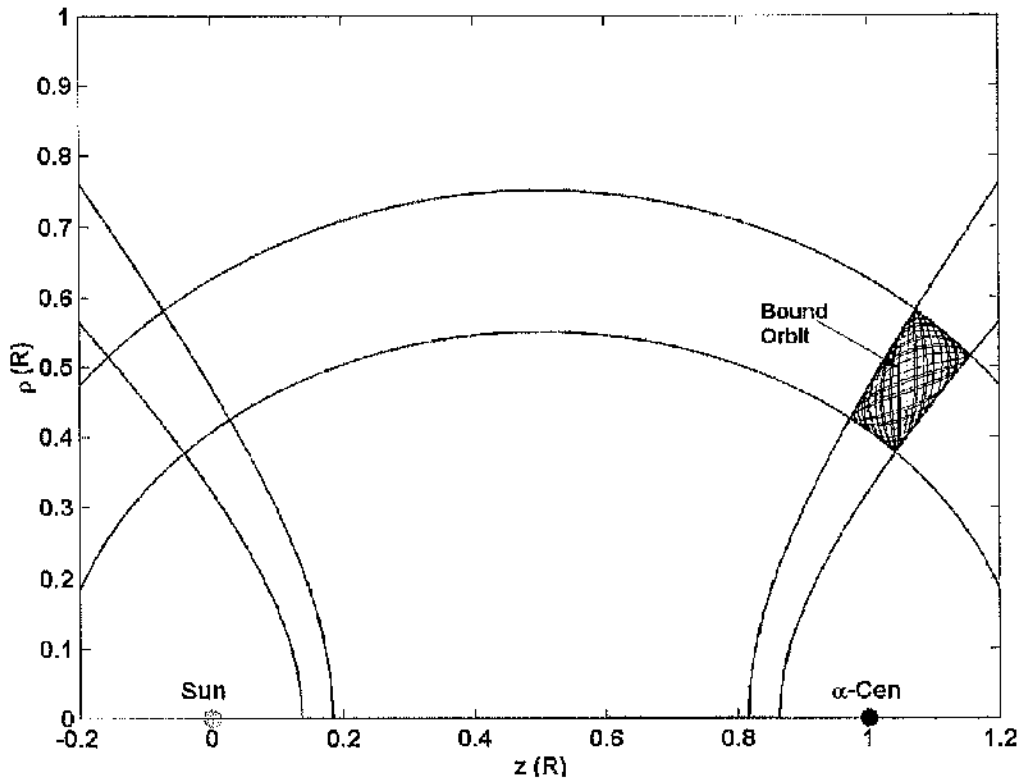


Figure 5-15 Stable orbit for particle with loading 0.7 gm^{-2}

Φ	ρ_o	z_o	$\dot{\rho}_o$	\dot{z}_o	ξ_1	ξ_2	η_1	η_2
1.8018	0.3367	0.1	-0.1	0	0.6678	0.6455	-0.3181	-0.2851
0.6138	0.4385	0.97	-0.1	0	0.7671	0.7384	0.3914	0.3050
-0.2524	0.4548	1.05	-0.1	0	0.9018	0.7431	0.3640	0.3172

Table 5-5 Elliptical coordinates representing surfaces bounding stable orbit

5.3.3 Elliptical bounding surfaces for unstable initial conditions

It has been demonstrated that four elliptical surfaces bound the motion of a stable orbit. Consider the elliptical surfaces bounding an unstable orbit. In the unstable case, the resulting trajectory can be described as homoclinic, winding off the nominal orbit and passing near to the Sun or Centauri system. Figure 5-16 shows a set of elliptical surfaces bounding a 'homoclinic-like' trajectory which loops around the Centauri system. The reflection of the η_1 surface is declared redundant as it evidently does not play a role in bounding the trajectory. A Cartesian plot of this trajectory is provided in Fig 5-17.

A homoclinic trajectory which loops around the Sun is produced by slightly perturbing the z_o condition sunward. A cylindrical polar coordinate plot of this orbit is provided in

Fig 5-18, including the elliptical surfaces which bound the orbit. A Cartesian plot of this trajectory is provided in Fig 5-19. The initial conditions and the elliptical coordinates of the bounding surfaces in the case of both trajectories are provided in Table 5-6.

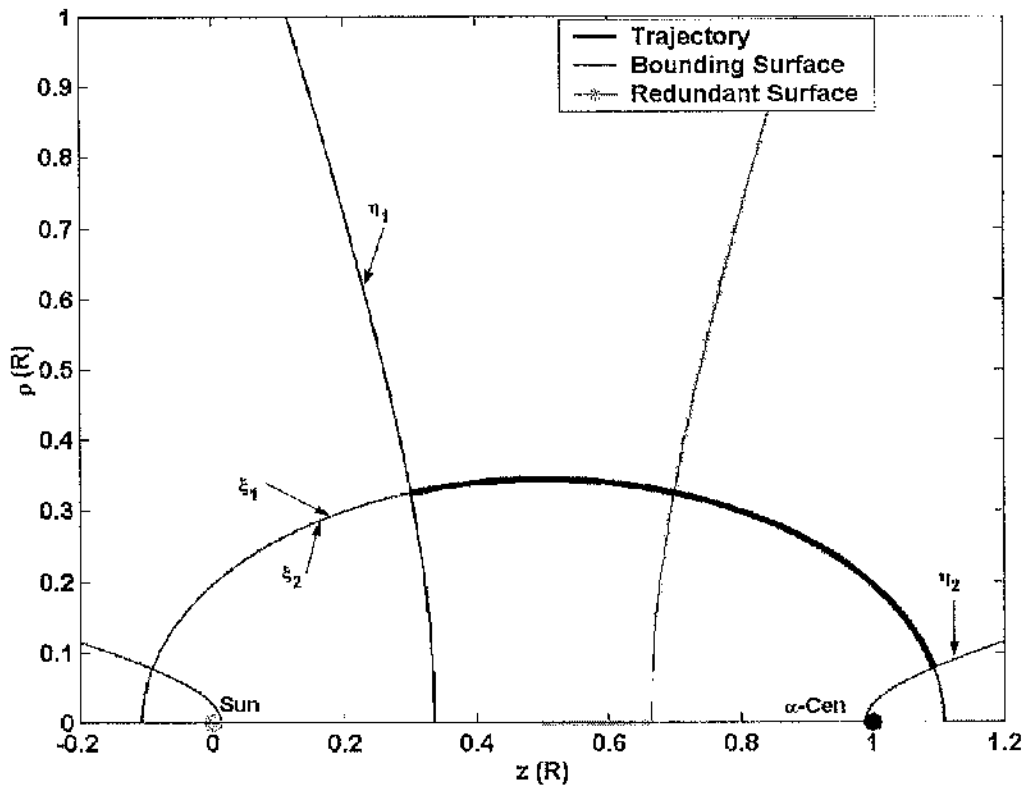


Figure 5-16 Elliptical surfaces bounding homoclinic trajectory between unstable limit cycle and the Centauri system

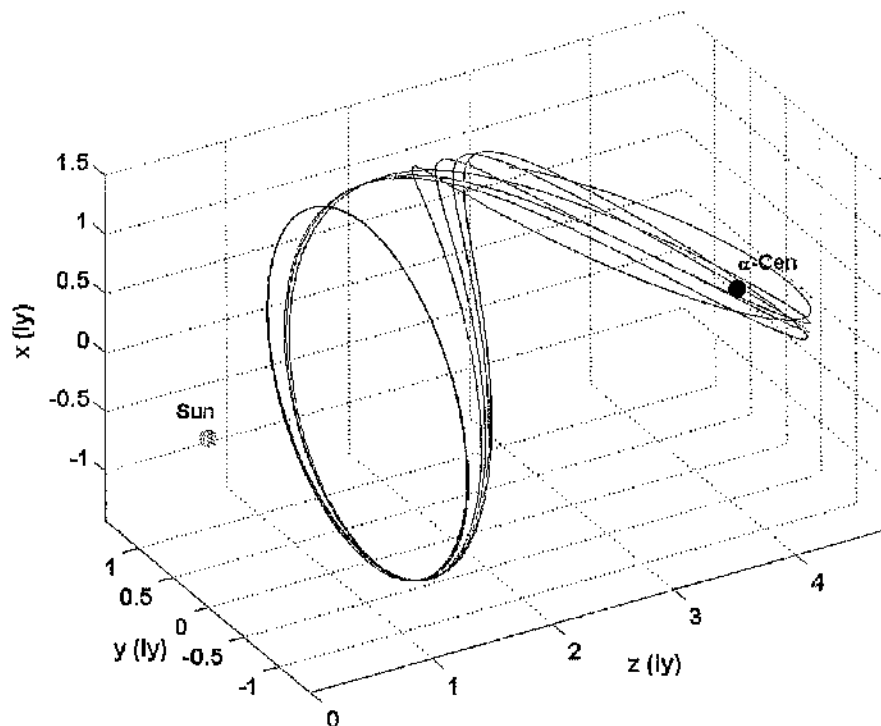


Figure 5-17 Homoclinic trajectory between unstable limit cycle and the Centauri system

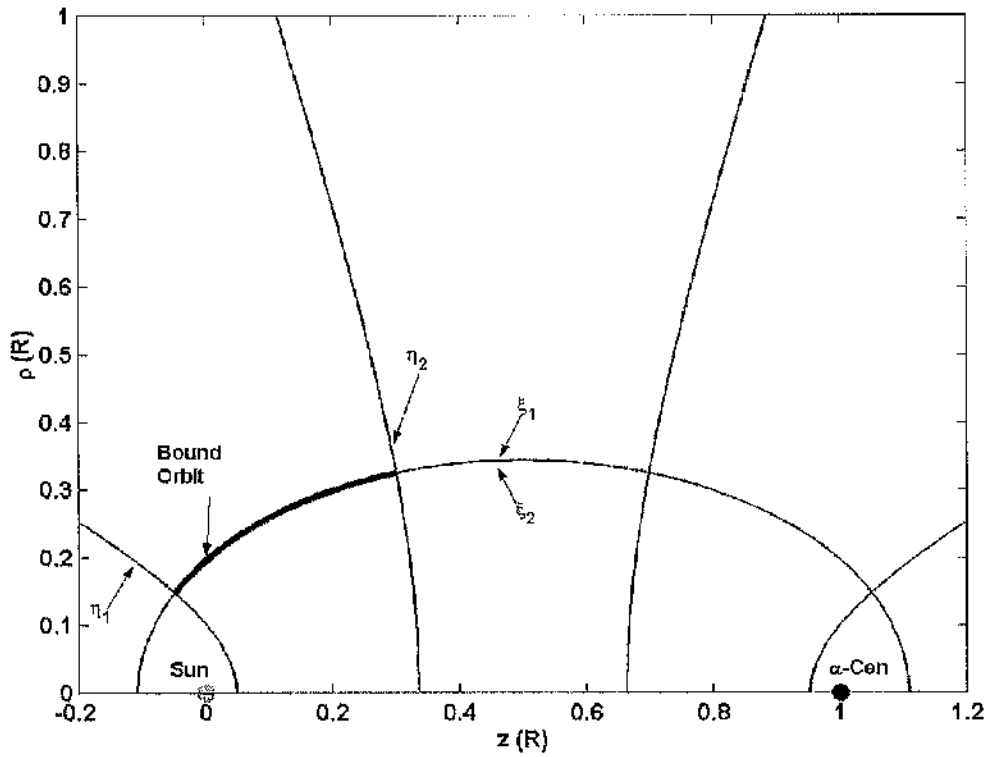


Figure 5-18 Elliptical surfaces bounding homoclinic trajectory between unstable limit cycle and the Sun

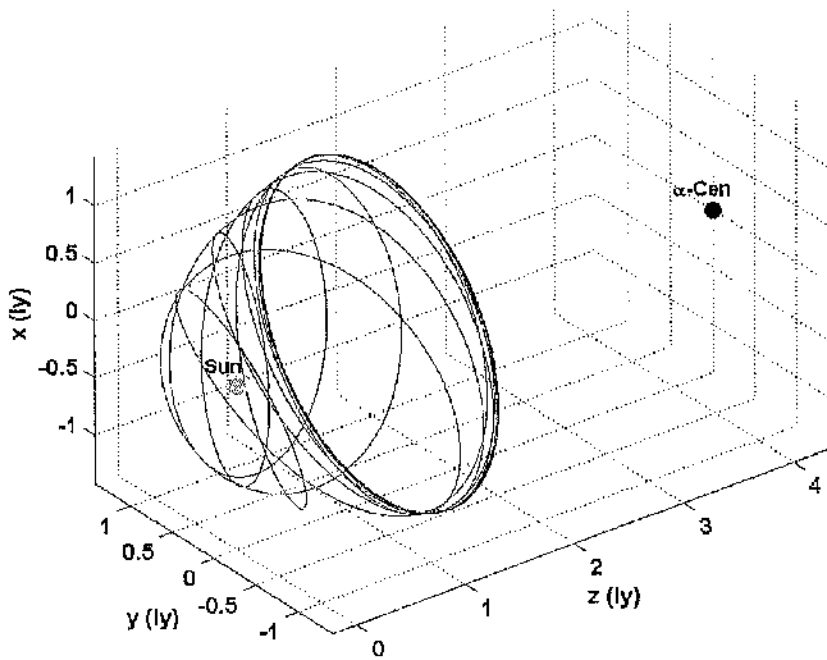


Figure 5-19 Homoclinic trajectory between unstable limit cycle and the Sun

Φ	ρ_0	z_0	$\dot{\rho}_0$	\dot{z}_0	ξ_1	ξ_2	η_1	η_2
1.1664	0.3251	0.3	0	0	0.6071	0.6071	-0.1647	0.4874
1.1666	0.3251	0.2999	0	0	0.6071	0.6071	-0.4521	-0.1647

Table 5-6 Elliptic coordinates representing surfaces bounding unstable orbit

5.3.4 Stellar transfer trajectories

Similar to the weak-stability boundary of the three-body problem, trajectories which asymptotically wind on and off a halo orbit produce a surface of manifolds. Depending on the energy, a particle can remain trapped on a manifold surface between the two stars. The invariant manifolds are bound by an ellipsoid surface determined using the explicit solution obtained with confocal elliptical coordinates. Using the manifold surfaces, it is possible to identify trajectories which could enable dust particles to be transferred between passing star systems.

The starting location can be determined from the bounding surface intersection. From Section 5.3.3, the closest approach to the Sun of the homoclinic trajectory occurs when surfaces η_1 and ξ_2 intersect. The values of z_i and ρ_i can be calculated by substituting the elliptic coordinate values of the intersecting surfaces into Eq (5.19.1) and Eq (5.19.2). The z -component of angular momentum, h_z , evaluated at the nominal halo orbit is used to calculate the angular velocity at the intersection point as $\dot{\theta}_i = h_z / \rho_i^2$. The calculated insertion conditions are $\rho_i=0.1471$, $z_i=-0.0490$ and $\theta_i=17.1284$. In order to complete the transfer and break through the boundary set by surface η_2 , a small velocity perturbation is applied, \dot{z} . The resulting transfer trajectory is provided in Fig 5-20 including the bounding surfaces.

The elliptic coordinates representing the bounding surfaces are provided in Table 5-7. The $\xi_{1,2}$ surfaces are slightly further separated due to the increased energy resulting from the applied \dot{z} velocity. The $\eta_{1,2}$ surfaces are identical to those obtained in the Sun and Centauri 'homoclinic-like' trajectories investigated in Section 5.3.3. The state-space representation of this transfer trajectory is provided in Figure 5-21. The transfer time between the Sun and the Centauri system is approximately 65 Myrs.

Φ	ρ_o	z_o	$\dot{\rho}_o$	\dot{z}_o	ξ_1	ξ_2	η_1	η_2
1.1675	0.1471	-0.0490	0	0.05	0.6098	0.6045	-0.4521	0.4874

Table 5-7 Elliptic coordinates representing surfaces bounding transfer trajectory

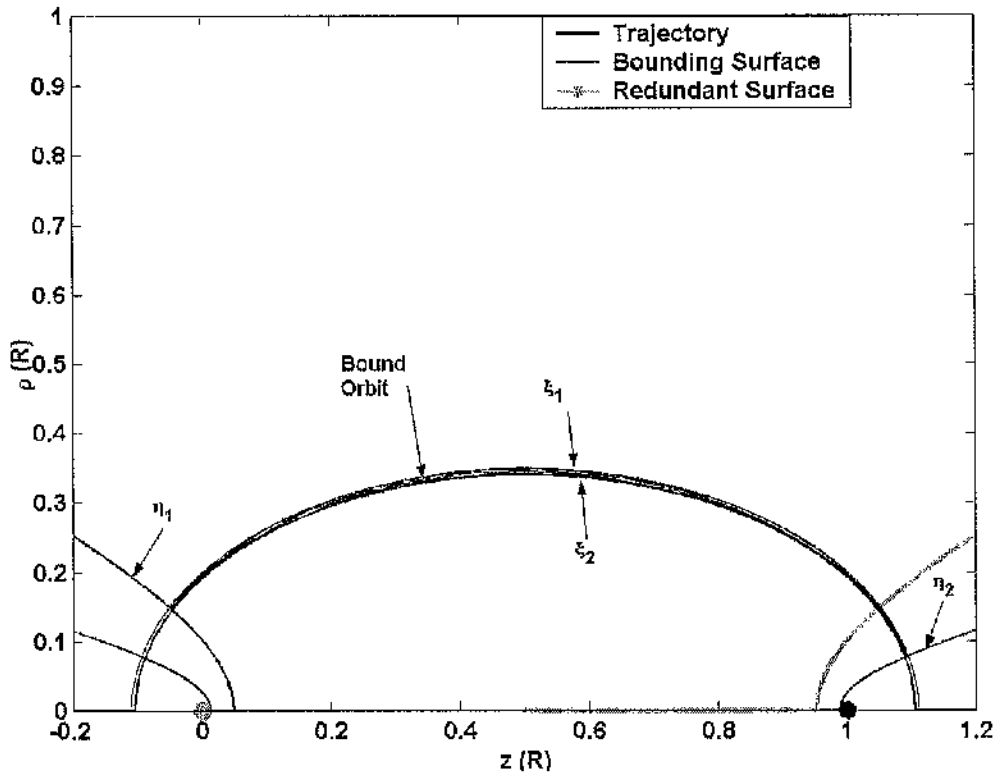


Figure 5-20 Elliptical surfaces bounding transfer trajectory between the Sun and Centauri

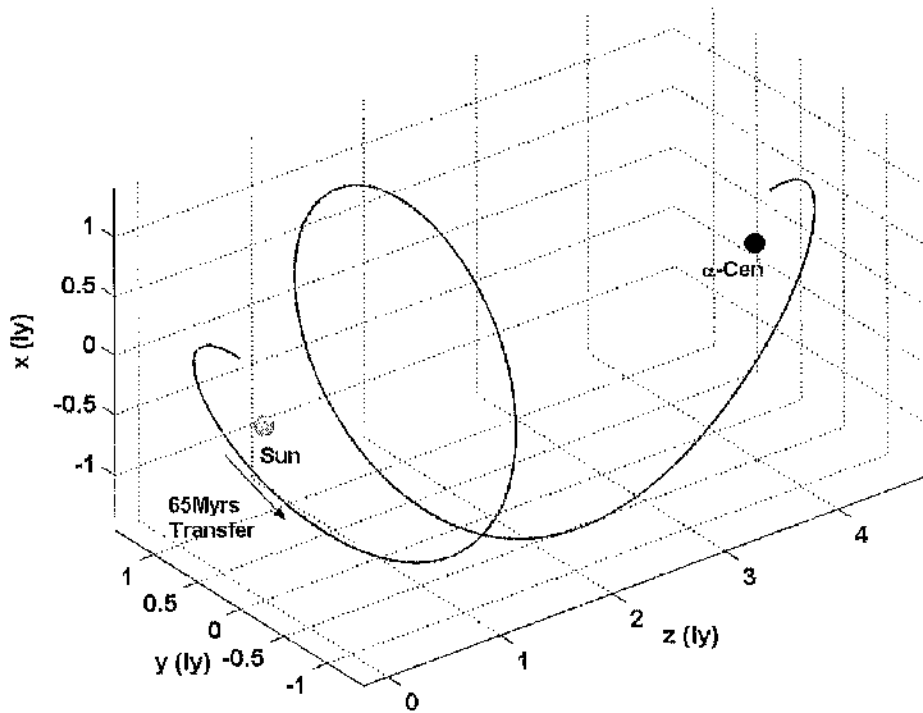


Figure 5-21 Transfer trajectory between the Sun and Centauri

5.4 Effect of additional body on two-centre dynamics

5.4.1 Local stellar neighbourhood

The perturbation caused by introducing the photo-gravitational potential of a third star will now be included in the two-centre equations of motion. The local stellar neighbourhood within 3pc (parsec) of our Sun is included in Fig 5-22. There are 11 stars in total including two binary systems (Sirius and Luyten 726-8A) and one ternary system, α -Centauri. The relative distances from the Sun, equatorial spherical coordinates and spectral class are provided in Table 5-8.

Right ascension is provided in the form (hours minutes seconds) where the 360° celestial sky is divided into 24 hours; 1 hour corresponds to 15° . Declination is provided in the form (degrees minutes seconds) which defines the angular location accurate to 1 arc second ($1/3600$ th degree). Combined with the separation distance from the Sun, this provides a spherical coordinate system representing a fixed reference frame with the Sun located at the origin.

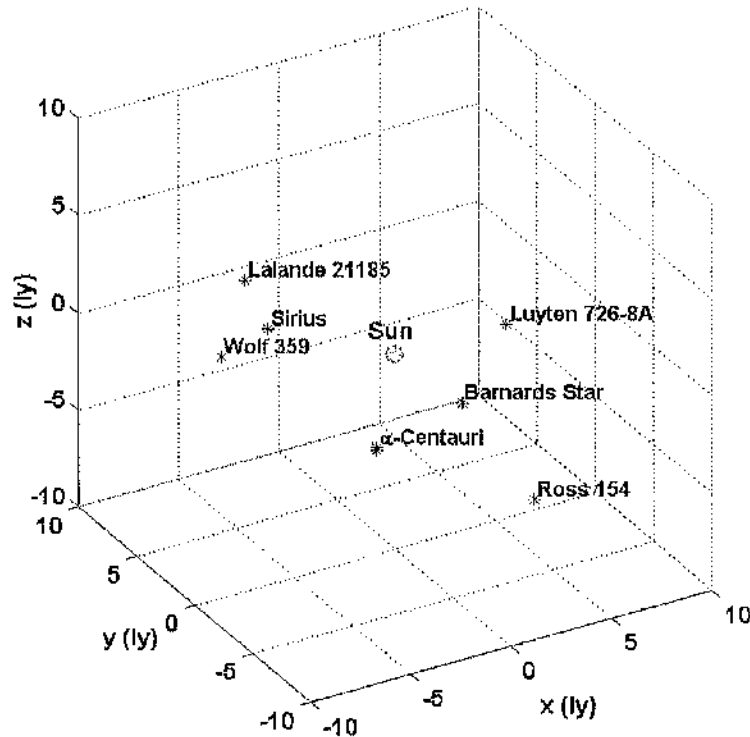


Figure 5-22 Local stellar neighbourhood within 3pc

Star name	Distance from Sun (ly)	Right Ascension	Declination (d m s)	Spectral Type
Proxima	4.22	14 29 43.0	-60 50 13.8	M5.5V
α -Centauri A	4.36	14 39 36.5	+04 41 36.2	G2.0 V
α -Centauri B	4.36	14 39 36.5	+04 41 36.2	K1.0 V
Barnard's Star	5.96	17 57 48.5	+04 41 36.2	M3.8V
Wolf 359	7.78	10 56 29.2	+35 58 11.6	M6.0V
Lalande 21185	8.29	11 03 20.2	+35 58 11.6	M2.0V
Sirius A	8.58	06 45 08.9	-16 42 58.0	A1.0 V
Sirius B	8.58	06 45 08.9	-16 42 58.0	DA2
Luyten 726-8A	8.72	01 39 01.3	-17 57 01.0	M5.5V
Luyten 726-8B	8.72	01 39 01.3	-17 57 01.0	M5.5V
Ross 154	9.68	18 49 49.4	-23 50 10.5	M3.5V

Table 5-8 Position and spectral data of all stars within 3pc of the Sun

Spectral Type	Colour	Surface Temperature ($^{\circ}$ K)
O	Blue	>30,000
B	Blue/White	11,000-30,000
A	White	7500-11,000
F	Yellow/White	5900-7500
G	Yellow	5200-5900
K	Yellow/Orange	3900-5200
M	Red	2500-3900

Table 5-9 Spectral classification of stars

A common method for categorising stars is to use the MK spectral scale devised by Morgan, Keenan and Kellman [1943]. The stars are classed according to their spectral and luminosity properties. The different spectral classes are represented by the letters O, B, A, F, G, K and M which categorise star surface temperature range and subsequently colour, see Table 5-9. The temperature range represented by each letter is sub-divided depending on the value following the letter *i.e.* A9 \rightarrow A0. The sequence is ordered such that the spectral type B9 is immediately followed by A0.

The stellar luminosity is defined using roman numerals I-V. Type I corresponds to a super-giant, type II to a bright giant star, type III to a giant star, type IV to a sub-giant and type V to a main sequence dwarf star.

It is clear from Table 5-8 that most stars within 3pc of the Sun fall into the category of red-dwarf. These stars have a long lifespan due to the slow burn rate. They have a relatively small mass compared to the Sun so the gravitational influence exerted on the ideal two-centre model will be neglected. The largest star within 3pc of the Sun is Sirius. The gravitational potential of this star will be included in the two-centre model.

Sirius is actually a binary system located 8.58 ly from the Sun. The larger star, Sirius A is one of the brightest stars in the night sky. The size is roughly $2 M_{\odot}$ and it has a luminosity of 8.0647×10^{27} W. Sirius B is a much smaller, but extremely heavy white dwarf, defined as spectral type DA2, with a mass similar to the Sun's compressed into a volume 90% that of the Earth. The total mass of the Sirius system is $3.2 M_{\odot}$ giving mass ratio $\lambda=3.2$. The extinction corrected luminosity of Sirius relative to the on-axis equilibrium point, located 9.55 ly from Sirius, is 8.0430×10^{27} W; a luminosity reduction of 0.27%.

5.4.2 Derivation of gravity perturbed two-centre equations

Figure 5-23 shows the Sun-Centauri-Sirius system, assuming all stars are fixed relative to each other. The coordinate system is selected such that the Sun and α -Centauri are positioned along the x -axis. Also, the three stars are coplanar with the x - y plane. The photo-gravitational potential energy can be expressed as

$$V = -Gm \left[\frac{M_1(1-\beta_1)}{|\mathbf{r}_1|} + \frac{M_2(1-\beta_2)}{|\mathbf{r}_2|} + \frac{M_3(1-\beta_3)}{|\mathbf{r}_3|} \right] \quad (5.33)$$

where β_1 , β_2 and β_3 are the respective lightness numbers of the Sun, Centauri and Sirius for a given particle size. Using Cartesian coordinates, the respective distances between the Sun, Centauri, Sirius and the point mass m , located at position (x,y,z) , are $|\mathbf{r}_1| = \sqrt{x^2 + y^2 + z^2}$, $|\mathbf{r}_2| = \sqrt{(R-x)^2 + y^2 + z^2}$ and $|\mathbf{r}_3| = \sqrt{(X-x)^2 + (Y-y)^2 + (Z-z)^2}$. The mass of the Sun $M_1=1M_{\odot}$, mass of Centauri $M_2=2.17M_{\odot}$ and the mass of Sirius $M_3=3.2M_{\odot}$.

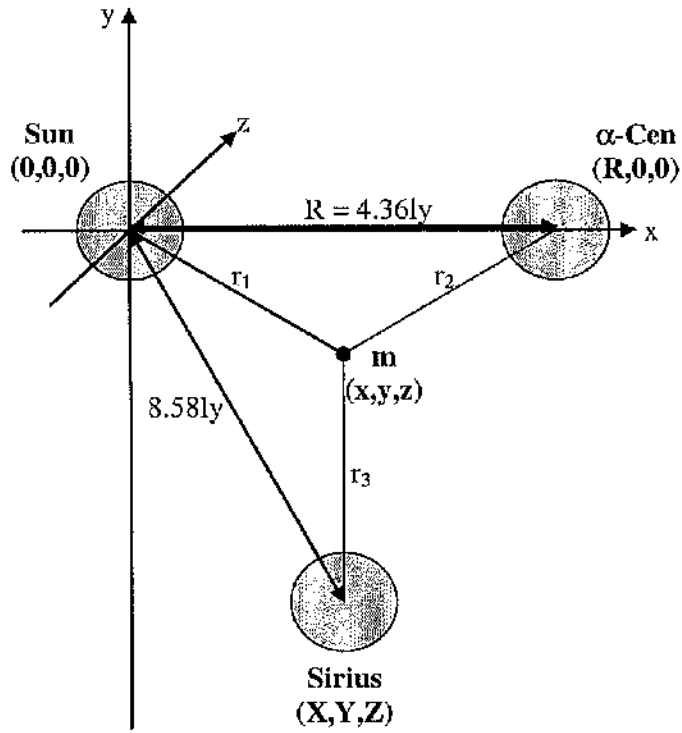


Figure 5-23 Schematic of three fixed stars Sun-Centauri-Sirius

The kinetic energy $T = (P_x^2 + P_y^2 + P_z^2)/2m$ where P_x , P_y and P_z are the components of momentum. The Hamiltonian function $H = T + V$ is equivalent to

$$H = \frac{1}{2m}(P_x^2 + P_y^2 + P_z^2) - Gm \left[\frac{M_1(1-\beta_1)}{|\mathbf{r}_1|} + \frac{M_2(1-\beta_2)}{|\mathbf{r}_2|} + \frac{M_3(1-\beta_3)}{|\mathbf{r}_3|} \right] \quad (5.34)$$

As before, the equations of motion can be obtained using partial derivatives $\partial H/\partial P_q = \dot{q}$ and $\partial H/\partial q = -\dot{P}_q$ where $q=(x,y,z)$. The non-dimensionalised equations have the form

$$\ddot{x} = -\frac{x(1-\beta_1)}{|\mathbf{r}_1|^3} + \frac{\lambda_1(1-\beta_2)(1-x)}{|\mathbf{r}_2|^3} + \frac{\lambda_2(1-\beta_3)(X-x)}{|\mathbf{r}_3|^3} \quad (5.35.1)$$

$$\ddot{y} = -\frac{y(1-\beta_1)}{|\mathbf{r}_1|^3} - \frac{\lambda_1(1-\beta_2)y}{|\mathbf{r}_2|^3} + \frac{\lambda_2(1-\beta_3)(Y-y)}{|\mathbf{r}_3|^3} \quad (5.35.2)$$

$$\ddot{z} = -\frac{z(1-\beta_1)}{|\mathbf{r}_1|^3} - \frac{\lambda_1(1-\beta_2)z}{|\mathbf{r}_2|^3} + \frac{\lambda_2(1-\beta_3)(Z-z)}{|\mathbf{r}_3|^3} \quad (5.35.3)$$

where the characteristic length $R=4.36\text{ly}$ and characteristic time $\tau = \sqrt{R^3/GM_1}$. The mass ratio between M_1 and M_2 , $\lambda_1=2.17$ and the mass ratio between M_1 and M_3 , $\lambda_2=3.2$. The

right ascension and declination angle of α -Centauri are rotated to position the stellar system at (1,0,0). Applying the same rotation to the right ascension and declination angles of Sirius, the co-planar position coordinates can be calculated as (-0.9425, -1.7275, 0). These equations can now be used to investigate the existence and stability of interstellar libration points.

5.4.3 Gravity perturbed two-centre libration points

Consider libration points between the three stars. The coordinate system is selected so that the three stars are co-planar with the x - y plane, thus libration points must also lie in this plane. The non-dimensionalised potential energy $U(x,y,z)$ is equivalent to

$$U(x, y, z) = -\frac{(1-\beta_1)}{|\mathbf{r}_1|} - \frac{\lambda_1(1-\beta_2)}{|\mathbf{r}_2|} - \frac{\lambda_2(1-\beta_3)}{|\mathbf{r}_3|} \quad (5.36)$$

Figure 5-24 shows the potential energy contours for the case $\beta_1=\beta_2=\beta_3=0$, excluding the solar radiation pressure terms. As expected, Sirius produces the largest potential-well followed by Centauri and then the Sun. A potential energy saddle point, E_1 , exists between the Sun and Centauri, which corresponds to the two-centre on-axis libration point. Another saddle point, E_2 , exists between Sirius and the combined system of the Sun and Centauri.

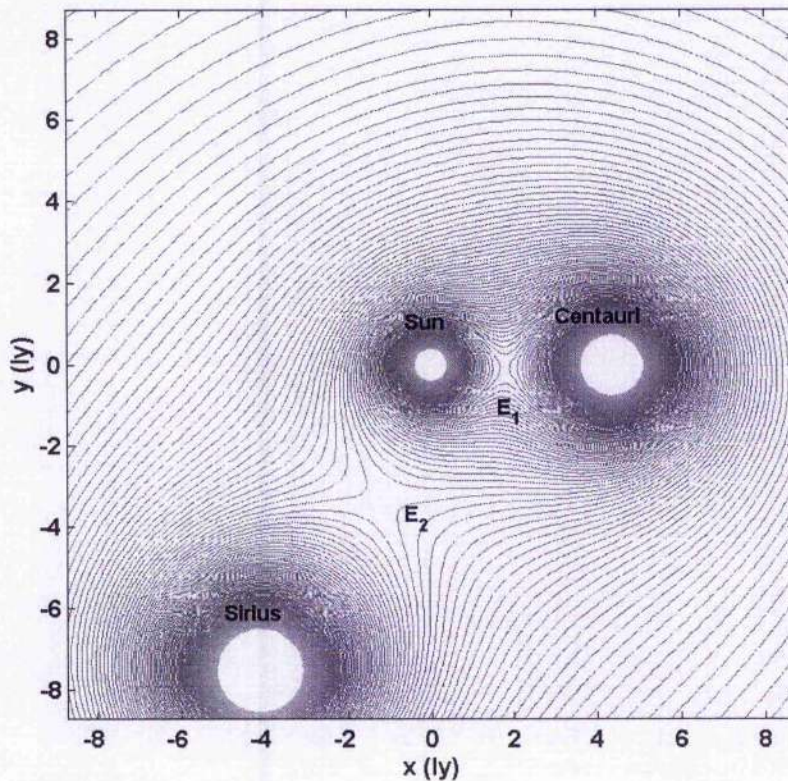


Figure 5-24 Potential energy contours of Sun-Centauri-Sirius system ignoring solar radiation pressure

The potential energy contours will be investigated for a number of particle loading cases:

$\beta_2 < \beta_1 < \beta_3 < 1$: Figure 5-25 shows the potential energy contours for a particle with loading parameter $\sigma = 7 \text{ gm}^{-2}$. Particles of this mass/area ratio would have lightness numbers $\beta_1 = 0.1096$, $\beta_2 = 0.0941$ and $\beta_3 = 0.7140$. The dominant force acting on these particles would be gravity from all three stars. There are two libration points which lie in this plane, one between α -Centauri and the Sun and one between both these stars and Sirius. Both of these points are unstable as determined from the saddle point in the potential energy function.

$\beta_2 < \beta_1 < 1 < \beta_3$: Figure 5-26 shows the case when particle loading $\sigma = 3 \text{ gm}^{-2}$. The corresponding lightness number values are $\beta_1 = 0.2558$, $\beta_2 = 0.2195$ and $\beta_3 = 1.6659$. In this case the dominant force exerted by Sirius is stellar radiation pressure; the other stars both have dominant gravitational forces. Particles corresponding to these lightness numbers are pushed away from Sirius and those which don't exceed the escape velocity of the Sun or α -Centauri, can become trapped within the potential-well of these stars.

$\beta_2 < \beta_1 < 1 \sim \beta_3$: Figure 5-27 shows the case for particles with loading parameter $\sigma = 5 \text{ gm}^{-2}$.

The lightness values would be $\beta_1 = 0.1535$, $\beta_2 = 0.1317$, and $\beta_3 = 0.9996$. As the lightness number due to Sirius, β_3 is approximately unity, the stellar radiation pressure cancels the gravitational force. There remains a saddle point in the potential function between the Sun and α -Centauri, but the potential well due to Sirius has vanished as it no longer influences the particle motion.

Interestingly, this indicates that the possible transfer of materials between star systems is dependant on the material mass and reflective surface area. If a particle has lightness number $\beta_i > 1$, it will be ejected by the star system and cannot be recaptured by M_j as radiation pressure is the dominant force. The particle can only be captured by a star where corresponding lightness number $\beta_i < 1$. This leads to a selection process of the possible material properties which may become trapped in the vicinity of a star.

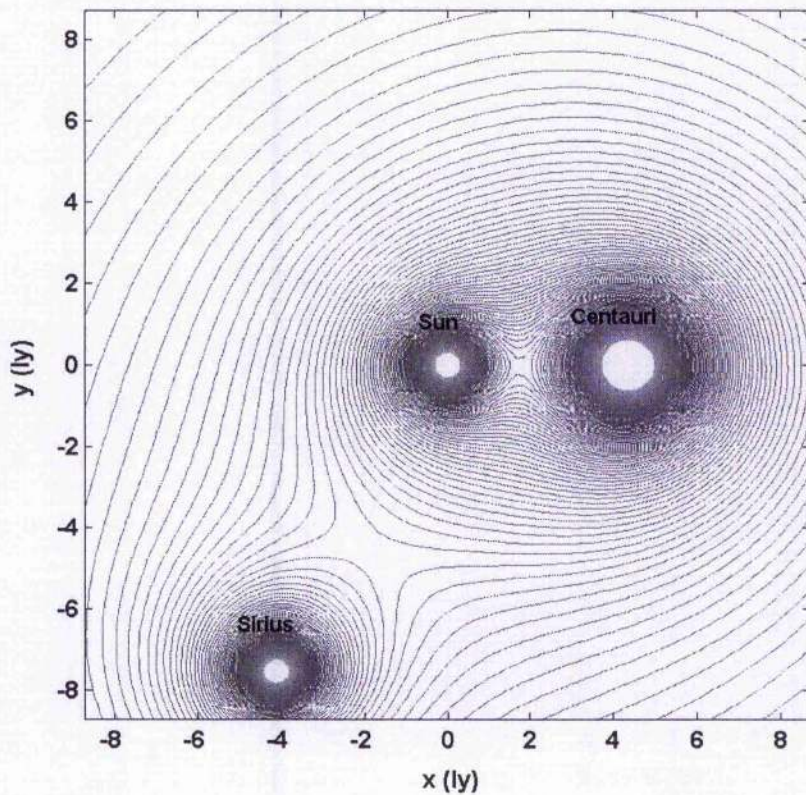


Figure 5-25 Potential energy contours for particle loading $\sigma = 7 \text{ gm}^{-2}$

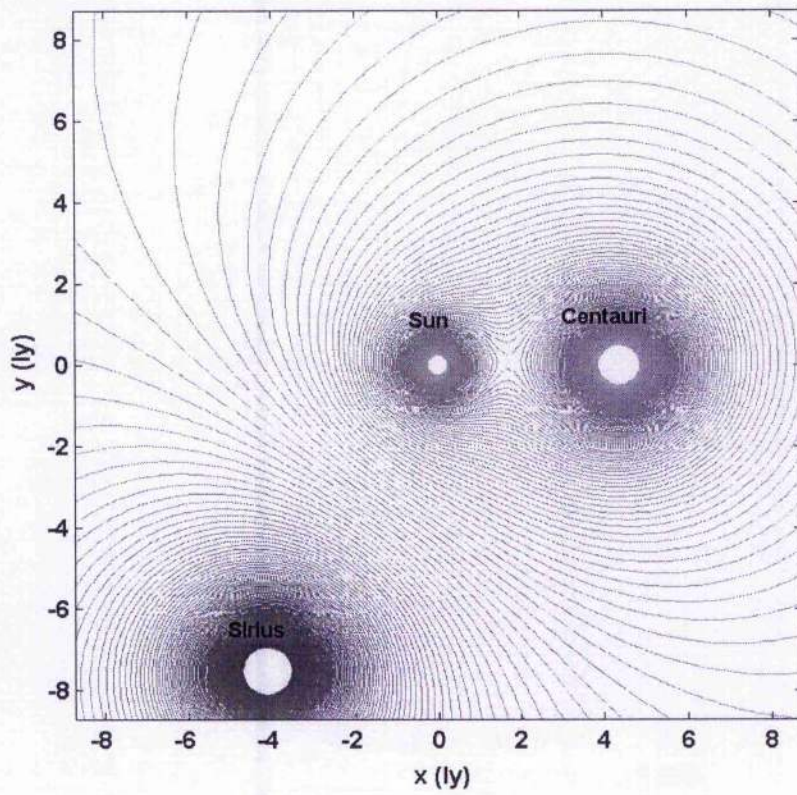


Figure 5-26 Potential energy contours for particle loading $\sigma=3 \text{ gm}^{-2}$

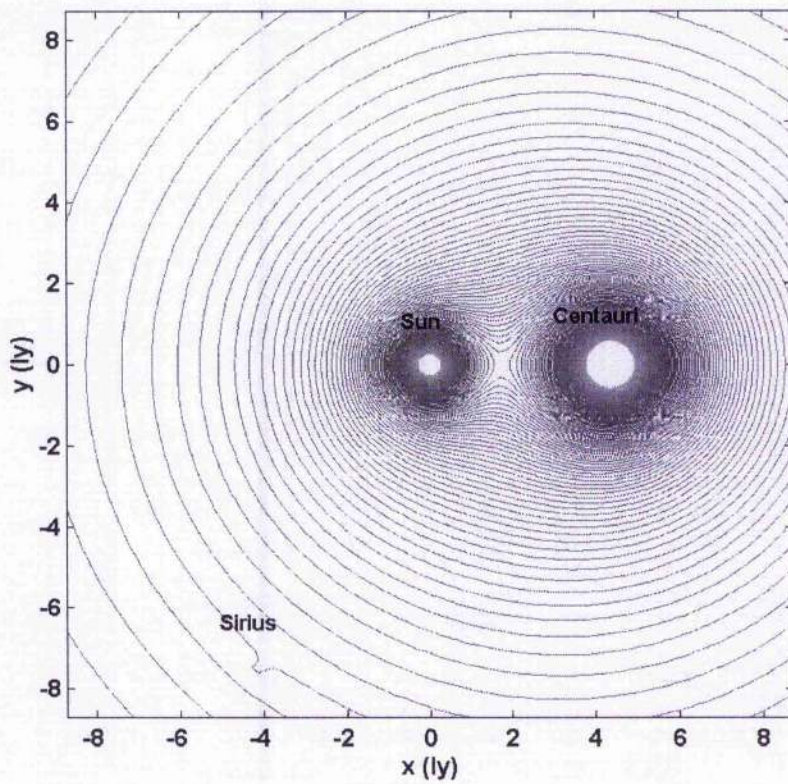


Figure 5-27 Potential energy contours for particle loading $\sigma=5 \text{ gm}^{-2}$

5.5 Two-centre problem with relative stellar motion

5.5.1 Relative stellar motion

The relative motion of the stars was first noticed by Edmund Halley during 1718 while comparing the positions of Sirius, Arcturus and Aldebaran with the measurements performed by the Greek astronomer, Hipparchus. It was noticed that the star positions were greater than half a degree from the positions measured 1850 years earlier.

Angular variation of the position of the stars is known as the proper motion and can be calculated by measuring parallax changes over a long period of time. Stellar motion along the line of site can be calculated using Doppler shift techniques, although effects such as gravitational red-shift, stellar atmospheric convection and stellar rotation can lead to inaccuracies of order 1 kms^{-1} [Lindgren and Dravins, 2003].

Barnard's star is found to move at high velocity relative to the Sun. First estimated by Edward Barnard [1916], Barnard's star has proper-motion of 10.31 arcsec/yr . Table 5-10 contains the radial and proper motion, taken from the Gliese Catalogue [1991], of some nearby stars. The velocity components (v_x , v_y) are provided which are co-planar to the Sun and the respective star.

Star	Dist (ly)	Radial vel (kms^{-1})	Proper Motion (arcsec/yr)	v_x (kms^{-1})	v_y (kms^{-1})
α -Centauri A	4.36	-26.2	3.689	-26.2	23.39
α -Centauri B	4.36	-18.1	3.689	-18.1	23.39
Proxima	4.22	-16.0	3.809	-16.0	23.38
Sirius	8.58	-9.4	1.328	-9.4	16.57
Barnards Star	5.96	-111.0	10.31	-111.0	89.37

Table 5-10 Proper and radial motion of stars relative to the Sun

It is clear that the stars move at high velocities relative to the Sun. Barnard's star has a velocity magnitude of 142.51 kms^{-1} relative to the Sun. The two-centre problem approximates that the stars are fixed in position relative to each other, which from these velocities it is evident that they are not. However, due to the immense distances between the stars, the model may still be valid if the period of trapping is relatively short. Despite the high relative stellar velocities, it is clear that the stellar positions vary only a few arc seconds per year. The stellar motion can be included in the two-centre equations of motion to examine the validity of the two-centre approximation.

5.5.2 Derivation of two-centre equations including relative stellar motion

Consider the relative motion of the Centauri system in the x - y plane, approximating that the velocity of all three stars is identical and the velocity remains constant throughout integration time. The radial motion is directed along the x -axis, $v_x = -26.2 \text{ kms}^{-1}$ and the proper motion is directed along the y -axis, $v_y = 23.39 \text{ kms}^{-1}$, using the velocity components of α -Centauri A from the Gliese Catalogue. Due to the changing position of Centauri, the separation distances from point m to the Sun and Centauri respectively are $|\mathbf{r}_1| = \sqrt{x^2 + y^2 + z^2}$ and $|\mathbf{r}_2(t)| = \sqrt{(1 + v_x t - x)^2 + (v_y t - y)^2 + z^2}$ which is dependant on time t .

The potential energy is now time dependant due to the changing position of the Centauri system

$$V(t) = -\frac{GM_1 m}{|\mathbf{r}_1|} (1 - \beta_1) + \frac{GM_2 m}{|\mathbf{r}_2(t)|} (1 - \beta_2) \quad (5.37)$$

and the kinetic energy $T = (P_x^2 + P_y^2 + P_z^2) / 2m$ where P_x , P_y and P_z are the components of momentum. The Hamiltonian function $H = T + V$ can be expressed as

$$H = \frac{1}{2m} (P_x^2 + P_y^2 + P_z^2) - Gm \left[\frac{M_1 (1 - \beta_1)}{|\mathbf{r}_1|} + \frac{M_2 (1 - \beta_2)}{|\mathbf{r}_2(t)|} \right] \quad (5.38)$$

The equations of motion can be obtained using partial derivatives $\partial H/\partial P_q = \dot{q}$ and $\partial H/\partial q = -\dot{P}_q$ where $q=(x,y,z)$. The non-dimensionalised equations have the form

$$\ddot{x} = -\frac{x(1-\beta_1)}{|\mathbf{r}_1|^3} + \frac{\lambda(1-\beta_2)(1+v_x t - x)}{|\mathbf{r}_2(t)|^3} \quad (5.39.1)$$

$$\ddot{y} = -\frac{y(1-\beta_1)}{|\mathbf{r}_1|^3} + \frac{\lambda(1-\beta_2)(v_y t - y)}{|\mathbf{r}_2(t)|^3} \quad (5.39.2)$$

$$\ddot{z} = -\frac{z(1-\beta_1)}{|\mathbf{r}_1|^3} - \frac{\lambda(1-\beta_2)z}{|\mathbf{r}_2(t)|^3} \quad (5.39.3)$$

where the characteristic length $R=4.36$ ly and the characteristic time $\tau = \sqrt{R^3/GM_1}$. The mass ratio $\lambda=2.17$ for the Sun-Centauri system. These equations will now be used to examine the motion and stability of the on-axis libration points.

5.5.3 Motion of on-axis libration point

The non-dimensionalised potential energy can be expressed in the form

$$V(x, y, z, t) = -\frac{(1-\beta_1)}{|\mathbf{r}_1|} - \frac{\lambda_1(1-\beta_2)}{|\mathbf{r}_2(t)|} \quad (5.40)$$

Figure 5-28 shows the potential energy contours evaluated at time $t=0$. The potential energy contours after a period of 100,000 years are provided in Fig 5-29, showing a translation of the Centauri system and subsequently, the on-axis libration point. The libration point remains unstable, indicated by the saddle point.

The translation of the Centauri system relative to the Sun is demonstrated in Fig 5-30 over a period of 1×10^5 years. The on-axis libration point between the stars, moves with horizontal velocity -10.44 kms^{-1} and vertical velocity 9.32 kms^{-1} . Due to the high velocity and instability of the on-axis libration point dust particles would not be temporarily trapped. An investigation into the possibility of particles becoming trapped on a stable halo orbit will be considered.

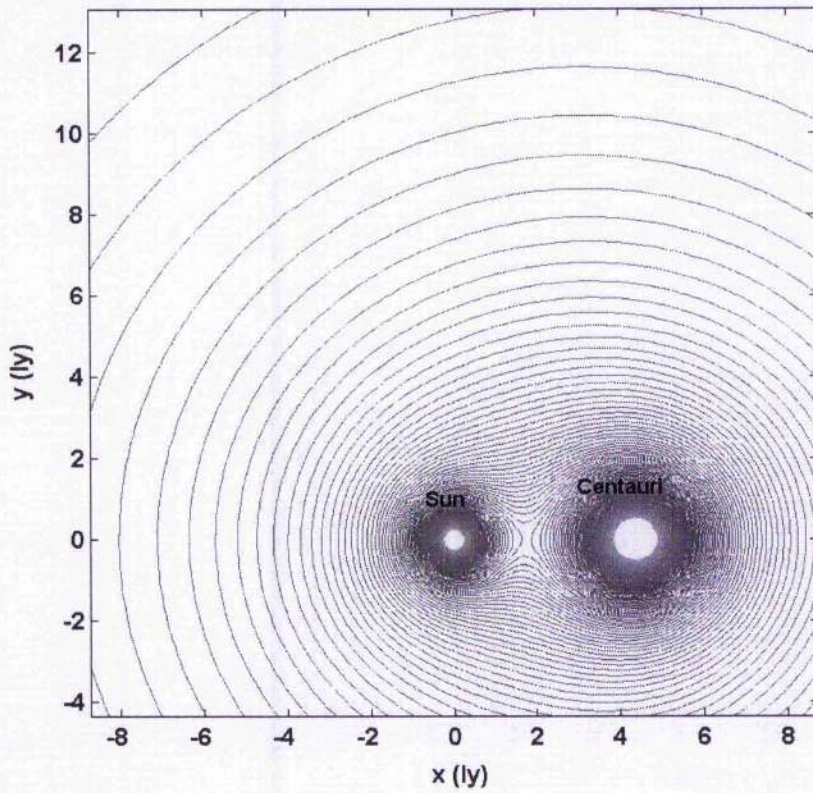


Figure 5-28 Potential energy contours of the Sun-Centauri system when time $t=0$

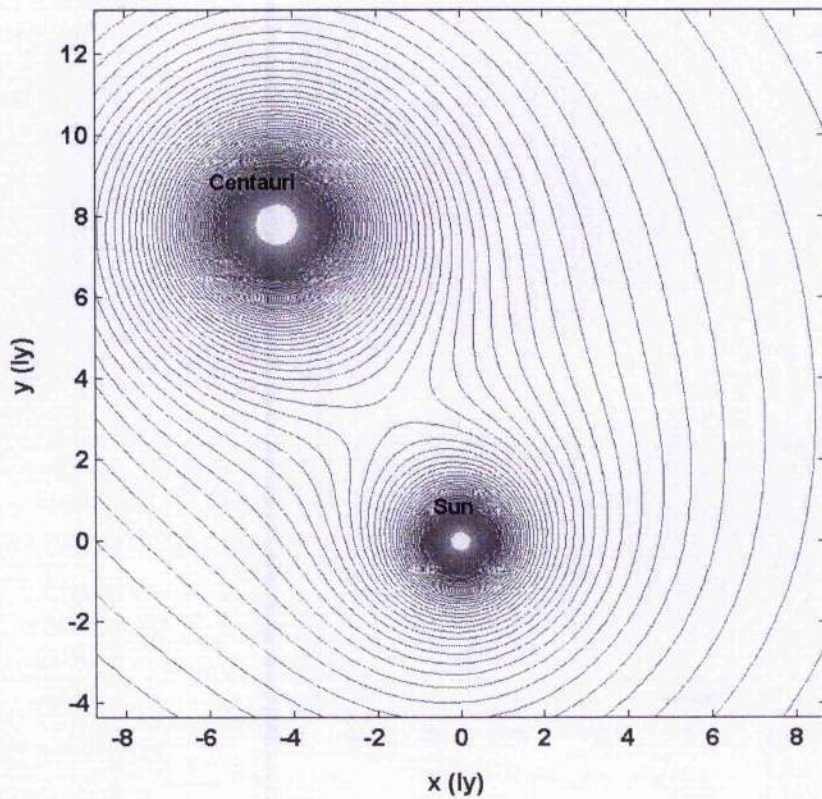


Figure 5-29 Potential energy contours of the Sun-Centauri system when time $t=1 \times 10^5$ years

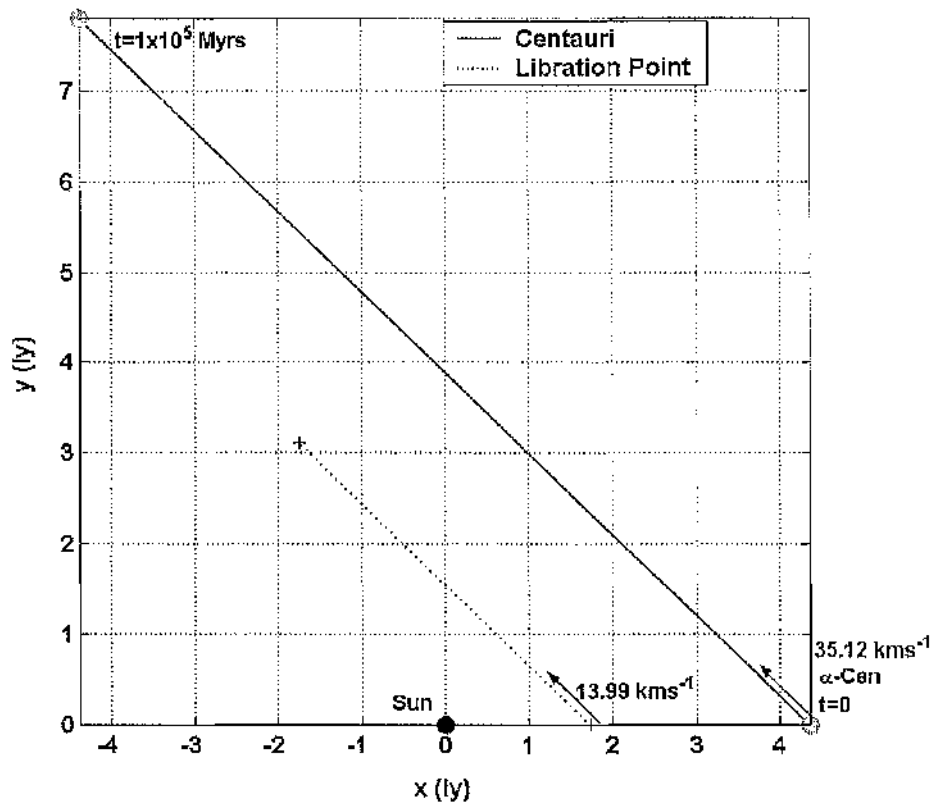


Figure 5-30 Motion of the Centauri system relative to the Sun

5.5.4 Halo orbits including the effects of stellar motion

When the motion of the Centauri system is considered, halo orbits around the libration points are not possible. Figure 5-31 shows a homoclinic trajectory when the motion of Centauri is not included. The nominal orbit is an unstable limit cycle with radius 0.34 ly located 0.3 ly from the Sun with a period of 36.81 Myrs. The lightness numbers correspond to a particle loading of $\sigma=3 \text{ gm}^{-2}$. When the motion of Centauri is included, the resulting orbit is provided in Fig 5-32. It is clear that the initial conditions produce an elliptical heliocentric orbit.

Halo orbits which are stable while the motion of the Centauri system is ignored are shown in Fig 5-33. In the case of a halo orbit near the Centauri system, particles with these initial conditions escape from the Sun when stellar motion is included, as shown in Fig 5-34. The stable halo-orbit near the Sun results in a heliocentric elliptical orbit when stellar motion is included, as demonstrated in Fig 5-35.

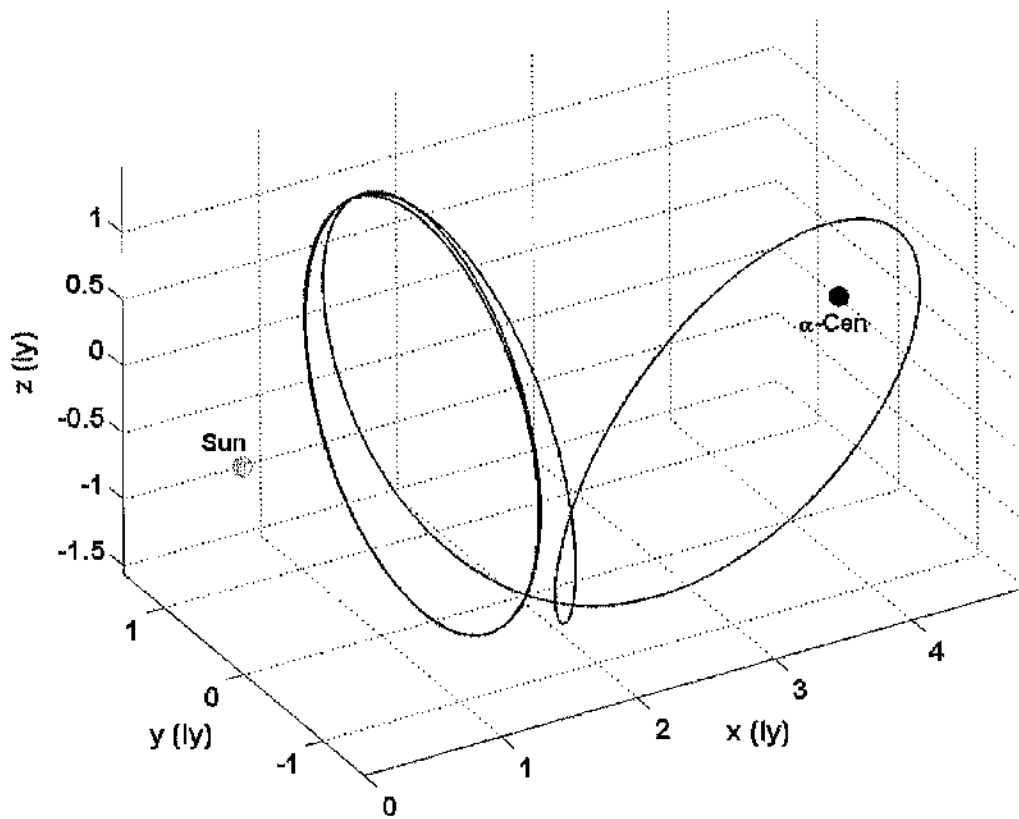


Figure 5-31 Unstable halo orbit excluding stellar motion

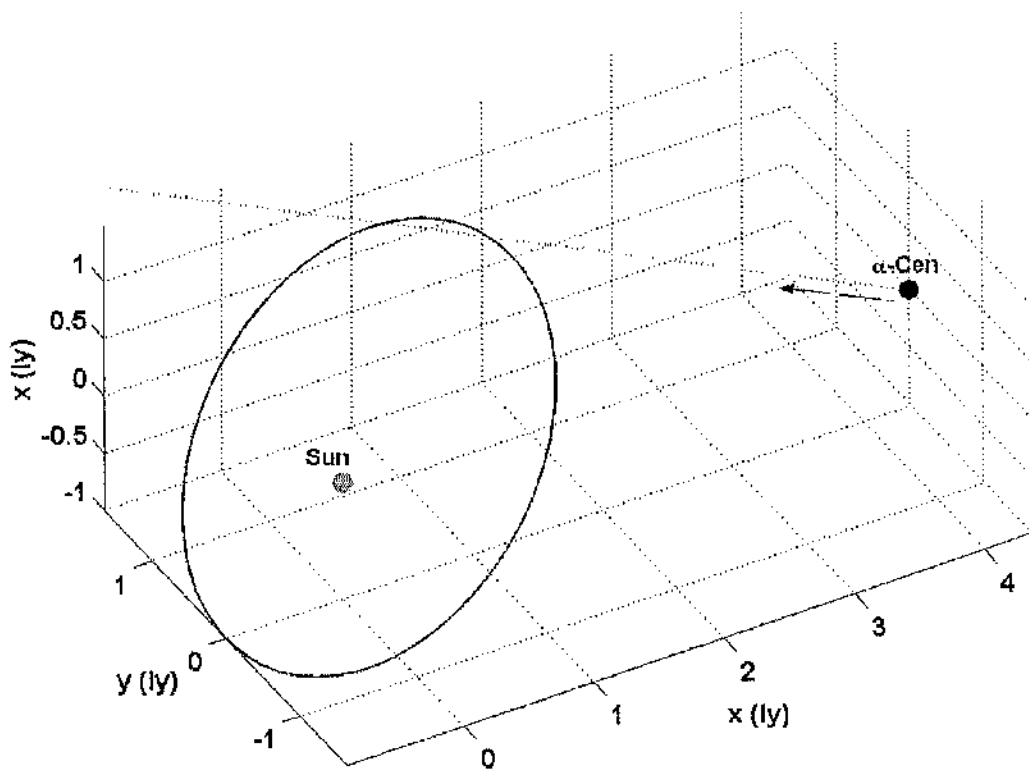


Figure 5-32 Unstable halo orbit including stellar motion

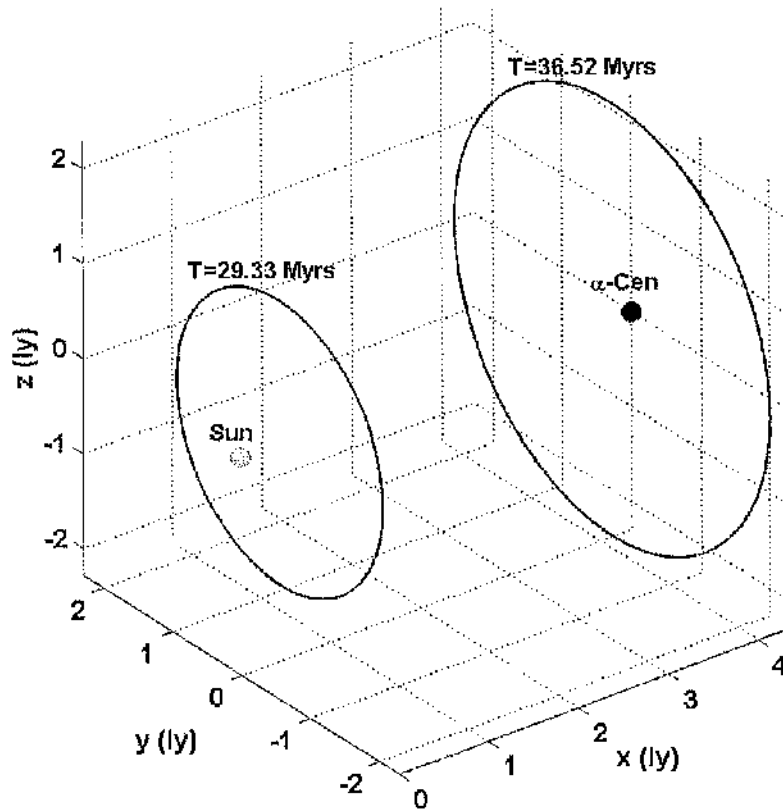


Figure 5-33 Stable halo orbits excluding stellar motion

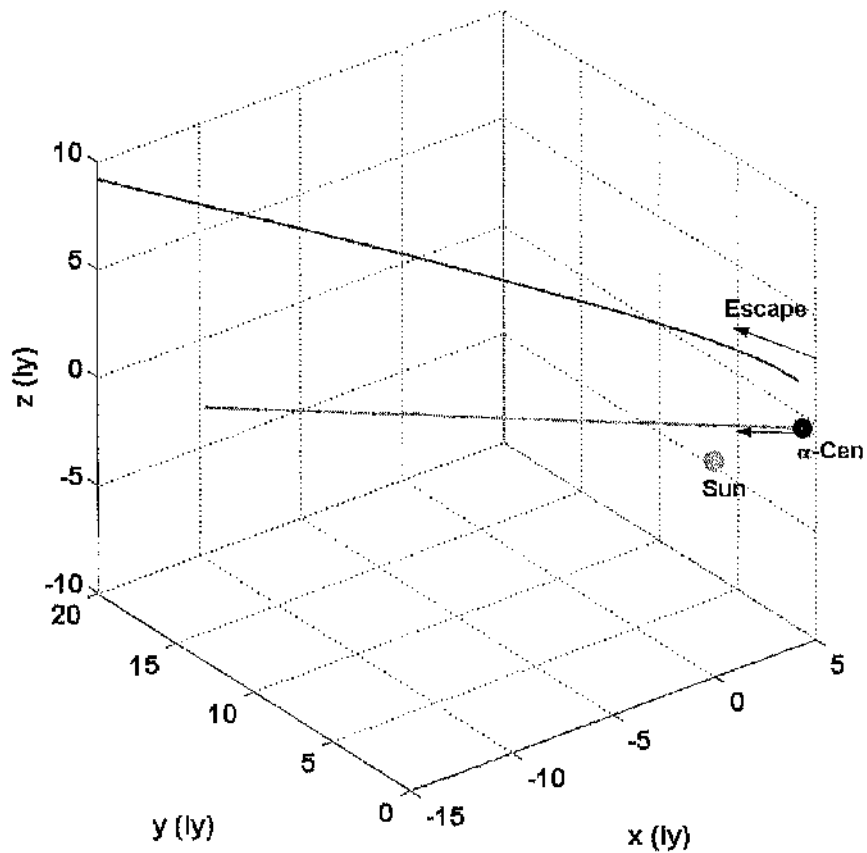


Figure 5-34 Stable halo orbit including stellar motion

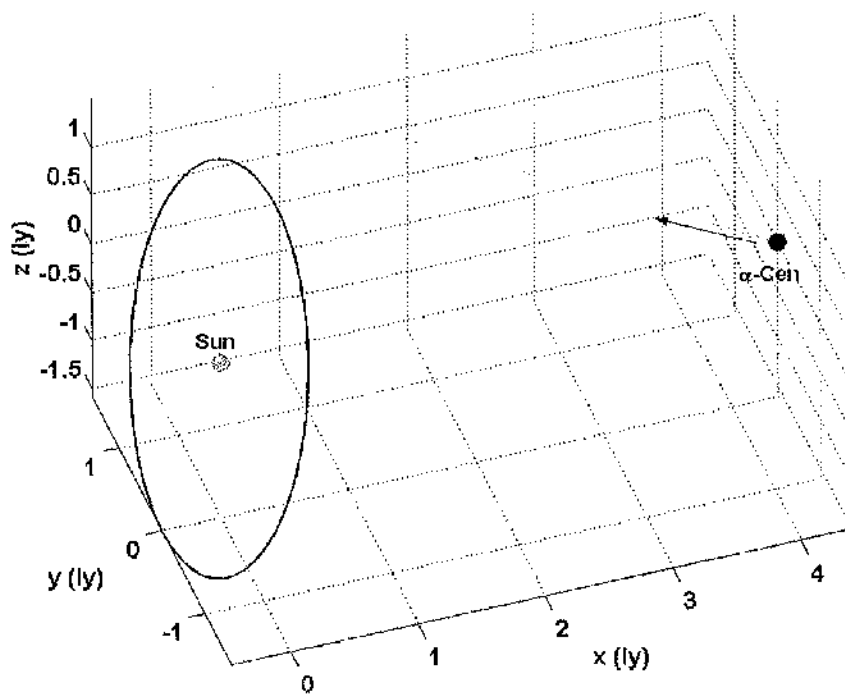


Figure 5-35 Stable halo orbit including stellar motion

The velocity of the Centauri system relative to the Sun is too large for particle trapping to be observed around the libration points. Searching through the Gliese catalogue for relative stellar velocities, it was found that all stars move with velocities of order several kms^{-1} relative to the Sun. For particle trapping to occur at the libration points between stars, the relative motion of the stars must be of order 1 ms^{-1} .

Figure 5-36 demonstrates a stable orbit near a star M_1 , which is located at the origin. Star M_2 is moving relative to M_1 with a velocity of 1.01 ms^{-1} . The effective mass ratio of this system corresponds to $\lambda=2.2759$. Figure 5-37 shows this trajectory viewed in the z - y plane. The orbit precesses as star M_2 moves such that the halo orbit is always centred on the star-line. The orbit has a period of 33 Myrs and the motion is computed for 1000 Myrs.

In this case, it would be envisioned that dust particles moving with a velocity of order 10 ms^{-1} relative to M_1 could become trapped temporarily in periodic halo orbits which precess as the stars move relative to each other. Heavier particles would become trapped in orbits with larger radius than lighter particles due to the effects of radiation pressure. Also, due to differing reflective properties, there would be a grouping of interstellar dust particles with similar material properties. Transfer of materials between passing stars, via the stable and unstable manifolds which wind onto the unstable halo orbit could also occur, as shown in Fig 5-38.

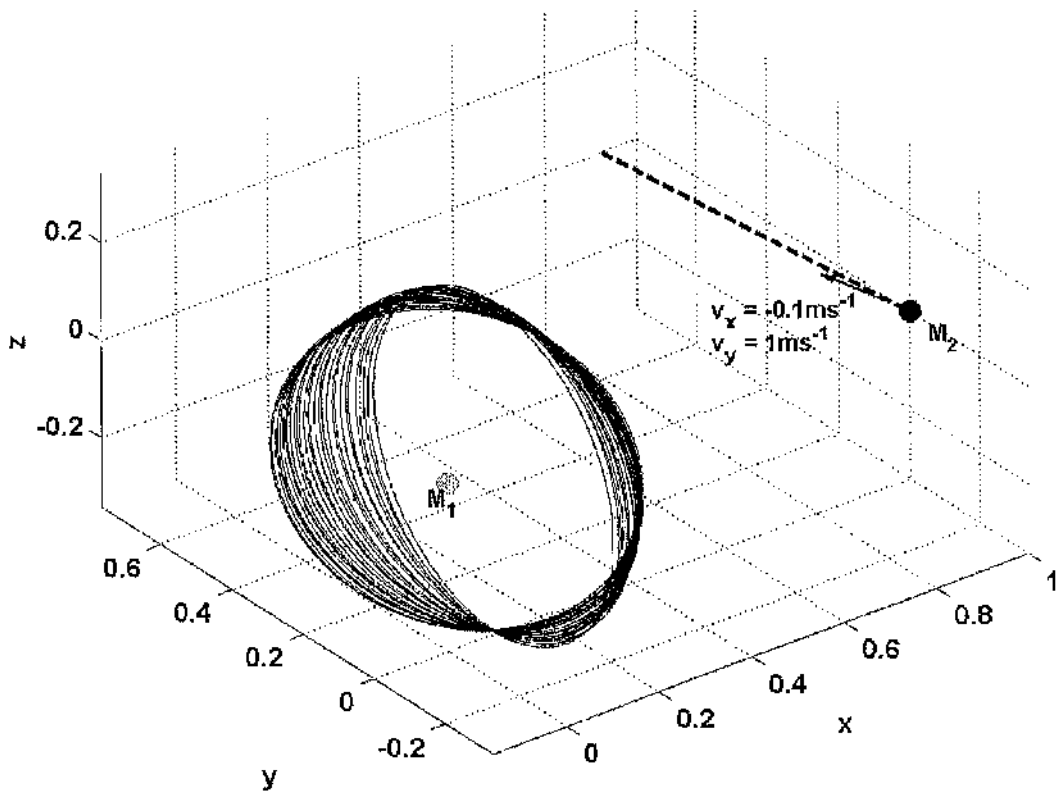


Figure 5-36 Bound orbit for case where relative star velocity is of order 1 ms^{-1}

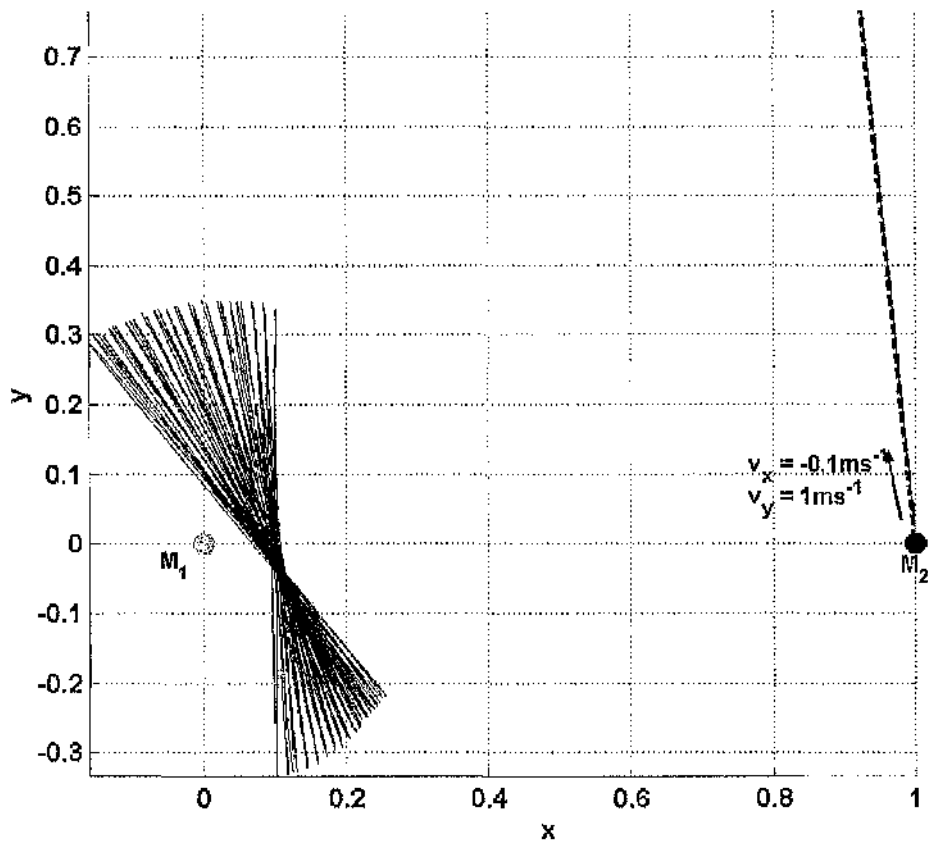


Figure 5-37 View of x - y plane for case where relative star velocity is of order 1 ms^{-1}

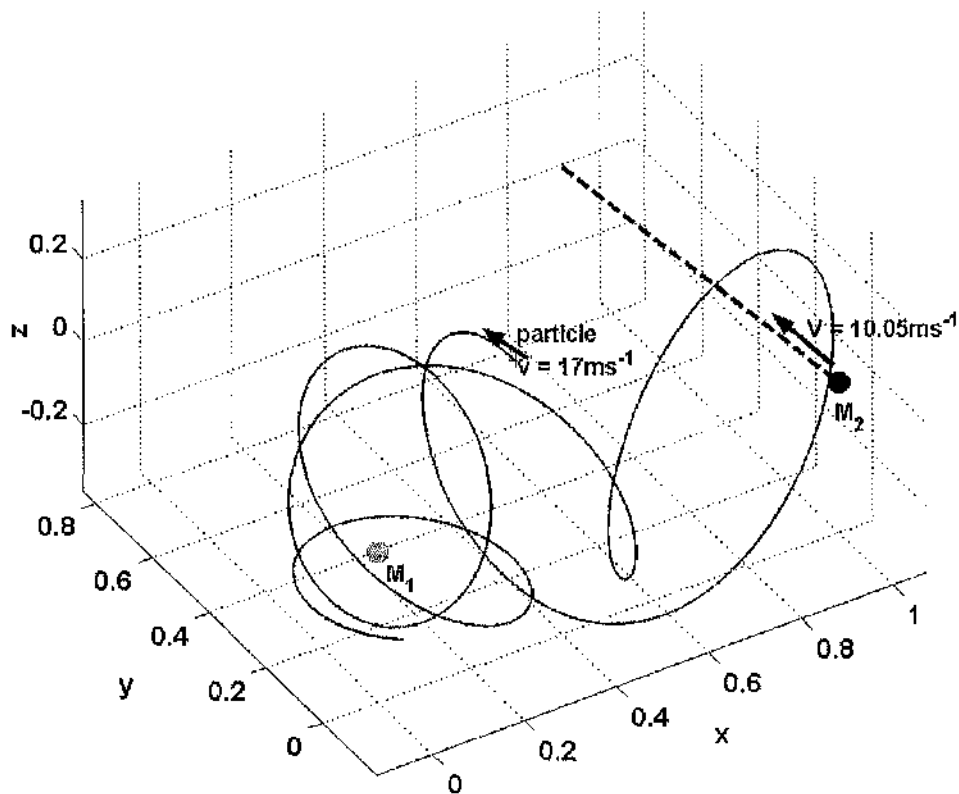


Figure 5-38 Transfer of particle between stars for relative stellar velocity of order 10 ms^{-1}

The precession of a stable orbit is still observed for stellar velocities of order 100 ms^{-1} . In the case of relative stellar velocities greater than 100 ms^{-1} , the star position changes rapidly with respect to the orbit period of order several million years. Initial conditions which produce a stable halo orbit near M_1 in the two-centre problem will result in a Keplerian orbit around M_1 when relative stellar motion is included. This can be explained by considering the relative velocity of the particle compared to M_1 and M_2 . Due to the inverse square dependency on distance, at interstellar distances the acceleration due to gravity acting on a particle is extremely small. For a relative stellar velocity of order 1 kms^{-1} , star M_2 does not remain in the vicinity of the particle long enough to noticeably perturb the particle velocity. In this case, the two-centre approximation is not accurate and results in trajectories similar to the two-body problem with M_1 as the central body. For slower relative stellar velocities, the particle motion is noticeably influenced by both stars and the two-centre problem represents a valid approximation of the dynamics.

5.6 Conclusions

The two-centre problem was investigated as a possible model to represent the gravitational dynamics of two nearby stars. An on-axis libration point was identified between the masses and potential energy analysis demonstrated that the point is unstable. Two stable and one unstable limit cycle were also shown to exist between the stars. The stable limit cycles represent possible halo orbits which could trap interstellar dust particles temporarily as they pass between the stars. The unstable limit cycle leads to a set of 'homoclinic-like' manifolds which represent a set of possible transfer trajectories between the two star systems. By converting the problem into confocal elliptical coordinates, it was shown that the manifolds are bound to an ellipsoidal energy surface.

The problem was thoroughly investigated in the case of the Sun and its nearest star system, α -Centauri. The photo-gravitational problem was studied including the accelerations due to stellar radiation pressure exerted on the interstellar dust particles by each star. It was demonstrated that including the influence of light pressure leads to families of halo orbits dependant on particle areal density. In the case of particles where lightness number parameters are greater than unity with respect to both stars, there exists no possible halo orbits between the stars.

To validate this model, the gravitational perturbation introduced by the presence of a third star and the effects of relative stellar motion were included. It was shown that particle trapping is unlikely in the Sun-Centauri system due to the large relative stellar motion. However, the model could be applied in the case of star systems with relative stellar velocities in the order 100 ms^{-1} .

6.1 Geomagnetic tail mission

6.1.1 Mission outline

The reconnection point within the geomagnetic tail is located less than $30 R_E$ (Earth Radii) from the Earth [Dungey, 1961; Russel, 1974]. Positioning a science payload within the tail to observe the electric and magnetic field variation would enable an accurate model of the dynamics to be constructed.

Several missions have gathered data on tail dynamics using satellites in highly elliptical orbits such as ISEEa and ISEEb [Richardson, 1980c]. As the orbit plane is co-planar with the Earth's centre, the payload is continually passing through the inner geomagnetic tail. Obtaining good temporal resolution of the changing dynamics within the geomagnetic tail is difficult as the charge density varies continuously throughout the tail. Also, the precession of the orbit around the Earth means the orbit only passes through the tail for a few months per year. A non-Keplerian orbit would be an improvement as the payload can be positioned at a constant displacement distance from the Earth. The data collected would represent the changing electrodynamics of the magnetic tail over a period of time.

Solar sail technology may be used to position a 100 kg science payload in a highly non-Keplerian orbit displaced $30 R_E$ from the Earth with radius $20 R_E$. Orbit insertion from a 200 km altitude, parking orbit will be performed using a kick-stage to perform a Hohmann transfer manoeuvre. The inclination of the orbit is chosen such that the resulting elliptical orbit intersects the insertion manifold. A second kick-stage supplies the required Δv to deliver the payload onto the stable manifold, which winds onto the desired non-Keplerian orbit. The solar sail is deployed immediately after the insertion kick-stage. Upon arrival at the nominal orbit, the solar sail controller is activated to prevent escape. Both sail area variation and sail angle variation control methods will be demonstrated [Bookless and McInnes, 2006].

6.1.2 Hohmann transfer manoeuvre

A Hohmann transfer ellipse can be used to insert the solar sail onto the correct manifold from a 200 km altitude circular parking orbit. The tangential velocity of the circular orbit is determined as $v = \sqrt{\mu/r_p}$ where r_p represents the radius of the circular orbit and μ is the Earth's gravitational parameter. The tangential velocity of the ellipse is defined as $v = \sqrt{\mu(2/r_a - 1/a)}$, where a is the semi-major axis and r_a represents the apogee of the transfer ellipse. As the equations of motion are non-dimensionalised, the gravitational parameter $\mu=1$ [Wie, 1998].

The change in velocity required to insert a transfer vehicle onto an elliptical orbit from an initial circular orbit is calculated using

$$\Delta v = \sqrt{\frac{2}{r_a} - \frac{1}{a}} - \sqrt{\frac{1}{r_p}} \quad (6.1)$$

The inclination of the circular orbit and the burn time is determined using three rotational transforms. The 1st rotation is performed about the z-axis for the angle $\theta_1 = \tan^{-1}(y_o/x_o)$, where the manifold insertion conditions are $(x_o, \dot{x}_o, y_o, \dot{y}_o, z_o, \dot{z}_o)$. The z-rotation transform, T_1 , can be expressed as

$$T_1 = \begin{bmatrix} \cos \theta_1 & \sin \theta_1 & 0 \\ -\sin \theta_1 & \cos \theta_1 & 0 \\ 0 & 0 & 1 \end{bmatrix} \quad (6.2)$$

Column vectors $P = [x_o \ y_o \ z_o]^T$ and $V = [\dot{x}_o \ \dot{y}_o \ \dot{z}_o]^T$, which represent the position and velocity coordinates, can be transformed using T_1 to obtain $P' = T_1 P$ and $V' = T_1 V$. The transformed coordinates can be used to determine the angle $\theta_2 = \tan^{-1}(z_o'/x_o')$. The second transform is performed about the y-axis using

$$T_2 = \begin{bmatrix} \cos \theta_2 & 0 & \sin \theta_2 \\ 0 & 1 & 0 \\ -\sin \theta_2 & 0 & \cos \theta_2 \end{bmatrix} \quad (6.3)$$

where the transformed column vectors are $P''=T_2P'$ and $V''=T_2V'$. These transformations are required to position the insertion point on the new x -axis. A rotation can now be performed about the x -axis to align the y - z plane velocity vector with the Hohmann transfer maneuver. The velocity vector angle is determined as $\theta_3 = \tan^{-1}(\dot{z}_o''/\dot{y}_o'')$.

These three angles can be used to select a Hohmann ellipse which intersects the manifold insertion point with matching velocity direction for the 2nd kick-stage to be applied. Initially, the circular and elliptical orbits are co-planar with the x - y plane. The initial position and velocity conditions which produce the circular orbit are represented as $P_c = [x_c \ y_c \ z_c]^T$ and $V_c = [\dot{x}_c \ \dot{y}_c \ \dot{z}_c]^T$. The initial conditions which produce the elliptical orbit are represented as $P_e = [x_e \ y_e \ z_e]^T$ and $V_e = [\dot{x}_e \ \dot{y}_e \ \dot{z}_e]^T$.

The velocity conditions are transformed using the reverse angle rotations about the x -axis, y -axis and z -axis as follows

$$T_4 = \begin{bmatrix} \cos(-\theta_1) & \sin(-\theta_1) & 0 \\ -\sin(-\theta_1) & \cos(-\theta_1) & 0 \\ 0 & 0 & 1 \end{bmatrix} \begin{bmatrix} \cos(-\theta_2) & 0 & \sin(-\theta_2) \\ 0 & 1 & 0 \\ -\sin(-\theta_2) & 0 & \cos(-\theta_2) \end{bmatrix} \begin{bmatrix} 1 & 0 & 0 \\ 0 & \cos(-\theta_3) & \sin(-\theta_3) \\ 0 & -\sin(-\theta_3) & \cos(-\theta_3) \end{bmatrix} \quad (6.4)$$

which can be expressed as

$$T_4 = \begin{bmatrix} \cos \theta_2 \cos \theta_1 & -\cos \theta_1 \sin \theta_2 \sin \theta_3 - \cos \theta_3 \sin \theta_1 & -\cos \theta_3 \cos \theta_1 \sin \theta_2 + \sin \theta_3 \sin \theta_1 \\ \cos \theta_2 \sin \theta_1 & \cos \theta_3 \cos \theta_1 - \sin \theta_2 \sin \theta_3 \sin \theta_1 & -\cos \theta_2 \sin \theta_3 - \cos \theta_3 \sin \theta_2 \sin \theta_1 \\ \sin \theta_2 & \cos \theta_2 \sin \theta_3 & \cos \theta_2 \cos \theta_3 \end{bmatrix} \quad (6.5)$$

The velocity coordinates are transformed using $V_c' = T_4V_c$ and $V_e' = T_4V_e$. The initial position coordinates are also transformed by applying a reverse rotation about the y -axis and z -axis using the transform

$$T_5 = \begin{bmatrix} \cos \theta_2 \cos \theta_1 & -\sin \theta_1 & -\cos \theta_1 \sin \theta_2 \\ \cos \theta_2 \sin \theta_1 & \cos \theta_1 & -\sin \theta_2 \sin \theta_1 \\ \sin \theta_2 & 0 & \cos \theta_2 \end{bmatrix} \quad (6.6)$$

The position coordinates for the circular orbit and the ellipse are transformed using $P_c' = T_5 P_c$ and $P_e' = T_5 P_e$. The transformed position and velocity coordinates produce a circular and elliptical orbit with the required orientation to intersect the manifold insertion point.

The period of the transfer ellipse is obtained using $T = 2\pi\sqrt{a^3}$. The second kick-stage is initiated at the apoapsis of the transfer ellipse. The time elapsed between the two burns is therefore $T/2 = \pi\sqrt{a^3}$. Evaluating the velocity magnitude at the transfer ellipse apoapsis enables the insertion Δv to be determined.

6.1.3 Trajectory analysis

For a nominal orbit with displacement distance $x_o=30 R_E$ and radius $\rho_o=20 R_E$ the nominal sail acceleration is $\kappa_o=6.26 \text{ mms}^{-2}$. A periodic looping trajectory was identified with acceleration reduction $\Delta=0.04$, such that $\kappa=6.01 \text{ mms}^{-2}$. The closest approach distance to the Earth is $3.39 R_E$ where the initial conditions are provided in Table 6-1.

Figure 6-1 shows the Hohmann ellipse necessary to insert the solar sail onto the correct manifold from a 200 km altitude parking orbit. The 1st kick stage requires $\Delta v=1.857 \text{ kms}^{-1}$ and the 2nd kick stage requires $\Delta v=2.680 \text{ kms}^{-1}$. The time elapsed between the two burns is 2 hours 18 minutes.

Figure 6-2 shows the non-Keplerian orbit produced by the initial conditions provided in Table 6-1. A sail area variation controller is activated upon arrival at the nominal orbit. The control period is over 100 days and the nominal orbit has a period of 12.7 days. The acceleration and corresponding area variation required to control this orbit is provided in Fig 6-3.

The solar sail acceleration varies between 6.636 mms^{-2} and 5.438 mms^{-2} . For a total sail mass and payload of 500 kg, this corresponds to an area variation between $3.6336 \times 10^5 \text{ m}^2$ and $2.9776 \times 10^5 \text{ m}^2$. For the sail to transport a 100 kg payload, the total sail mass is 400 kg requiring a sail loading of 1.1 gm^{-2} .

Figure 6-4 shows a non-Keplerian orbit controlled using sail pitch and yaw angle variation. The sail orientation over 100 days is provided in Figure 6-5. The controller is activated when the solar sail x -displacement distance $x > 0.99x_0$. The solar sail acceleration is also increased to $\kappa = 1.05\kappa_0$, which is equivalent to 6.57 mms^{-2} . This is to prevent the solar sail escaping Earthwards, as increasing the pitch or yaw angle reduces the component of acceleration directed along the x -axis.

The pitch angle varies between 7.2° and -15.4° , and the yaw angle varies between 7.9° and -11.8° . Figure 6-6 represents the yaw against pitch angle variation which represents the attitude of the sail surface normal vector. For a total sail mass and payload of 500 kg, the required sail area is $3.5994 \times 10^5 \text{ m}^2$ which corresponds to a sail loading of 1.111 gm^{-2} .

Figure 6-7 shows the required sail area and Fig 6-8 sail loading parameter for a total mass ranging between 200 kg and 5000 kg. For 3 cases of payload mass – 100 kg, 50 kg and 20 kg, the varying sail loading parameter is demonstrated to exponentially increase towards 1.389 gm^{-2} . It is clear that achieving smaller loading parameters will increase the possible payload mass.

$x_0 (\text{R}_E)$	$\dot{x}_0 (\text{kms}^{-1})$	$y_0 (\text{R}_E)$	$\dot{y}_0 (\text{kms}^{-1})$	$z_0 (\text{R}_E)$	$\dot{z}_0 (\text{kms}^{-1})$
-2.2652	2.5952×10^{-3}	2.1185	3.3506	1.3728	-4.4995

Table 6-1 Insertion conditions for Geomagnetic tail mission

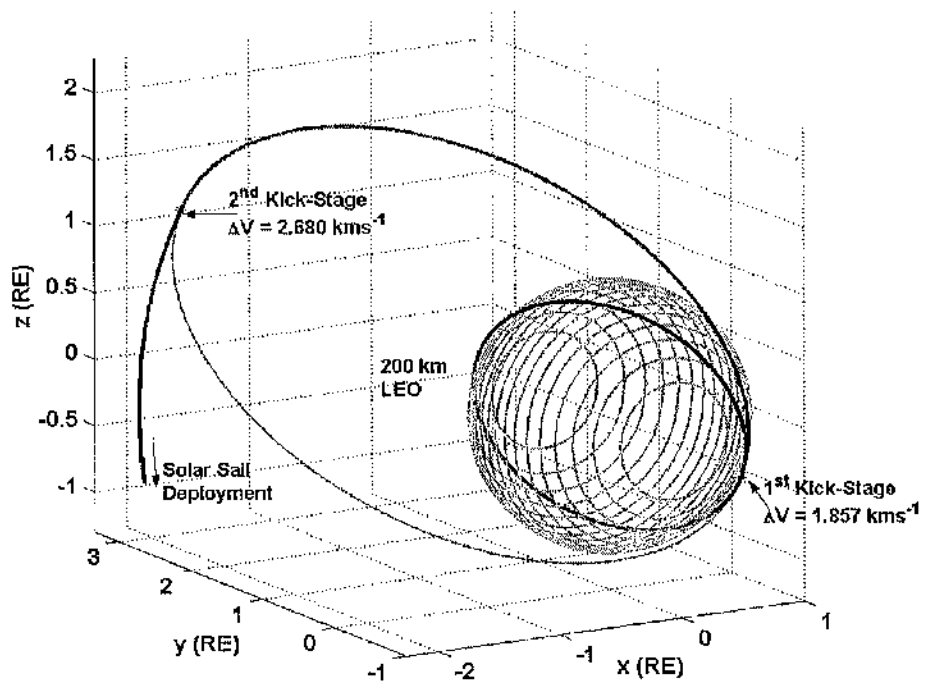


Figure 6-1 Insertion to non-Keplerian orbit with two kick stages

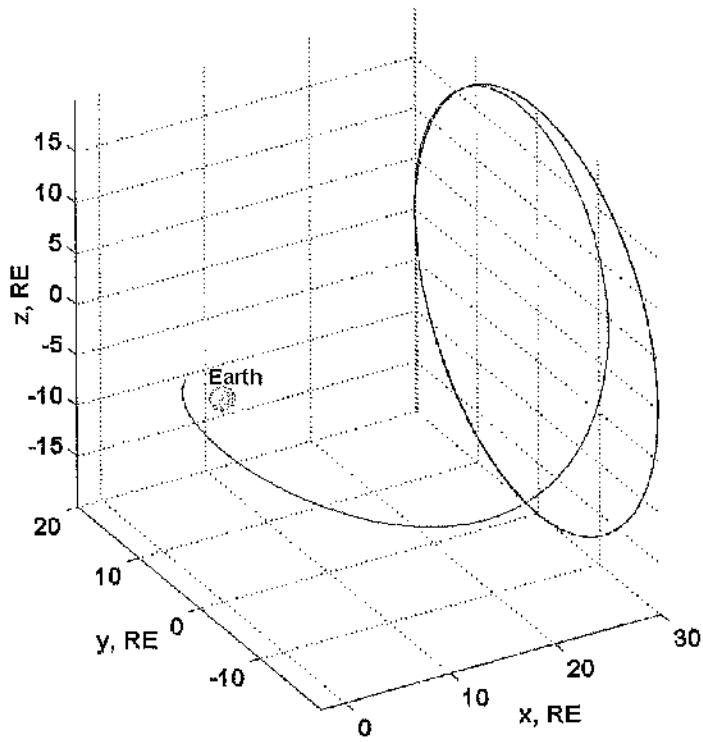


Figure 6-2 Sail area variation controlling a non-Keplerian orbit within the Geomagnetic tail

$$\rho_0 = 20 R_E, x_0 = 30 R_E \text{ (Earth Radii)}$$

$$\kappa = 6.01 \text{ mms}^{-2}, Q = 1500(I_{4x4}), N = 1 \times 10^{10}$$

$$G = [-1.1562 \times 10^{-4} \quad 5.1455 \times 10^{-4} \quad 0.044469 \quad 0.032082]$$

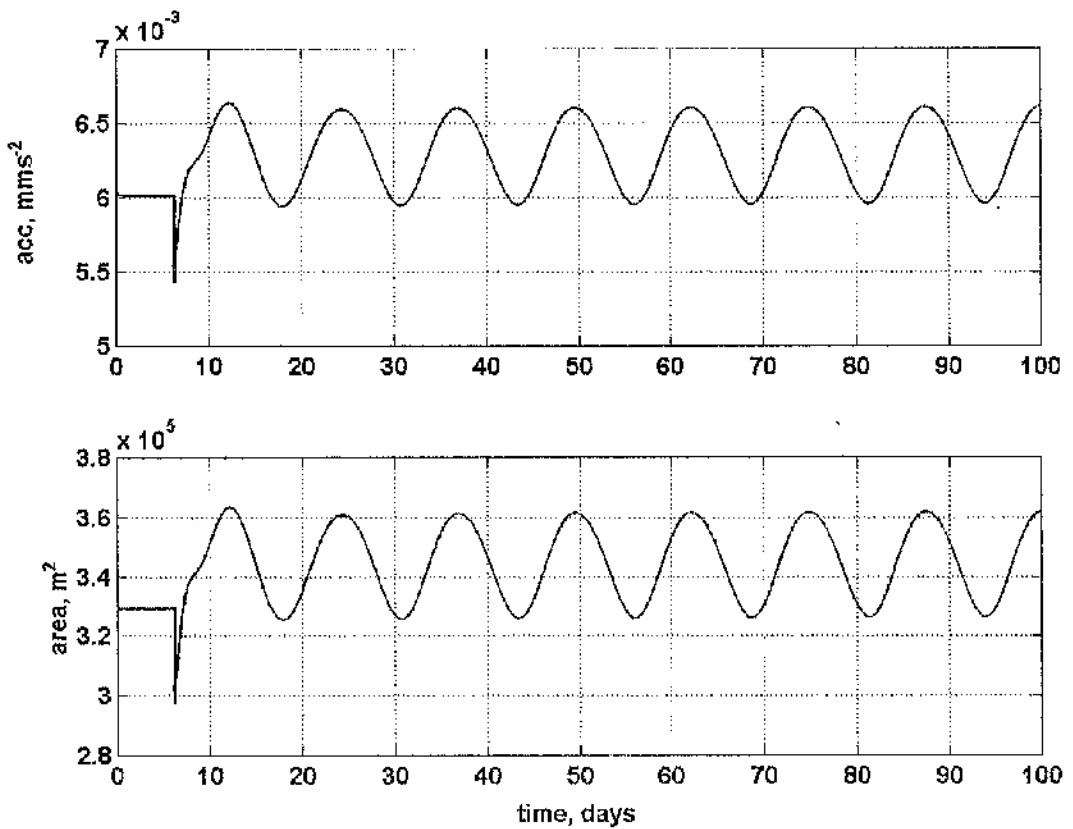


Figure 6-3 Required sail area and acceleration variation to prevent escape from a non-Keplerian orbit

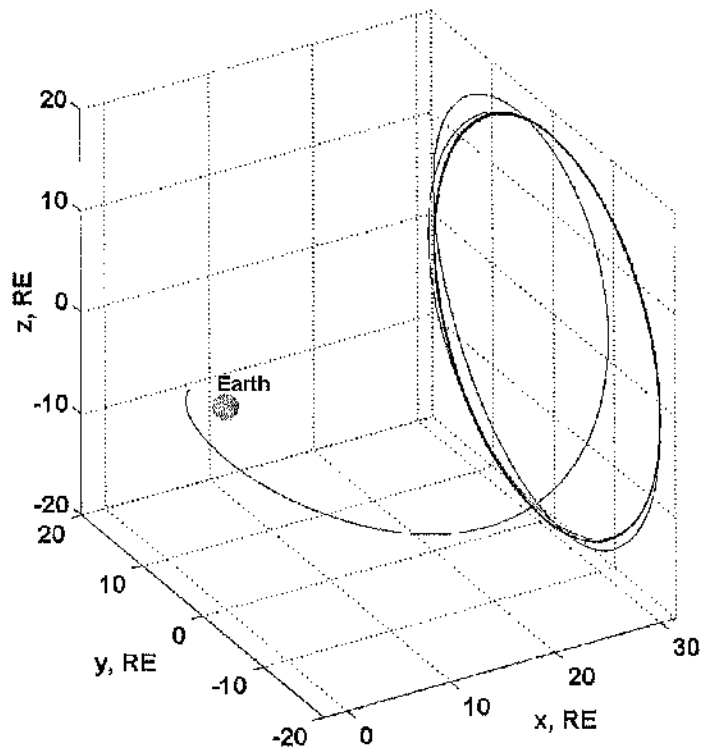


Figure 6-4 Sail pitch and yaw angle variation controlling a non-Keplerian orbit within the Geomagnetic tail

$$\rho_0 = 20 R_E, \lambda_0 = 30 R_E \text{ (Earth Radii)}$$

$$Q = 100(I_{4 \times 4}) \quad N = 1 \times 10^4, \quad \kappa = 6.57 \text{ mms}^{-2}$$

$$G = [0.2533 \quad 0.4914 \quad 27.4537 \quad 90.5139]$$

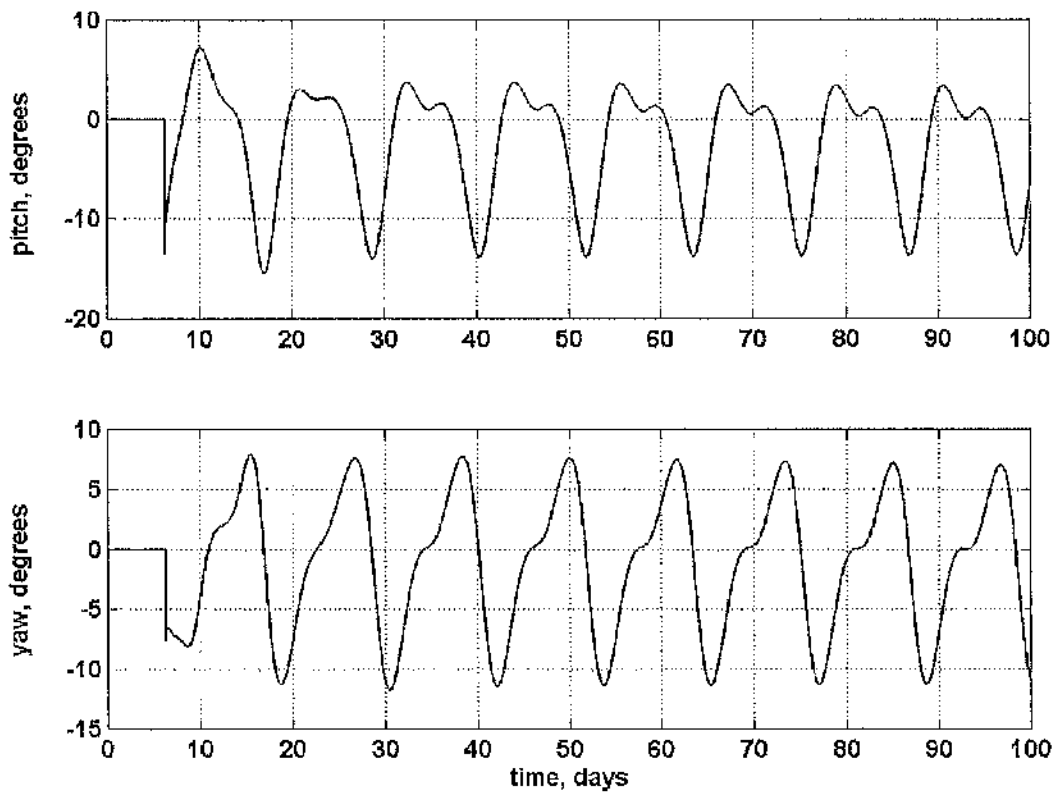


Figure 6-5 Required sail pitch and yaw angle variation to prevent escape from a non-Keplerian orbit

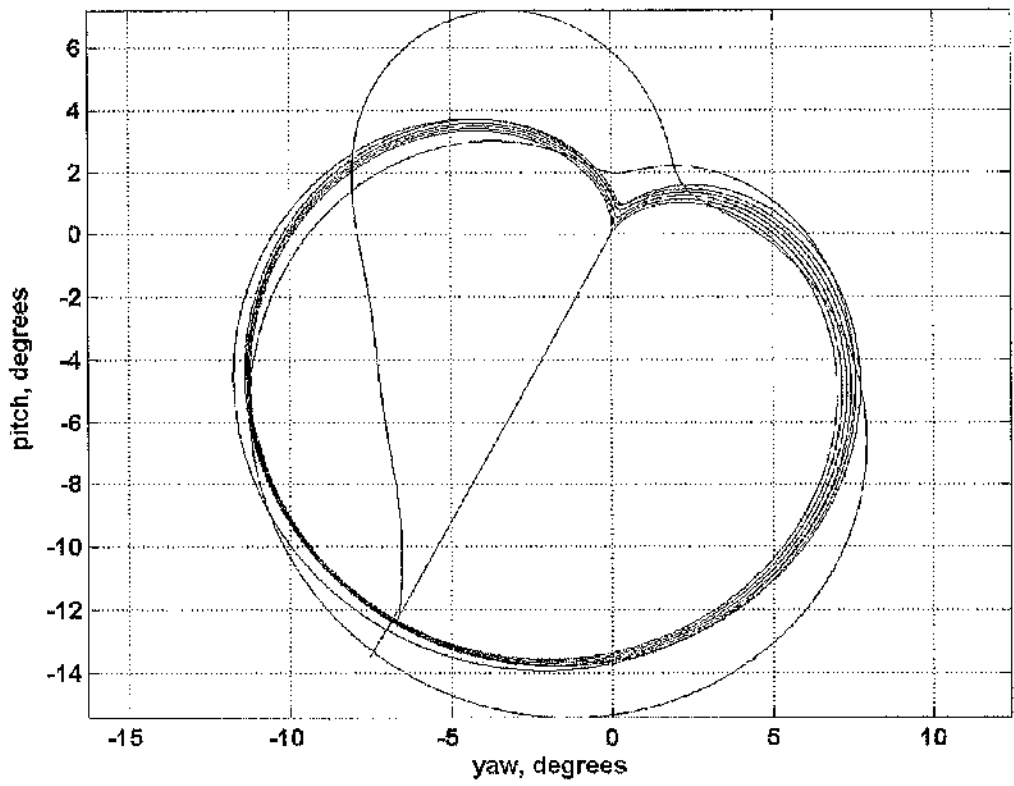


Figure 6-6 Pitch and yaw variation required to control orbit

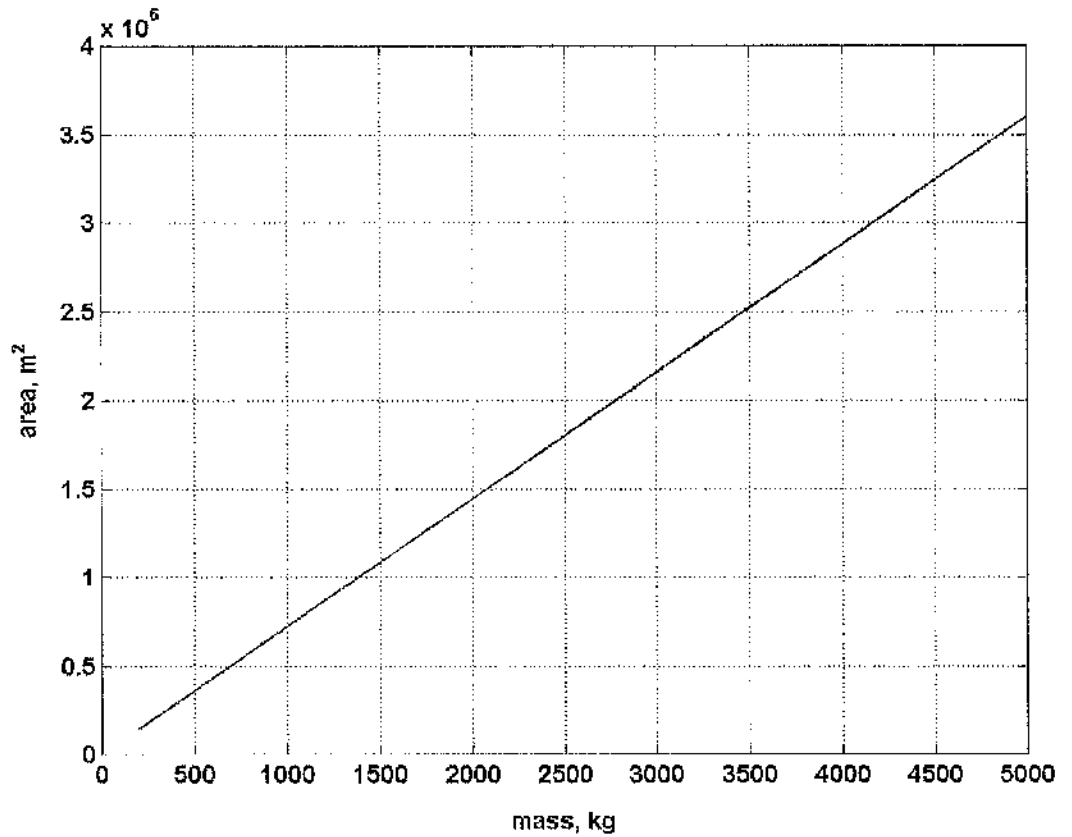


Figure 6-7 Required solar sail surface area for increasing total mass

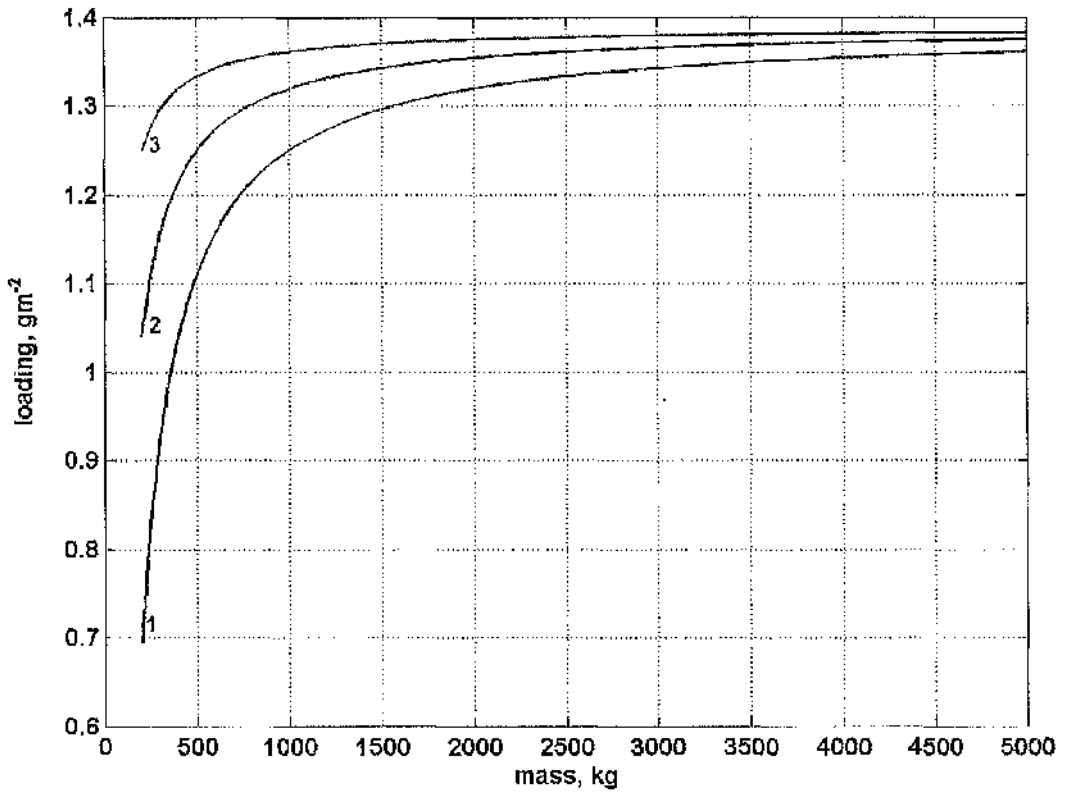


Figure 6-8 Required solar sail loading parameter for increasing total mass
Payload mass contours (1 – 100 kg, 2 – 50 kg, 3 – 20 kg)

6.1.4 Conclusions

This mission would require an extremely high performance solar sail. A sail loading parameter of $\sigma=1.1\text{gm}^{-2}$ results in a solar sail lightness number $\beta=1.4$. Improved substrate technology could achieve lower sail loading parameters [Murphy et al, 2004]. Novel fabrication techniques such as sublimation of the substrate from the reflective aluminium layer [Enea and Telespazio, 1999; Genta and Brusa, 1999], or micro-pore perforation of the sail surface could be employed to increase the performance of large area solar sails [Forward, 1985].

6.2 Geostorm mission

6.2.1 Mission outline

Positioning a science payload sunward of the L_1 point would enable continuous monitoring of the solar wind charge density upstream of the magnetosphere. Currently, the spacecraft SOHO (Solar and Heliospheric Observatory) and ACE (Advanced Composition Explorer) follow a halo orbit trajectory around L_1 . These spacecraft can detect interplanetary shock fronts prior to encounter with the Earth's magnetosphere [Huttunen et al, 2002].

Delivering a solar sail to an initial Lissajous trajectory around L_1 can be achieved by identifying a stable manifold which passes near to the Earth. Initial conditions are provided using the linear solution of Hill's approximation of the three-body problem. Small variations to the x -axis velocity are applied to converge the resulting trajectory toward an improved Lissajous orbit. The closest approach distance to the Earth is calculated and the mirror image theorem is then applied to find conditions starting from near to the Earth which wind onto a Lissajous trajectory. The necessary kick-stages to intercept the insertion manifold with the correct velocity are investigated starting from a 200 km altitude parking orbit.

After insertion to the Lissajous trajectory at L_1 , the solar sail is slowly deployed using a linear controller to select optimal gains. These gains are used to track the nominal Lissajous trajectory while the x -displacement distance is steadily increased sunward. Once the desired displacement distance is reached, the sail deployment stops and area control techniques are employed to prevent the solar sail escaping the final orbit [Bookless and McInnes, 2005].

6.2.2 Trajectory analysis

The corrected initial conditions, which lead to the desired Lissajous orbit around L_1 with amplitude $A_y=50 R_E$, are provided in Table 6-2. The manifold insertion conditions are located $11.15 R_E$ from the Earth and the transfer vehicle initially travels in the anti-Sun direction eventually arriving at an orbit around L_1 after 186.5 days. Figure 6-9 shows the insertion trajectory contained within a zero-velocity surface with Jacobi constant $C = -0.01226$.

The insertion from a 200 km parking orbit is achieved using a Hohmann transfer, shown in Fig 6-10. The parking orbit is inclined 4.86° relative to the equator. The 1st kick-stage requires $\Delta v=2.749 \text{ kms}^{-1}$ to insert the transfer vehicle onto an elliptical path which intercepts the manifold insertion coordinates. The 2nd kick-stage requires $\Delta v=2.259 \text{ kms}^{-1}$ with the burn directed at a 12° angle sunward of the direction of motion.

The solar sail is deployed after 373 days, having spent 186.5 days following the Lissajous trajectory around L_1 . During deployment, the optimal gains are recalculated every 5 days for a new libration point, $1 R_E$ further sunward than the previous. The desired orbit conditions are also displaced $1 R_E$ further thus increasing the nominal acceleration gradually. As the solar sail acceleration can only be directed in the anti-Sun direction, the condition $\kappa(t) \geq 0$ must be met. After 1 year of gradually shifting the nominal libration point, the position is $73 R_E$ sunward of L_1 .

As the solar sail spirals sunwards from the Lissajous orbit, the area variation controller generates a larger control signal to drive the solar sail towards the desired orbit. Eventually, the control signal is large enough that the trajectory arrives at a Lissajous orbit around an artificial libration point on the Sun-line. This libration point is sunward of the nominal orbit, as the sail acceleration is the result of the difference between the nominal orbit and the actual orbit. The solar sail arrives at an orbit around an artificial libration point displaced $390 R_E$ sunward of the Earth, 2.56 years after launch and 561 days after initial deployment.

Figure 6-11 shows the complete ballistic insertion from near the Earth to the Lissajous trajectory around L_1 followed by sail deployment and the gradual spiral to a Lissajous orbit

around an artificial libration point. A section of the final orbit is provided in Fig 6-12, which represents the trajectory between 2.56 years and 5.1 years.

A 3.5° angular radius exclusion zone is required to prevent excessive interference from the solar radio disc with the telemetry system [Farquhar et al, 1977]. This corresponds to an exclusion radius of about 90,000 km centered on the y - z plane at L_1 . At the area controlled orbit around the artificial libration point, the required exclusion zone has a radius of 150,000 km. It is clear from Fig 6-12, that the solar sail does not cross the radio exclusion zone during the control period.

The acceleration and area variation required to produce the final trajectory is shown in Fig 6-13. The maximum acceleration is 0.27 mms^{-2} and the corresponding area for a total sail and payload mass of 100 kg is 2864 m^2 . For a generous solar sail loading of $\sigma=12 \text{ gm}^{-2}$, the total sail mass is 34.4 kg. The remaining possible payload mass is 65.6 kg.

$x_o (\text{R}_E)$	$\dot{x}_o (\text{kms}^{-1})$	$y_o (\text{R}_E)$	$\dot{y}_o (\text{kms}^{-1})$	$z_o (\text{R}_E)$	$\dot{z}_o (\text{kms}^{-1})$
-10.8281	-0.7225	1.7271	-2.7658	-2.0226	1.5108

Table 6-2 Insertion conditions to uncontrolled Lissajous orbit around L_1

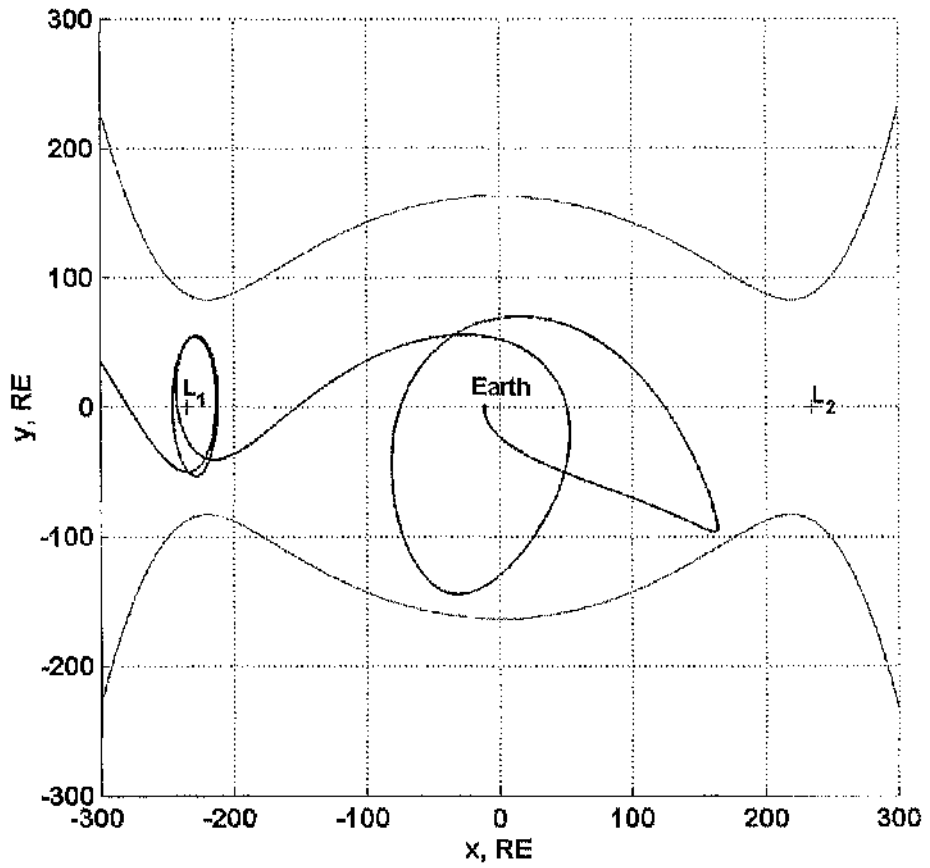


Figure 6-9 Uncontrolled insertion to a Lissajous orbit from near the Earth with Jacobi Constant $C=-0.01226$

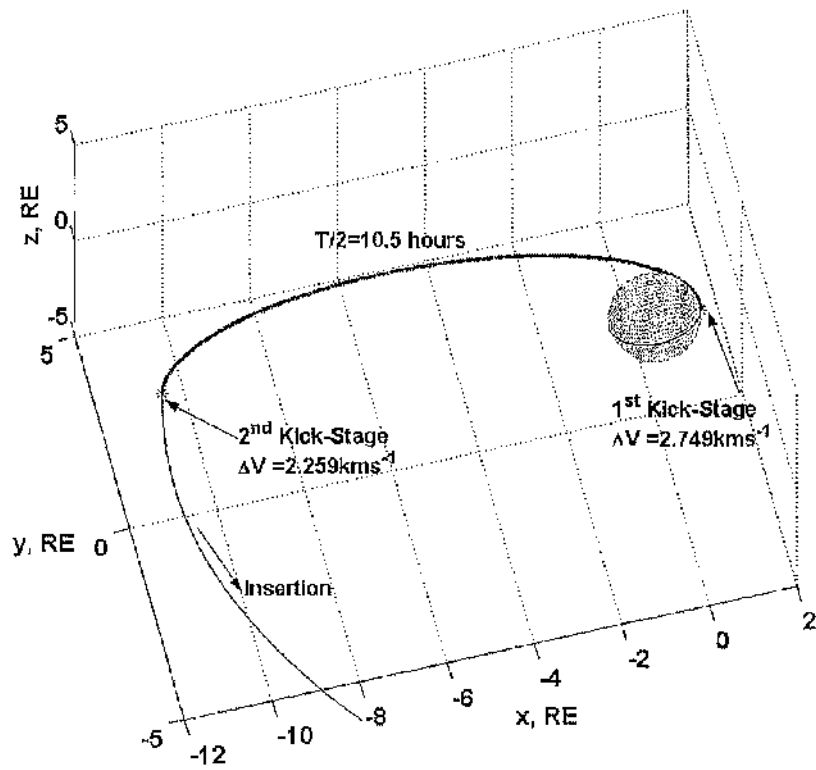


Figure 6-10 Insertion from LEO to stable manifold using Hohmann ellipse

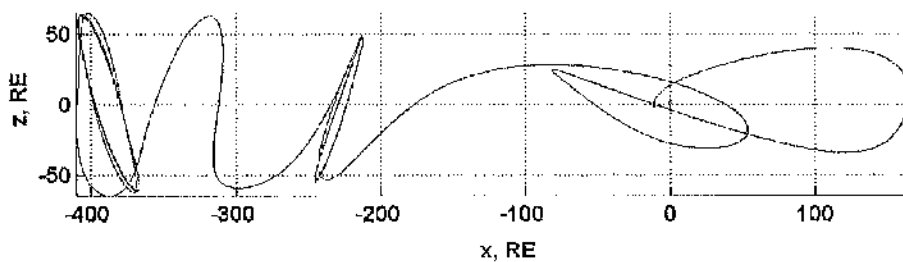
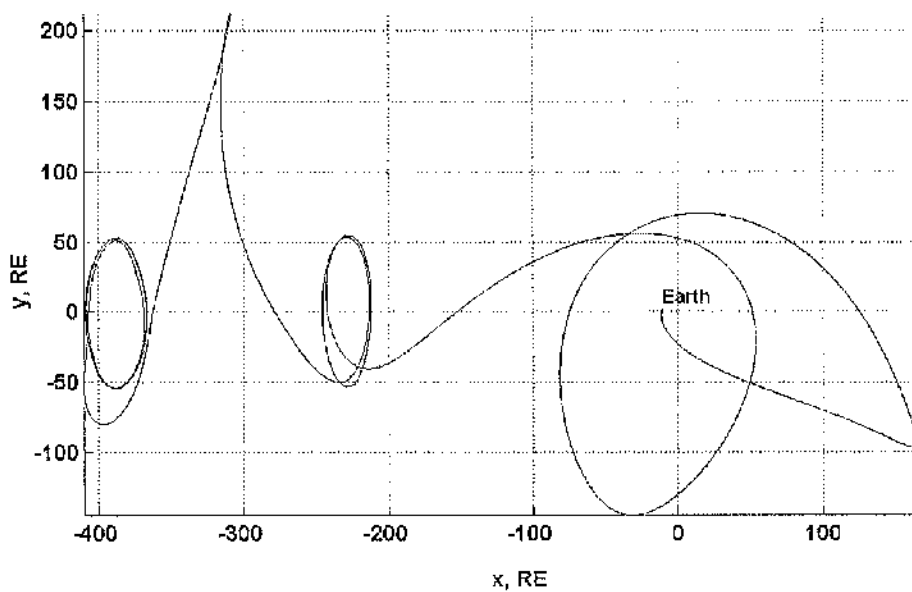
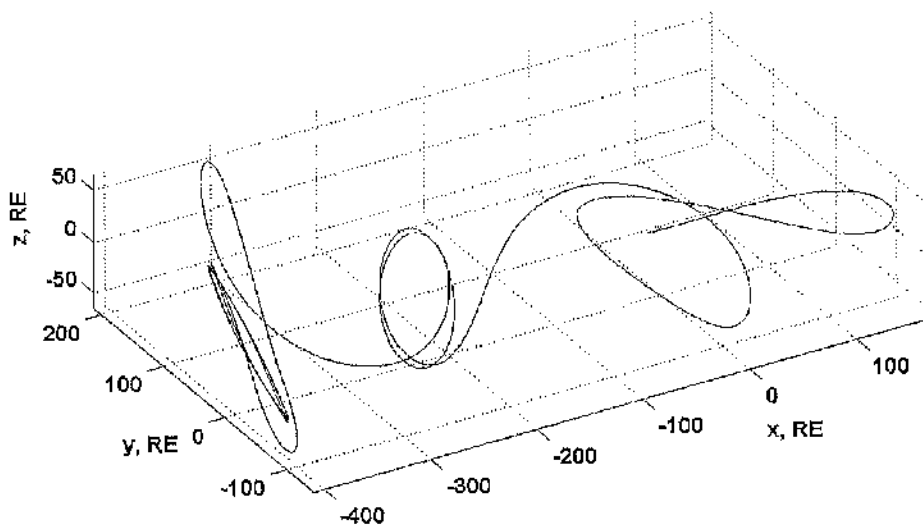


Figure 6-11 Insertion to Lissajous trajectory at L_1 followed by slow solar sail deployment

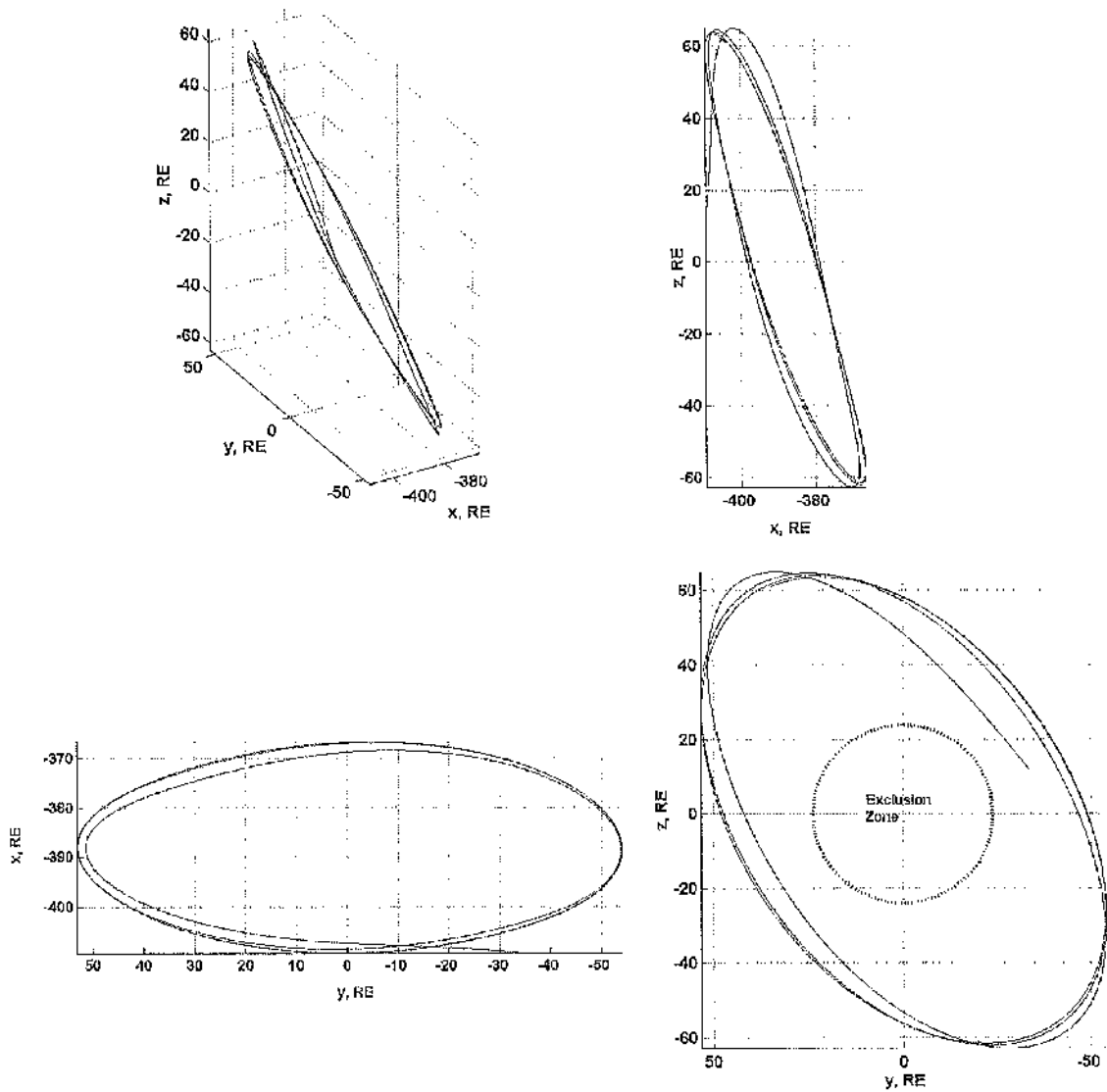


Figure 6-12 Lissajous trajectory around libration point sunward of L_1

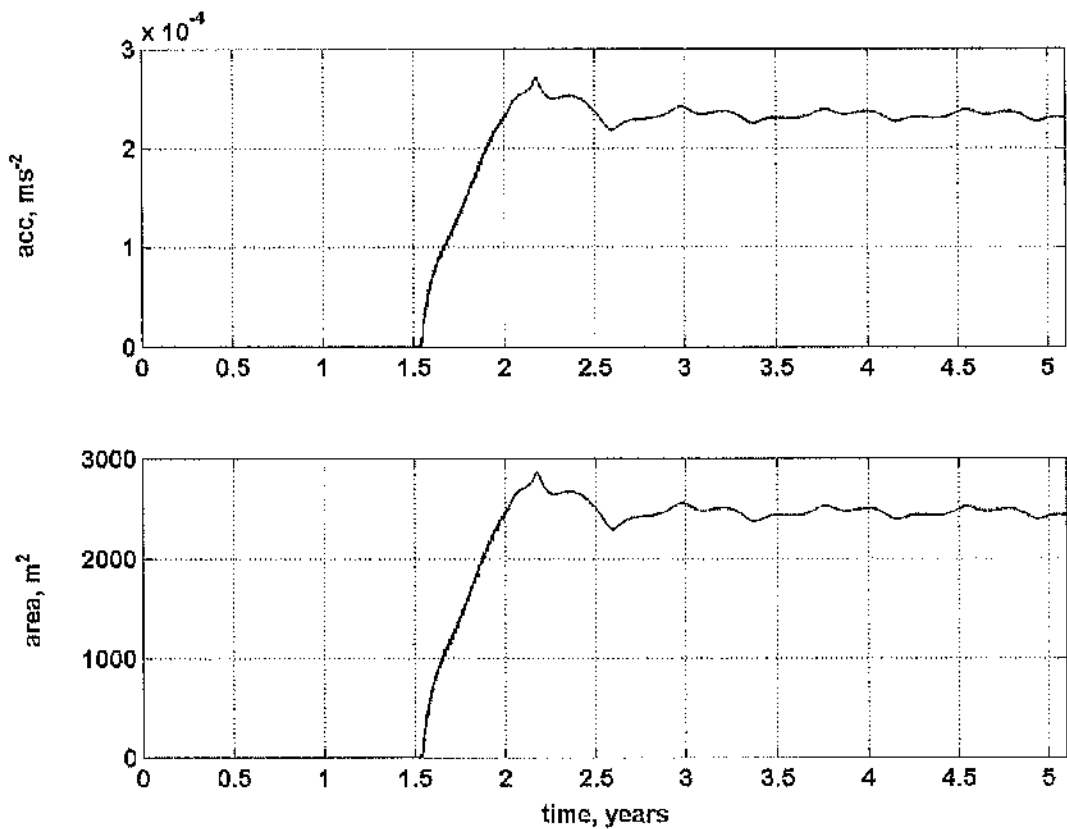


Figure 6-13 Solar sail area variation for Geostorm mission

6.2.3 Conclusions

This study demonstrates a possible near-term mission for solar sail technology. The sail loading of 12 gm^{-2} is comparable to the Cosmos 1 solar sail which has sail loading of 11 gm^{-2} [Freidman, 2005]. The total sail area of 2864 m^2 is achievable using near-term gossamer structure fabrication techniques.

As the transfer vehicle is initially inserted onto a Lissajous trajectory orbiting L_1 , the option exists for transfer to be achieved as a 'piggy-back' on a mission destined for orbit at L_1 . The sail could be deployed gradually spiralling sunwards while the transfer vehicle is left in a controlled orbit about the Lagrange point. For a new propulsion technology, it is important to lower the mission risks to improve feasibility. If an error occurs during sail deployment, the primary mission at L_1 could still achieve some useful science goals.

Chapter 7 Conclusions and Further Work

Five key work objectives to be investigated for this thesis were listed in Section 1.6. These objectives are reproduced below along with the relevant findings and conclusions. Suggestions for further study are also outlined.

1. *Develop appropriate dynamical models representing the motion of a solar sail in the vicinity of a planet. These models should include both the gravitational influence of the relevant bodies and the acceleration due to solar radiation pressure.*

The dynamics of an ideal solar sail in the vicinity of a planet were initially investigated in a two-body context. The two-body equations of motion, including a constant axial force to represent the acceleration due to solar radiation pressure, were derived using cylindrical polar coordinates in Section 2.1. It was demonstrated in Section 1.5 that the ideal sail acceleration model provides a good approximation of the force exerted on the sail provided the sail surface normal vector does not deviate greatly from the Sun-line.

The problem was further investigated in a three-body context including the solar gravitational influence and the rotational effects of the planet orbiting the Sun. Three models were investigated including Hill's approximation of the three-body problem, the circular restricted and elliptical restricted three-body problems with complete derivations provided in Section 3.1, Section 4.1.1 and Section 4.1.2 respectively. The sail acceleration model was improved to include the perturbations due to the time varying distance between the Sun and the solar sail.

In addition, the photo-gravitational two-centre problem was also derived to investigate temporary trapping of interstellar matter at libration points between nearby stars. This model represents a special case of the three-body problem which assumes a scenario where the two primary bodies are fixed relative to each other. The two-centre problem was shown to represent a reasonable approximation of the interstellar dynamics provided the relative stellar motion is less than 100ms^{-1} .

2. *Identify artificial libration points using these dynamical models including the acceleration due to solar radiation pressure. The stability of these libration points can be determined using eigenvalue analysis methods.*

Artificial libration points were investigated in each of the derived dynamics models. In the two-body case, the solar sail acceleration can be used to produce a continuum of libration points in the anti-Sun direction by cancelling a component of gravity. In the three-body cases, as the solar sail acceleration is constrained to the anti-Sun direction, artificial libration points are restricted to a region sunwards of L_1 or between the central body and L_2 . As demonstrated in Section 1.5, if the non-perfect sail acceleration model is applied, the distance above the ecliptic plane which a libration point can be generated is reduced due to the restriction on the achievable sail pitch angle relative to the Sun-line.

A Jacobi integral was derived in the three-body cases and a series of Hill's surfaces were generated using Jacobi constants calculated at the artificial libration points. Jacobi constants evaluated at an on-axis libration point were shown to represent critical values which define a closed zero-velocity surface. For energies greater than the critical energy, a gap in the Hill's surface opens around the libration point. Hill's surfaces are a useful tool for investigating bound motion as gaps in the surface can facilitate escape. The acceleration due to solar radiation pressure reduces the energy required for escape in the anti-Sun direction therefore, the surface is closed sunward of the central body in the case of libration points between the central body and L_2 .

It was apparent that the Jacobi integral evaluated at a libration point with zero-velocity is analogous to generating a pseudo-potential energy surface in the vicinity of the libration point. A local saddle point exists in the vicinity of the on-axis libration points which suggests that these points are likely to be unstable. This was verified using eigenvalue analysis of the linearised equations which yields two oscillatory and two divergent modes of the in-plane motion.

In the two-centre model, an on-axis libration point was identified at the centre of mass of the two primary bodies. Including the acceleration due to solar radiation pressure was found to reduce the effective mass of the primary bodies displacing the centre of mass depending on the stellar luminosity.

3. *Generate non-Keplerian orbits around artificial libration points. This will include both Lissajous and halo orbits demonstrated around the L_1 and L_2 Lagrange points of the three-body problem. The stability of these orbits will be evaluated using eigenvalue and energy analysis methods.*

Circular displaced orbits were investigated in both a two- and three-body context. A stability condition was derived for these orbits as $\rho_o > 2\sqrt{2}z_o$, using a linear approximation of the two-body equations and a nonlinear analysis. Further analysis of the orbit stability was performed using a Jacobi-type integral where by it was demonstrated that the motion of a stable orbit is bound within a closed zero-velocity surface. As expected, the two-body stability condition agrees closely with the observed three-body stability in cases where the orbit is near to the central body.

Further from the Earth, the solar sail experiences a comparable gravitational influence from the Sun therefore the circular displaced orbit no longer represents an accurate solution of the dynamical equations. A more accurate solution was developed using a linear approximation of Hill's equations, which yields initial conditions that converge toward a quasi-periodic Lissajous orbit.

Periodic halo orbits were also investigated around artificial libration points in the circular and elliptical three-body problem. Richardson's third order approximation was applied to obtain initial conditions which converge toward a halo orbit. These large amplitude trajectories have the advantage that the solar sail avoids the telemetry exclusion zone sunwards of the Earth, unlike the smaller amplitude quasi-periodic Lissajous orbits.

Halo orbits were also investigated in the two-centre problem. It was demonstrated that for constant angular velocity, an unstable orbit exists in the vicinity of the centre of mass and two stable orbits near each of the fixed masses. The stable orbits correspond to the two-body circular orbits displaced from the respective star due to the uniform axial gravity exerted by the distant star. In the photo-gravitational problem, the effective stellar mass is reduced due to the repelling stellar radiation pressure, which leads to a range of possible orbit radius depending on the particle areal density.

4. *Identify manifolds associated with the non-Keplerian orbits which can be utilised for orbit insertion from a point near to the central body.*

Manifold surfaces were investigated for the two-body circular displaced orbits and three-body Lissajous trajectories. A closed-form solution was obtained by transforming the two-body problem into parabolic coordinates and applying the Hamilton-Jacobi method. It was demonstrated that manifolds which wind-off and onto a circular displaced orbit are bound between a set of paraboloid surfaces. A new family of highly perturbed orbits were identified by slightly perturbing the nominal acceleration. In the case of unstable circular displaced orbits, the resulting trajectories were shown to provide transfer trajectories which pass near to the Earth. These new manifold families were used in Section 6.1 to identify a set of initial conditions to insert a solar sail onto a circular displaced orbit for a novel Geomagnetic tail mission.

Manifolds were also investigated which wind-off and onto a Lissajous trajectory around artificial libration points near L_1 and L_2 . Hill's surfaces were generated in order to identify the closest approach distances to the Earth. It was apparent that, in some cases, the closest approach distance occurred after several encounters with the Earth. This results in a trade-off between the time duration for insertion and the mission Δv requirements. In the case of orbits around libration points sunwards of L_1 , the Hill's surface is open around L_2 which indicates that escape is likely in the anti-Sun direction. In this case, the first encounter of the solar sail with the Earth is selected as the closest approach distance for orbit insertion. An example of insertion to a Lissajous orbit around L_1 was investigated in Section 6.2 for the proposed Geostorm mission.

Manifolds were also investigated in the photo-gravitational two-centre problem. A closed-form solution, similar to the two-body case, was derived by transforming the problem into confocal elliptical coordinates. It was demonstrated that the manifolds are bound between ellipsoid surfaces. These surfaces represent possible transfer trajectories for particle transits between passing star systems. An implication of stellar radiation pressure is that particles can only be captured by star systems where the areal density corresponds to lightness number less than unity. This implies there would be a natural selection of the particle surface areas which can be captured by a star depending on the stellar luminosity.

5. *Investigate solar sail station-keeping techniques to prevent escape from the desired orbits after insertion. Two possible methods to control the solar sail acceleration include variation of the solar sail area and variation of the solar sail attitude.*

Solar sail control techniques were investigated to provide orbit control after insertion to circular displaced orbits, Lissajous trajectories and periodic halo orbits generated around artificial libration points. A two-body controller was developed which applies trims to the sail area or sail pitch angle based on an error between the actual trajectory and a reference trajectory. Optimal gains were calculated using a linear quadratic regulator. Both techniques were demonstrated for control of circular displaced orbits generated in a two- and three-body context. Due to the close proximity to the Earth, circular displaced orbits require solar sail accelerations of order 1 mms^{-2} , which corresponds to a sail area of order $1 \times 10^5 \text{ m}^2$ for a 100 kg payload. Due to the large sail area, the sail pitch angle variation technique is the more appropriate of the two control methods to avoid damaging the thin solar sail. For the Geomagnetic tail mission, investigated in Section 6.1, the required sail acceleration is approximately 6 mms^{-2} which corresponds to a $3 \times 10^5 \text{ m}^2$ solar sail with total payload mass of 100 kg. This mission clearly requires an extremely high performance solar sail which is not achievable in the foreseeable future.

Similar control methods were developed to provide station-keeping at a nominal Lissajous orbit. Again, optimal gains were selected using a linear quadratic regulator. Both techniques were demonstrated to provide control after near Earth insertion to Lissajous orbits sunwards of L_1 and L_2 . Near to the Lagrange points, the required sail acceleration is of order 0.01 mms^{-2} which requires sail areas of order 100 m^2 for a 100 kg payload. These small sail accelerations could be achieved using four reflective tip-vanes attached to a central payload. The sail area variation technique is the more appropriate method in this case as control can be achieved with small variations to the reflecting sail surface area. The sail area variation controller was applied in Section 6.2 to produce a trajectory which gradually spirals sunwards from L_1 to a controlled Lissajous orbit $390 R_E$ from the Earth. This mission would require a sail acceleration of 0.3 mms^{-2} , which can be achieved using a 3000 m^2 solar sail with a total mass of 100 kg. This reasonable sail performance could be achieved with near-term solar sail technology.

By combining the sail area and sail pitch angle variation control methods, a three-axis control method was developed which provides full controllability in a three-body context. This method was demonstrated to provide control at periodic halo orbits in both the circular and elliptical restricted three-body problems. In the case of an artificial libration point generated near to L_1 in the elliptical three-body problem, the required y -axis acceleration is comparable to the x -axis acceleration. The resulting sail yaw angle tends toward $\pi/2$ which produces an unbound sail area due to the $\cos^2 \phi$ acceleration dependency. It was found that generating an artificial libration point displaced further sunward of L_1 requires a larger x -axis acceleration which subsequently reduces the required yaw-angle for orbit control.

The dynamics of a solar sail in the vicinity of a planet have been thoroughly investigated in a two- and three-body context. Recommended further work includes extending the problem to include the gravitational influence of the moon forming a Sun-Earth-Moon-sail four body problem. The lunar gravity would have a significant influence on the two-body circular orbits displaced $60 R_E$ from the Earth. It would be interesting to examine how the insertion manifolds are mutated by the inclusion of the lunar tide terms.

Solar sail area and pitch angle variation has been demonstrated to provide control at a nominal reference orbit. The three-axis solar sail control method could also be applied to prevent escape from the transfer trajectory during orbit insertion. This would enable the solar sail to perform correction maneuvers during transit to the orbit and prevent gradual divergence from the manifold.

The investigation of circular displaced orbits could be extended to near-Earth asteroids. Due to the reduced gravity of these comparatively smaller bodies, artificial libration points could be generated using lower performance solar sails than in the case of the Earth. This would offer a possible near-term application of circular displaced orbits generated using solar sail propulsion. However, the non-uniform gravitational field due to the often irregular shape of the asteroids would require complicated dynamics models to be developed to accurately represent the solar sail motion. Alternatively, circular displaced orbits could be investigated at planets nearer to the Sun, such as Mercury. The increased solar radiation pressure would enable displaced orbits to be generated using smaller solar sails.

Other possible applications of solar sails could be considered to increase mission lifetimes by enabling improved orbit control. This may include pitching the solar sail to increase/reduce the orbit angular velocity to alter the radius of a circular displaced orbit. Also, a process of furling/unfurling the solar sail could be adopted to enable patching of heteroclinic and homoclinic manifolds. This would enable transfer of the solar sail between Lissajous trajectories or halo orbits around artificial libration points near L_1 and L_2 . Similarly, the displacement distance of circular displaced orbits could be altered by identifying intersecting manifolds which wind onto alternative orbits requiring negligible Δv .

Finally, it would be useful to determine the limitations of the sail area and sail pitch angle variation controllers. The optimal gain method determines the required sail surface area or sail orientation to prevent escape from a reference orbit. The rate at which the solar sail can be furlled/unfurled, to modulate the sail surface area, or the sail orientation controlled, using reflective tip-vanes or centre-of-mass/centre-of-pressure offset, will restrict the accuracy of the actual control signal compared to the required control signal.

Chapter 8 References

- 1) Astakhov, S.A., Farrelly, D., (2004) 'Capture and escape in the elliptic restricted three-body problem', *Monthly Notices of the Royal Astronomical Society*, Vol 354, pp 971
- 2) Baker, R.M., Makemson, M.W., (1960), 'An Introduction to Astrodynamics', Academic Press, pp 3-7
- 3) Barnard, E.E. (1916), 'A Small Star with a Large Proper-Motion', *The Astronomical Journal*, Vol 29, No 23, Sept 15th, pp 181-3
- 4) Barr, M, (2002), 'Closed-Loop Control', *Embedded Systems Programming*, Aug, pp. 55-56
- 5) Barrabés, E, et al, (2004), 'Notes for the gravitational assisted trajectories lectures', *Advanced Topics in Astrodynamics*, Summer Course, Barcelona, July, Ch2
- 6) Beckman, M, (2002), 'Orbit Determination Issues for Libration Point Missions', *Libration Point Orbits and Applications - Proceedings of the Conference*, Aiguablava, Spain, 10 - 14 June
edited by Gómez, G, Lo, M and Masdemont, J.J.
- 7) Bennet, C.L, et al, (2003), 'The Microwave Anisotropy Probe Mission', *The Astrophysical Journal*, Vol. 583 part1, pg 1-23
- 8) Belbruno, E.A. and Carrico, J.P., (2000), 'Calculation of weak stability boundary ballistic lunar transfer trajectories', *American Institute of Aeronautics and Astronautics*, AIAA 2000-4142
- 9) Belbruno, E.A. and Miller, J.K., (1993), 'Sun perturbed Earth-to-Moon Transfers with Ballistic Capture', *Journal of Guidance, Control and Dynamics*, Vol. 16, No. 4, Jul-Aug pp 770-775
- 10) Bertin, G, (2000), 'Dynamics of Galaxies', Cambridge University Press, Ch 2
- 11) Bookless, J and McInnes, C.R., (2006), 'Dynamics and Control of Displaced Periodic Orbits using Solar Sail Propulsion', *Journal of Guidance, Control and Dynamics*, Vol 29, No3, May-June, pp 527-537
- 12) Bookless, J, and McInnes, C.R., (2005), 'Control of Lagrange Point Orbits Using Solar Sail Propulsion', 56th IAC Congress, Fukuoka, Japan, IAC-05-C1.6.03
- 13) Bookless, J and McInnes, C.R, (2004), 'Study on Libration Points of the Sun and the Interstellar Medium for Interstellar Travel', *Ariadna Study*, ESA Technical Report, Contract No. ITT AO/1-4532/03/NL/MV

- 14) Born, M, (1927), 'The Mechanics of the Atom', G. Bell and Sons Ltd, pp 212-220
- 15) Breakwell, J.V. and Brown, J.V., (1979), 'The "Halo" Family of 3 Dimensional Periodic Orbits in the Earth-moon Restricted 3-Body Problem', *Celestial Mechanics*, No. 20, pp 389-404
- 16) Broucke, R, (1979), 'Travelling Between the Lagrange Points and the Moon', *Journal of Guidance, Control and Dynamics*, Vol 2, No 4, pp 257-263
- 17) Broucke, R, (1969), 'Stability of Periodic Orbits in the Elliptic, Restricted Three Body Problem', *AIAA Journal*, Vol 7, No 6, pp 1003-1009
- 18) Burns, R.E., (1968), 'Motion of an artificial satellite under combined influence of planar and Keplerian force fields', NASA Technical Note, NASA TN D-4622, George C. Marshall Space Flight Center, Huntsville, Ala
- 19) Cielaszyk, D and Wie, B, (1996), 'New Approach to Halo Orbit Determination and Control', *Journal of Guidance, Control and Dynamics*, Vol. 19, No. 2, Mar-Apr
- 20) Cobos, J and Masdemont, J, (2002), 'Astrodynamical Applications of Invariant Manifolds Associated with Collinear Lissajous Libration Orbits', *Libration Point Orbits and Applications - Proceedings of the Conference, Aiguablava, Spain, 10 - 14 June, edited by Gómez, G, Lo, M and Masdemont, J.J.*
- 21) Colombo, G, (1961), 'The Stabilization of an artificial satellite at the inferior conjunction of the Earth-Moon system', SAO Special Report No. 80, Smithsonian Institution Astrophysical Observatory
- 22) Dachwald, B and Wolfgang, S, 'Solar Sailerft of the First Generation: Mission Applications to Near-Earth Asteroids', 54th International Astronautical Congress, Bremen, Germany, IAC-03-Q.5.03
- 23) Dankowicz, H, (1994), 'Some Special Orbits in the Two-body Problem with Radiation Pressure', *Celestial Mechanics and Dynamical Astronomy*, Vol. 58, pp 353-370
- 24) D'Azzo, J.J and Houpis, C.H., (1995), 'Linear Control System Analysis and Design: Conventional and Modern', *McGraw-Hill Series in Electrical Engineering*, 4th Ed, Chap 13, pp 423-461
- 25) D'azzo, J.J and Houpis, C.H., (1966), 'Feedback Control and System Analysis and Synthesis', *McGraw-Hill Inc.*, 2nd Ed, Ch 7
- 26) Dougherty, T, (1995), 'Systems and Control – An Introduction to Linear, Sampled and Non-Linear Systems', *Advanced Series in Electrical and Computer Engineering*, World Scientific Publishing Co. Pte. Ltd, Ch 4
- 27) Dungey, J.W., (1961), 'Interplanetary Magnetic Field and the Auroral Zones', *Physics Review Letters*, Vol. 6, No.2, pp 47-48

- 28) Dunham, D and Farquhar, R, (2002) 'Libration point missions 1978 – 2002', *Libration Point Orbits and Applications - Proceedings of the Conference, Aiguablava, Spain, 10 - 14 June* edited by Gómez, G, Lo, M and Masdemont, J.J.
- 29) Ehrenfreund, P and Foing, B.H., (1996), 'Resolved profiles of diffuse interstellar bands: evidence for rotational contours of gas-phase molecules', *Astronomy and Astrophysics*, Vol. 307, pp L25-L28
- 30) Enea, S.S and Telespazio, G.V., 'The Aurora Project: Removal of Plastic Substrate to Obtain an All-Metal Solar Sail', *Acta Astronautica*, Elsevier Science Ltd, Vol. 44, Nos 2-4, pp147-150
- 31) Escobal, P.R., (1968), 'Methods of Astrodynamics', John Wiley & Sons Inc., Chap 5.2, pp 153-165
- 32) Farquhar, R.W., (2001), 'The Flight of ISEE-3/ICE: Origins, Mission History and a Legacy', *The Journal of Astronautical Sciences*, Vol 49, No. 1, Jan-Mar, pp 23-73
- 33) Farquhar, R.W., et al, (1980), 'Optimal Maneuvers for the First Libration-Point Satellite', *Journal of Guidance, Control and Dynamics*, Vol. 3, No. 6, pp 549-554
- 34) Farquhar, R.W, Muilhonen, D.P. and Richardson, D.L., (1977), 'Mission Design for a Halo Orbiter of the Earth', *Journal of Spacecraft and Rockets*, Vol 14, No 3, pp 170-177
- 35) Farquhar, R.W. and Kamel, A.A, (1973), 'Quasi-periodic orbits about the trans lunar libration point', *Celestial Mechanics*, Vol. 7, pp 458-473
- 36) Farquhar, R.W., (1970a), 'The Control and use of Libration-Point Satellites', NASA Technical Report, NASA-TR R-346
- 37) Farquhar, R.W. (1970b), 'Limit Cycle Analysis of a controlled libration-point satellite', *The Journal of the Astronautical Sciences*, Vol XVII, No. 5, pp 267-291
- 38) Folta, D (2004), 'Formation flying design and applications in weak stability boundary regions', *Annals New York Academy of Sciences*, pp 95-111
- 39) Forward, R.L., (1991), 'Statite: A Spacecraft that Does Not Orbit', *Journal of Spacecraft*, Vol 28, No 5, pp 601-611
- 40) Forward, R.L., (1985), 'Starwisp: An ultra-light interstellar probe', *Journal of Spacecraft*, Vol. 22, No. 3, May-June, pp 345-350
- 41) Friedland, B, (1986), 'Control System Design: An Introduction to State-Space Methods', McGraw-Hill Series in Electrical Engineering, McGraw-Hill Inc., New-York, Chap 9, pp 337-369

- 42) Friedman, L. (2005), 'The End of Cosmos 1, The Beginning of the Next Chapter', available at www.planetary.org/solarsail
- 43) Friedman, L, et al, (2004), 'Cosmos 1: The world's first solar sail spacecraft', American Astronautical Society: Space Flight Mechanics Conference, 8th – 12th Feb, Maui, Hawaii, AAS 04 101
- 44) Garwin, R.L., (1958), 'Solar Sailing – A Practical Method of Propulsion within the Solar System', Jet Propulsion, Mar, pp 188-190
- 45) Genta, G and Brusa, E, (1999), 'The Aurora Project: A New Sail Layout', Acta Astronautica, Elsevier Science Ltd, Vol. 44, Nos 2-4, pp141-146
- 46) Glendinning, P, 'Stability, instability and chaos: an introduction to the theory of nonlinear differential equations', Cambridge Texts in Applied Mathematics, pp 77-88
- 47) Gliese Catalogue (1991), Centre de Données Astronomiques de Strasbourg, VizieR Service, Nearby Stars, Preliminary 3rd Version, <http://cdswcb.u-strasbg.fr/viz-bin/VizieR?-source=V/70A>
- 48) Goldstein, H, (1959), 'Classical Mechanics', Addison-Wesley Publishing Company, Chap 9, pp 273-288
- 49) Gómez, G, et al, (2004), 'Connecting orbit and invariant manifolds in the spatial three-body problem', Nonlinearity, Vol 17, No 5, pp 1571 - 1606
- 50) Groth, S.I., (2004), 'Fullerenes and Buckyonions in the Interstellar Medium', Lecture Notes and Essays in Astrophysics I, proceedings of the astrophysics symposium held during the first centennial of the Royal Spanish Physical Society, Madrid, available on <http://www.slac.stanford.edu/econf/C0307073/>
- 51) Hagihara, Y, (1975a), 'Celestial Mechanics – Differential Equations in Celestial Mechanics', Vol III, part 1, pp 10-21
- 52) Hagihara, Y, (1975b), 'Celestial Mechanics – Periodic and Quasiperiodic Solutions', Vol IV, part 1, pp 33-47
- 53) Hénon, M and Petit, J, (1986), 'Series Expansions for Encounter-type Solutions of Hill's Problem', Celestial Mechanics, **38**, pp 67-100
- 54) Herbeck, L, et al, (2003), 'Review on Present Solar Sail Hardware Developments', 54th IAC Congress, Bremen, Germany, IAC-03-I.1.04
- 55) Howard, J.E, (1995a), 'Saddle-point ionization and the Runge-Lenz invariant', Physical Review A, Vol 51, No 5, May, pp 3934-3946

- 56) Howard, J.E., Wilkerson, T.D., (1995b), 'Problem of two fixed centers and a finite dipole: A unified treatment', *Physical Review A*, Vol 52, No 6, Dec, pp 4471-4492
- 57) Howell, K.C. and Pernicka, H.J., (1993), 'Stationkeeping Method for Libration Point Trajectories', *Journal of Guidance, Control and Dynamics*, Vol. 16, No. 1, pp 151-9
- 58) Howell, K.C., (1984), 'Three-dimensional, Periodic, "Halo" Orbits', *Celestial Mechanics*, No 32, pp 53-71
- 59) Huttunen, K.E.J., et al, (2002), 'April 2000 magnetic storm: Solar wind driver and magnetospheric response', *Journal of Geophysical Research*, Vol 107, No A12, pp 1440-1461
- 60) Jacobs, O.L.R., (1993), 'Introduction to Control Theory', 2nd Ed, Oxford Science Publications, Oxford University Press
- 61) Jordan, D.W. and Smith, P, (1999), 'Nonlinear Ordinary Differential Equations – An Introduction to Dynamical Systems', 3rd Ed, Oxford Applied and Engineering Mathematics, Oxford University Press, Ch 8, 12
- 62) Kim, M and Hall, C.D., (2001), 'Lyapunov and Halo Orbits about L_2 ', AAS/AIAA Astrodynamics Specialists Conference, Quebec City, Canada, Jul 30 – Aug 2
- 63) Koon, W.S., et al, (2002), 'Constructing a Low Energy Transfer between Jovian Moons' *Celestial Mechanics*, Dedicated to Donald Saari for his 60th Birthday. Proceedings of an International Conference on Celestial Mechanics, 15-19 December, 1999 at Northwestern University, Evanston, Illinois. Edited by Alain Chenciner et al, American Mathematical Society, Contemporary Mathematics, Vol 292, p 129
- 64) Koon, W.S., et al, (2001a), 'Low Energy Transfer to the Moon', *Celestial Mechanics and Dynamical Astronomy*, **81**, pp 63-73
- 65) Koon, W.S., et al, (2001b), 'Resonance and Capture of Jupiter Orbits', *Celestial Mechanics and Dynamical Astronomy*, **81**, pp 27 - 38
- 66) Koon, W.S, et al, (1999), 'Dynamical Systems, the Three-body Problem and Space Mission Design', International Conference on Differential Equations, Berlin, Edited by Fiedler, B, Gröger, K and Sprekels, J, *World Scientific*, 2000, pp 1167-1181
- 67) Krivov, A.V., et al, (1996), 'Dynamics of Mars-orbiting Dust: Effects of Light Pressure and Planetary Oblateness', *Celestial Mechanics and Dynamical Astronomy*, No. 63, pp 313-339
- 68) Landau L.D. and Lifschitz, E.M., (1976), 'Mechanics – Course of Theoretical Physics', Vol. 1, Oxford, Pergamon Press, pp. 151-154

- 69) Leipold, M, et al, (2003), 'Solar Sail Technology Development and Demonstration', Acta Astronautica, Vol 52, pp 317-326
- 70) Leipold, M, et al, (1999), 'ODISSEE – A Proposal for Demonstration of a Solar Sail in Earth Orbit', Acta Astronautica, Vol 45, Nos 4-9, pp 557-566
- 71) Leipold, M, et al, (1996), 'Mercury Sun-Synchronous Polar Orbiter with a Solar Sail', Acta Astronautica, Vol 39, No 1, pp 143-151
- 72) Lindgren, L and Dravins, Dainis, (2003), 'The Fundamental definition of "radial velocity"', Astronomy and Astrophysics, No. 401, pp 1185-1201
- 73) Li-Xiang, L, (2001), 'On Feedback Control of Delayed Chaotic System', Chinese Physics, Chinese Physics Society and IOP Publishing Ltd, Vol 10, No 9, Sept, pp 796-804
- 74) Lo, M.W. and Ross, S.D. (2001), 'The Lunar L1 Gateway: portal to the stars and beyond', AIAA Space 2001 Conference, Albuquerque, New Mexico, Aug 28-30
- 75) Macdonald, M and McInnes, C.R., (2004), 'A Near-term Roadmap for Solar Sailing', 55th IAC Congress, Vancouver, Canada, IAC-04-U.1.09
- 76) Marchal, C, (1990), 'The Three-body Problem', 'Studies in Astronautics, Volume 4, Elsevier, Ch 9,
- 77) Marsden, J.E. and Ross, S, (2005), 'New methods in celestial mechanics and mission design', Bulletin (New Series) of the American Mathematical Society, Vol 43, No 1, pp 43-73
- 78) Marshall, S.A., (1978), 'Introduction to Control Theory', Macmillan Publishers Ltd, London, Chap 6
- 79) Massa, D and Savage, B.D. (1998), 'Measurements of Interstellar Extinction', 'Section 1: Dust in the Diffuse Interstellar Medium', Interstellar Dust, proceedings of the 135th symposium of the International Astronautical Union, Kluwer Academic Publishers, pp 3-21
- 80) McInnes, C.R., Macdonald, M and Hughes, G, (2004), 'Solar Polar Orbiter', Technical Assistance in the Study of Science Payloads Transported Through Solar Sailing, Technical Note 10, ESTEC 16534/02/NT/NR
- 81) McInnes, C.R., (1999a), 'Solar Sailing Technology, Dynamics and Mission Applications', Springer-Praxis Series in Space Science and Technology, Springer-Verlag, Berlin, Ch 3
- 82) McInnes, C.R., (1999b), 'Artificial Lagrange Points for a Non-Perfect Solar Sail', Journal of Guidance, Control and Dynamics, Vol 22, No 1, pp. 185-187

- 83) McInnes, C.R., (1998a), 'Dynamics, Stability and Control of Displaced Non-Keplerian Orbits', *Journal of Guidance, Control and Dynamics*, Vol 21, No 5, Sept-Oct, pp 799-805
- 84) McInnes, C.R., (1998b), 'Passive Control of Displaced Solar Sail Orbits', *Journal of Guidance, Control and Dynamics*, Vol.21, No 6, pp 975-982
- 85) McInnes, C.R., (1994), 'Solar Sail Parking in Restricted Three Body Systems', *Journal of Guidance, Control and Dynamics*, Vol 17, No 2, pp 399-406
- 86) McInnes, C.R., Simmons, J.F.L., (1992a), 'Solar Sail Halo Orbits I: Heliocentric Case', *Journal of Spacecraft and Rockets*, Vol. 29, No. 4, pp 466-471
- 87) McInnes, C.R., Simmons, J.F.L., (1992b), 'Solar Sail Halo Orbits II: Geocentric Case', *Journal of Spacecraft and Rockets*, Vol 29, No. 4, pp 472-479
- 88) Miele, A, (1960), 'Theorem of Image Trajectories in the Earth-Moon Space', *Acta Astronautica*, Vol 6, pp 225-232
- 89) Mignard, F, (1982), 'Radiation Pressure Dust Particle Dynamics', *Icarus*, No. 49, pp 347-366
- 90) Molostov, A.A, Shvartsburg, A.A, (1992), 'Heliocentric halos for a solar sail with absorption', *Soviet Physics Doklady*, Vol. 37, No. 3, pp 149-152
- 91) Morgan, W.W, Keenan, P.C., Kellman, E., (1943), 'An Atlas of Stellar Spectra with an Outline of Spectral Classification', University of Chicago Press, Chicago
- 92) Morrow, E, et al, (2001), 'Solar Sail Orbit Operations at Asteroids', *Journal of Spacecraft and Rockets*, Vol 38, No 2, pp 279-286
- 93) Murphy, D, et al, (2004), 'Demonstration of a 10m Solar Sail System', AIAA 2004-1576, 45th AIAA/ASME/ASCE/AHS/ASC Structures Dynamics and Materials Conference, Palm Springs California, 19th-22nd Apr
- 94) Nayfeh, A, (1973), 'Perturbation Methods', *Pure and Applied Mathematics*, John Wiley and Sons, London, pp 56-60
- 95) NStars Database (1988), NASA, Ames Research Centre, California, <http://nstars.arc.nasa.gov/index.cfm>
- 96) Palutin, F, (1994), 'Stability and control problems in Earth-Moon Lagrangian Point L2', *Journal of the British Interplanetary Society*, Vol. 47, pp 497-504

- 97) Peters, P.N., J.C. Gregory and J.T. Swann, (1986), 'Effects on optical systems from interactions with oxygen atoms in low Earth orbits', *Applied Optics*, Vol 25, No. 8, pp 1290-1298
- 98) Richardson, D.L., (1980a), 'Analytic Construction of Periodic Orbits about the Collinear points', *Celestial Mechanics*, Vol. 22, pp 241-253
- 99) Richardson, D.L., (1980b), 'A Note on a Lagrangian Formulation for Motion about the Collinear Points', *Celestial Mechanics*, Vol. 22, pp 231-236
- 100) Richardson, D.L., (1980c), 'Halo Orbit Formulation for the ISEE-3 Mission', *Journal of Guidance, Control and Dynamics*, Vol 3, No 6, pp 543-548
- 101) Roberts, C.E., (2004), 'Sun-Earth L1 region Halo-to-Halo orbit and Halo-to-Lissajous orbit transfers', 18th International Symposium on Space Flight Dynamics, 11th -15th Oct
- 102) Ross, S.D., et al, (2003), 'Design of a Multi-Moon Orbiter', 13th AAS/AIAA Space Flight Mechanics Meeting, AAS 03-143, 9-13 Feb, Ponce, Puerto Rico
- 103) Russel, C.T., (1974), 'The Solar Wind and Magnetospheric Dynamics', *Correlated Interplanetary and Magnetospheric Observations*, edited by D.E. Page, D. Reidel Publications Co.
- 104) Salama, F, et al, (1996), 'Assessment of the Polycyclic Aromatic Hydrocarbon-Diffuse Interstellar Band Proposal', *The Astrophysical Journal*, No 458, pp 621-636
- 105) Scaglione, S, Vulpett, G, (1999), 'The Aurora Project: Removal of Plastic Substrate to Obtain an All-Metal Solar Sail', *Acta Astronautica*, Vol 44, Nos 2-4, pp 147-159
- 106) Scheeres, D.J. and Bellerose, J, (2005), 'The Restricted Full 4-body Problem: application to spacecraft motion about binary asteroids', *Dynamical Systems: An International Journal*, Vol. 20, No. 1, pp 23-44
- 107) Scheeres, D.J., (1995), 'Analysis of orbital Motion Around 433 Eros', *The Journal of the Astronautical Sciences*, Vol. 43, No. 4, Oct-Dec, pp 427-452
- 108) Scheffler, H and Elsässer, H, (1988), 'Physics of the Galaxy and Interstellar Matter', Springer-Verlag, Berlin, Heidelberg, Ch 1
- 109) Seboldt, W, Dachwald, B, (2003), 'Solar Sailcraft of the First Generation - Technology Development', 54th International Astronautical Congress, Bremen, Germany, IAC-03-S.6.03
- 110) Serban, R, et al, (2002), 'Halo orbit mission correction maneuvers using optimal control', *Automatica*, Elsevier Science Ltd, Vol 38, pp 571-583

- 111) Smart, W.M. (1953), 'Celestial Mechanics', Longmans Green and Co Ltd, Chap 2,3, pp 11 – 42
- 112) Soderblom, D.R., (1987), 'The Alpha Centauri System', Mercury, Sept-Oct, pp138-140
- 113) Stiefel, E.L and Scheifele, G, (1971), 'Linear and Regular Celestial Mechanics', Springer-Verlag, Chap 1-3
- 114) Szebehely, V, (1967), 'Theory of Orbits - The restricted problem of three bodies', Academic Press Inc., New York and London, Ch 1, 4, 5
- 115) Thurman, R and Worfolk, P.A., (1996), 'The geometry of halo orbits in the circular restricted three-body problem', The Geometry Centre, University of Minnesota
- 116) Tsander, F.A., (1924), 'From a Scientific Heritage', NASA Technical Translation TT F-541, pg 29, (quoting a report produced by Tsander - translated into English during 1967)
- 117) Tsu, T.C., (1959), 'Interplanetary Travel by Solar Sail', American Rocket Society Journal, Vol 29, pp 442-447
- 118) Villac, B.F. and Scheeres, D.J., (2003), 'Escaping Trajectories in the Hill Three-body problem and applications', Journal of Guidance, Control and Dynamics, Vol. 26, No. 2, pp 224-232
- 119) Waalkens, H, Jungc, A, Dullin, H.R., (2003) 'Quantum Monodromy in the two-centre problem', Journal of Physics A: Mathematical and General, Vol. 36, No 20, May 2003, pp307-314
- 120) West, J.L., Derbes, B, (2000), 'Solar Sail Vehicle System Design for the Geostorm Warning Mission', American Institute of Aeronautics and Astronautics, AIAA-2000-5326
- 121) Wie, B, (2002), 'Dynamics Modeling and Attitude Control of Solar Sail Spacecraft', NASA Solar Sail Technology Working Group Final Report, JPL Contract No. 1228156
- 122) Wie, B, (1998), 'Space Vehicle Dynamics and Control', AIAA Education Series, pp 240-260
- 123) Williams, D.R., (2001), 'Planetary Fact Sheets', NSSDC, NASA Goddard Space Flight Center, available online at <http://nssdc.gsfc.nasa.gov/planetary/planetfact.html>
- 124) Wright, J, (1992), 'Space Sailing', Gordon and Breach Science Publishers, Ch 3
- 125) Yen, C.L., (2004). 'Solar Sail Geostorm Warning Mission Design', 14th AAS/AIAA Space Flight Mechanics Conference, Maui, Hawaii, AAS 04-107

1st Order Coefficients

$$\lambda = \sqrt{\frac{(c_2 - 2) - \sqrt{9c_2^2 - 8c_2}}{2}}$$

$$\kappa = \frac{2\lambda}{\lambda + 1 - c_2}$$

2nd Order Coefficients

$$\alpha_{20} = \frac{3}{2}c_3A_x^2 - \frac{3}{4}c_3k^2A_x^2 - \frac{3}{4}c_3A_z^2$$

$$\beta_{21} = \frac{3}{2}c_3kA_x^2$$

$$\alpha_{21} = \frac{3}{2}c_3A_x^2 + \frac{3}{4}c_3k^2A_x^2$$

$$\gamma_{21} = \frac{3}{2}c_3A_xA_z = \gamma_{22}$$

$$\alpha_{22} = \frac{3}{4}c_3A_z^2$$

$$\rho_{20} = \frac{-\alpha_{20}}{(1 + 2c_2)}$$

$$\rho_{21} = \frac{4\lambda\beta_{21} - \alpha_{21}(4\lambda^2 - c_2 + 1)}{16\lambda^4 + 4\lambda^2(c_2 - 1) - 2c_2^2 + c_2 + 1}$$

$$\sigma_{21} = \frac{4\lambda\alpha_{21} - \beta_{21}(4\lambda^2 + 2c_2 + 1)}{16\lambda^4 + 4\lambda^2(c_2 - 1) - 2c_2^2 + c_2 + 1}$$

$$\rho_{22} = \frac{\alpha_{22}(-4\lambda^2 + c_2 - 1)}{16\lambda^4 + 4\lambda^2(c_2 - 1) - 2c_2^2 + c_2 + 1}$$

$$\sigma_{22} = \frac{4\lambda\alpha_{22}}{16\lambda^4 + 4\lambda^2(c_2 - 1) - 2c_2^2 + c_2 + 1}$$

$$\delta_{21} = -\frac{\gamma_{21}}{3\lambda}$$

$$\delta_{22} = \frac{\gamma_{22}}{\lambda}$$

3rd Order Coefficients [Thurman and Worfolk, 1996]

$$\alpha_{31} = -3c_3 \left(A_x \left(2\rho_{20} + \rho_{21} + \frac{k}{2}\sigma_{21} \right) + \frac{1}{2}A_z(\delta_{21} + \delta_{22}) \right) + \frac{3}{2}c_4 A_x (A_x^2(k^2 - 2) + 2A_z^2)$$

$$\alpha_{32} = -\frac{3}{2}c_3 A_x (2\rho_{21} - k\sigma_{21}) - \frac{1}{2}c_4 A_x^3 (2 + k^2)$$

$$\alpha_{33} = \frac{3}{2}c_3 (kA_x\sigma_{22} + A_z\delta_{21} - 2A_x\rho_{22}) - \frac{3}{2}c_4 A_x A_z^2$$

$$\alpha_{34} = -\frac{3}{2}c_3 (2A_x\rho_{22} + kA_x\sigma_{22} - A_z\delta_{22}) - \frac{3}{2}c_4 A_x A_z^2$$

$$\beta_{31} = \frac{3}{2}c_3 A_x (\sigma_{21} - 2k\rho_{20} + k\rho_{21}) + \frac{3}{2}c_4 k A_x \left(A_x^2 \left(\frac{3}{4}k^2 - 1 \right) + \frac{1}{2}A_z^2 \right)$$

$$\beta_{32} = \frac{3}{2}c_3 A_x (\sigma_{21} - k\rho_{21}) - \frac{3}{8}k c_4 A_x (4 + k^2)$$

$$\beta_{33} = \frac{3}{2}c_3 A_x (\sigma_{22} - k\rho_{22}) - \frac{3}{8}c_4 k A_x A_z^2$$

$$\beta_{34} = \frac{3}{2}c_3 A_x (\sigma_{22} + k\rho_{22}) + \frac{3}{8}c_4 k A_x A_z^2$$

$$\gamma_{31} = \frac{3}{2}c_3 (A_x(\delta_{21} + \delta_{22})) + A_z(\rho_{22} - 2\rho_{20}) + \frac{3}{2}c_4 A_z \left(\frac{3}{4}A_z^2 + \left(\frac{1}{2}k^2 - 2 \right) A_x^2 \right)$$

$$\gamma_{32} = -\frac{3}{2}c_3 \rho_{22} A_z - \frac{3}{8}c_4 A_z^3$$

$$\gamma_{33} = \frac{3}{2}c_3 (A_x\delta_{22} - A_z\rho_{21}) - \frac{3}{8}c_4 A_z A_x^2 (4 + k^2)$$

$$\gamma_{34} = -\frac{3}{2}c_3 (A_x\delta_{22} - A_z\rho_{21}) + \frac{3}{8}c_4 A_x^2 A_z (4 + k^2)$$

Final solution coefficients [Richardson, 1980a]

$$\begin{aligned}
 a_{21} &= \frac{3c_3(k^2 - 2)}{4(1 + 2c_2)} & a_{22} &= \frac{3c_3}{4(1 + 2c_2)} \\
 a_{23} &= -\frac{3c_3\lambda}{4kd_1} [3k^2\lambda - 6k(k - \lambda) + 4] & a_{24} &= -\frac{3c_3\lambda}{4kd_1} (2 + 3k\lambda) \\
 a_{31} &= -\frac{9\lambda}{4d_2} [4c_3(ka_{23} - b_{21}) + kc_4(4 + k^2)] + \\
 &\quad \left(\frac{9\lambda^2 + 1 - c_2}{2d_2} \right) [3c_3(2a_{23} - kb_{21}) + c_4(2 + 3k^2)] \\
 a_{32} &= -\frac{9\lambda}{4d_2} [4c_3(ka_{24} - b_{22}) + kc_4] - \\
 &\quad \frac{3}{2d_2} (9\lambda^2 + 1 - c_2) [c_3(kb_{22} + d_{21} - 2a_{24}) - c_4] \\
 b_{21} &= -\frac{3c_3\lambda}{2d_1} (3k\lambda - 4) & b_{22} &= \frac{3c_3\lambda}{d_1} \\
 b_{31} &= \frac{3}{8d_2} \{ 8\lambda [3c_3(kb_{21} - 2a_{23}) - c_4(2 + 3k^2)] + \\
 &\quad (9\lambda^2 + 1 + 2c_2) [4c_3(ka_{23} - b_{21}) + kc_4(4 + k^2)] \} \\
 b_{32} &= \frac{1}{d_2} \{ 9\lambda [c_3(kb_{22} + d_{21} - 2a_{24}) - c_4] + \\
 &\quad \frac{3}{8} (9\lambda^2 + 1 + 2c_2) [4c_3(ka_{24} - b_{22}) + kc_4] \} \\
 d_{21} &= -\frac{c_3}{2\lambda^2} & d_{31} &= \frac{3}{64\lambda^2} (4c_3a_{24} + c_4) \\
 d_{32} &= \frac{3}{64\lambda^2} [4c_3(a_{23} - d_{21}) + c_4(4 + k^2)] \\
 d_1 &= \frac{3\lambda^2}{k} [k(6\lambda^2 - 1) - 2\lambda] \\
 d_2 &= \frac{8\lambda^2}{k} [k(11\lambda^2 - 1) - 2\lambda]
 \end{aligned}$$

$$s_1 = \frac{1}{2\lambda[\lambda(1+k^2)-2k]} \left\{ \frac{3}{2}c_3[2a_{21}(k^2-2) - a_{23}(k^2+2) - 2kb_{21}] - \frac{3}{8}c_4(3k^4 - 8k^2 + 8) \right\}$$

$$s_2 = \frac{1}{2\lambda[\lambda(1+k^2)-2k]} \left\{ \frac{3}{2}c_3[2a_{22}(k^2-2) - a_{24}(k^2+2) - 2kb_{22} + 5d_{21}] - \frac{3}{8}c_4(12 - k^2) \right\}$$

$$l_1 = a_1 + 2\lambda^2 s_1$$

$$l_2 = a_2 + 2\lambda^2 s_2$$

$$a_1 = -\frac{3}{2}c_3(2a_{21} + a_{23} + 5d_{21}) - \frac{3}{8}c_4(12 - k^2)$$

$$a_2 = \frac{3}{2}c_3(a_{24} - 2a_{22}) + \frac{9}{8}c_4$$